Fabrication and Characterization of Macroscopic Graphene Layers on Metallic Substrates

Víctor Manuel Freire Soler

Departament de Física Aplicada i Òptica
Universitat de Barcelona

Fabrication and Characterization of Macroscopic Graphene Layers on Metallic Substrates

Víctor Manuel Freire Soler

Directores: Dr. Carles Corbella Roca (RUB)

Prof. Enric Bertran Serra (UB)

Programa de doctorado: Nanociencias, bienio 2010/2012

Memoria presentada para optar al grado de Doctor

Barcelona, Julio de 2014

“Research is what I’m doing
when I don’t know what I’m doing”

Wernher von Braun

CONTENTS

Agradecimientos

Voldria començar aquesta primera secció agraïnt en primer lloc al Prof. Enric Bertran (el meu tutor) la seva confiança amb mi i per haver-me fet un lloc al seu grup, FEMAN. La seva aportació científica i personal ha estat crucial en les diferents fases d'aquest treball. Els seus ànims i idees en moments on tot semblava perdut, sens dubte han marcat la diferència. Moltes gràcies!

Inestimable també ha estat l'ajuda del Dr. Carles Corbella (director d'aquesta tesi doctoral) elevant el nivell d'aquest document. Apart de la quantitat ingent de coneixements que m'ha aportat, el seu sentit de l'humor i la seva motivació científica m'han fet donar un pas endavant des que vaig començar amb ell la fase de Master fins ara.

Vull agraïr també la gran tasca realitzada pels Serveis Científico-Tècnics de la UB (CCTiUB), sense els quals no podria de cap manera haver desenvolupat la major part de la meva feina. En especial als tècnics de microscopia electrònica (SEM i EDS), i sobretot al Tariq i les meves mesures setmanals (sino diàries) d'espectroscòpia Raman. També al Taller Mecànic que ens ha proporcionat a mida totes les peces necessàries per poder dur a terme la construcció d'un reactor CVD i d'altres "invents". No em puc anar tampoc sense comentar la gran professionalitat de les secretàries i el secretari del departament, sobretot a la Maite i el Jordi. El caliu humà que he rebut de la seva part ha estat notable, apart de moltes de les millors converses aquests anys: relaxants algunes, i subversives d'altres.

Ich danke herzlichst Prof. Dr. Marika Schleberger vom Duisburg-Essen Universität (Fakultät für Physik) in Duisburg für die Möglichkeit, 3 Monate in ihrer Arbeitsgruppe zu arbeiten. Während meines Praktikum war ich in Kontakt mit sehr profesionellen Kollegen, die auch meine Freunde im Alltagstrott waren: Herr Ochedowski, Herr Ernst, Herr Reichert, Herr Osmani, Frau Bukowska, Frau Adam, usw. Vielen Dank an Alle für Euer Interesse und Geduld, die mir groβe Fortschritte meiner Deutsch Kenntnisse ermöglichten.

Gràcies també a tot el grup FEMAN pels quantiosos moments viscuts. Sobretot a l'Edgar "rojo", to my hard-working and office partner Shahzad, to the very "malaka" Stefanos, el Dr. Roger Amadé; dels inicis a la Coté i la Noemí pels sopars FEMAN, i de la última època la Leyre i sobretot el

David. Voldria agraïr també als incansables estudiants de màster que en el seu dia vaig ajudar i de retruc, també em van ajudar molt: el Jordi Badia, l'Adrià, l'Arevik, el Pep, l'Albert, i sobretot als "geordies", Jordi Salvat i Jorge Villena, que li van donar "el extra" de diversió a aquest últim any. Al grup FEMAN i al Departament de Física Aplicada i Òptica li devem també les calçotades, barbacoes, paelles, pops i demés aquelarres gastronòmiques (i els seus partits de futbol).

Aunque no haya tenido una influencia directa sobre este trabajo, me gustaría dar las gracias de todo corazón también a Juan Garay, profesor que sin duda fue pieza clave en mi formación científica durante mis años del "pavo", y en el presente también a nivel personal. Creo que por fin empiezo a ver la luz, parece que el cascarón ya se rompe. Eskerrik asko Juan!

A todos mis amigos que han estado por ahí, algunos más y otros menos, durante esta andadura. En especial a mi gran amigo Rubén por las "rutas" ciclistas y montañeras a las que le liaba una y otra vez. A Jaume y Félix (SIX PACK), la música amansa a las fieras. Y por supuesto, dedico también esta tesis doctoral a los del "Curs Zero" (si no me equivoco la primera del grupo), la mejor hornada de físicos y amigos que pudo dar la UB.

Para terminar, y por ello, lo más importante, quería agradecer infinitamente (jamás podrá ser retornado) todo el apoyo y cariño recibidos por mi familia: mis padres Manuel y Mª Luisa, y mi hermano David. Sin haber estado relacionados con la ciencia no han dudado un solo momento en darme todo lo necesario para llegar donde estoy ahora. Sé también que a mis abuelos les hubiera gustado ver esto (aunque no lo hubieran entendido), en especial mi abuela Pepita. Y qué decir de Bea, la mejor de las compañías, ha soportado lo indecible durante mis meses de escritura y la soledad durante la estancia y los congresos, y aún así ha sido capaz de quererme.

Muchas gracias a todos otra vez,

Víctor

(Barcelona, Julio 2014)

Resumen en castellano

El carbono es uno de los elementos más importantes en nuestra vida y el cuarto más abundante en la naturaleza. No sólo constituye uno de los elementos básicos para la vida, sinó que además es ampliamente utilizado en la industria para la fabricación de materiales. La principal característica del carbono es su capacidad para crear enlaces con otros elementos y moléculas, y se debe mayormente a su configuración electrónica $1s^2$ $2s^2$ $2p^2$ en estado fundamental. Por ejemplo, los bien conocidos hidrocarburos están formados por carbonos e hidrógenos en cadenas o anillos. Al añadir radicales metilo, nitrógeno y oxígeno, se da lugar a la formación de moléculas aún más complejas como ácidos, alcoholes, etc.

No obstante, los alótropos de carbono como el grafito, el diamante y el carbono amorfo y DLC (carbono amorfo tipo diamante) se han convertido en las variantes de carbono más importantes debido a sus propiedades físicas y a sus innumerables aplicaciones. El grafito, comúnmente utilizado en las minas de los lápices, es también utilizado por sus propiedades conductoras y como lubricante seco desde los inicios de la industria armamentística. La unión de sus átomos se lleva a cabo mediante tres orbitales sp^2 superpuestos y el grafito tiene una disposición en planos paralelos de capas de carbono. El diamante, por su parte, posee la mayor dureza hasta la fecha, además de ser deseado como objeto de joyería. Su completa hibridación sp^3 le confiere las propiedades mecánicas como la dureza y el más alto módulo de elasticidad conocido. Tenemos también el carbono amorfo y el DLC, que han disfrutado de un estatus transitorio entre ambas formas. Tienen un gran comportamiento en dureza y muy bajos coeficientes de fricción. Además, debido a su triple hibridación de orbitales y dependiendo del cociente en los enlaces sp^3/sp^2 da lugar a toda una familia de posibilidades que se suma a la opcional hidrogenación del material.

Estas formas tridimensionales del carbono vieron como otras con distintas y mejores (en algunos casos) propiedades, llegaban al cabo de los años. Con ello se descubría el “cerodimensional” fulereno (buckyball) en los años 1980, que consistía en una esfera de 60 átomos de carbono unidos mediante orbitales sp^2 con aplicaciones potenciales sobretodo en

biomedicina. Años más tarde, en 1991, se descubría también el nanotubo de carbono, unidimensional, que consistía en una estructura cilíndrica de carbono que podía tener una o varias paredes. Entre sus más interesantes propiedades se encuentra la dureza y la conductividad eléctrica dependiendo de su quiralidad.

Solamente quedaba ya el alótropo bidimensional del carbono. A comienzos del siglo XX, varios científicos teóricos constataron que los cristales 2D eran termodinámicamente inestables, y que su bajo punto de fusión (mucho más bajo por ser láminas del orden del átomo) hacía imposible su existencia. No obstante, en 2004, los científicos A. Geim y K. Novoselov de la Universidad de Manchester (UK) lograban exfoliar grafito pirolítico mecánicamente con cinta adhesiva, aislando de esta manera y por primera vez, una monocapa atómica de carbono, el grafeno había nacido. Un material con unas propiedades eléctricas y mecánicas extremas no conocidas hasta la fecha. En el año 2010 fueron galardonados con el Premio Nobel de Física, y desde entonces el mundo científico y tecnológico ha sufrido una de las mayores revoluciones a nivel global. Esta tesis doctoral, pues, se dedica al estudio de este nuevo material y sobretodo a su síntesis por un método escalable a nivel industrial.

Introducción:

El grafeno consiste en una capa monoatómica de átomos de carbono densamente empaquetados en una red hexagonal, y se sitúa como la madre de todos los alótrops de carbono, lo que quiere decir que con una capa de grafeno podemos obtener de forma adecuada, grafito, nanotubos de carbono o fulerenos. Sus enlaces sp^2 están hibridizados, lo que le confiere tres enlaces σ fuertes y otros enlaces π débiles.

Los enlaces σ mantienen una distancia interatómica de 0.142 nm, la distancia más pequeña de entre todos los materiales, y son los responsables de sus grandes propiedades mecánicas:

- Más duro que el diamante.
- 200 veces más fuerte que el acero (130 GPa).
- Con un módulo de Young de 0.5-1 TPa.
- Densidad de 0.77 mg/m^2.

Por otro lado, los enlaces π son responsables de sus propiedades electrónicas:

- Las bandas electrónicas y de valencia intersectan en un solo punto, gap cero.
- Cerca del punto de Dirac, los portadores de carga (electrones o huecos) se comportan como si no tuvieran masa, con una velocidad de 10^6 m/s.
- Una movilidad electrónica teórica de 200000 cm^2/Vs para grafeno suspendido y de 120000 cm^2/Vs teniendo en cuenta el scattering de fonones. Unas 100 veces más conductor que el cobre.
- Se observa Efecto Hall Cuántico a temperatura ambiente y Efecto Hall Cuántico Entero.
- Ambipolaridad. En la configuración de Efecto Campo, los portadores pueden convertirse en electrones y huecos si se les aplica un potencial adecuado.

A todas estas propiedades se le suman las propiedades ópticas: una transmitancia óptica en el visible del 97.7% lo que lo hace casi transparente, una conductividad térmica por encima del diamante y de los nanotubos de carbono, etc. Siendo además químicamente muy inerte y biocompatible (está hecho solamente de carbono) el grafeno se asegura una gran cantidad de aplicaciones futuras que ya están aquí, o están por llegar: materiales estructurales, pinturas conductoras, transistores de grafeno, capas conductoras transparentes, superbaterías, células fotovoltaicas, etc.

Si bien el primer método utilizado para obtener grafeno fue suficiente para que Geim y Novoselov ganaran un premio Nobel, no parece serlo para la industria y el mercado. La exfoliación mecánica de grafito mediante cinta adhesiva para depositarlo sobre silicio, además de simple, asegura la obtención de varias escamas o capas de grafeno de alta calidad. Éstas tienen las mejores propiedades eléctricas y son las más estables, sin embargo, el máximo tamaño de las capas apenas supera las 20 micras. Se requiere, por ello, de otros métodos capaces de superar esta limitación manteniendo la calidad y las propiedades, y sobretodo que puedan llevar

a cabo la producción en masa de grafeno con el fin de introducirlo en la industria y posteriormente en el mercado. No obstante, en este trabajo y como parte de una estancia doctoral, se utilizó este método para la obtención de grafeno de alta calidad con el fin de fabricar un transistor de Efecto Campo basado en grafeno.

Aparte de la exfoliación mecánica, existe también la llamada exfoliación química, donde una disolución de grafito permite mediante reactivos concretos, la separación de las capas de grafeno existentes en el grafito, que finalmente y mediante ultrasonidos se logran dispersar. El resultado, aunque con una gran capacidad de producción, normalmente consta de grafeno oxidado y otras impurezas que obligan a una reducción del mismo, con un mínimo del 5% atómico de contenido en oxígeno.

Otro método sería el crecimiento epitaxial. Una oblea de SiC se somete a altas temperaturas (1300 °C), sublimando así gran parte del silicio presente y descubriendo el carbono en la superficie. Éste último forma una fina lámina y se reordena (con los parámetros adecuados) en forma de grafeno. El método facilitaría la implementación del grafeno en la electrónica (basada en el silicio), y los dominios de las monocapas dependerían en un principio solamente del tamaño de la oblea. Sin embargo, las altas temperaturas necesarias dificultan su escalabilidad.

Finalmente, y como método principal llevado a cabo en esta tesis, tenemos el Depósito Químico en estado Vapor (CVD en inglés, siglas de Chemical Vapor Deposition). Un hidrocarburo como gas precursor (metano o acetileno) se descompone por temperatura (pirólisis) catalizado por un metal (cobre, níquel…) en el que se depositan los átomos de carbono por precipitación o segregación, formando grafeno. Este método parece tener el mayor compromiso entre calidad y escalabilidad en la producción de grafeno. Sin embargo, su mayor contrapunto estriba en la obligación de transferir el grafeno desde el metal catalizador, inconveniente para la mayor parte de la caracterización y aplicaciones, a un sustrato aislante como el silicio o polímeros.

Parte experimental:

El objetivo de esta tesis es superar las limitaciones actuales de las técnicas de crecimiento del grafeno, a unas pocas μm^2, y extender las posibles aplicaciones del grafeno a sistemas que requieran superfícies macroscópicas. Para ello, diferentes tareas se han realizado:

a) Se han investigado los principios de crecimiento del grafeno mediante la técnica CVD en un reactor ya existente en el grupo. Utilizando acetileno como gas precursor, cuya temperatura de pirólisis (700 °C) más baja que la del metano (850 °C) y con una tasa de depósito mayor, permite un proceso a más baja temperatura aunque dicho gas se encuentra normalmente a menor pureza. El estudio se basó también en la comparativa con diferentes sustratos de cobre como metal catalizador: láminas, fragmentos, capas producidas por sputtering sobre obleas de silicio, y finalmente trozos con la superfície pulida por diamante. La temperatura del proceso se alcanzó mediante una resistencia de grafito que permitía llegar a 800-900 °C en aproximadamente unos 10 min. Una vez allí se procedía a hacer un recocido de la muestra en atmósfera de hidrógeno con el fin de reducir el óxido de cobre (también en la rampa de temperatura) a 10 Pa de presión y 5 sccm (centímetros cúbicos standard por minuto), y de cristalizar la superfície del cobre. El acetileno se libera a unos 50 Pa de presión y un flujo de 30 sccm durante 10 min, con la posibilidad también de introducir hidrógeno con el fin de arrastrar todos los productos intermedios producidos por la pirólisis, y el proceso finalmente acaba en una frase de enfriamiento hasta temperatura ambiente. Los resultados fueron analizados mediante microscopía electrónica de barrido (SEM) para analizar la superfície de las muestras de cobre antes y después del proceso. También con espectroscopía de energía dispersada de Rayos-X (EDS) para valorar la composición química después del recocido de las muestras. Y finalmente con espectroscopía Raman, la herramienta no invasiva más utilizada para caracterizar el grafeno. Basada en la dispersión inelástica de una fuente de luz láser enfocada en la muestra, la espectroscopía Raman es capaz de definir la calidad

y el número de capas del grafeno a partir de tres picos principales: D (defectos), G (carbono) y 2D (armónico del D). Cuanto más pequeño sea el pico D, menos defectos tendrá la capa; y cuanto más grande sea el cociente en intensidades 2D/G, menor número de capas (hasta 4 para una sola).

b) Se ha diseñado y construido un reactor nuevo de alto vacío en la Sala Blanca de la Facultad de Física (Universidad de Barcelona) con el fin último de crecer grafeno mediante la técnica CVD. El reactor, llamado *GRAPHMAN*, incorpora los siguientes elementos:

- Un cabezal de magnetron sputtering (pulverización catódica) que permite depositar capas finas de metales (cobre y níquel) en condiciones controladas.
- Un tubo de cuarzo como cámara donde se lleva a cabo la reacción. El tubo está envuelto de un horno cilíndrico de resistencias capaz de llegar a los 1000 °C.
- Un espectrómetro de masas cuadrupolar (QMS) capaz de monitorizar en vivo la presión parcial de hasta 10 gases presentes en el reactor durante todo el proceso.
- Un sistema de gestión de gases que controla la presión y el flujo que consta de cuatro líneas independientes.
- Un sistema de vacío con dos líneas distintas para gases comburentes y gases combustibles. Consta de dos bombas mecánicas y una turbomolecular. El sistema puede llegar a vacíos del orden de 10^{-5} Pa.
- Todo el reactor está computerizado por medio de un entorno Labview® desarrollado también por el grupo. El sistema puede controlar la apertura y cerrado de todas las válvulas, puede fijar la temperatura del proceso, así como la presión en la cámara principal a un valor dado y la presión en la precámara. Además de automatizar todo el proceso.

c) Se ha desarrollado un método CVD modificado con el fin de mejorar los resultados actuales en términos de tiempo de depósito (del orden de horas), temperatura (del orden de 1000 °C), presión (1-100 Pa), y cantidad de gas precursor (del orden de 700 sccm de flujo constante) para crecer grafeno de alta calidad. Para ello y a partir de la teoría cinética de gases, se desarrolló una ecuación que permitía calcular el tiempo de formación de una monocapa atómica en una superfície libre de gas (no utilizada todavía con este fin), reduciendo así el tiempo de formación, la cantidad de gas precursor y la presión del proceso. Usando el metano como gas precursor, una temperatura de proceso de 1000 °C, un coeficiente de adherencia de 1, obtenemos la siguiente expresión: $\tau = \frac{2.1\times10^{-3}}{\mathrm{P}}$

Con lo que este tiempo de formación dependería únicamente de la presión del gas precursor. Entonces con un proceso CVD a una presión de metano de ~10^{-3} Pa podríamos obtener una monocapa de carbono (grafeno) en ~1 s. Con esta premisa se diseñó un sistema para liberar el gas en forma de pulso instantáneo, tampoco utilizado hasta la fecha con ese fin. El sistema se basa en un tren de válvulas (2+2) con una cámara de despresurización en medio, que permite bajar la presión de la botella principal hasta 10^{8} veces para poder llegar a pulsos de incluso 10^{-4} Pa. El pulso tiene una forma característica de salto súbito seguido de un descenso en forma exponencial negativa debido al bombeo del sistema de vacío. El espectrómetro de gases cuadrupolar fue crucial en el análisis del pulso y su presión. El método está protegido intelectual e industrialmente mediante una patente.

d) Se han fabricado capas de grafeno de gran área en sustrato metálico mediante el comentado método CVD modificado. Se utilizaron dos sustratos de cobre básicos: láminas de 76 y 127 μm, y capas finas (600 nm) de cobre sobre obleas de silicio obtenidas mediante sputtering. Debido a la formación de una aleación eutéctica entre el cobre y el silicio disminuyendo su punto de fusión, se depositó una capa de níquel (100 nm) como barrera de difusión entre ambos. En ambos tipos de muestras se aplicó una rampa de temperatura hasta

los 900-1000 °C, a partir del cual empezó la fase de recocido y CVD (inyección de metano en forma de pulso). Una vez finalizado, el proceso entra en una fase de enfriamiento que resultó ser también importante. En la fase final de esta tesis se investigó el uso de otros precursores como el benceno o el tolueno, que son líquidos pero con suficiente fase vapor; ambos con una semejanza química y estructural con la red hexagonal de carbonos propia del grafeno. Debido a su baja pirólisis (500-600 °C), el uso de benceno y tolueno permitió bajar drásticamente la temperatura del proceso a la mitad. Con el objetivo de optimizar el proceso y las propiedades físicas del grafeno, las muestras obtenidas fueron caracterizadas mediante microscopía óptica, SEM, EDS, microscopía de fuerza atómica (AFM) y mayormente mediante espectroscopía Raman.

e) Se ha investigado el método para transferir muestras de grafeno en cobre a silicio. La técnica se basa en la idea de cubrir el grafeno con un polímero (como PMMA) que proteja y sirva de medio mientras se ataca el cobre con ácido para separar la monocapa del metal catalizador. Acto seguido se transfiere el polímero/grafeno sobre silicio, al cual se le aplica un tratamiento térmico para evaporar el polímero.

f) Se ha fabricado un transistor de Efecto Campo (FET) con grafeno obtenido mediante la técnica de exfoliación mecánica, como parte de una estancia doctoral en la Universidad de Duisburg-Essen (Alemania). La alta calidad de las capas obtenidas se traduce en altas prestaciones eléctricas, siendo por ello conveniente para tal dispositivo. Se depositaron dos contactos de oro, que hicieron de drenador y fuente, y el óxido de silicio (90 nm) que hizo de puerta. Se extrajeron las curvas características I(V) para evaluar la movilidad de los portadores y caracterizar eléctricamente la muestra de grafeno. Las muestras obtenidas, juntamente con MoS_2, CNM (nanomembranas de carbono) y h-BN, también fueron utilizadas para estudiar cómo la radiación rasante (1-3°) de iones pesados rápidos, como Xe^{23+} y U^{28+}, induce defectos en la superficie, creando rastros y pliegues característicos.

Conclusiones:

- La exfoliación mecánica es un proceso simple y confiable para obtener grafeno monocapa de forma exitosa. Los espectros Raman adquiridos demuestran la presencia de grafeno de alta calidad: un pico G pequeño y un 2D (unas cuatro veces superior al G en intensidad) están presentes, y una completa ausencia del pico D. Sin embargo, el tamaño de las capas (alrededor de las 20 μm) no es adecuado para aplicaciones industriales, concretamente para aplicaciones que necesiten grandes áreas.

- La fina capa de óxido de silicio de 90 nm (o 300 nm) resultó crítica para aumentar el contraste óptico de cualquier proceso relacionado con la detección óptica y seguimiento del grafeno.

- El AFM en modo tapping fue especialmente sensible para detectar la presencia de contaminación de las muestras de grafeno obtenidas por exfoliación mecánica, como pegamento o agua atrapada entre capas. No obstante, no fue tan eficiente a la hora de medir el salto de una monocapa de carbono debido a la interfície grafeno-sustrato y la fina capa de agua formada entre ellos. Por otra parte, en el grafeno obtenido mediante CVD, el AFM no fue tampoco una técnica demasiado útil. Las dendritas y las capas de carbono no son ópticamente detectables, y por tanto, imposibles de localizar. La interferencia entre el cobre y el grafeno tampoco ayudó. A pesar de todo, el AFM fue muy útil para caracterizar y determinar las características de la superfície de nuestro sustrato/catalizador.

- La exfoliación mecánica proporciona grafeno monocapa de alta calidad: fácil de obtener y caracterizar, homogéneamente no defectivo, y con dominios suficientemente grandes para fabricar transistores de Efecto Campo mediante las técnicas actuales. Las curvas características obtenidas I(V) son similares a los obtenidas previamente en otras publicaciones, lo que asegura la reproducibilidad del proceso de pequeña a gran escala. Los resultados en la movilidad de portadores (-5120 cm^2/Vs) de nuestro FET basado en grafeno sobre silicio son comparables a aquellos

encontrados en literatura. Aunque puede ser mejorado con respecto a la conductividad, es especialmente interesante para aplicaciones en transistors o en capas conductoras transparentes.

- La radiación de iones pesados rápidos bajo ángulos rasantes puede ser usado para introducer pliegues en una variedad de cristales bidimensionales como el grafeno, MoS_2 y el h-BN. Los pliegues pueden, también, ser introducidos en materiales 2D como el grafeno producido por CVD y CNM, que pueden crecer a gran escala, pero no en MoS_2 sintetizado con CVD. Se ha mostrado que una capa intersticial de agua o adsorbidos, es necesario para que el mecanismo de los pliegues tenga lugar y que la calidad cristalina de los materiales determina la calidad de los pliegues resultantes.

- En cuanto a la técnica CVD, se necesita la presencia de superficies puras, cristalinas, y suficientemente planas, de los catalizadores para depositar grafeno de alta calidad. Si el cobre inicial es demasiado áspero o tiene defectos cristalinos, las especies de carbon encontraran demasiados puntos de nucleación, produciendo defectos en el grafeno. Estos defectos pueden facilitar la formación de islas desordenadas de a-C, multicapas de grafeno, y otras estructuras defectivas de carbon sobre la superfície del cobre.

- Las capas finas de Cu/Si obtenidas mediante sputtering, que son amorfas pero suficientemente gruesas como para evitar la difusión completa y la evaporación, demostraron ser sustratos útiles para el depósito de carbono directamente sobre obleas de silicio. Aunque en los trabajos previos, la mayor parte del carbono depositado fue amorfo, grafeno de unas pocas capas (FLG) creció localmente en forma de escamas.

- Las medidas Raman mostraron la presencia de FLG en los fragmentos de cobre pulidos con diamante. El pico D sugiere una baja cristalinidad de un grafeno de unas 4-10 capas. Teniendo en cuenta el dominio cristalino del cobre, se estimó un dominio medio de unas 10 μm para el grafeno. Estos resultados también demostraron la factibilidad del calentamiento mediante la

resistencia de grafito para crecer grafeno en sustratos de cobre y el uso de acetileno para procesos a más baja temperatura.

- En los sustratos producidos por sputtering, capas de cobre de 600 nm con una barrera de 100 nm de níquel previamente depositadas en obleas de c-Si pulidas, nuclearon ligeramente en gotas e islas durante el proceso de recocido. Estas estructuras fueron observadas mediante microscopía óptica y electronica (SEM), y el EDS confirmó la composición química de estas estructuras: Cu, Ni, Si, y C estaban presentes en la superficie después de todo el proceso. El fenómeno real que ocurre en este tipo de sustrato durante el recocido es afectado por la formación de una aleación eutéctica entre el cobre y el silicio. Esto baja el punto de fusion de ambos elementos creando una superfície más compleja donde la afinidad del grafeno es sorprendentemente elevada.

- El grafeno creció exitosamente sobre capas finas de sputtering de Cu/Ni sobre c-Si mediante el método CVD de baja presión pulsada; reduciendo así el tiempo de depósito al orden de los 10 s usando pulsos de metano de presión parcial de 10^{-4} Pa. El análisis Raman, SEM y EDS demostraron la sola presencia de grafeno de una o dos capas mediante su característica banda 2D y su cociente $I_{2D}/I_G \geq 1$. Los espectros Raman también reflejan la presencia de defectos en las capas, probablemente debido a la existencia de múltiples terrazas cristalinas y bordes, evidenciados por el SEM. Y también probablemente debido a la superfície irregular del sustrato/catalizador. Aún así, el mapeado Raman mostró la presencia de grandes áreas de grafeno del orden de 10^4 μm^2.

- La mayor parte de los mejores resultados del grafeno sintetizado fueron sin hidrógeno añadido. Aunque funciona también como catalizador, el efecto erosionador del hidrógeno limita el crecimiento del grafeno drásticamente dentro de las bajas presiones usadas con este método CVD modificado.

- El análisis Raman presenta efectos secundarios debido a la fluorescencia del cobre subyacente, y la inclusión de nuevos picos

procedentes del cobre. Esto evitó la extracción de relaciones señales/ruido elevadas comparadas con las obtenidas en las señales Raman sobre grafeno exfoliado en óxido de silicio. No obstante, se considera igualmente una valiosa herramienta, rápida y sencilla, de comprobar la presencia de carbon en cualquier forma.

- El grafeno también creció en las láminas de cobre de forma eficiente, teniendo grandes dominios cristalinos y muchas menos capas con defectos, tal com esperábamos por los resultados encontrados en literatura. La importancia de una superfície plana y suave en los metales catalizadores, y las altas temperaturas del proceso se traducen en picos D más pequeños en los análisis Raman.

- El uso de nuevos precursores como benceno o tolueno pueden engrosar la lista de parámetros para obtener grafeno de altas prestaciones. Teniendo una temperatura de pirólisis mucho más baja (500 °C) permite reducir la temperatura del proceso hasta la mitad, lo que facilita un escalado industrial. Además, el cambio en los precursores sugiere también un cambio en el sistema y el método para seguir obteniendo grafeno de alta calidad.

- El proceso de transferencia es todavía una desventaja en la producción de grafeno mediante el CVD. La eliminación del metal subyacente añade pasos químicos que complican la calidad final del grafeno. En este trabajo se ha llevado a cabo un proceso estándar de transferencia de cobre a silicio mediante PMMA, con resultados satisfactorios. El grafeno transferido tenía características similares al presente en cobre, pero la inclusión de estos pasos reduce su escalabilidad.

- Finalmente, los resultados respaldaron el uso de nuestra tecnología CVD de baja presión pulsada, basada en pulsos de presión muy baja de gas con el uso de la ecuación del tiempo de formación de una monocapa. Este método permite el crecimiento de grafeno monocapa y bicapa de gran área con un tiempo de depósito de sólo 10 s con un pulso de metano de sólo 10^{-4} Pa. Sin embargo, hay que

seguir trabajando para optimitzar el enfoque teórico de la ecuación del tiempo de formación de una monocapa: el coeficiente de adherencia ha de evaluarse estrictamente; así como la importancia del grosor de la capa de cobre necesaria, las condiciones óptimas de recocido, y la eliminación del Cu/Ni durante el recocido antes del proceso CVD para crecer grafeno directamente sobre silicio u óxido de silicio. Esto es especialmente importante para la implementación de procesos litográficos y la posibilidad de producir dispositivos electrónicos basados en grafeno.

Preface

In 2004 there were newly conditions for a scientific revolution, with very important technology implications and yet to be completely developed. It is the isolation of atomic carbon layers, better known as *graphene*, whose extreme mechanical and electronic properties stand out above all known materials: it presents the highest electron mobility, ambipolarity, it supports large current densities, the highest elastic modulus, increased thermal conductivity, it shows high impermeability, and reconciles fragility and ductility. The study of graphene was about to be the next step to the boom in nanotechnology. In this case, the system to consider is purely two-dimensional, being the thinnest structure known to date. In 2010, this discovery was acknowledged with the Nobel Prize to the scientists A. Geim and K. Novoselov from the Manchester University (UK).

This PhD thesis started officially in October 2010 after a year in which the author obtained his Master's degree on Plasma Enhanced Chemical Vapor Deposition (PECVD) technique with the deposition of a-C:H:F thin films on nanostructured surfaces.

The research during the master thesis and the beginning of the PhD thesis started in the framework of the project "Amorphous carbon molds for micro and nanoimprint of polymeric surfaces" (DPI2007-61349), which started in January 2007 and it was financed by the science and innovation department (MICINN) of the Spanish Government. This project finished in 2010, and the doctoral thesis actually began within the project "Growth of ultrathin layers of graphene on metallic substrates for biomedical applications" (MAT2010-20468), which started in 2011 (and finished in 2013) and it was also financed by MICINN.

All the research carried out by the author was done within the research group FEMAN, in the *Departament de Física Aplicada i Òptica* of the *Universitat de Barcelona* (UB), also financed by AGAUR of *Generalitat de Catalunya* (2009GR00185). Also, a substantial part of the characterization of the samples was done in the Scientifical and Technical Services of the UB (CCTiUB). During the last year of the thesis, the author worked as researcher in the Duisburg-Essen Universität (Duisburg,

Germany) from September 2013 to December the same year under the supervision of Prof. Dr. Marika Schleberger, also on the production and characterization of graphene and MoS_2, but through a different approach. The work was framed in the SPP 1459 Graphene (O.O.) and SFB 616 (DFG): Energy dissipation at surfaces (H.B., U.H.) and in the European Community as an Integrating Activity Support of Public and Industrial Research Using Ion Beam Technology (SPIRIT) under EC Contract No. 227012SPIRIT. Markus Bender and Daniel Severin supported at the GSI during the irradiation experiments.

The project MAT2010-20468 "BIOGRAPH" framed in the "Plan Nacional de Investigación Científica, Desarrollo e Innovación Tecnológica 2008 – 2011" in the Line 1: Nanotechnologies, applied to materials and new materials in the health field. The goal was to develop new materials in ultrathin structures of few monoatomic layers, based on graphene, with extreme surface properties (very high wear resistance, ultra low friction and surface energy, extreme chemical resistance, biocompatibility) for applications in biotechnology and biomedicine. The scope of this objective is to overcome the limitations of current techniques in terms of the growth surface of graphene (of some μm^2) and to extend the possible applications of graphene to systems and devices requiring macroscopic size surfaces. For this purpose, the project had different tasks consisting of:

a) The design and construction of a new high vacuum reactor in the Clean Room of the Universitat de Barcelona that will work with high-temperature chemical vapor deposition (CVD) and magnetron sputtering.

b) Development of a modified CVD method that will improve the current results in terms of deposition time, temperature, pressure, and quantity of precursor gas needed to grow high quality graphene.

c) Fabrication of graphene-based ultrathin layers on metal substrates of large area and high quality by this modified CVD technique, focusing on obtaining the material as effectively as possible towards an implementation of this technique in the biomedical industry or for other potential applications.

d) Characterization of the graphene obtained through different techniques in order to optimize their physical and surface properties; such as structural and morphological studies by Raman spectroscopy, SEM and Optical Microscopy. And to complete together with the functional properties, an electrical and optical characterization.

To this regard, we wanted to take advantage of the engineering, exploring in detail the technology of production of graphene by CVD and other variants on metallic substrate, to make fundamental progression of the graphene growth technology and in the comprehension of the control of the growth kinetics, monolayer discontinuities, to explore the occurrence of novel materials or unique functional properties.

The thesis is divided into four main parts: Part I: Introduction, Part II: Experimental Set, Part III: Results, and Part IV: Conclusions. The Part I will introduce the state of the art of graphene as novel material and its outstanding properties, its discovery, and all the technologies that triggered its development during these years until the first applications.

The Part II will describe the experimental setups used throughout this work, regarding the fabrication and characterization of substrates by magnetron sputtering, the growth mechanisms of the new developed CVD system, and a brief explanation of the fundamentals of each technique.

Finally, in the part III, a complete review of all the results of the samples obtained by mechanical exfoliation of graphite and CVD on copper will be exposed; together with their characterization.

Part IV includes the main conclusions of the work, which are summarized. Afterwards, a list of the scientific results published is shown, as well as the contributions in conferences and meetings.

In the end of the manuscript, an Appendix with three sections is shown: a complete CVD review, the abstract of the patent developed during this thesis, and a complete list of all the samples produced.

List of figures and tables

Part I
Introduction

Chapter 1

CARBON MATERIALS RETROSPECTIVE

1. Carbon materials retrospective

Carbon is one of the most important elements in our life, and it is the fourth most abundant chemical element in nature. Not only constitutes one of the basic elements for life (an average representation of carbon in the mass of living matter is 19.4%), it is also widely used in industry for materials manufacturing. The fundamental feature of carbon is its unique capability for combining with other elements. For example, the so-called hydrocarbons are formed by the grouping of carbon and hydrogen atoms either in chains or in rings. The addition of methyl radicals, nitrogen, oxygen and other new elements provides more complex molecules (acids, alcohols, etc.), whose periodical attachment leads to polymeric structures. In order to understand why carbon achieves such an elevated coordination degree, we must study its electronic structure. Carbon occupies the 6th position within the Periodic Table, which provides an electron configuration at ground state of $1s^2\ 2s^2\ 2p^2$. Figure 1.1 shows a scheme of the electron distribution in atomic orbitals, where the arrows indicate the spin polarization. [1]

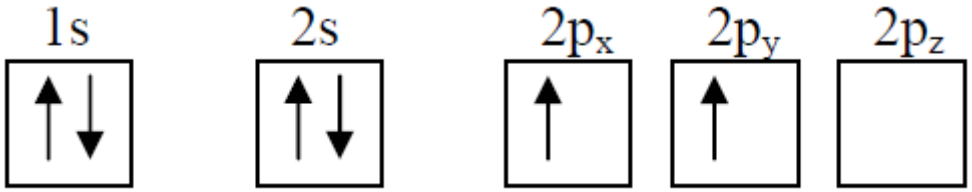

Figure 1.1: Electron distribution in the carbon orbitals for a carbon atom with valence number 2. The subindexes x, y, and z indicate the orientation of p orbitals with respect to the corresponding axis. This differentiation is not required in s orbitals, since they are spherical.

Electronic orbitals of the carbon atom contain only two unpaired electrons, behaving thus as bivalent element. In order to justify the tetravalence of carbon, one of the two electrons from the *2s* orbital must occupy an empty *2p* orbital. As a result of the previous redistribution, carbon has four dangling bonds and all the electrons in the outer layer are unpaired. Then, the linear combination of *s* and *p* atomic orbitals generates the so-called hybrid orbitals. Hybridization comprises three cases: The *s* orbital together with one *p* gives rise to two *sp* orbitals, when

two *p* orbitals are added to *s* we obtain three sp^2, and finally, the hybridization of all the orbitals from the second layer provides four sp^3.

Figure 1.2 shows the possible geometric configuration in the carbon atom depending of the type of hybridization. Diametrically opposed orientation takes place in the case of *sp* orbitals. In this configuration, both *sp* orbitals make strong frontal *σ* bonds to an adjacent atom, whereas there are two weak lateral *π* bonds with neighboring *p* orbitals. On the other hand, trigonal planar configuration is typical of sp^2, which form *σ* bonds. The pure *p* orbital forms a *π* bond. Finally, sp^3 lobes are oriented towards the vertexes of a regular tetrahedron. In this case, all the four orbitals are hybridized and form *σ* bonds.

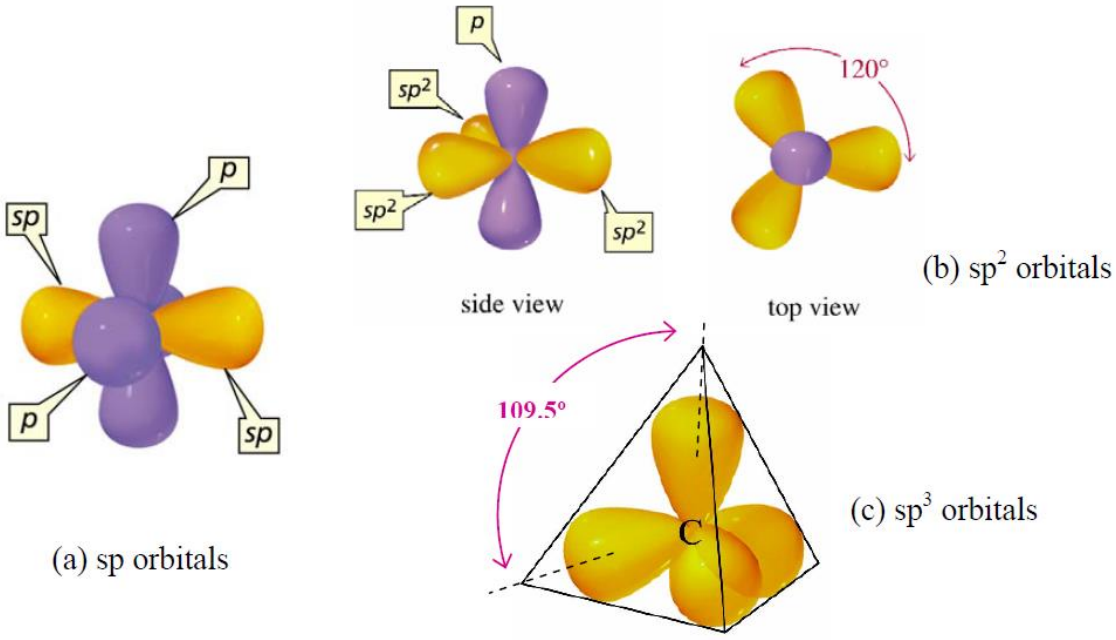

Figure 1.2: Spatial arrangement of orbitals in the carbon atom in the case of (a) sp, (b) sp^2 and (c) sp^3 hybridizations. [1]

Carbon presents allotropy, i.e. three main different phases have been found in solid state: graphite, diamond, and amorphous carbon. They are constituted by carbon atoms bonded by sp^2, sp^3 and combinations of both hybridizations, respectively. There exists another configuration of carbon: the polymer-like form. It is found when carbon is diluted with hydrogen, and it presents low hardness, high transparency, and electrically it behaves as an insulator. The spatial distribution of polymeric carbon comprises a rich variety of shapes and lengths, which

gives rise to compounds with different chain types. They are divided into aliphatic (lineal, branched, or alicyclic) and aromatic (benzene, etc.) Below, we find summarized some of the most important carbon allotropes.

1.1. Graphite

Graphite shows a stable trigonally bonded crystal structure (figure 1.3). Carbon atoms become bonded by σ bonds due to three superposed sp^2 orbitals, adding a π bond that results from the interaction of pure p orbitals. This material is soft, optically opaque, chemically active, and is a good electric conductor. The atoms are organized in parallel and single-atom planes, which are called graphene layers and are the center of this thesis. Carbon atoms from adjacent planes are bonded by weak dispersion van der Waals forces, which allow two layers of graphene to slip one on each other and confers softness and special lubricating properties to graphite. The in-plane bond length is 0.142 nm, whereas the inter-plane distance is 0.335 nm. Graphite crystallizes in hexagonal close-packed (h.c.p.) network, and its most important applications are pencil tips, electrodes, and solid lubricants. [1]

1.2. Diamond

Diamond structure results from the metastable tetragonal σ bonding of carbon atoms, and is only stable at high pressure and high temperature. It is considered to be a material with various extreme physical properties. First of all, it exhibits the highest elasticity module known to date. In fact, diamond establishes the ultimate hardness limit basically due to the superior strength of its chemical bonds. Complete sp^3 hybridization occurs and, therefore, all atoms become bonded *via* strong frontal σ bonds. The C-C bond (sp^3) is 0.154 nm long, a bit longer and weaker than that in graphite (sp^2), and its crystallographic structure consists of two superimposed face-centered cubic (f.c.c.) lattices shifted by one-quarter of the cube diagonal (figure 1.3). Such bonds confer the extreme hardness of diamond, and the highest atom density among all solids.

Diamond is mostly employed in cutting tools (edges), abrasive coatings (dust), and jewelry. A prominent use of diamond in electronic

applications has taken place due to the interesting properties when the material is chemically doped, especially in superconductivity applications [2]. Diamond conventional preparation requires high-pressure and high-temperature processes (HPHT). Thin films of single crystal diamonds in thin film form are usually prepared by CVD method at high deposition rates.

Furthermore, there is also a hexagonal diamond called Lonsdaleite (named in honor of Kathleen Lonsdale). In nature, it forms when meteorites containing graphite strike the Earth. The great heat and stress of the impact transforms the graphite into diamond, but retains graphite's hexagonal crystal lattice. It is theoretically harder (58% more) than conventional diamond but it is not demonstrated in practice, where impurities and lattice defects play a fundamental role. [3]

1.3. Diamond-like carbon (DLC) and amorphous carbon

Besides diamond and graphite, carbon can form an amorphous phase. Amorphous carbon (a-C) is obtained under controlled deposition of the amount of diamond, graphite, and polymeric phases [4-6]. Its close relationship with DLC is currently defined by the IUPAC as:

- *Diamond-like carbon (DLC) films are hard, amorphous films with a significant fraction of sp^3-hybridized carbon atoms and which can contain a significant amount of hydrogen. Depending on the deposition conditions, these hard films can be fully amorphous or contain diamond crystallites.*

- *Amorphous carbon is a carbon material without long-range crystalline order. Short range order exists, but with deviations of the interatomic distances and/or interbonding angles with respect to the graphite lattice as well as to the diamond lattice.*

Actually, the IUPAC suggested that *hard amorphous carbon films* and *diamond-like carbon films* are synonym expressions. From the structural point of view, the short order up to 6-10 atomic distances is synonymous of systems with nanocrystalline structure.

The DLC matrix does not contain only one determined hybridization, but contains all three in different proportions. Preparation of a-C containing large sp^3/sp^2 ratio is desirable to obtain "diamond-like" properties. In this way, plasma deposition techniques like sputtering and Plasma Enhanced Chemical Vapor Deposition (PECVD) increase sp^3 bonding, although the latter technique provides H-rich samples. High plasma density PECVD reactors are necessary to maximize sp^3 bonding and simultaneously diminish hydrogen content. When the sp^3 fraction reaches a high degree (80-88%), a-C is denoted as tetrahedral a-C (ta-C) because tetrahedral bonding due to this hybridization is predominant. [7]

We can imagine the microstructure as a system of covalently bonded carbon atoms organized in a 3D network, containing a random distribution of sp^2 and sp^3 bonds (figure 1.3). Polymeric carbon can also host a great fraction of sp^3 bonds, although the majority of them come from C-H groups and therefore the material is soft. This ensures a rich variety of a-C microstructures and properties.

1.4. Fullerenes and nanotubes

Although there already were a very well-known variety of carbon based materials (graphite, diamond, and a-C), a more exotic forms of carbon were about to appear. Buckminster fullerenes were introduced in 1980s as an additional form of carbon. They were formulated as C_{60}, and consisted on spherical lattices formed by 60 sp^2-bonded carbons (figure 1.3). Extensive research on fullerenes has been undertaken for medical applications using fullerenes as substitutive ligands or in biosensor devices. In the early 1990s, even a subset of fullerene science appeared. C_{70}, C_{76}, C_{82}, and C_{84} are other common members of the fullerene family. They are present in soot and produced in nature by lightning discharges in the atmosphere. Even a giant icosahedral molecule C_{540} can be seen within interstellar gas clouds. However, the expectations of these "carbon balls" quickly decreased. [8]

Right after, in 1991, Ijima reported the preparation of new cylindrical structures called carbon nanotubes. They were called multi-walled nanotubes (MWCNT), since they consisted on multiple graphene layers that formed a cylinder surface (figure 1.3) [9]. Further refinements

permitted the deposition of single-wall nanotubes (SWCNT), whose chirality determines their electric properties. Both fullerenes and nanotubes were initially grown by arc discharge and laser ablation techniques, and recently they have been produced by CVD method. Most carbon nanotubes applications include field emission devices, fuel cells, cold cathodes, and ultrahigh-strength structural materials.

Few people in the world had any idea that another, and probably the definitive "son" of the carbon was about to get into the stage.

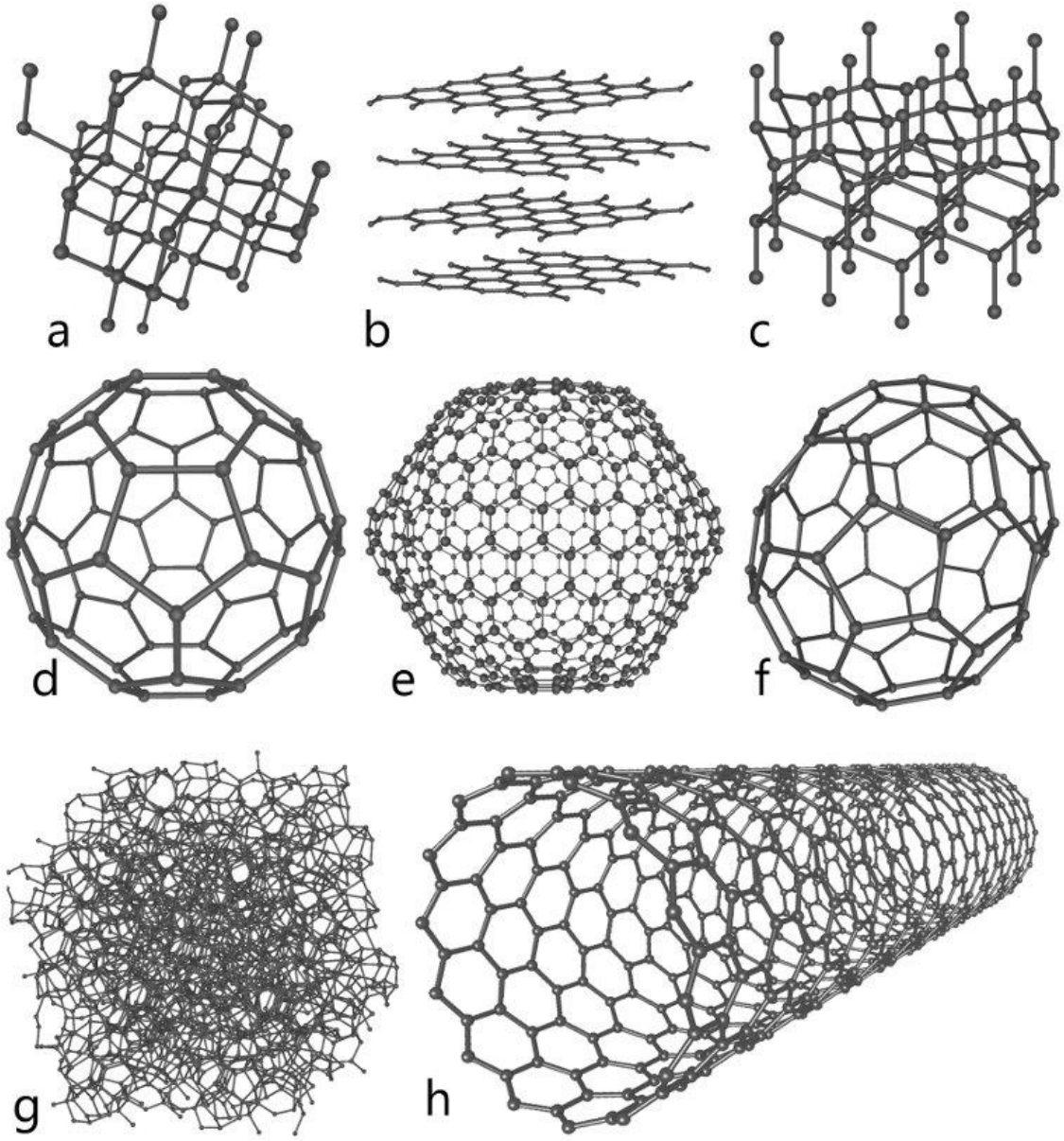

Figure 1.3: The structures of eight allotropes of carbon: (a) Diamond, (b) Graphite, (c) Lonsdaleite, (d) C_{60} (Buckminsterfullerene), (e) C_{540} Fullerene, (f) C_{70} Fullerene, (g) Amorphous carbon, and (h) Single-walled carbon nanotube. [10]

1.5. References

[1] C. Corbella, *Thin film structures of diamond-like carbon prepared by pulsed plasma techniques*, PhD Thesis, Universitat de Barcelona (2005).

[2] E.A. Ekimov, V.A. Sidorov, E.D. Bauer, N.N. Melnik, N.J. Curro, J.D. Thompson, S.M. Stishov, *Superconductivity in diamond*, Nature 428, 542-545 (2004).

[3] C. Frondel, U.B. Marvin, *Lonsdaleite, a new hexagonal polymorph of diamond*, Nature 214, 587-589 (1967).

[4] J. Robertson, *Diamond-like amorphous carbon*, Mater. Sci. Eng. R 37, 129-281 (2002).

[5] A. Erdemir, C. Donnet, *Tribology of diamond-like carbon films: recent progress and future prospects*, J. Phys. D: Appl. Phys. 39, R311–R327 (2006).

[6] K. Bewilogua, D. Hofmann, *History of diamond-like carbon films — From first experiments to worldwide applications*, Surface & Coatings Technology 242, 214–225 (2014).

[7] D.R. McKenzie, *Tetrahedral bonding in amorphous carbon*, Rep. Prog. Phys. 59, 1611-1664 (1996).

[8] H.W. Kroto, J.R. Heath, S.C. O'Brien, R.F. Curl, R.E. Smalley, *C_{60}: Buckminsterfullerene*, Nature 318, 162 - 163 (1985).

[9] S. Ijima, *Helical microtubules of graphitic carbon*, Nature 354, 56-57 (1991).

[10] www.chemicool.com/elements/carbon.html

Chapter 2

GRAPHENE AND 2D CRYSTALS

2. Graphene and 2D crystals

2.1. General

Probably graphene stands as the top of all the carbon forms, or at least as the last member in the carbon family. Graphene consists on a monoatomic layer composed of carbon atoms densely packed in a hexagonal lattice (2500 billion at/cm^2). Its bounds are sp^2 hybridized, what forms three strong in plane σ bonds per carbon atom. These strong bonds maintain the interatomic distance in 0.142 nm, the shorter distance of all the materials that provides to the graphene outstanding mechanical properties. Out of graphene plane, the not completely filled p_z orbitals (also called π orbitals) forms weak π bonds and are the responsible of the conductive properties. This honeycomb structure is the basis of other allotropes of carbon such as graphite, carbon nanotubes and fullerenes (figure 2.1).

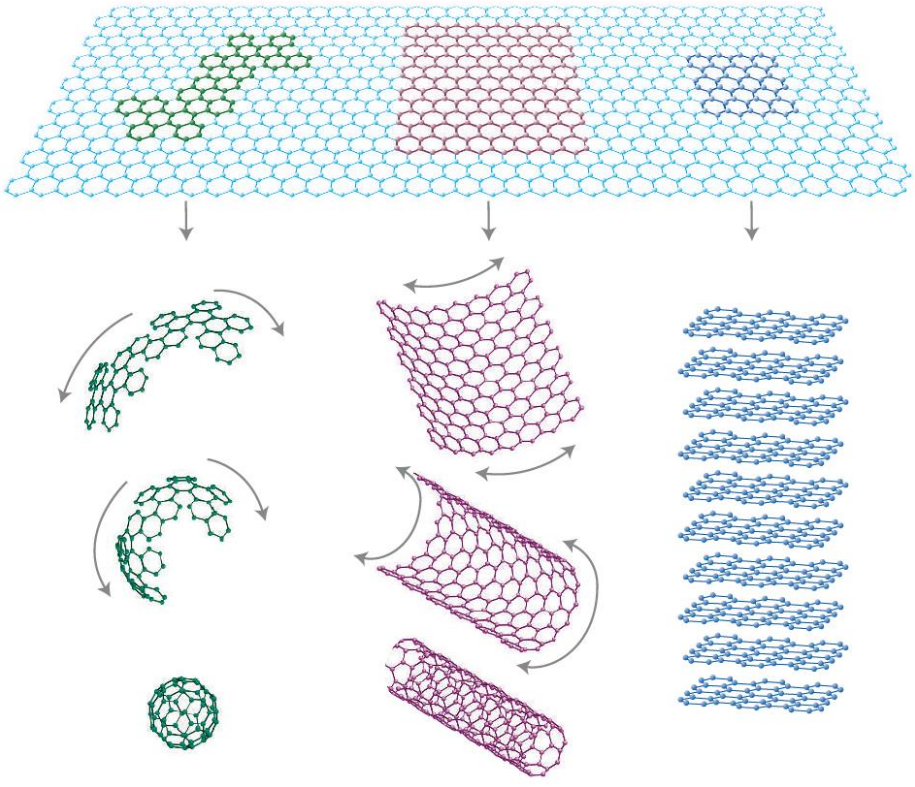

Figure 2.1: Mother of all graphitic forms. Graphene is a 2D building material for carbon materials of all other dimensionalities. It can be wrapped up into 0D buckyballs, rolled into 1D nanotubes or stacked into 3D graphite. These approximations (0D, 1D, and 2D) are due to the reduced dimensions of the nanostructures. [1]

Graphene sheets can stack with three main different ways: hexagonal (AA), bernal (AB), and rhombohedral (ABC) stacking. The differences between them are the coordination of the equivalent atoms of the different planes. Figure 2.2 shows the three types of stacking order. Notably, the interplane distance of approximately 0.335 nm is roughly the same in the three cases. All the stacking forms are known with the generic name of graphite. [2]

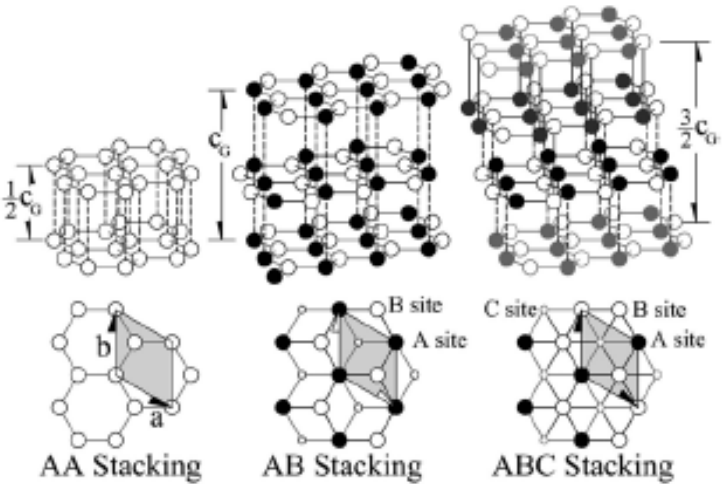

Figure 2.2: Three main types of staking order in graphite. [2]

The atoms of the graphene structure do not correspond to the points of a Bravais lattice. Indeed, the primitive cell contains not one but two atoms. In order to find the primitive vectors of graphene, one has to be in the centre of each cell as it is shown below in the figure 2.3:

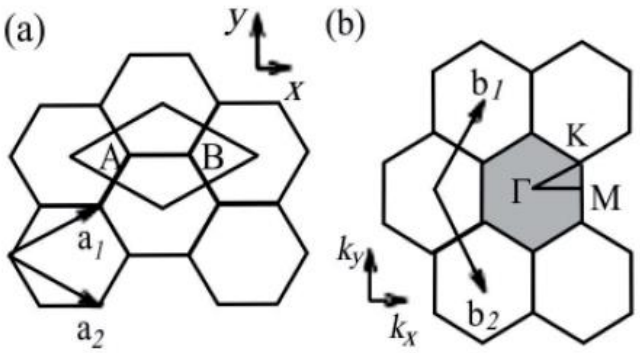

Figure 2.3: (a) Graphene structure, a_i primitive vectors. (b) Reciprocal lattice of (a) with its vectors b_i and its zone of Brillouin. [3]

$$\vec{a}_1 = a\left(\frac{\sqrt{3}}{2},\frac{1}{2}\right), \vec{a}_2 = a\left(\frac{\sqrt{3}}{2},-\frac{1}{2}\right)$$

$$\vec{b}_1 = \frac{2\pi}{a}\left(\frac{1}{\sqrt{3}},1\right), \vec{b}_2 = \frac{2\pi}{a}\left(\frac{1}{\sqrt{3}},-1\right) \quad (2.1)$$

Where the lattice parameter is a = 2.46 Å, and the distance of the link carbon-carbon is approximately 1.42 Å.

Another interesting feature of graphene is the edge effect. Regarding the orientation, graphene can have an arm chair or zig-zag edge. This affects also some properties in structures like nanoribbons of graphene, as it will be shown later.

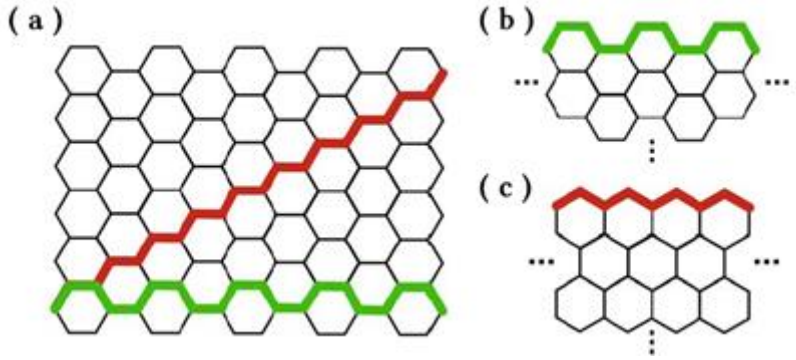

Figure 2.4: Honeycomb lattice of Graphene. (a) both directions: zig-zag (red) arm chair (green), (b) arm chair, (c) zig-zag. [4]

2.1.1. Discovery

In the early 20th century, Landau and Peierls argued that strictly 2D crystals were thermodynamically unstable and could not exist [5,6]. In 1947, their theory pointed out that thermal fluctuation in low-dimensional crystal lattices should lead to displacements of atoms comparable to interatomic distances at any finite temperature [7]. The argument was extended by Mermin 30 years later [8] and was strongly supported by a large number of experimental observations. Indeed, the melting temperature of thin films rapidly decreases with decreasing thickness as its surface/volume ratio is increased due to the fact that a material melting begins in its surface [1,9]; and the films become unstable (segregate into islands or decompose) at a thickness of, typically, dozens

of atomic layers [10,11]. Also the latent heats show large size-dependent fluctuations. In some cases, the melting temperatures change by hundreds of degrees with the addition of a single atom [12]. For this reason, atomic monolayers have so far been known only as an integral part of larger 3D crystal, usually grown epitaxially on top of monocrystals with matching crystal lattices. Without such a 3D base, 2D materials were presumed not to exist. Yet in 1962, the word “graphene” started to be used in order to define a graphite monolayer.

It was not until 2004 when the experimental discovery of graphene [13] and other free-standing 2D atomic crystals [14-16] showed the world that this kind of material can physically exist. Two scientists from the University of Manchester (United Kingdom), Andre Geim and Konstantin Novoselov (figure 2.5), isolated for the first time a layer of graphene using ordinary scotch tape and graphite. This particular method, known as mechanical exfoliation, leaded to the acknowledgment in 2010 with the Nobel Prize in Physics for the discovery of graphene and its characterization.

Figure 2.5: Andre Geim and Konstantin Novoselov, University of Manchester, UK. [17]

The experiment consisted in preparing graphitic sheets of thicknesses down to a few atomic layers to fabricate devices from them, and to study their electronic properties [12]. Despite being atomically thin (figure 2.6), the films remained of high quality, so that 2D electronic

transport is ballistic at submicrometer distances. No other film of atomic thickness is known to be even poorly metallic or continuous under ambient conditions. Using few layer graphene (FLG) and the new monolayer graphene, they succeeded in fabricating a metallic field-effect transistor in which the conducting channel was able to be switched between 2D electron and hole gases by changing the gate voltage. It was shown that the electronic structure rapidly evolves with the number of layers, approaching the 3D limit of graphite at 10 layers. Moreover, only graphene and, to a good approximation, its bilayer has simple electronic spectra: they are both zero-gap semiconductors with one type of electron and one type of hole. For three or more layers, the spectra become increasingly complicated: Several charge carriers appear, and the conduction and valence bands start notably overlapping. This allows single-, double- and FL- (3 to <10) graphene to be distinguished as three different types of 2D crystals (“graphenes”). Thicker structures should be considered, to all intents and purposes, as thin films of graphite.

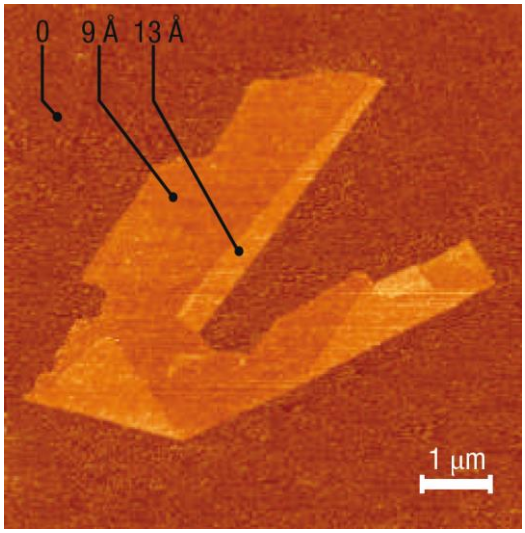

Figure 2.6: Graphene visualized by atomic force microscopy (AFM). The folded region exhibiting a relative height of ≈4 Å clearly indicates that it is a single layer. (Copyright National Academy of Sciences, USA) [1]

2.1.2. Properties

From the main characteristics of graphene, several important properties can be derived; and some of them are, in addition, unique and extreme. Two molecular and delocalized π orbitals perpendicular to the σ ones, have the electrons weakly attached and are responsible for the electronic properties of the system. Most of the properties of graphene are then, related to the electronic band structure [2,18], plotted in figure 2.7. The main characteristic of the electronic band occurs at the Fermi energy (E_F), where the π orbitals intersect in six points of two different equivalences, named K and K', the so-called Dirac points. The energy dispersion close to the Dirac points is linear with the momentum, being described by $E = \hbar k v_F$. The parameter v_F is the Fermi velocity with its value of $v_F \approx c/300$ (where c is the velocity of light in vacuum), and k is the wave vector.

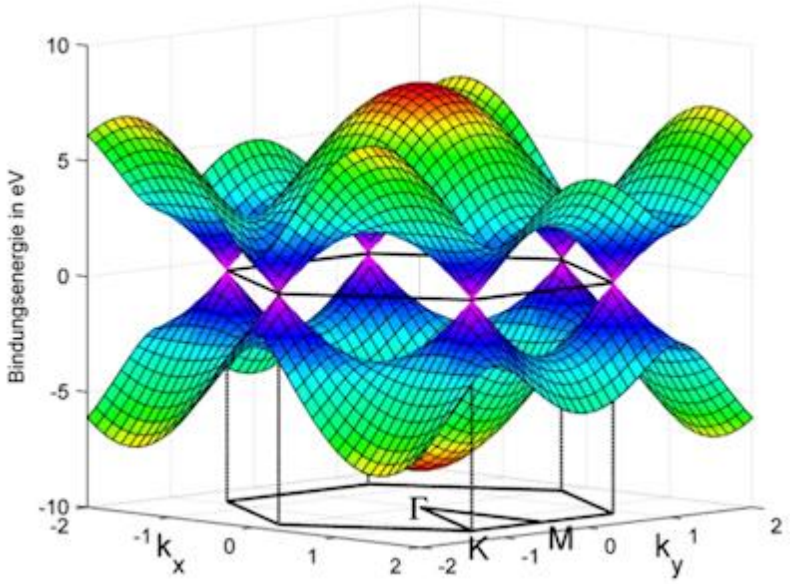

Figure 2.7: Electronic band structure of graphene. Dirac cones are plotted where the linear relation between k and E is evident. [19]

Close to the Dirac points, electrons (and also holes) behave as massless charge carriers with a speed of 10^6 m/s (faster than any other material) and a carrier charge density in the order of 10^{13} cm^{-2} [12]. This explains the very high mobilities predicted and detected in graphene and implies that graphene acts as if it was a semiconductor of zero-gap and

like a semimetal, a metal with a negligible density of states at the Fermi level (figure 2.8). The quasi-particle description and the Dirac equation describes better the system than Schrödinger equation because electron and holes behave as relativistic particles. Coming from relativistic treatment, the electrons and holes of the two different K and K' points are described by a pseudospin. The conservation of pseudospin forbids the hopping between K and K' Dirac cones. Coulomb potentials (may be due to impurities) cannot trap Dirac quasi-particles. The last two phenomena give rise to a long coherent transport (ballistic transport) in graphene.

The electronic band structure of a graphene monolayer, described above, can be modified breaking the symmetry of the crystallographic structure of the graphene sheet [18]. It can be done by stacking more layers, so the energy band in multilayer graphene is different. Also, as pointed out above, in graphene nanoribbons the band structure depends on the edge geometry and type of termination: arm chair or zig-zag.

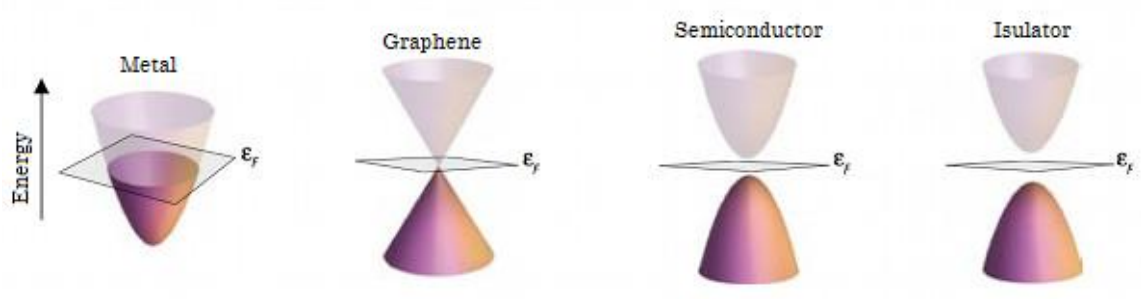

Figure 2.8: Dirac cones regarding the electronic properties. The cone below is the valence band (electrons), and the above cone is the conduction band (holes). [20]

Coming from its electronic band structure, the most relevant property of graphene is its very high carrier mobility. In graphene, on top of substrates, it is believed that the optical phonon scattering limits the mobility to 120000 $cm^2/V{\cdot}s$ at room temperature. In suspended graphene, the mobility has been shown to theoretically exceed 200000 $cm^2/V{\cdot}s$ at Room Temperature (RT), higher than any known semiconductor [21]. Because of the ballistic behaviour of graphene, RT Quantum Hall Effect (QHE) and Integer Quantum Hall Effect (IQHE) have been observed in graphene flakes. Interestingly, due to the peculiarities of graphene, we

find what is called anomalous QHE, in which the standard sequence of the conductivity with the magnetic field observed in conventional QHE appears shifted in graphene. [1]

It is important to mention the anomalous quantum Hall effect as an evidence of the existence of the Dirac Fermions. The origin of the electrons/fermions properties lies on their interaction with the periodic potential given by graphene structure. The attributes are described in the Dirac hamiltonian: $\widehat{H} = v_F \vec{\sigma} \cdot \widehat{p}$. The quantum Hall effect is a version of the Hall effect [22], observed in 2D systems with electrons submitted to low temperatures and strong magnetic fields, in which conductivity becomes a quantizable value. By the classical Hall effect, one obtains a linear relationship between the magnetic field applied on the sample and the Hall resistance. Otherwise the quantum effect shows a non-linear relationship: Different steps of Hall resistance for high magnetic fields and low temperatures are observed. The particularity of graphene is that electrons in it behave as massless Dirac fermions and that there is a zero energetic state which brings to an anomalous quantum Hall effect: it has a half-integer quantization of the Hall conductivity instead of an integer one.

Another important point about charge transport in graphene is ambipolarity. In the field-effect configuration, this implies that carriers can be tuned continuously between holes and electrons by supplying the requisite gate bias. Under negative gate bias, the Fermi level drops below the Dirac point, introducing a significant population of holes into the valence band. Under positive gate bias, the Fermi level rises above the Dirac point, promoting a significant population of electrons into the conduction band. The access to a truly ambipolar semiconductor enables a number of novel device structures. These are fundamentally different from silicon-based logic because doping levels can be dynamically controlled entirely by gating. Momentarily providing local gate biases to different parts of the same flake can form junctions or even more complicated logic. Subsequently rearranging the biases can then completely redefine the device without making any physical changes to the channel material [23]. As we will see, Chapter 9 is devoted to the

fabrication of a field-effect transistor (FET) with graphene. Other effects as plasmon amplification have also been reported.

On the other hand, three molecular and strong σ orbitals in trigonal shape are responsible for maximizing the links among the carbon atoms where the hexagonal structure is built (figure 2.9). The orbitals also provide this structure a great stability. This fact implies a wide range of mechanical, optical and thermal attributes, which are also relevant [24,25]. Regarding mechanical properties, graphene presents record values like other allotropes of carbon. Harder than diamond, its tensile strength is about 130 GPa (200 times higher than those of the steel) and the Young modulus has been estimated to be in the range of 0.5-1.0 TPa. Elastic and super flexible, graphene is even very light, weighing only about 0.77 mg/m^2 [26]. Some works also indicated that graphene has promise as a solid lubricant with thickness on the order of nanometers due to its atomically-thin configuration and high load carrying capacity. When tri-layer graphene is benchmarked with a 2 nm repulsive asperity against an 86% sp^3 content diamond-like-carbon (DLC) coating of the same thickness (1.0 nm), the graphene supports up to 8.5 times the normal load of DLC during indentation, and up to twice the normal load of DLC during sliding even after failure of one or more layers. [27]

In optics, the main characteristic is the strong light absorption for one monoatomic layer (around 2.3% for visible) but that, in global terms, makes it almost transparent. It can be demonstrated that the absorbance is the result of multiplying $\pi\alpha$ for the number of graphene layers, where $\alpha = e^2/\hbar c$ is the fine-structure constant. This linearity has been demonstrated for up to 5 layers [28], and it is further confirmed that such unique absorption could become saturated when the input optical intensity is above a threshold value, which makes graphene an ideal transparent conductor where optical transparency and low electric resistance are required [29].

Also the thermal properties are relevant. Thermal conductivities in the basal plane of the order of $5 \cdot 10^3$ Wm^{-1}K^{-1} have been reported [30], exceeding the record values of diamond and carbon nanotubes. This superb thermal conduction property of graphene is beneficial for

electronic applications and establishes graphene as an excellent material for thermal management.

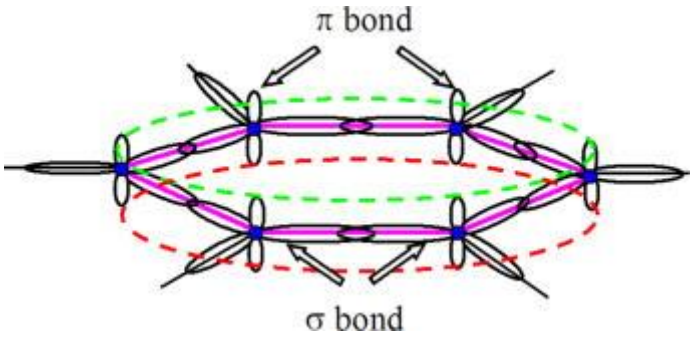

Figure 2.9: Scheme of the graphene hexagonal structure and σ and π bonds. [31]

As a visual and summarized example of some of the properties we have the "INVISIBLE CAT HAMMOCKS" of figure 2.10. It claims that an invisible graphene monolayer of 1 m^2 would only have a weight of 0.77 mg, and tied between two trees could hold a 4 kg body (e.g. a cat).

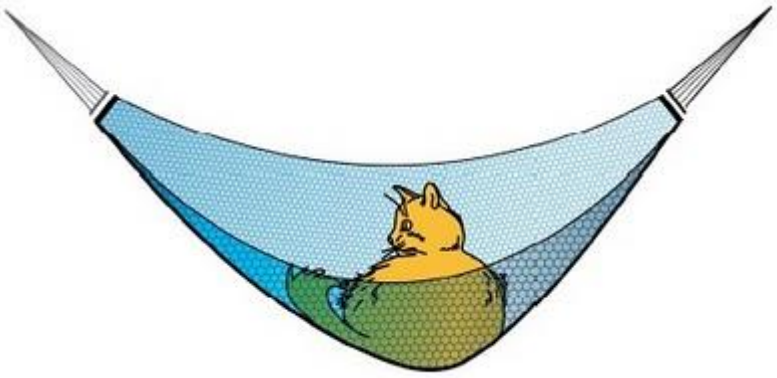

Figure 2.10: A monolayer graphene hammocks placing a cat before breaking. [32]

Also, graphene shows a chemical inertness, which makes it suitable for lithographic processes [33-34] in addition to show high chemical and thermal stability, great energy properties, and biocompatibility (as it is completely made of carbon). This bunch of interesting properties leaded to an intensive research, both theoretical and experimental, to try to understand and use graphene in applications that will be described in the next section.

2.1.3. Potential applications

The high mobility of graphene makes this material promising for future electronics. The first and main drawback that we have to tackle is the lack of a band gap. In addition, because of the linear dispersion relation, the density of the states in the Fermi energy level does not allow the non-linear response required in electronic applications. It is necessary to substantially modify the conductance when an electric field is applied. Engineering a band gap in graphene samples may be the solution. As it has been explained above, the electronic band structure of graphene can be modified changing the particular structure that has originated it. One of the methods can be functionalizating the graphene surface with other species. Another way is producing graphene nanoribbons. The finite size effects are present in this kind of structures. Also the edges are important. The type of the nanoribbon edge (zig-zag or arm chair) plays a similar role as the chirality does in carbon nanotubes. Moreover, the spin coherence length is also high in graphene which makes it a suitable material for applications in spintronics. If the production methods acquire the sophistication that nowadays semiconducting technology demands, graphene is postulated as one of the main candidates to replace silicon in a hypothetical post-Si and post-CMOS era. [24]

The high conductivity combined with the low absorbance of graphene warrants properties required for transparent electrodes. Nowadays the standard material for this purpose, indium tin oxide (ITO), can find a competitor in graphene. Once the growth techniques have been developed, graphene can offer a high quality low cost alternative to ITO in applications such as solar cells, liquid crystal displays and touchscreens. Several works have been done with this objective [33,35,36]. New generation of touchscreens would be in principle possible through very high quality and extremely thin and flexible displays. Due to the high thermal conductivity, graphene-based devices would show less degradation in front of heat and, therefore, have longer lifetimes.

Sensing is another possible field of application due to the extraordinary electronic properties, mechanical resistance and large specific surface area of graphene. The adsorption of molecules in the surface can modify the local charge carrier concentration and this can be

detected in a Field Effect Transistor (FET) configuration. A single molecule detection has been achieved, which demonstrates the potential high sensitivity of graphene-based sensors [37]. Sensing is not limited only to chemical species; it can be applied to any phenomena that modify the carrier concentration such as magnetic field and mechanical deformation. The extraordinary mechanical properties also make graphene a suitable material for constructing Nano-ElectroMechanical Systems (NEMS) such as pressure sensors or resonators. [24,25]

Further application fields that, likely, will be a reality in the near future are:

- **Ultracapacitors and microbatteries:** able to store big quantities of energy, 20 times more powerful than the current ones; and with a charging time 1000 times faster.
- **Bio-related material:** biomedicine and biosystems like graphene-coated implants, biosensors, and drug delivery.
- **Thermal management material:** high thermal conductivity, and consequently fast cooling.
- **Structural materials (paper, powder):** much harder, stronger, and more flexible than current ones.
- **High performance computation:** terahertz oscillators and high-speed field-effect transistors with switching speeds between 100 GHz and a few THz, and a performance 30 times higher than current.
- **Junction diodes:** p–n and Schottky diodes are used in a wide variety of electronic/photonic systems as building blocks.
- **Photovoltaics:** more efficient solar cells by using graphene as a charge collector. Electrons in graphene which have been excited to a higher energy state by absorbing incoming light, transfer their energy to neighbouring electrons, rather than radiating it as photons.
- **Conductive ink:** graphene-based coatings for printed electronics (circuits can be printed almost on any substrate) and smart packaging

(electrical-conductive applications), and also coatings for heat dissipation or other thermal management.

- **Graphene based quantum dots:** nanolight with extraordinary properties due to their remarkable quantum confinement and edge effects: systematic photoluminescent mechanisms, bandgap engineering, in addition to the potential applications in bioimaging, sensors, *etc.*

- **Graphene aerogel:** is seven times lighter than air, and 12% lighter than the previous record holder (aerographite). Its density is just 0.16 mg/cm^3, and has a superb elasticity and absorption. It can recover completely after more than 90% compression, and absorbs up to 900 times its own weight in oil, at a rate of 68.8 g/s.

- **Optical modulators:** are commonly used in communication and information technology to control intensity, phase, or polarization of light. Graphene allows broadband light-matter interactions with ultrafast responses and can be readily pasted to surfaces of functional structures for photonic and optoelectronic applications.

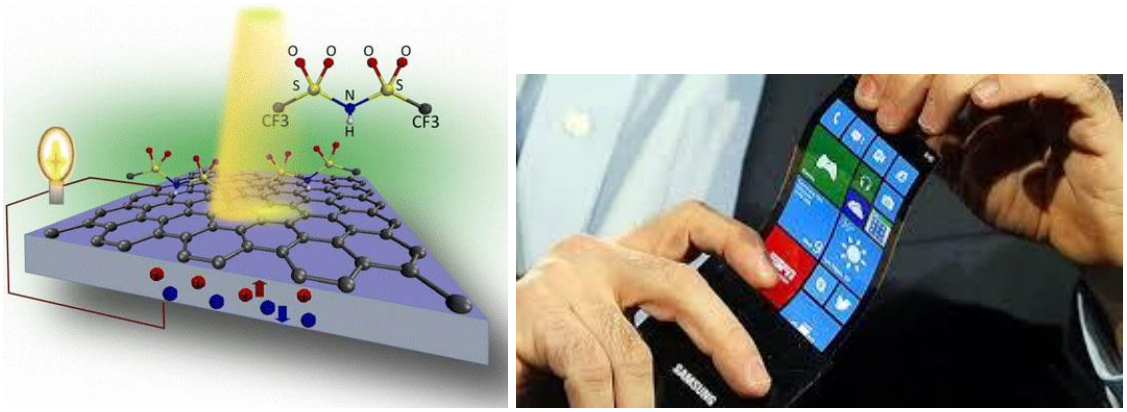

Figure 2.11: (left) Graphene solar cell; (right) a flexible cell phone made of graphene (Samsung). [38,39]

2.1.4. Market expectations and regulations

The fantastic and extreme properties of graphene quickly boosted a large number of potential applications in almost every sector of research and industry. But, what about the *market*? Another interesting way to evaluate the significance of this material is checking how the world of investors and international markets is reacting. Although the discovery of graphene was made 10 years ago, the real revolution is about to come from now on. This section is devoted to introduce the economic impact of graphene.

The main market driver so far has been the R&D sector. The industry is now gearing up to move beyond research activities and a diverse range of other applications are actively being developed. These include RFID, smart packaging, supercapacitors, composites, ITO replacement, sensors, logic, and memory. There are many different types of graphene-based materials, each offering a different set of properties. The differentiating parameters include the number of layers, purity, oxygen content, crystallinity and form (powder or sheet). Depending on the specifics of these parameters, the quality of the so-called graphene can vary, from that of the ideal material towards that of graphite oxide. Indeed, most companies today produce different types of graphene, which means different material properties and therefore different target markets. Taking into account all of these variables, *IDTechEx* forecasts a first approach of 100 M$ (millions of US dollars) market for graphene in 2018. [40]

There are numerous indications that graphene is around the peak of its *hype cycle*: there has been the launch of prototypes and the first-generation of products; we have witnessed a mushrooming of start-up formations (at National and International levels); and the industry has seen a flurry of seed and early-stage funding (figure 2.12). The IP (Intellectual Property) patenting activity has also been on the rise too, exponential growth in the world (figure 2.13). Here, the focus is fast shifting from covering the manufacturing techniques towards protecting the formulation and the end uses of graphene. In the background, there has been an intense press full of praise and optimism.

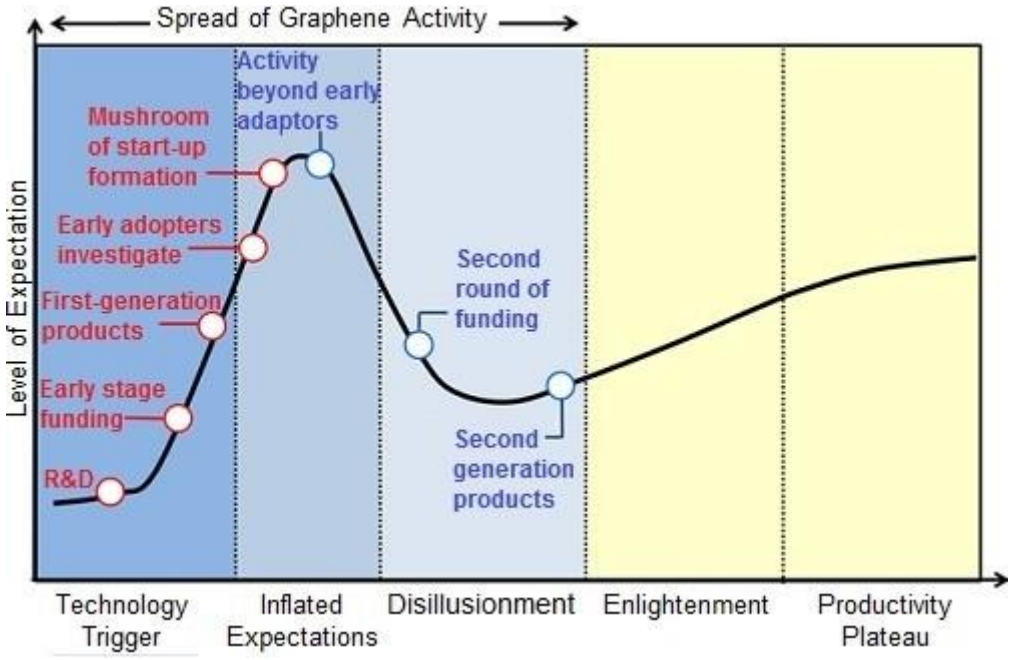

Figure 2.12: Hype cycle of the emergent technologies of graphene. Presently, the graphene-based activity is in the second round of funding, but just after the peak. Every division represents a period of approximately five years, beginning from 2002. [40]

Interestingly, *IDTechEx* also finds many emerging indications that this fledging industry is beginning to move past the peak: several companies are already within the second or third round of financing; the second generation of products is being launched with more realistic assessment of the near- to medium-term market opportunity; and a more realistic press is also being formed with calibrated expectations.

The composites and the energy storage (supercapacitors) will constitute bigger opportunities in the market in short term beyond R&D. *IDTechEx* expects that graphene will get first into the low-cost market, but demanding high performance levels.

IDTechEx also forecasts that graphene will have limited success in the transparent conductor market, because it falls short both on cost and performance compared to incumbent and alternative options. Market success will be probably limited in the transistor area, both in analogue and digital applications. This is partly due to a lack of bandgap and the high level of standards set by incumbent solutions. Figure 2.13 shows a chart of overall largest patent portfolios with Samsung being the clear

leader with 210 patent families (inventions) in 405 published patent applications. The most notable change in the top applicants since 2011 is the large influx of Chinese applicants. Only 8 of the top 20 applicants in the 2011 remain the same with 8 of the 12 new entrants to the top 20 list coming from China.

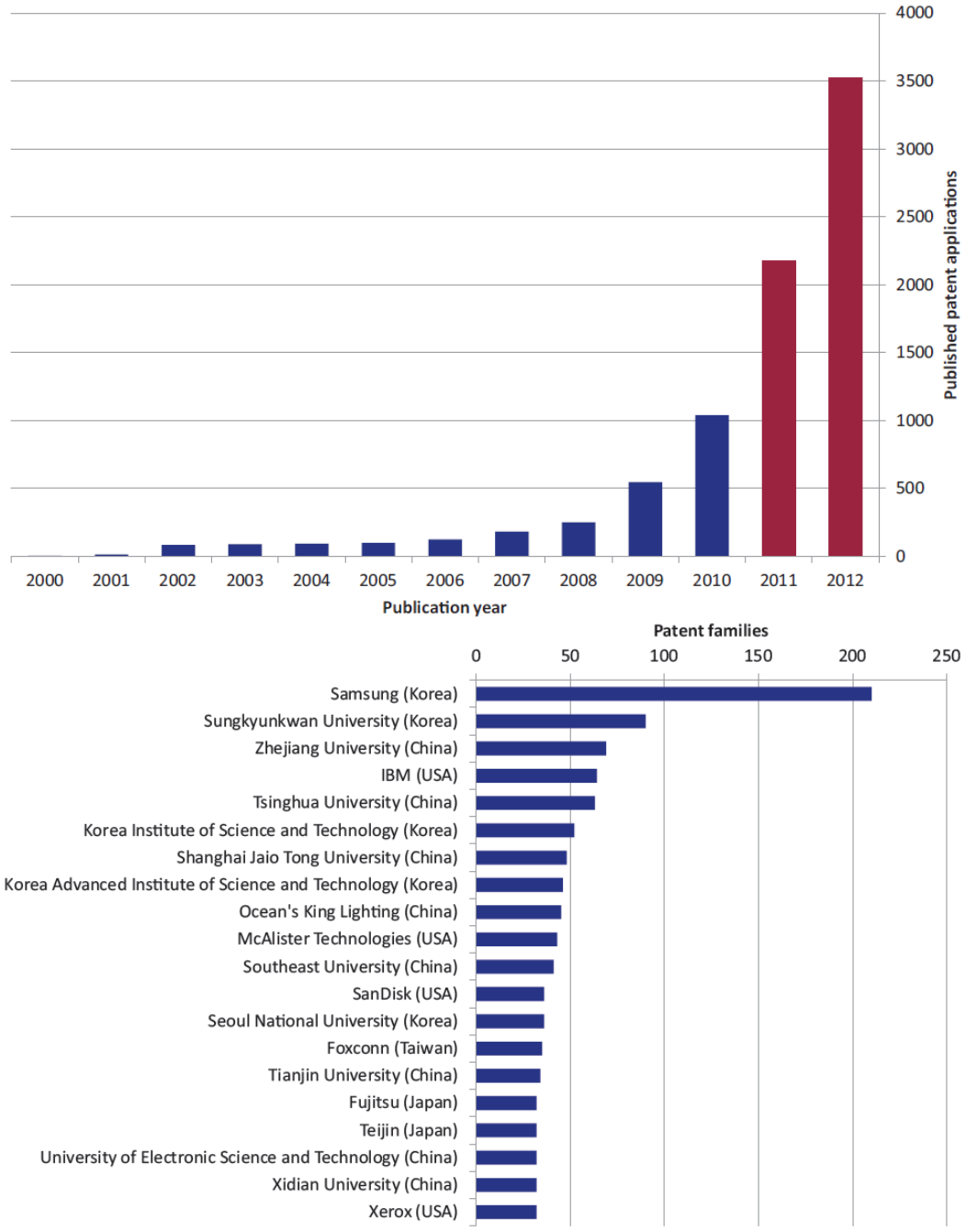

Figure 2.13: (Up) Worldwide patent publications related to graphene by publication year. (Down) Number of patent families of the Top 20 applicants. [41]

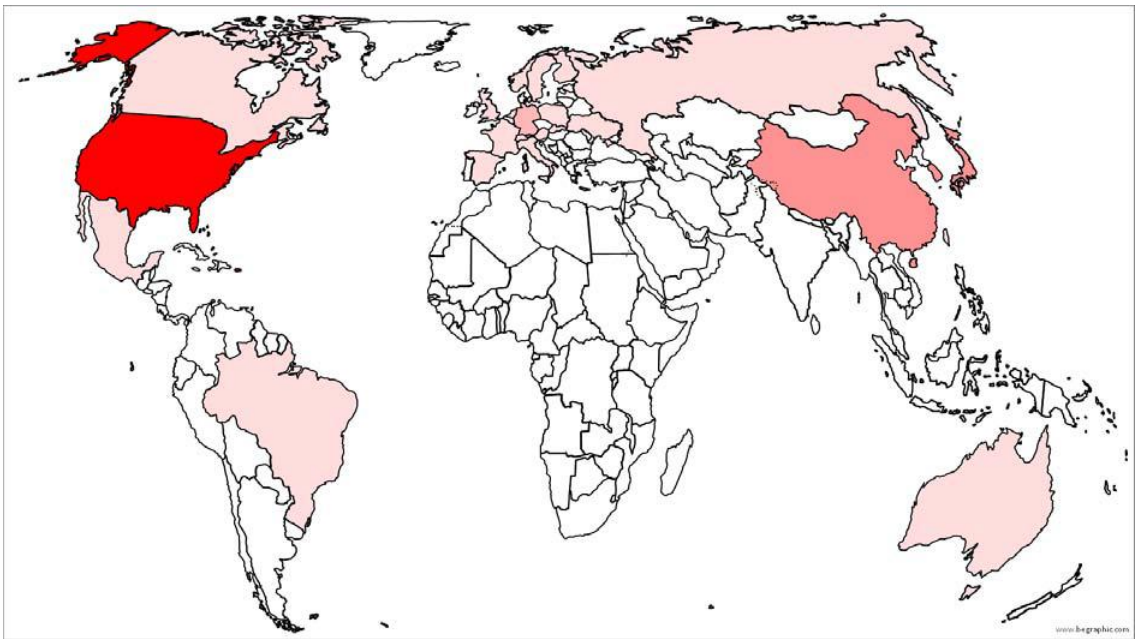

Figure 2.14: Patents density related with graphene per country. [41]

On the other hand, *BCC Research* (formerly as *Business Communications Company, Inc.*) does a wide research work of the graphene market matching in the basic aspect that the technologies associated with graphene are reaching the *hype cycle* peak, and that supercapacitors will lead the graphene market. The study covers the forecast period from 2011 to 2022 (figure 2.15), and the highlights are [42]:

- The global market for graphene-based products is projected to reach $122.9 million in 2017 and $986.7 million in 2022, increasing at a five-year compound annual growth rate (CAGR) of 51.7%.
- The segment made up of capacitors is projected to be the largest segment in 2022. Capacitors are expected to increase from $31 million in value in 2017 to $410 million in 2022, a CAGR of 67.6%.
- Structural materials are expected to jump from $44.5 million in 2017 to $167.6 million in 2022, a CAGR of 30.4%.

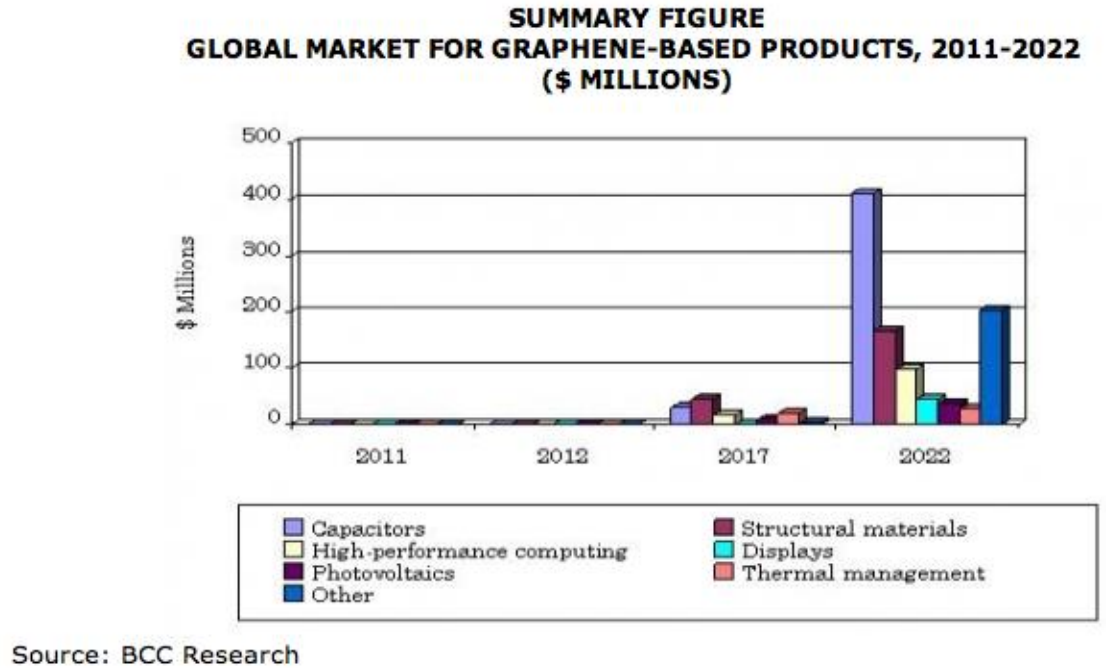

Figure 2.15: Global market for products based on graphene, 2011-2022. [42]

Last *BCC Research* studies (2013) show that significant sales of graphene products are expected to develop between 2013 and 2018. The market is projected to be worth almost $195 million by 2018, reaching $1.3 billion by 2023, with a five-year compound annual growth rate (CAGR) of 47.1% from 2018 to 2023.

The growth of the graphene market seems unavoidable, even taking into account that it is still a non-regulated market; in long-term there are not expectations of hard legislations in this regard.

So far neither health nor environmental risk exist concerning the development of a technology or a product related to graphene and its equipment; most of the components are standard and are already regulated by itselves. Furthermore, there is a lot of documentation of the processes that take place in all the growth technology of graphene. Thus, we only could evaluate the risks regarding the regulations of graphene as a nanomaterial. Sectors as electronics and materials, the existing regulation in those fields are not enough developed yet. Actually, there is a lack of International laws that regulate nanotechnology or nanomaterials. As a reference we have what seem to be the first steps to a regulation at country and/or International level:

In the European Union there is a group called SCENIHR (*Scientific Committee on Emerging and Newly Identified Health Risks*) in order to study the implication in the nanotechnology. This organism has redefined the word "Nanomaterials" and it also has published a list of the possible risks associated with the nanoparticles. [43]

In the United States of America, the EPA (*Environmental Protection Agency*) regulates the nanotechnology with two different laws carried by two different offices: the FIFRA (*Federal Fungicide, Insecticide & Rodenticide Act*) and the TSCA (*Toxic Substances Control Act*). Nanomaterials as graphene and carbon nanotubes are regulated by the TSCA.

On the other hand, states as California (USA), have developed their own regulations regarding nanomaterials and even graphene, that it has a specific regulation and is placed as a "green chemical", non-toxic. The particularity is that nanomaterials are included into the definition of chemical product, and they also have the own definition of: [44]

"any form of an intentionally engineered chemical, substance or material that is intended to be composed of a discrete nanostructure that meets either of the following criteria: 1. at least one spatial dimension of the nanostructure is at the nanoscale, or 2. the nanostructure is larger than nanoscale in any spatial dimension, but is 1000 nanometers or less in at least one spatial dimension, and the nanostructure exhibits one or more nanoscale phenomena."

But the market is not the unique business. Besides it, several graphene research projects around the world are still rising due to the large impact of results and applications in graphene. Especially in Europe, where it reached its top in research funding. One year ago, the European Commission decided to support two projects with €1000 Million each during 10 years: the Graphene and the Human Brain flagships. The Graphene project, coordinated by Jari Kinaret from Chalmers in Gothenburg, comprises 176 different research groups from 17 European countries; and it is devoted to work through 16 Work Packages that cover almost all the areas of graphene: from fundamental science and

production, or optoelectronics and spintronics, to health and environment or management. [45]

All these ingredients will make sure that graphene will become a future product at our homes, probably in the shape of a smartphone, packaging, in cars or even between the walls of our house.

2.2. Synthesis methods of graphene

Since the discovery of graphene through mechanical exfoliation of pyrolytic graphite, several approaches from many disciplines have been developed in order to obtain it. However, different synthesis methods lead to "different qualities and characteristics" of the graphene produced. Ones may be close to "perfect", mainly for research purposes but extremely expensive. Others may not be that "perfect" but cheap enough to make it real and carry it to the industry. Among them, Chemical Vapor Deposition (CVD) process (e.g. on copper, nickel, ruthenium…) seems to meet both requirements in quality and cost, as shown in figure 2.16.

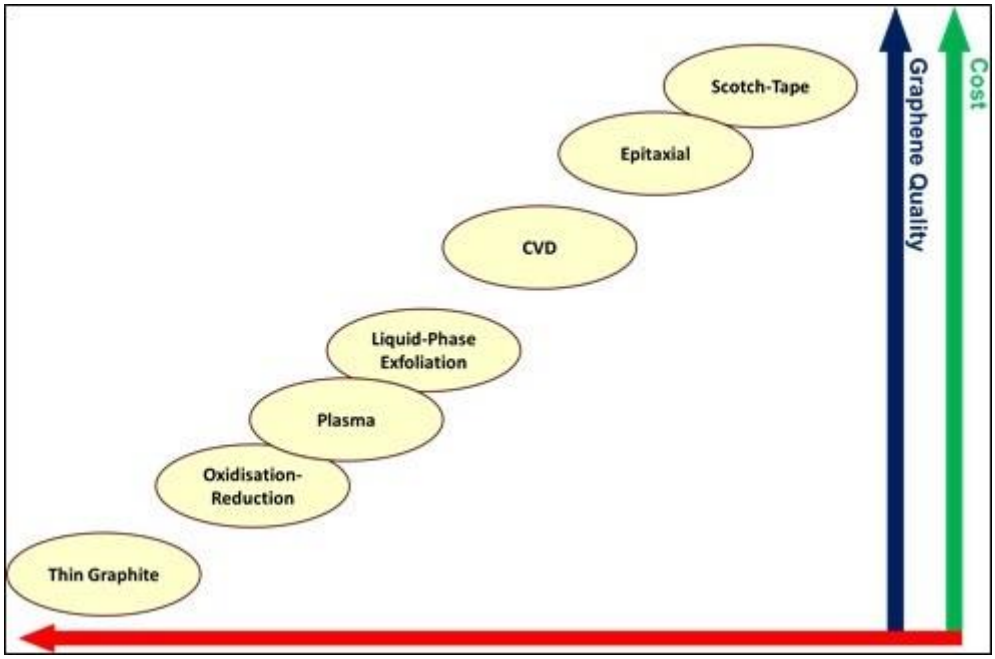

Figure 2.16: Plot of the main graphene synthesis methods regarding quality and cost (Y axis) and scalability (X axis). [40]

Some of the most important synthesis methods of graphene are summarized in the next sections.

2.2.1. Mechanical exfoliation

Made popular by the Nobel Prizes A. Geim and K. Novoselov, it was the first technique used to isolate one monolayer of graphite, as explained in section 2.1.1. Its simple mechanism is based on repeating peeling of highly oriented graphite. As it was one of the methods used in this thesis to obtain graphene, it will be described more in detail in section 3.1.

2.2.2. Chemical exfoliation

Another possibility is to obtain graphene *via* wet chemical routes like chemical exfoliation, which consists in the intercalation of a reactant among the graphene sheets (of graphite) that softens the van der Waals interactions. This is achieved immersing graphite in an acid solution (sulfuric and/or nitric acid). The soften interlayer interactions will be broken then, by means of two steps: first, a thermal process (solvothermal), and finally ultra-sonication to disperse them. The result consists in graphene oxide sheets suspended in a colloidal solution, which are deposited on a substrate (figure 2.17). For the final objective of obtaining pure graphene flakes, the oxide has to be removed in a reducing atmosphere using alkaline solutions, or applying hydrogen plasma, or hydrazine vapours, figure 2.18, or through heat treatments. Graphene flakes partially oxidized are obtained because, unfortunately, the reduction processes are not very efficient (a highest C/O ratio of ~17, what means a 5.5 at.% of oxygen content [46]).

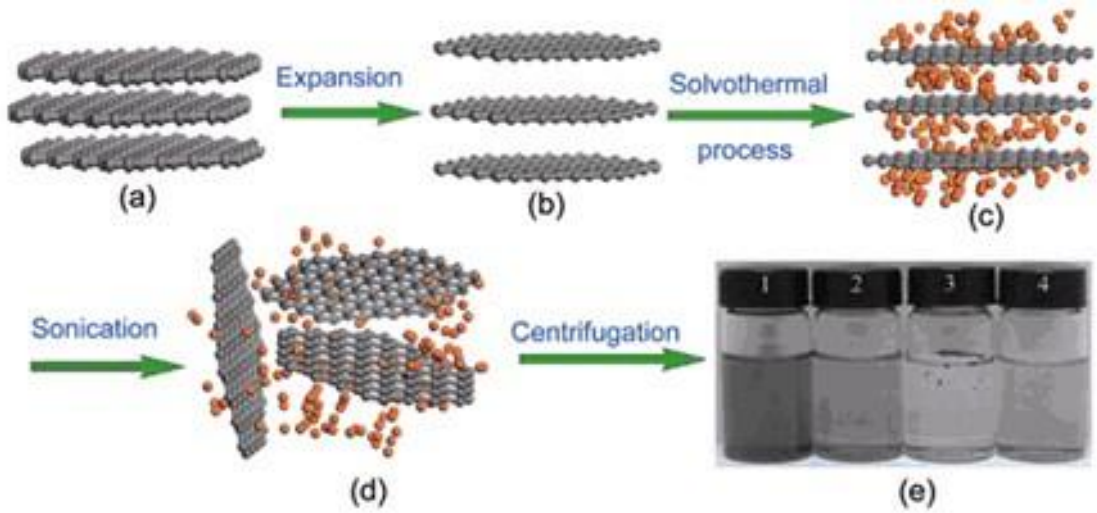

Figure 2.17: Solvothermal-assisted exfoliation and dispersion of graphene sheets: (a) pristine expandable graphite, (b) expanded graphite, (c) insertion of acid into the interlayers of the expanded graphite, (d) exfoliated graphene sheets dispersed, and (e) optical images of four samples obtained under different conditions. [47]

Another drawback is that in the chemical exfoliation process, the sp^2 like graphene bounds are partially degraded to sp^2-sp^3 structures. Nonetheless, the process involving chemical exfoliation permits an accurate control of the size of the graphene sheets. For example, the longer the sonication process, the smaller the graphene sheets because fragmentation progressively occurs, being possible to obtain solutions with graphene flakes smaller than 10 nm. The graphene size range can be completed with the molecular approach, where the production of polycyclic aromatic molecules (hexabenzocoronene, HBC) reaches the size comparable to the smaller graphene sheets obtained by other approaches, while offering a continuous path to mesoscopic and even macroscopic dimensions. [24]

The main advantage of the chemical exfoliation is the high output, which makes it economically competitive and also convenient to manipulate; but due to the chemical steps, the purity and quality is not of a high-performance graphene. Chemical exfoliation is a very popular method used for the production of inks, powder coatings, composite materials, and biological applications.

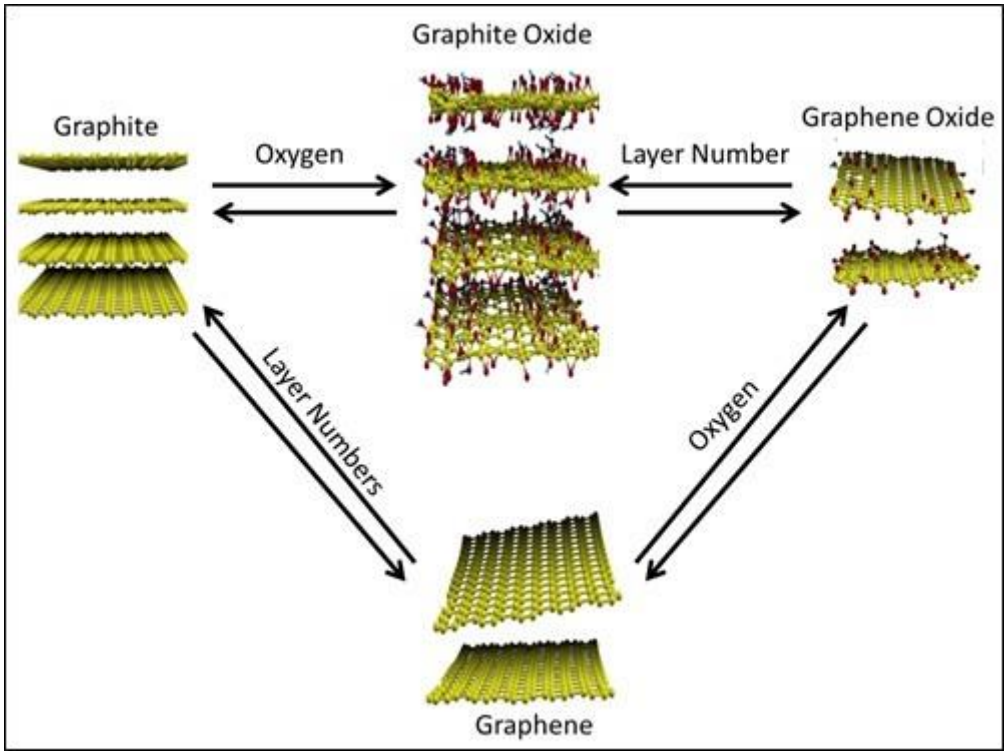

Figure 2.18: Schematic illustration of the possibilities to obtain graphene, graphene oxide, graphite, and graphite oxide from each others. [40]

2.2.3. Epitaxial growth

An alternative growth technique on a substrate is the epitaxial growth on crystalline silicon carbide wafers. By heating c-SiC at high temperatures in a controlled atmosphere of Ar (or even vacuum) the silicon near the surface is sublimated but not the carbon atoms. For high enough temperatures (about 1300 °C) the carbon reorganizes and the graphitization is achieved [48]. The result is a very thin graphite layer that, under suitable conditions, produces graphene monolayers (figure 2.19). From the different polytypes of SiC, most of the studies have focused on the hexagonal ones, being the most commonly used forms the 4H-SiC and the 6H-SiC. Significant differences in graphene growth have been found for the two polar faces of SiC: the SiC(0001) that is Si-terminated and the SiC(000-1) that is C-terminated. The high surface roughness of graphene obtained from the Si-face or the lower sublimation temperature from the C-face are features limiting the performance of graphene in determined applications. [2]

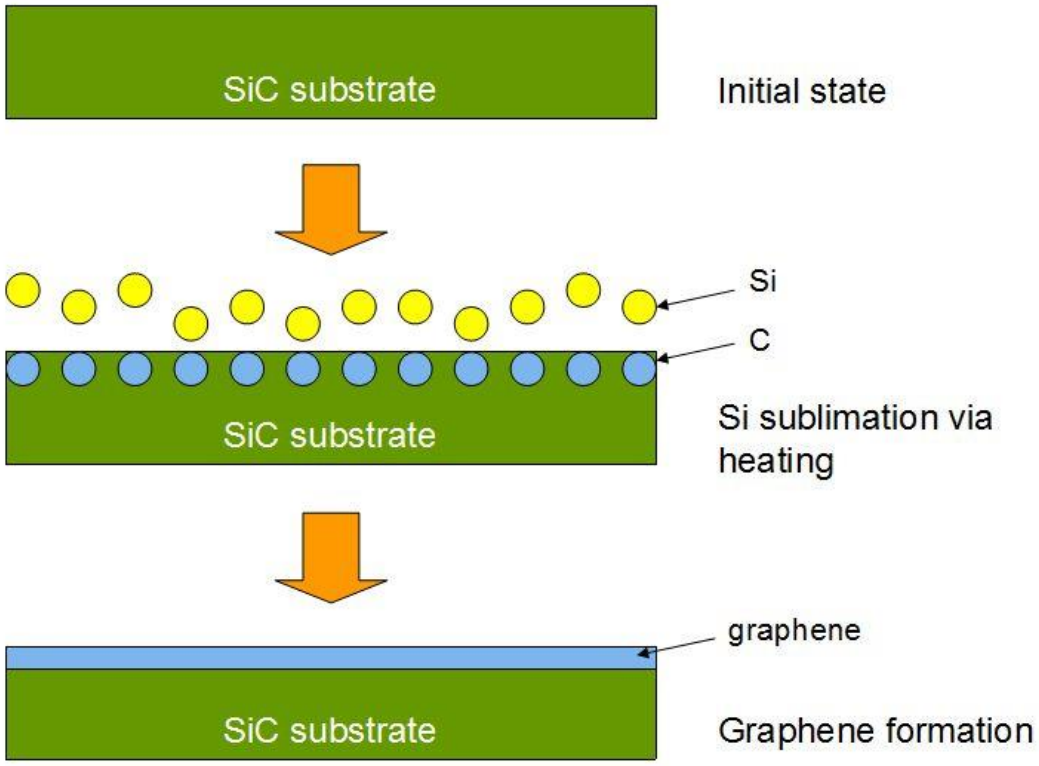

Figure 2.19: Illustration of an epitaxial growth on a SiC substrate. After the sublimation of silicon, carbon remains on the surface where it would became graphene later. [49]

Epitaxial growth is promising because it is easily deployable to the semiconductor industry, transistors, and other electronic devices. On the other hand, the quality of graphene under low-temperature processes still have to be improved in comparison to other technologies like mechanical exfoliation or CVD processes on transition metals. However, the final extension of graphene is only limited by the substrate (SiC wafer) area.

2.2.4. Chemical Vapor Deposition (CVD)

In a CVD process, the graphene growth on a surface is due to thermal decomposition of molecules of a hydrocarbon gas (methane, acetylene, propane...) catalyzed by a metal surface or because of the segregation/precipitation of carbon atoms from the bulk metal [50]. Presently, transition metals are widely used as catalysts in production process of other carbon allotropes like nanotubes. Therefore, it is not surprising that the transition metals (Ru, Ir, Co, Cu, Ni, Re, Pt, Pd) are the

main focus of research for the production of graphene. Transition metals are particularly appealing for obtaining large-area high quality graphene and for developing a process ready to be integrated to the existent semiconductor industry. The main drawback of the CVD method is the need for a step where the graphene is transferred from the metal onto a more suitable substrate.

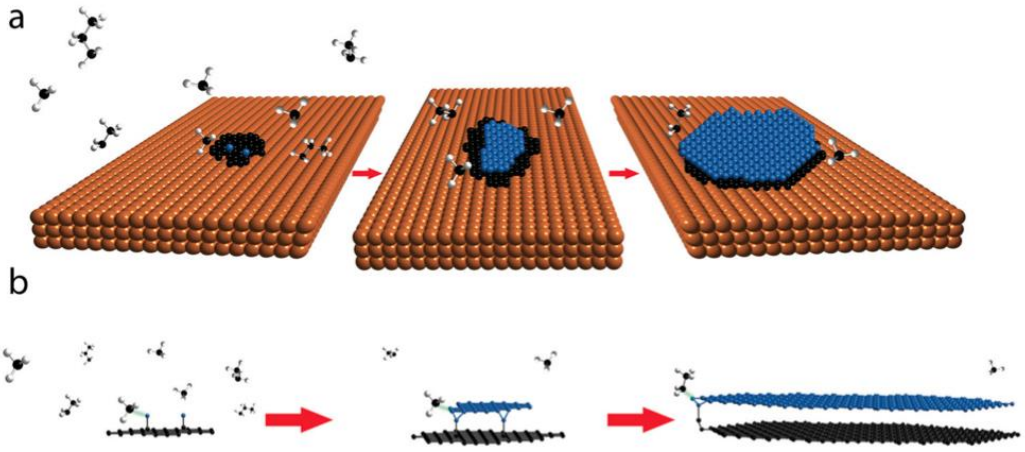

Figure 2.20: A schematic of one and bilayer graphene growth with ethane and/or propane feedstock gas. (a) Top view is shown with a space-filling model and (b) side view is shown with a ball-and-stick model. Copper atoms are shown as orange spheres, carbon in black (first layer) and in blue (second layer), and hydrogen in gray. [51]

Chemical vapor deposition is the main method used and investigated in this thesis and it will be deeply discussed in section 3.2.

2.3. MoS_2, h-BN, and Silicene

Graphene demonstrated not only the feasibility of a 2D stable crystal; it opened a new wide field where the monolayer materials and their unique characteristics are the main features. Actually, this new horizon would not finish with graphene or carbon based materials. Every day, scientists around the world are trying to synthesize as much 2D materials as possible with different chemical elements and compounds in order to improve certain features (or even discover new ones), reduce costs, and adequate them to a concrete application. Good examples are MoS_2, h-BN, and silicene; a brief description right next.

- MoS_2

Molybdenum disulfide is a transition-metal dichalcogenide semiconductor which has attracted great interest because of its distinctive electronic, optical, and catalytic properties, as well as its importance for dry lubrication in space engineering or vacuum technology. The bulk MoS_2 crystal, an indirect-gap semiconductor with a band gap of 1.29 eV, is built up of van der Waals bonded S-Mo-S units. They consist of two hexagonal planes of S atoms and an intermediate hexagonal plane of Mo atoms coordinated through covalent interactions with the S atoms in a trigonal prismatic arrangement. The formation of ultrathin crystals of MoS_2 by the micromechanical cleavage (mechanical exfoliation) technique is possible, as demonstrated by Novoselov et al. The research has been focused especially in the hybrid structure MoS_2/graphene as high-sensitive photodetectors. The rest of the transition metal dichalcogenides encompasses a larger class of 2D layered materials: as WS_2, $MoSe_2$ and WSe_2 (still largely unexplored), and finally $MoTe_2$ and WTe_2. [52,53]

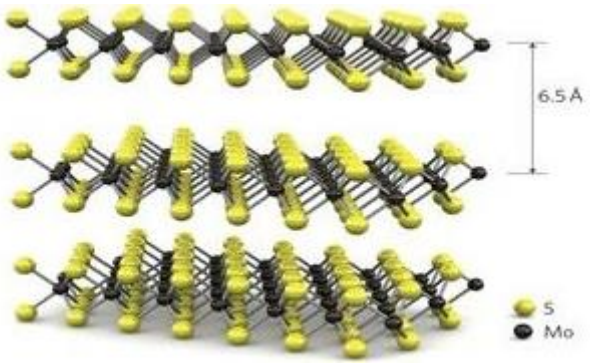

Figure 2.21: Diagram of MoS_2 monolayers. [54]

- h-BN

Boron nitride is a chemical compound found normally as amorphous powder with excellent lubricating properties. Its most stable crystalline form is the hexagonal (h-BN), analogous to graphite; but it also exists in the same crystallographic group of diamond, the cubic form (c-BN). h-BN is an insulator with a direct band gap of 5.97 eV. Due to its strong covalent sp^2 bonds in the plane, the in-plane mechanical strength and

thermal conductivity of h-BN has been reported to be close to that of graphene [55]. It has an even higher chemical stability than graphene; in air up to 1000 °C (in contrast, for graphene the corresponding temperature is 600 °C). Because of its high thermal stability, it is often used as parts of high-temperature equipment and lubrication (e.g. aeronautics and space applications).

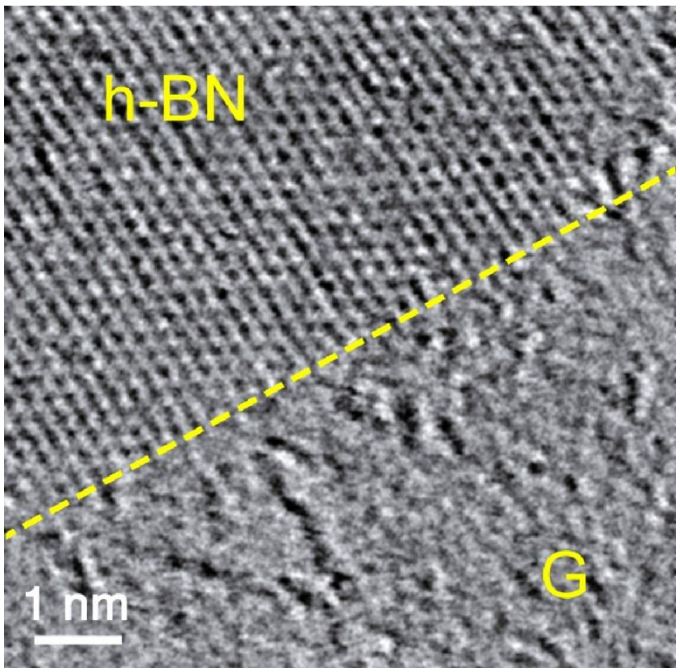

Figure 2.22: Top view TEM image of a junction between a h-BN monolayer and graphene. [56]

- Silicene

It is the silicon-based analogue of graphene, a 2D crystal made of hexagonal rings of silicon not fully planar, but with surface ordered ripples. Commonly grown on silver, Ag (111), it has similar electronic properties as graphene. Silicene has, as the most relevant highlight, the potential compatibility with existing semiconductor techniques, almost completely based on silicon; but the main drawbacks of silicene are that it does not naturally align in the honeycomb structure, and that it reacts easily with oxygen.

For low buckling (LB) structures, the Si-Si nearest-neighbour distance is reduced to 0.225 nm from that of the bulk, and that the electronic density of states indicates the system is ambipolar (like graphene). Moreover, silicone nano-ribbons (NRs) exhibit electronic

and magnetic properties likewise very similar to those of graphene. [57]

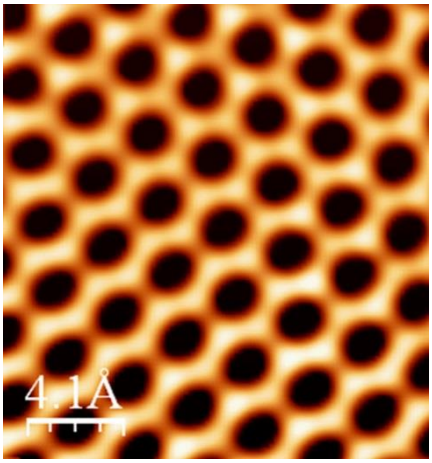

Figure 2.23: Detailed scanning tunneling microscope (STM) image showing the honeycomb structure of a silicene net. [58]

In the same group of silicon there is also germanium, and its graphene-like germanene, right now being investigated. The stanene, an atomic layer of tin, has theoretically no electrical resistance at 100 °C. Although it has not been synthesized yet, it could be a revolution in the electrical consumption. So far, the list of 2D crystals only seems to increase as well as the new-brand characteristics that this kind of materials offers. However, graphene is still on the top of this classification and the main theme of this thesis.

2.4. References

[1] A.K. Geim, K.S. Novoselov, *The rise of graphene*, Nature materials 6, 183-191 (2007).

[2] J. Haas, W.A. de Heer, E.H. Conrad, *The growth and morphology of epitaxial multilayer graphene*, J. Phys. Condens. Matters 20, 323202 (2008).

[3] R. Saito, G. Dresselhaus, M.S. Dresselhaus, *Physical properties of carbon nanotubes*, Imperial college press, Singapur 24-25 (1998).

[4] electronicstructure.wikidot.com/yasmin

[5] R.E. Peierls, *Quelques proprietes typiques des corpses solides*, Ann. I. H. Poincare 5, 177–222 (1935).

[6] L.D. Landau, *Zur Theorie der Phasenumwandlungen II*, Phys. Z. Sowjetunion 11, 26–35 (1937).

[7] L.D. Landau, E.M. Lifshitz, *Statistical Physics, Part I*, Pergamon, Oxford (1980).

[8] N.D. Mermin, *Crystalline order in two dimensions*, Phys. Rev. 176, 250–254 (1968).

[9] J.S. Bunch, S.S. Verbridge, J.S. Alden, A.M. van der Zande, J.M. Parpia, H.G. Craighead, P.L. McEuen, *Impermeable atomic membranes from graphene sheets*, Nano Lett. 8, 2458 (2008).

[10] J.A. Venables, G.D.T. Spiller, M. Hanbucken, *Nucleation and growth of thin films*, Rep. Prog. Phys. 47, 399–459 (1984).

[11] J.W. Evans, P.A. Thiel, M.C. Bartelt, *Morphological evolution during epitaxial thin film growth: Formation of 2D islands and 3D mounds*, Sur. Sci. Rep. 61, 1–128 (2006).

[12]K.S. Novoselov, A.K. Geim, S.V. Morozov, D. Jiang, Y. Zhang, S.V. Dubonos, I.V. Grigorieva, A.A. Firsov, *Electric Field Effect in Atomically Thin Carbon Films***,** Science 306, 666 (2004).

[13]K.S. Novoselov, Z. Jiang, Y. Zhang, S.V. Morozov, H.L. Stormer, U. Zeitler, J.C. Maan, G.S. Boebinger, P. Kim, A.K. Geim, *Room-Temperature Quantum Hall Effect in Graphene*, Science 315, 1379 (2007).

[14] F. Rana, *Graphene terahertz plasmon oscillators*, IEEE Trans. Nanotechnol. 7, 91 (2008).

[15] G. Liang, N. Neophytou, D.E. Nikonov, M.S. Lundstrom, *Performance projections for ballistic graphene nanoribbon field-effect transistors*, IEEE Trans. Electron Devices 54, 677 (2007).

[16] J.R. Williams, L. DiCarlo, C.M. Marcus, *Quantum Hall effect in a graphene p-n junction*, Science 317, 638 (2007).

[17] assets.inhabitat.com/wp-content/blogs.dir/1/files/2012/01/Kostya-Novoselov-e1325514414733.jpg

[18] A.H. Castro-Neto, F. Guinea, N.M.R. Peres, K.S. Novoselov, K. Geim, *The electronic properties of graphene*, Rev. Mod. Phys. 81 (1), 109-162 (2009).

[19] www.uni-muenster.de/imperia/md/images/physik_pi/zacharias/research/graphene/graphene_band_structure.png

[20] J. González, M.A. Hernández, F. Guinea, *La electrónica del grafeno*, Investigación y Ciencia (2010).

[21] J.H. Chen, C. Jang, S. Xiao, M. Ishigami, M.S. Fuhrer, *Intrinsic and extrinsic performance limits of graphene devices on SiO_2*, Nat. Nanotech. 3, 206-209 (2008).

[22] C. Rodríguez, O. Vasilievna, *Propiedades y aplicaciones del grafeno*, UANL (2008).

[23] M.J. Allen, V.C. Tung, R.B. Kaner, *Honeycomb Carbon: A Review of Graphene*, Chem. Rev. 110, 132–145 (2010).

[24] C. Soldano, A. Mahmood, E. Dujardin, *Production, properties and potential of graphene*, Carbon 48, 2127-2150 (2010).

[25] A.K. Geim, *Graphene: Status and Prospects*, Science 324, 1530-1534 (2009).

[26] C. Lee, X. Wei, Q. Li, X. Wei, J.W. Kysar, J. Hone, *Measurement of the Elastic Properties and Intrinsic Strength of Monolayer Graphene,* Science 321, 385 (2008).

[27] E.J. Sandoz-Rosado, O.A. Tertuliano, E.J. Terrell, *An atomistic study of the abrasive wear and failure of graphene sheets when used as a solid lubricant and a comparison to diamond-like-carbon coatings*, Carbon 50, 4078 (2012).

[28] R.R. Nair, P. Blake , A.N. Grigorenko, K.S. Novoselov, T.J. Booth, T. Stauber, N.M.R. Peres, A.K. Geim, *Fine structure constant defines visual transparency of Graphene*, Science 320, 1308 (2008).

[29] A.B. Kuzmenko, E. van Heumen, F. Carbone, D. van der Marel, *Universal optical conductance of graphite*, Physical Review Letters. 100, 117401 (2008).

[30] A.A. Balandin, S. Ghosh, W. Bao, I. Calizo, D. Teweldebrhan, F. Miao, C.N. Lau, *Superior Thermal Conductivity of Single-Layer Graphene*, Nano Lett. 8 (3), 902-907 (2008).

[31] D. Qian, M.F. Yu, R.S. Ruoff, G.J. Wagner, W.K. Liu, *Mechanics of carbon nanotubes*, *Appl. Mech. Rev.* 55 (6), 495-533 (2002).

[32] Nobel Academy, *Appendix, some properties of graphene*, The Royal Swedish Academy of Sciences (5th October 2010).

[33] K.S. Kim, Y. Zhao, H. Jang, S.Y. Lee, J.M. Kim, K.S. Kim, J.H. Ahn, P. Kim, J.Y. Choi, B.H. Hong, *Large-scale pattern growth of graphene films for stretchable transparent electrodes*, Nature 457 5 (2009).

[34] X. Li, Y. Zhu, W. Cai, M. Borysiak, B. Han, D. Chen, R.D. Piner, L. Colombo, R.S. Ruoff, *Transfer of Large-Area Graphene Films for High-Perfomance Transparent Conductive Electrodes*, Nano Letters 9 (12), 4359-4363 (2009).

[35] X. Li, G. Zhang, X. Bai, X. Sun, X. Wang, E. Wang, H. Dai, *Highly conducting graphene sheets and Langmuir-Blodgett films*, Nat. Nanotech. 3, 538-542 (2008).

[36] S. Bae, H. Kim, Y. Lee, X. Xu, J. Park, Y. Zheng, J Balakrishnan, T. Lei, H.R. Kim, Y.I. Song, Y. Kim, K.S. Kim, B Özyilmaz, J. Ahn, B.H. Hong and S. Iijima, *Roll-to-roll production of 30-inch graphene films for transparent electrodes*, Nat. Nanotech 5, 574-578 (2010).

[37] F. Schedin, A.K. Geim, S.V. Morozov, E.W. Hill,P. Blake, M.I. Katsnelson, K.S. Novoselov, *Detection of individual gas molecules adsorbed on graphene*, Nat. Mater. 6, 652–657 (2007).

[38] X. Miao, S. Tongay, M.K. Petterson, K. Berke, A.G. Rinzler, B.R. Appleton, A.F. Hebard, *High Efficiency Graphene Solar Cells by Chemical Doping*, *Nano Lett.* 12 (6), 2745–2750 (2012).

[39] ambiently.files.wordpress.com/2013/04/fold-screen-smartphone-from-samsung.jpg

[40] K. Ghaffarzadeh (IDTech EX), *IDTech Ex forecasts a $100 million Graphene Market in 2018*, idtechex.com (2012).

[41] Intellectual Property Office, *An Analysis of Worldwide Patent Fillings Relating to Graphene*, ipo.gov.uk/informatics (2010-2013).

[42] BCC Research Market Forecasting, *Graphene: Technologies, Applications and Market*, bccresearch.com (July 2012, September 2013).

[43] SCENIHR, (ec.europa.eu/health/opinions2/es/nanotecnologias/index.htm)

[44] EPA / TSCA / FIFRA, (edgcomb-law.com/2010/10/california-proposes-to-regulate-nanomaterials-as-chemical-substances)

[45] GRAPHENE FLAGSHIP, (graphene-flagship.eu)

[46] K. Parvez, Z.S. Wu, R. Li, X. Liu, R. Graf, X. Feng, K. Müllen, *Exfoliation of graphite into graphene in aqueous solutions of inorganic salts*, *J. Am. Chem. Soc.* 136 (16), 6083–6091 (2014).

[47] www.xfnano.com/en/about.asp?id=60

[48] C. Berger, Z. Song, T. Li, X. Li, A.Y. Ogbazghi, R. Feng, Z. Dai, A.N. Marchenkov, E.H. Conrad, P.N. First, W.A. de Heer, *Ultrathin Epitaxial Graphite: 2D Electron Gas Properties and a Route toward Graphene-based Nanoelectronics*, J. Phys. Chem. 108, 199912-19916 (2004).

[49] graphenewiki.org/graphene/graphene-platform-supplies-the-worlds-largest-single-layer-single-crystal-graphene-samples

[50] C. Mattevi, H. Kim, M. Chowalla, *A review of chemical vapour deposition on copper*, J. Mater. Chem. 21, 3324-3334 (2011).

[51] J.K. Wassei, M. Mecklenburg , J.A. Torres, J.D. Fowler, B.C. Regan, R.B. Kaner, B.H. Weiller, *Chemical Vapor Deposition of Graphene on Copper from Methane, Ethane and Propane: Evidence for Bilayer Selectivity*, Small 8 (9), 1415–1422 (2012).

[52] K.F. Mak, C. Lee, J. Hone, J. Shan, T.F. Heinz, *Atomically Thin MoS_2: A New Direct-Gap Semiconductor*, PRL 105, 136805 (2010).

[53] J.C. Shaw, H. Zhou, Y. Chen, N.O. Weiss, Y. Liu, Y. Huang, X. Duan, *Chemical vapor deposition growth of monolayer $MoSe_2$ Nanosheets*, Nano Research (2014).

[54] actu.epfl.ch/image/1817/324x182.jpg

[55] L. Liu, Y.P. Feng, Z.X. Shen, *Structural and electronic properties of h-BN*, Phys. Rev. B 68, 104102 (2003).

[56] news.rice.edu/wp-content/uploads/2013/01/G-hBN-2-WEB1.jpg

[57] B. Lalmia, H. Oughaddoub, H. Enriquez, A. Karae, S. Vizzinif, B. Ealeta, B. Aufray, *Epitaxial growth of a silicene sheet*, arXiv:1204.0523.

[58] A. Kara, J.L. Lemaire, H. Enriquez, H. Oughaddou, *3rd International Meeting on Silicene (IMS-3)*, Journal of Physics: Conference Series 491, 011001 (2014).

Part II
Experimental Set

Chapter 3

SYNTHESIS METHODS AND FABRICATION TECHNIQUES

3. Synthesis methods and fabrication techniques

3.1. Mechanical exfoliation

Also mentioned as micromechanical cleavage, mechanical exfoliation was the first technique used to isolate one monolayer of graphite in 2004. It is possible due to the weak bonds between the atomic planes of graphite. The van der Waals interactions between planes are of the order of 2 eV/nm^2. Then, the required normal force to cleave off a 1 μm^2 graphite sheet from the top of the crystallite is about 300 nN, considering 1 μm as path and assuming as unity the graphene-substrate friction coefficient (adhesion is an important friction mechanism at low normal loads) [1]. The force can be exerted using an adapted AFM tip or, more simply, by the resistance to the release of a conventional scotch tape. The last method was the one used to obtain the first isolated graphene sheets based on repeating peeling of highly oriented pyrolytic graphite (HOPG) [2], as seen in figure 3.1. This process statistically results in some graphene monolayer flakes (among bi, tri and few-layer graphene) which can be transferred to different substrates, usually silicon/silicon dioxide for subsequent characterization purposes.

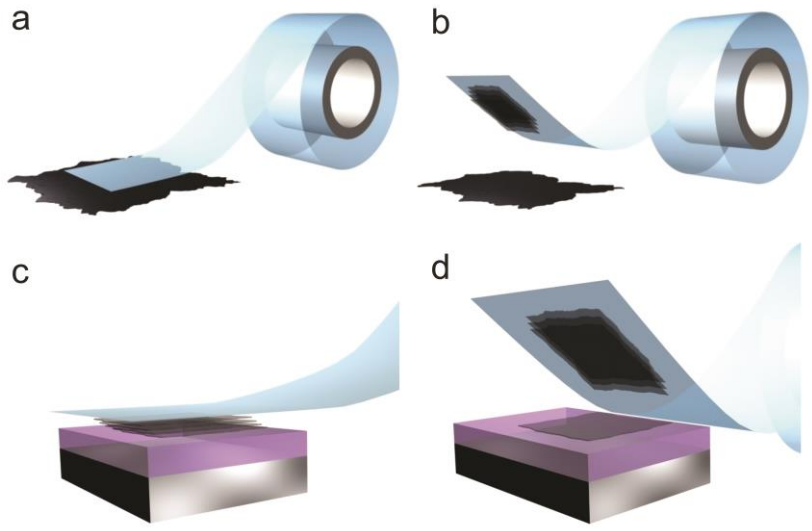

Figure 3.1: Step by step of a mechanical exfoliation process: (a) adhesive tape is pressed against a HOPG surface so that the top few layers are attached to the tape (b), (c) the tape with crystals of layered material is pressed against a surface of choice, and (d) upon peeling off, the bottom layer is left on the substrate. [3]

At the moment, graphene obtained by mechanical exfoliation is the one which presents the best electronic properties and less crystalline defects, but the difficulties for scaling up the process and to make it compatible with the existent technologies have triggered the investigations to other fabrication techniques. Another drawback of this method is the size of the flakes. In the best of cases, one can obtain flakes of 20x20 μm^2, which can be enough for several fields of research but not suitable for industrial purposes. This method is also useful to obtain monolayers of MoS_2 and h-BN.

In this PhD thesis, mechanical cleavage of graphite is used as a first approach to obtain high-quality monolayer graphene due to its simplicity and results, perfect for some applications. The graphite chosen was a Highly Ordered Pyrolitic Graphite (HOPG), grade ZYA (mosaic spread angle of 0.4° +/- 0.1°), from *HQGraphene*.

3.2. Chemical Vapor Deposition (CVD)

3.2.1. Basics

As summarized in section 2.2.4., graphene can be grown on a surface due to the thermal decomposition of a hydrocarbon gas catalyzed by a metal surface or because of the segregation/precipitation of carbon atoms from the bulk metal. This method is called Chemical Vapor Deposition (CVD) and is described in detail in the Appendix A.

CVD is a synthesis process in which the chemical constituents react in the vapor phase near or on a heated substrate to form a solid deposit. The CVD technology combines several scientific and engineering disciplines including thermodynamics, plasma physics, kinetics, fluid dynamics, and of course chemistry. The number of chemical reactions used in CVD is considerable and include thermal decomposition (pyrolysis), reduction, hydrolysis, disproportionation, oxidation, carburization, and nitridation. They can be used either singly or in combination. The most important methods to activate these reactions are as follows: [4]

- Thermal activation which typically takes place at high temperatures, i.e., >900 °C, although the temperature can also be lowered considerably if metallo-organic precursors (MOCVD) or aromatic hydrocarbons are used.
- Plasma activation which typically takes place at much lower temperatures, i.e., from RT to 500 °C.
- Photon activation, usually with shortwave ultraviolet radiation, which can occur by the direct activation of a reactant or by the activation of an intermediate.

Until recently, most CVD operations were relatively simple and could be readily optimized experimentally by changing the reaction chemistry, the activation method, or the deposition variables until a satisfactory deposit was achieved. However, many of the CVD processes are becoming increasingly complicated with much more exacting requirements, which would make the empirical approach too inconvenient. A theoretical

analysis is, in most cases, an essential step which should predict any of the following: chemistry of the reaction (intermediate steps, by-products), reaction mechanism, composition of the deposit (i.e., stoichiometry), and the structure of the deposit (i.e., the geometric arrangement of its atoms). This analysis may then provide a guideline for an experimental program and considerably reduce its scope and save a great deal of time and effort.

A CVD reaction is governed by *thermodynamics,* that is the driving force which indicates the direction the reaction is going to proceed; and by *kinetics*, which defines the transport process and determines the rate-control mechanism, in other words, how fast it is going. The sequence of events taking place during a CVD reaction can be summarized as follows: [4]

a) Transport of the reactants from the gas inlets by forced flow to the reaction zone.

b) Reactions in vapor-phase that form the gas precursors of the film and by-products.

c) Transport of the reactants and their products from the gas phase to the substrate through the boundary layer.

d) Adsorption of these species on the substrate surface.

e) Surface diffusion, chemical reactions and incorporation of these species on different growth sites.

f) Desorption of the volatile by-products of surface reactions, through the boundary layer.

g) Transport of the by-products away from the reaction zone.

In the case of carbon produced by CVD processes, graphite is probably the most similar case to graphene. Graphite is commonly produced by CVD and is often referred to as pyrolytic graphite. The CVD of graphite is theoretically simple and is based on the thermal decomposition (pyrolysis) of a hydrocarbon gas. The most common precursor is methane (CH_4), which is generally pyrolyzed at 900-1000 ^{o}C, over a wide range of pressure

from about 100 Pa (0.001 atm) to 10^5 Pa (1 atm). The reaction in a simplified form is as follows: [5,6]

$$CH_4(g) = C(s) + 2H_2(g) \quad (3.1)$$

Other common precursors are acetylene (C_2H_2), ethylene (C_2H_6), and propylene (C_3H_6).

Regarding the applications, coatings are by far the largest area of CVD at the present but by no means the only one. Other areas of CVD, such as production of powders, fibers, monoliths, and composites, are growing rapidly. With CVD, it is possible to produce almost any metal and non-metallic element, including carbon or silicon, as well as compounds such as carbides, nitrides, oxides, inter-metallics and many others. This technology is now an essential factor in the manufacture of semiconductors and other electronic components, in the coating of tools bearing and other wear resistant parts and in many optical, opto-electronic and corrosion applications.

3.2.2. CVD on copper

Copper seems to be the most appropriated catalyst among the different transition metals. The reason is the different growth behavior of graphene: the carbon solubility in Ni, Co, Fe and other metals is high, which produces the diffusion of carbon into the materials at high temperatures. When the substrate is cooled down, the solubility decrease and, as a result, carbon segregates or precipitates on the surface forming crystalline sp^2 bonded carbon layers. A precise control of process parameters and high cooling rates are needed in order to form only one layer of graphene. Nevertheless, good quality graphene can be obtained using these catalysts, but with small domains.

On the other hand, Cu presents very low carbon solubility because of its electronic configuration. This means that, during the CVD process, the weak bond between carbon and Cu enhances the decomposition of the hydrocarbon molecules of the gas precursor [7]. Graphene starts to nucleate in some specific sites and the process stops when the Cu surface is fully covered. This self-limited process has been demonstrated by an *in-situ* study of graphene growth *via* Raman spectroscopy and isotope

labeling [8]. The advantage of using isotopes in this investigation was tracking the carbon during the growth process, since the ^{12}C and ^{13}C Raman modes are separated and allow to observe the spatial distribution of graphene domains. The key factor is, then, to have a material with low affinity to carbon but that it can still form weak bonds acting as catalysts and maintaining the carbon on the surface.

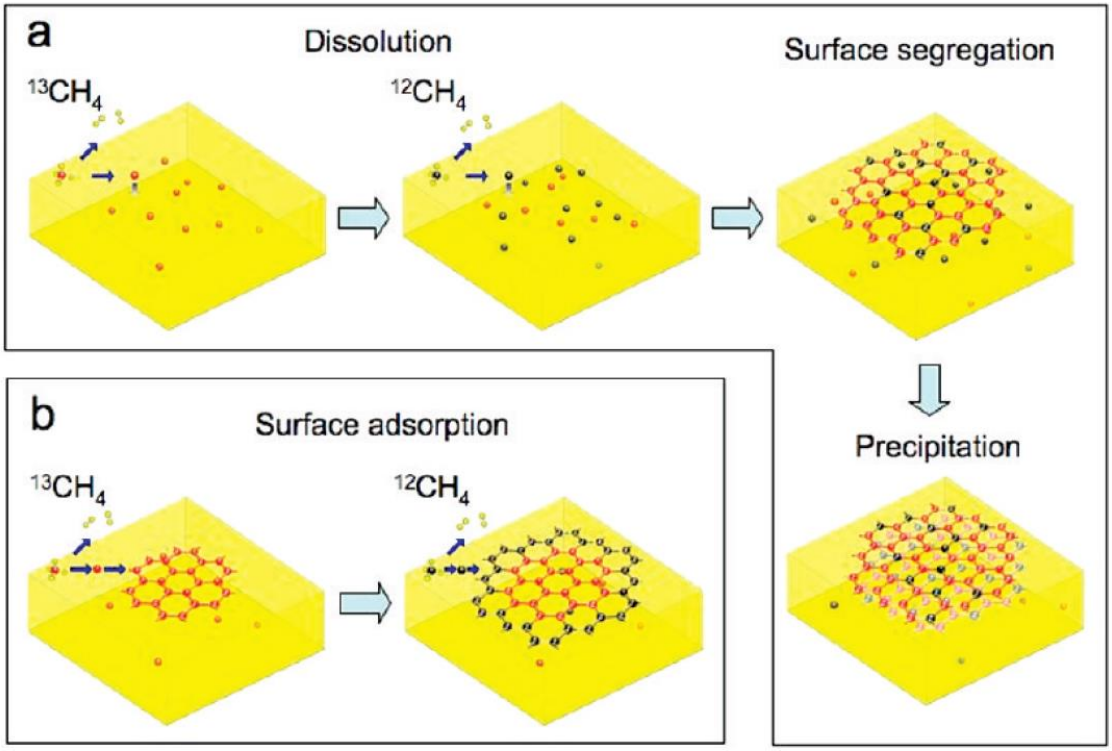

Figure 3.2: Schematic diagrams of the possible distribution of C isotopes in graphene films based on different growth mechanisms for sequential input of C isotopes (red spheres for ^{13}C, black for ^{12}C, and green for CH_4 containing both isotopes). (a) Graphene deposited with randomly mixed isotopes might originate/grow from surface segregation and/or precipitation. (b) Graphene with separated isotopes might occur by surface adsorption. [8]

Graphene growth on copper substrates is a surface mediated process [8]. The molecules of the gas precursor dissociate in different C_xH_y species that are adsorbed by the surface providing a low energy pathway that facilitates the deposition of carbon. Under the appropriate conditions, the carbon nucleation starts and carbon layer grows to completely coat the surface. Depending on whether the concentration of the carbon species supersaturates, saturates or undersaturates the substrate surface, the carbon availability will be enough to allow full

coverage of the surface, partially coverage or simply no nucleation respectively [9]. The optimum experimental conditions for graphene growth *via* standard CVD have been widely investigated [9-11]. A low graphene nucleation sites density is achieved decreasing the gas partial pressure and flux rate. If both values are too small (saturated surface), then the fully graphene coverage of Cu is not achieved and for smaller values (unsaturated surface) the graphene growth is even disabled. [9]

The most commonly used temperature in CVD process is 1000 ^{o}C, but there are also works reporting successful results with lower temperatures [10]. Decreasing the temperature and the pressure process are the main goals to design a more economic and scalable technique for graphene mass production. Acetylene (C_2H_2) and methane (CH_4) are the most popular choices. The latter has higher ionization potential and therefore lower growth rate, but opposed to acetylene it is available in high purity form. On the other hand, acetylene pyrolysis starts at a temperature of around 700 °C, lower than methane (850 °C). Moreover, methane can also provide more hydrogenated films [12]. Other carbon gases and even liquid or solid precursors have been reported. Interesting results, though, have been achieved with aromatic hydrocarbon gases such as benzene (C_6H_6) and toluene ($C_6H_5CH_3$), whose structure composed of benzene rings, resembling the graphene structure, and their low-temperature pyrolysis allows growing graphene at 500-600 °C. [13,14]

Special care should be taken in the surface state of the copper for graphene growth. Cu samples are covered by native oxide that reduces the catalytic effect. For this reason usually Cu substrates are treated before the deposition. One way is immersing the Cu samples in a soft acid solution, like acetic acid, to remove the oxide [15]. Another option is annealing the Cu under a reductive atmosphere, e.g. H_2. The annealing can also improve the Cu domain grain size and the surface morphology in order to obtain large graphene domains [7]. If there is no preferential crystallographic orientation of the graphene grown on Cu, there will be a mismatch at the edges of the graphene domains avoiding the formation of large area graphene domains. This problem is especially relevant in polycrystalline copper substrates. In monocrystalline substrates, the crystalline structure of graphene and those of the <111> face of copper

substrate show a relation regarding the similarity in their lattice parameters. The parameter mismatch between both lattices produces a superstructure visible with Scanning Tunnelling Microscopy (STM). Otherwise, the <100> face of copper substrates presents two possible orientations for some graphene layers whereas in other cases the layers are oriented randomly [16]. Moreover, the different graphene domains of different nucleation sites do not always match perfectly. The presence of impurities can introduce defects in the graphene crystals and also the atomic terrace steps in some cases.

Besides the carbon precursor gas, hydrogen (H_2) plays also an important role. During the process, the hydrogen can be introduced to catalyze the reaction by reducing the copper oxide present on Cu (not suitable as a catalyst), and to drag the by-products (radicals). However, the reductive action of hydrogen exposure at high temperature is known to efficiently etch graphene and to limit its growth. A hydrogen atmosphere is also expected to suppress carbon enrichment at high temperature at the defect sites in Cu, thus allowing to efficiently inhibit carbon segregation. [17]

In the very end of the process, the cooling ramp still has an important influence in the final sample. Large stresses can be generated in a CVD coating during the cooling period from deposition temperature to room temperature, if there is a substantial difference between the coefficient of thermal expansion (CTE) of the deposit and that of the substrate. In addition, the quality of graphene depends on the quenching curve too. Fast-cooling processes have been used to suppress the amount of precipitated carbon, by suddenly stopping the pyrolysis of the carbon precursor gas. However, this process still yields films with a wide range of graphene layer thicknesses, from one to a few tens of layers and with defects associated with fast cooling [18]. Medium cooling led to graphene; and slow cooling induces the total diffusion of the carbon atoms deep into the bulk catalyst, leaving nothing on the surface.

3.2.3. Monolayer formation time concept

CVD of graphene on copper is one of the most efficient technologies for producing high quality graphene for large areas. Nevertheless, still high

pressures (1 Pa) and big quantities of precursor gas (700 sccm; standard cubic centimeters per minute) are currently required [9-11,19]. One of the objectives of this work was to develop a new method based on the CVD trying to deposit graphene with the minimum quantity of precursor gas needed and the minimum time possible; using the monolayer formation time concept (τ) from the kinetic theory of gases. This would, in principle, lead to an economization of the precursor gas, a minimization of the process pressure and the quantity of the precursor, and the time needed to grow a graphene monolayer. Our process has been designed taking into account the dependence of τ on the pressure, the mass particle of the gas, the sticking coefficient, and the growth temperature.

From the kinetic theory of gases one can easily calculate the time required to form a monomolecular or monoatomic layer on a gas-free surface. This monolayer formation time is closely related with the so-called impingement rate Γ; it is inversely proportional. With a gas at rest the impingement rate Γ (or particle flux) will indicate the number of molecules which collide with the surface inside the vacuum vessel per unit of time and surface area:

$$\Gamma = n\left(\frac{kT}{2\pi \mathrm{m}}\right)^{1/2} \tag{3.2}$$

Where *m* is the mass of the particle (precursor gas), *k* is the Boltzmann's constant and *T* is the temperature; and from ideal gas law (*P* is the pressure) we can reformulate it as: [20,21]

$$\Gamma = \frac{P}{(2\pi \mathrm{mkT})^{1/2}} \tag{3.3}$$

The inverse of the gas impingement rate is related to the monolayer formation (or coverage) time through the sticking coefficient *S*, and the number of spaces per unit of surface area *a* (graphene surface has ~3.6×10^{19} sites/m^2), then the monolayer formation time is, in SI units [21]:

$$\tau = \frac{a}{\mathrm{S}\Gamma} = a\sqrt{(2\pi k)}\frac{\sqrt{mT}}{SP} = 3.4\times10^{8}\frac{\sqrt{mT}}{SP} \tag{3.4}$$

As a first approach to obtain a suitable equation, we can assume that every molecule will stick to the surface (sticking coefficient $S = 1$, common value in most of metals), and usual working temperatures of 1273 K (1000 °C). The main precursor gas used in this work was methane, then, $m_{CH4}=m_C+4m_H$. Thus, one-atom thick layer of carbon spread onto a surface can be formed in a time defined by:

$$\tau = \frac{2.1\times10^{-3}}{\mathrm{P}} \tag{3.5}$$

What means that a monolayer formation time could only be dependent, in principle, on the pressure of the precursor gas. For example, a CVD process under a ~$2x10^{-3}$ Pa of methane would have a monolayer formation time of graphene of only ~1 s.

This equation, then, is useful to determine the time needed to grow a monolayer, stable or not, depending on the sticking coefficient. In the case of graphene, however, the growth is likely to be at the edges of the nucleation sites, and not everywhere on the surface. This implies that growth occurs by two coupled mechanisms. One is the influx of molecules to the surface, regulated by the *monolayer formation time equation*. The other mechanism is the *surface diffusion* of adsorbed molecules to the edges of every nucleation site. This kind of growth gives rise to dendrites. That is it, the carbon atoms or the hydrocarbon molecules are physisorbed on the graphene surface, and they diffuse along the surface to the edge, where they can be chemisorbed. This would explain why it is enough with just one pulse to grow graphene. In an ideal case, all the molecules deposited on the surface of copper and graphene (monolayer) would go to the edges after the pulse or between pulses (if there is more than one). This method, moreover, avoids having an excessive nucleation, favoring a free growth of monocrystalline islands, bigger and more separated.

The short time needed to grow graphene, 1-10 s regarding this result, leaded to the idea of the pulsed-delivered system (not used before). If the process needed such a short time, we could release only a short pulse of very low pressure instead of having a high constant flux of methane. The developed Pulsed-CVD system will be explained later.

3.3. Deposition reactor: *GRAPHman*

A part of the work during the M.Sc. thesis and almost half of the whole PhD thesis was the construction of a new CVD reactor which would be placed in the Clean Room of the Physics Faculty of *Universitat de Barcelona*. This Clean Room is classified as ISO 7 (10000) in the main room of 200 m^2 and as ISO 6 (1000) in the photolithography zone of 50 m^2. The Clean Room, then, gave the opportunity to the group to perform the experiments under stable conditions regarding room temperature and humidity, and an easy access to facilities for sample preparation like, plasma and ion etching, lithography and, lastly, to the FIB (focused ion beam) microscope. Avoiding the sample contamination would improve the quality of the samples and the afterward results. In the past, all the reactors were placed in other standard laboratories.

One of the goals during the first year of the PhD was designing and finishing this new CVD graphene reactor. The main idea was attaching a quartz tube to the main chamber so it would be the pre-chamber where the CVD process would take place. Surrounding that tube an oven would be needed; most of CVD graphene processes occurred at high temperatures of around 1000 °C.

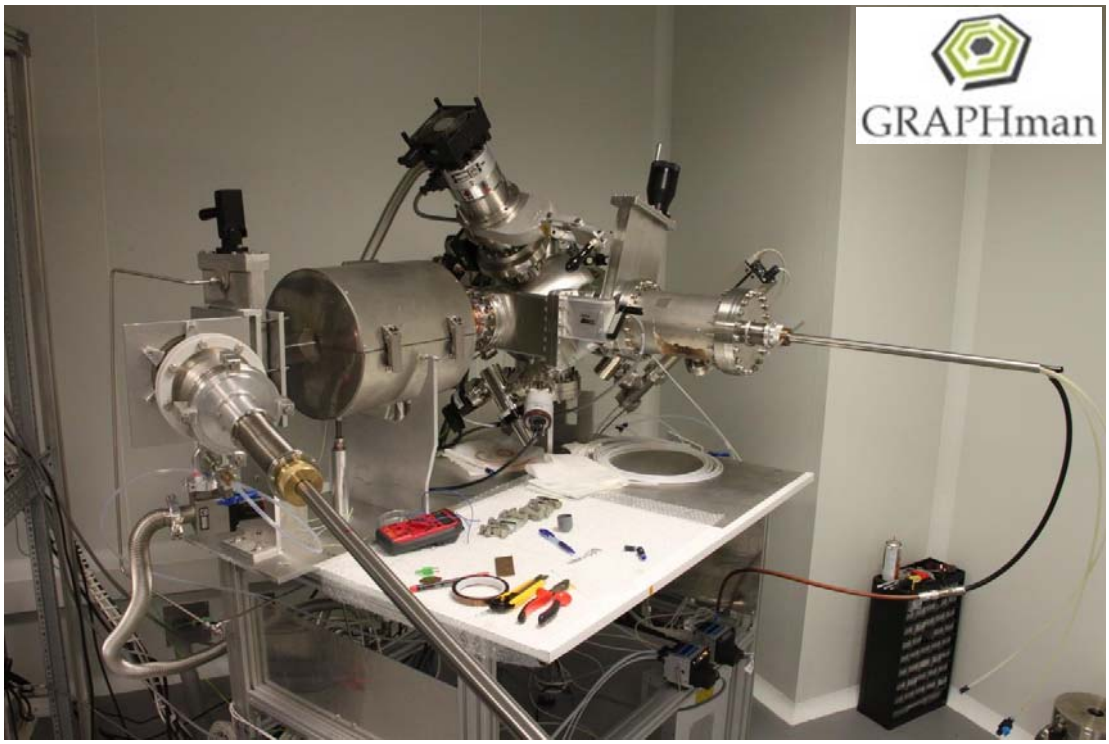

Figure 3.3: Picture of the CVD reactor placed in the Clean Room (UB).

The real challenge of this new reactor was the way we were going to release the precursor gases. From the monolayer formation time concept, we already knew that the gas pressure was the most important parameter. The introduction of the gas into the chamber through one or more instant pulses allows releasing a low pressure and controlled quantity of a gas. A gas management system was especially designed and built directly from the bottle gas to the CVD chamber through a controlled leakage, see section 3.3.1. [22]

The details of the reactor *GRAPHman* (the "man" who makes graphene) are described as follows (figure 3.4):

- A spherical ultra-high vacuum chamber, (1) in figure 3.4. This sphere supports the vacuum system (10), the pressure sensors (8), the residual gas analyzer (9), the magnetron sputtering head (5), the gas management system (6), the automatic conductance valve (7), and the quartz tube (4).

- A pre-chamber system ((2) in figure 3.4) permits a fast introduction of samples into the high vacuum zone. In this way, the pressure inside the quartz tube (CVD chamber) never exceeds 1 Pa, avoiding reactor contamination.

- A CVD process chamber comprises a horizontal quartz tube ((4) in figure 3.4) that communicates the pre-chamber with the main spherical chamber, plus a tube furnace (3) surrounding the central part of the quartz tube. The oven is made of resistors and can reach temperatures over 1000 °C.

- A magnetron sputtering head ((5) in figure 3.4) is mounted in the spherical vacuum chamber. The sputtering head has a copper target of 3", located in front of the substrate at a distance of 8 cm. To perform the sputtering process the substrate must be displaced from the pre-chamber to the center of the spherical chamber.

- The gas management system ((6) in figure 3.4) controls the partial pressure and the introduction of gases needed for each process, CVD and sputtering. The gas lines comprise 4 different

gases: CH_4, H_2, Ar, and N_2. In addition, it was designed to introduce gases at partial pressures up to 200. This system can reduce the gas bottle pressure down to the low gas pressures needed for the deposition of a one-layer graphene (10^{-4} Pa), and the gas can be introduced in the main chamber with a synchronized sequence of pulses. See details in section 3.3.1.

- The residual gas analyzer (RGA) ((9) in figure 3.4) is mounted in the spherical chamber. This RGA unit continuously measures the partial pressure of 10 gases at the same time, and can effectively monitor high vacuum processes. See details in section 3.3.3.

- The vacuum system is constituted by two vacuum lines. One for combustible/inert gases (CH_4, C_6H_6, C_7H_8, Ar, N_2), which is the one used and comprises a mechanical and a turbomolecular pump ((10) in figure 3.4); and a second line for combustive gases (air, O_2). The base pressure achieved by the system is a High Vacuum (HV) of 10^{-5} Pa in the main spherical chamber.

- The computerized system is composed by different control units; a computer centralizes the control of the processes. We carried out the control by means of a LabView 7.1® program developed by the group.

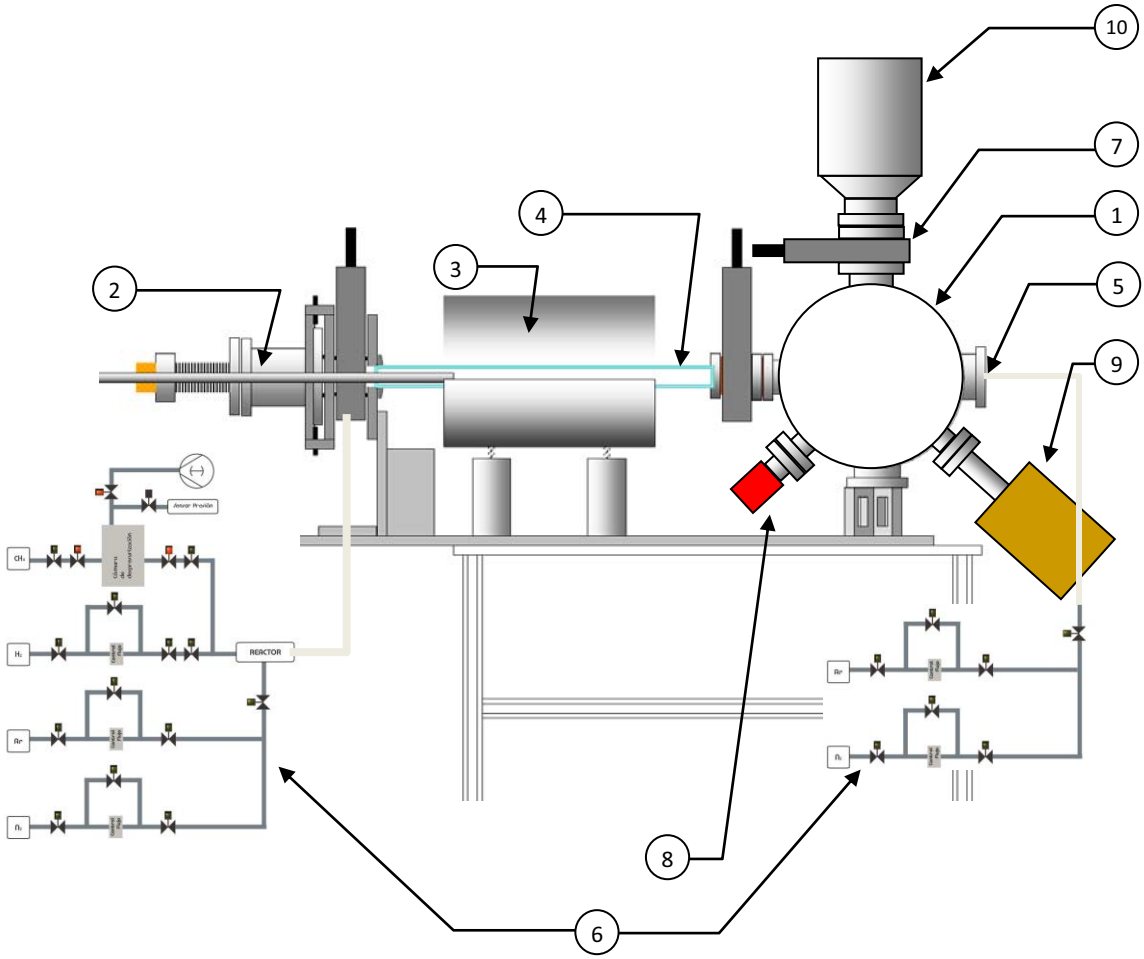

Figure 3.4: (1) Main spherical chamber, (2) Pre-chamber, (3) CVD oven, (4) Quartz tube, (5) Magnetron sputtering head, (6) Gas management system, (7) Automatic conductance valve, (8) Pressure sensors, (9) Residual gas analyzer (RGA), and (10) Turbomolecular pump.

The LabView 7.1® computer program (figure 3.5) controls the following operations: (a) opening and closing the valves of the reactor and setting the mass flow controllers; (b) monitoring the pressure inside it; (c) controlling the working pressure by a valve of variable conductance fixing a total pressure at a given set-point; (d) fixing the temperature of the CVD oven at a given set-point; (e) carrying out a complete and automatic sequence of a pre-programmed process and having control on valves, temperature, gas pulses, vacuum levels and power supplies.

This program and another one that manages the residual gas analyzer (RGA), the RGAapp, can control all processes performed in the reactor. During the CVD process, the RGA monitors the partial pressures of gas species inside the chamber.

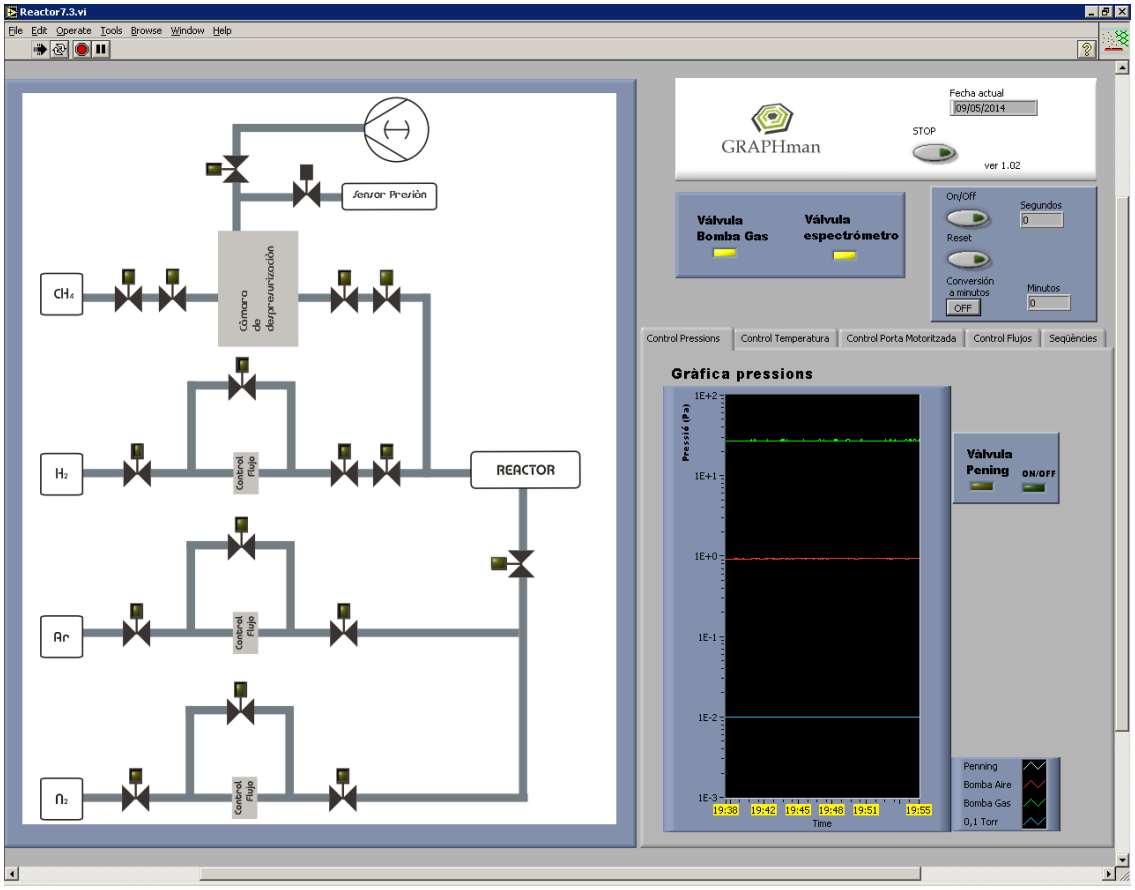

Figure 3.5: Screenshot of the Labview interface used for the computer-controlled CVD process.

3.3.1. New Pulsed-CVD system

The gas management system is one of the novelties of the method used and a relevant part of the patent we developed [22]. Using the relation between the monolayer formation time of graphene and the pressure of the precursor gas, we only needed a very-low pressure in a short time of seconds, which suggested the idea of an instantaneous pulse of gas. The pressure pulse can be achieved by a specific valve design, which makes possible that the amount of gas (carbon precursor and/or hydrogen) depends uniquely on the pressure. This pulse time, although can be controlled, is actually due to the time needed to entry the carbon precursor gas into the chamber. The RGA analyzer (or also the quadrupolar mass spectrometry system, QMS) was used in order to control in real time the inside-reactor composition and partial pressure of the carbon precursor gas and residual gas before, during, and after the

deposition, as well as the determination of the constants of time associated to the pulses of partial pressure of the carbon precursor gas.

This system (figure 3.6) is arranged to control the partial pressure of gas needed for sputtering, and to control the carbon precursor gas introduction during the CVD process; wherein the gas management system comprises a gas injection system that consists on at least a sequence of 4 valves in series (2+2) with a depressurization chamber in the middle of them. Every valve is controlled independently as they are connected to independent vacuum systems, ensuring every time the same amount of gas delivered and avoiding the influence of the bottle and the main chamber. [22]

To ensure such low-pressure pulses of 10^{-3}-10^{-4} Pa inside the reactor, we had to place a suitable depressurization chamber. By means of the Boyle-Mariotte law (*PV=constant* if *T=constant*) we can decrease the pressure from the bottle of the gas, e.g. CH_4, by simply increasing the volume through an intermediate chamber. In our case, from the volume ratio of the main gas bottle and the depressurization chamber: $P_{DC} = \frac{P_{bottle}}{2500}$. The same way, the volume ratio of the depressurization chamber and the reactor determines that: $P_R = \frac{P_{DC}}{40000}$. Therefore, the final relation between the pressure inside the main chamber of the reactor and the initial pressure of the bottle would be: $P_R = \frac{P_{bottle}}{1 \times 10^8}$

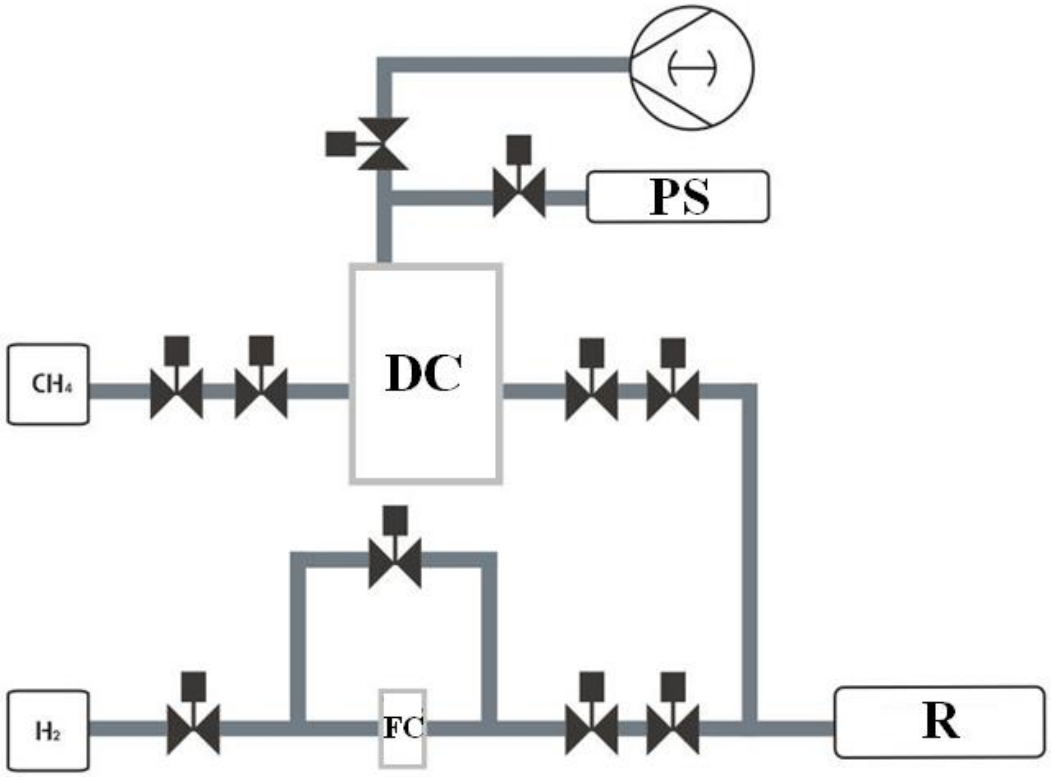

Figure 3.6: Scheme of the gas management of the Pulsed-CVD system. The series of valves controls the release of the gases (CH_4 and H_2). The pressure sensor (PS), the depressurization chamber (DC), the mass flow controller (FC), and the main chamber of the reactor (R) are shown.

The valves are computer-controlled with a synchronized sequence of pulses, wherein each pulse has a specific time of exhaustion of the carbon precursor gas due to the pumping. The pulse of pressure consists then, of a nearly instantaneous increase of pressure (step) due to the instantaneous opening of a valve, followed by an exponential decrease of the pressure (the length of the pulse can be defined by the characteristic time associated to the decreasing exponential, i.e. the time passed in the decrease of a factor *e* (number *e* = 2.718282)), and being the time as function of the specific time of exhaustion of the carbon precursor given by:

$$p(t) = p_0 e^{-t/\tau} + p_{base} \tag{3.6}$$

Wherein $p(t)$ is the pressure of the pulse as function of time; p_0 is the original instantaneous pressure when the valve is open (~10^{-4} Pa); t is

anytime during the exhaustion of the pulse gas; τ is, in addition to the monolayer formation time, the characteristic pumping time (~10 s), and p_{base} is the base vacuum pressure (~10^{-5} Pa) [22]. The resulting pulses are shown later in Chapter 7.

Although the system also allows constant fluxes by means of mass flow controllers (if needed), the novelty of this Pulsed-CVD relies on how the precursor gas is released.

3.3.2. Magnetron Sputtering

This is one of the most common industrial processes for plasma deposition of thin films together with Plasma Enhanced Chemical Vapor Deposition (PECVD). The impinging species are sputtered from a target, which is RF, MF, HiPIMS, DC or pulsed-DC powered in a noble gas glow discharge (normally Ar, He, Kr…), and deposited on a substrate [23]. Figure 3.7 shows a typical equipment setup for sputtering deposition.

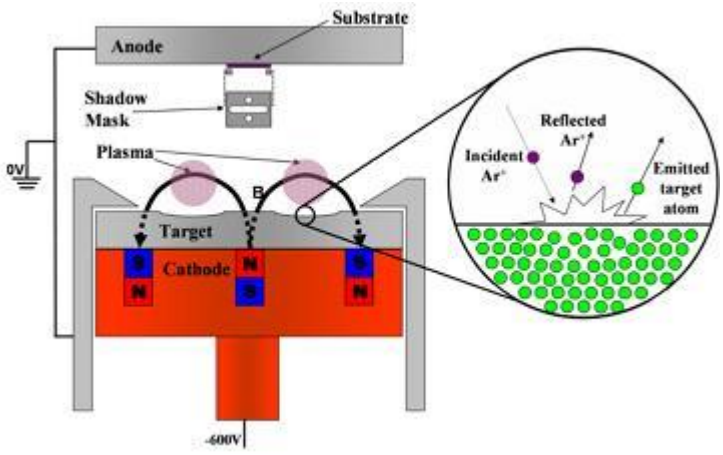

Figure 3.7: Schematic of experimental setup for deposition by DC magnetron sputtering. [24]

Sputtering occurs at the target when an energetic ion (e.g. Ar^+) makes a series of collisions with atoms in the target (e.g. Cu). The incident ion actually becomes a neutral atom because of Auger neutralization [25,26] before impact; that is, it picks up an electron from the target, so that it is an energetic Ar atom. A Cu atom that gains enough energy from the collision will be displaced from its normal lattice site. In a single

collision between Ar (mass M_1) and Cu (mass M_2), the maximum fraction of energy transfer to Cu is $4M_1M_2/(M_1+M_2)^2$, which has a value of 0.95 for the Ar-Cu case.

Three regimes of sputtering have been identified: for low-energy (< 300 eV) [26] sputtering, the process is in the single knock-on regime; so the Ar transfers energy to target atoms that make a few collisions with other target atoms and are ejected from the target. The ejected Cu atom gets its energy from a collision cascade with the Ar atom but loses some of this energy in collisions with other Cu atoms. As the Ar^+ energy increases, sputtering moves into the linear cascade region, and for even higher energies, the process jumps to a spike regime. A Cu atom gets enough energy from the Ar to eject Cu atoms from the target in subsequent collisions. Essentially, Cu atoms are sputtered forward into the target and backward out of the target, obviously only the latter are useful for deposition process. Some energetic Ar atoms (a few percent) are implanted in the Cu and are then sputtered later. An important factor, then, is the sputter yield *S*, which is the number of sputtered atoms (e.g. Cu) per number of incident particles (e.g. Ar), and it depends on how close to the surface the Ar loses its energy. This *S* normally ranges from 0.1 to 10 in most of the sputtering processes and it is a measure of the efficiency of sputtering. The Sigmund theory provides the specific dependence of *S* on *E* for both low and high energies: [23]

$$S = \frac{3\alpha 4 M_1 M_2 E}{4\pi^2 \left(M_1 + M_2\right)^2 U_s} \qquad \text{(E < 1 keV)} \qquad (3.7)$$

$$S = 0.042\alpha \, S_n(E)/U_s \qquad \text{(E ≥ 1 keV)} \qquad (3.8)$$

Here M_1 and M_2 are the masses of the projectile (e.g. Ar) and target atoms (e.g. Cu) respectively, *E* is the energy of incoming ions, *Us* is the binding surface energy, α measures the efficiency of momentum transfer in collisions, and $S_n(E)$ is defined as the nuclear stopping power being a function of energy, masses and atomic numbers of the involved atoms. For a given ion energy, the higher the atom density in the target

and the shorter the mean free path between collisions, the higher the yield. Being the mean free path:

$$\lambda[cm] = 0.66/p[Pa] \text{ (air at Room Temperature)} \quad (3.9)$$

Besides the mean free path, there is also an important region called the plasma sheath, the zone where the ions are accelerated to the target. So we can have a collisional sheath (high pressures, low efficient sputtering) and a non-collisional sheath (more efficient sputtering because the ions do not lose energy due to the collisions).

Moving now to the substrate position, if the sticking coefficient is 1, all the incident atoms remain on the substrate, which is generally the case for metals for usual substrate temperatures. The film grows from these nuclei into larger islands that merge as deposition continues. For Cu atom deposition, a monolayer of Cu would deposit on a glass substrate, and subsequent arrival of Cu atoms would produce 3D Cu islands.

Both tensile and compressive stresses are observed in sputtered films, but the stress must be significantly less than the adhesion strength for films to be useful. If a film separates from the substrate after deposition or subsequent use, it is usually due to poor adhesion. However, it can be due to structural failure in the substrate. [26]

Most films are deposited on oxides because nearly all materials have a surface oxide. Metal surfaces are usually oxidized, except for Au, Pt, and so on. Semiconductors have an oxide layer, such as SiO_2, unless it is removed before deposition by plasma etching, for instance. Thus, often the primary requirement is the adhesion of metal films to oxides. If not, an adhesion buffer layer can be grown. Also, film purity is very important because impurities can seriously affect film properties; since all sputtered atoms come from the target, it must have also high purity. Water vapor is usually the principal source of contamination, and many metals react with the oxygen in the water vapor; the system must be thoroughly outgassed and the sputtering gas must be pure.

Normally, the target is heated by the ion beam; the limit on sputter rates is this heating process, which is intrinsic to the sputtering technique. The target should be homogeneous and as pure as the desired films because any atom in the target will be sputtered. Since nearly all the

power used for sputtering results in target heating, the suitability of the target for dissipating this heat is important. To remove the heat, the target must be bonded to a water-cooled holder to provide a good thermal contact that transfers heat to the water. Another possible solution to avoid excessive heating of the target is applying pulsed energy, like in HiPIMS (High Power Impulse Magnetron Sputtering). [27]

To overcome the rate limitations of diode sputtering systems, various approaches have been tried, but magnetrons have become the most widely used because of their flexibility. In magnetrons, a magnetic field, *B*, is applied parallel to the target surface. With a cylindrical target arrangement, this magnetic field can be parallel to the target and have the same magnitude at all points on the cylindrical target surface. A pair of Helmholtz coils at either end of the target and with the same axis as the target would provide this. The negative voltage on the target accelerates the secondary electrons produced by the ion bombardment along a radius away from the target. A magnetron is usually placed behind the target in order to enhance the sputtering rate by increasing the ionization degree in the plasma. The energy of the ion species being deposited can be modulated by applying a DC bias to the substrate; also by employing the commented magnetron, whose magnetic field lines open confining the electrons and reaching the substrate surface due to the non-compensated magnetic fluxes of the internal and external magnets (unbalanced magnetron).

The magnetron operation requires that the system meets the following conditions: [26]

- The magnetic flux path is closed (general); that is, the ionizing electrons must be trapped within the magnetic field region. In the planar magnetron, the vertical component of the magnetic field constrains the electrons above the target within the region of field parallel to the surface. In the cylindrical magnetron, the electrostatic mirror provides this “closure”.

- The magnetic field strength is high enough to trap electrons. There is a minimum value required for each geometry, but it is usually more than 200 Gauss.

- The anode (the electrostatic confining, e.g. lateral target cover) should be located where electrons in the plasma region can easily reach it by following a magnetic field line.

Magnetron sputtering has many advantages, but it is in principle not well suited to magnetic materials because a magnetic target shorts out the magnetic field need for magnetron operation. On the other hand, sputtering is not only successful to grow pure metal films, the use of metallic-alloy targets is a key advantage of sputtering since it makes it possible to deposit films with the same composition as the target). It is also common to deposit some forms of carbon, like DLC or amorphous carbon, from a graphite target. Reactive sputtering process is also possible if hydrogen or hydrocarbon source gases are added to Ar. An alternative sputtering process can be performed without plasma: an Ar ion beam from an ion gun sputters a target and another beam bombards the growing film to improve the film characteristics. This method is called ion beam assisted deposition (IBAD). Like in the ion beam process, sputtering provides poorly-ionized flows of particles. Nevertheless, being simple, widespread and versatile, sputtering is an ideal technique for industrial processes [28]. Being mostly used as a coating technology, it has opened the door to novel or improved products like anti-reflective stacks on large glass panes or improved low emissivity coatings; as well as optical coatings with high performance (high index of refraction). [29]

The magnetron sputtering head is placed in the *GRAPHman* reactor of the Clean Room, FEMAN group (UB).

3.3.3. Residual Gas Analyzer (RGA)

Although this corresponds to a small part of the CVD process characterization, this instrument is of an extreme importance in order to control precisely the partial pressures of residual gases before, during and after the process. Moreover, it provides an efficient way to demonstrate the feasibility of the low-pressure pulsed system and to monitor the radicals derived from the precursor gas.

A Residual Gas Analyzer (RGA) is a mass spectrometer of small physical dimensions that can be connected directly to a vacuum system and whose function is to measure the concentrations of the gases inside the vacuum chamber.

The principle of operation is the same for all RGA instruments: A small fraction of the gas molecules are ionized (positive ions), and the resulting ions are separated, detected and measured according to their molecular masses. RGA's are widely used to quickly identify the different molecules present in a residual gas environment and, when properly calibrated, can be used to determine the concentrations or absolute partial pressures of the components of a gas mixture. Partial pressure measurements are determined with the help of previously calculated sensitivity (i.e. calibration) factors by reference to the abundance of the individual mass numbers attributed to each gas type.

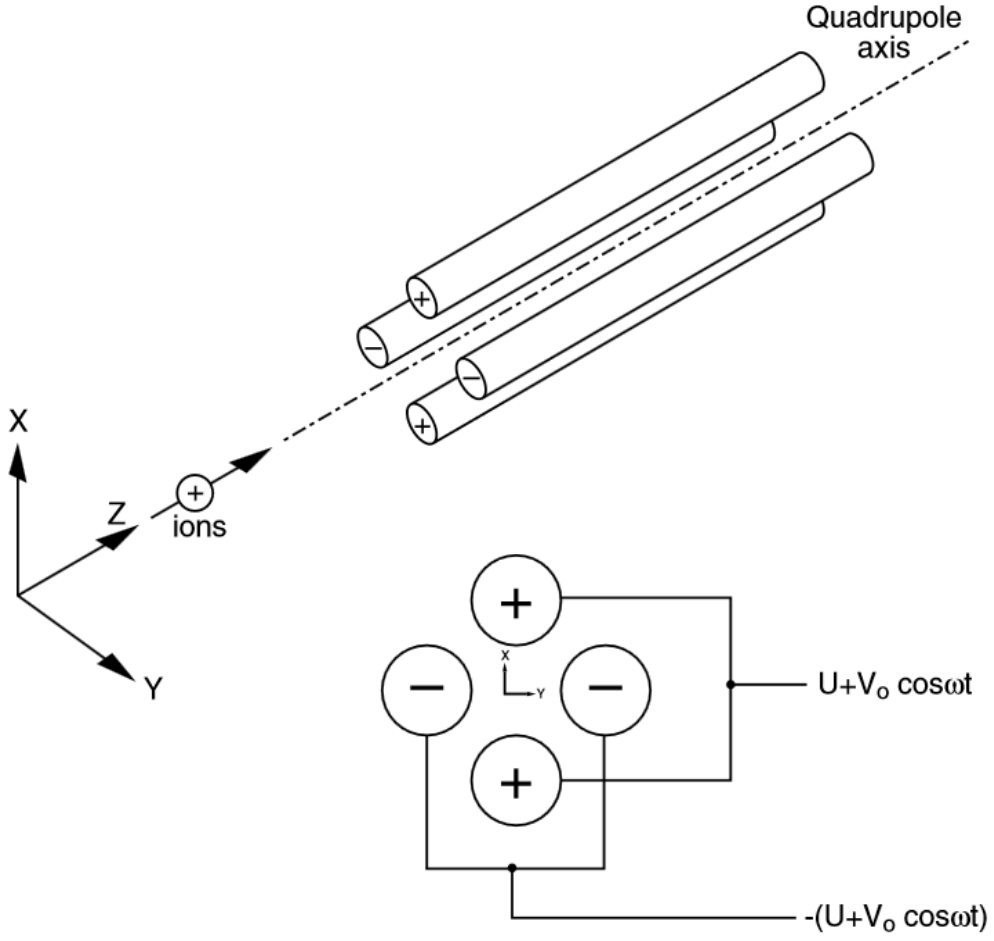

Figure 3.8: Quadrople diagram with the connections. [30]

During analysis, positive ions are formed within the ionizer and directed towards the spectrometer's quadrupole mass-filter. The mass filter determines which ions reach the detector at any given time. It is operated by a combination of RF and DC voltages and the filtering action is based on the mass-to-charge dependency of the ion trajectories on the RF and DC fields. A two dimensional (X-Y) quadrupole field is established between the four cylindrical electrodes with the two opposite rods connected together electrically. Ions enter the filter along the Z-axis and start oscillating in the X- and Y- directions. The ions are separated based on their mass-to-charge ratio (m/q) by lateral forces resulting from the electric potentials applied to the rods. Successful separation of a specific mass species requires setting the RF and DC voltage values such that only the ions of interest have stable trajectories down the quadrupole rod assembly. The RF/DC ratio determines the filter selectivity. By simultaneously varying the amplitude of the DC and RF voltages an entire mass spectrum can be scanned. The magnitude and frequency of the RF determine the m/q of the ions that can pass through the filter without striking the rods. Ions that successfully pass through the filter are focused towards the detector and the resulting analog current is measured by an electrometer. [33]

The analyzer used in the processes was the SRS RGA300 from Stanford Research Systems, and it was attached to the *GRAPHman* reactor. The computer program (rgaApp) has two modes of plotting the data detected. One simply consists on displaying the partial pressure of gases of any molecular masses (1-65 u.m.a.); this mode is interesting to check which gases are in general present in the vacuum chamber and its relative abundance in a first approximation. The other mode plots the pressure of each selected gas (regarding its mass) versus time; necessary to check the pulse-shaped release of the precursor gas, its pressure, and the different components or radicals.

The SRS RGA300 is attached to the *GRAPHman* reactor and is also property of the FEMAN group (*UB*).

3.3.4. Preliminary studies

Before building the reactor especially made for graphene (*GRAPHman*), we carried out a previous work in another of the existent reactors (normally used to grow carbon nanotubes), whose results will be detailed in Chapter 6. It was built by the FEMAN group as a part of the PhD thesis of Dr. Jordi Garcia-Céspedes in the *Universitat de Barcelona* [31]. Due to the similarities of the features to any standard CVD reactor, we used it to make the first approach to the growth of graphene by CVD.

The reactor has a flattened cylindrical shape and a rotating system is placed in the vertical axis. The rotation of the substrate holder permits the movement of the sample through four different stages (figure 3.9). In one of the stages, the heating system for CVD is mounted. The other stages are equipped with two magnetron sputtering systems (600 W of nominal RF power, water cooled, and with 3" targets) and with a magnetron sputtering (500 W) header provided by *Teer Coatings*, with a target of Cu. The plasma in the sputtering stages is excited by the RF power supply through a tuned matching unit. In addition, the reactor has a load-lock chamber system that prevents atmospheric contamination into the main chamber during the substrate introduction. The vacuum system is composed of a double-stage mechanical pump for generating the primary vacuum, a roots pump, and a turbomolecular pump for achieving high vacuum. The base pressure achieved in the main vacuum chamber is 10^{-4} Pa. An automatic butterfly valve of variable conductance, located between the chamber and the roots pump, keeps the pressure conditions constant during the growth process. One of the novelties introduced in this reactor was the heating system, a hot-wire. This consists of a resistive element (2 Ω graphite resistance) connected to a DC power supply with an output voltage limited to 60 V and an electric power of 1800 W. The temperature was monitored using an external optical pyrometer and proportional-integrative-derivative (PID) controlled by a feedback loop with the DC power supply. The main characteristics of this technology are as follows:

a) Faster temperature ramp.

b) Absence of catalysis. Decomposition is only due to the high temperature and heat radiation from the hot-wire.

c) Low contamination and long life in reductive atmospheres.

d) Homogeneous radiative conditions.

e) Easy diffusion of species to the substrate.

The management of gases was performed using six independent gas lines, each one equipped with a mass flow controller and connected to the reactor. Gas flow rate, total pressure, hot-wire DC power, and the plasma process were computer-controlled with a LabView® interface. Also a specific schedule for these actuators can be programmed.

Figure 3.9: View of the reactor used in the preliminary work. The relevant parts are indicated by numbers; the load-lock chamber (1), the sputtering stages (2), the PECVD/CVD stage (3), the turbomolecular pump (4), the pyrometer (5), and the gas lines (6).

This reactor is devoted to the growth of carbon nanotubes, and it is located in the Applied Physics and Optics department, FEMAN group (*UB*).

3.4. Transfer to polymers

The growth of high quality graphene is, as explained during this chapter, highly efficient by CVD. But, since the catalyst must be metallic (Cu, Ni, Fe…), this adds a major drawback in the subsequent characterization and most of the current applications; in the electrical characterization of graphene, a conducting substrate will short the electrical current out. It appears, then, the necessity to transfer graphene from the catalytic substrate onto an insulating one, e.g. Si/SiO_2 or polymer substrates. Such a transferring step increases the number of defects in the synthesized graphene, reduces the process scalability, and it is not fully reproducible. [15]

Graphene transfer techniques that are suitable for CVD graphene, are usually performed by etching the underlying catalyst and then scooping the graphene directly or using some kind of media such as Polymethyl methacrylate (PMMA), Polydimethylsiloxane (PDMS) or thermal tape. Other techniques, such as mechanical or chemical exfoliation, are definitely not convenient for this purpose due to the higher adhesion force between copper and graphene than in the latter processes.

Transfer with media: The key idea is to remove the catalyst film underneath the graphene so that the graphene sheet can be separated and deposited. After the CVD growth, graphene is not isolated; it sits on the catalyst on the substrate. Besides direct transfer, an additional media is introduced to protect graphene. Figure 3.10 shows an example of graphene transfer using PMMA as a media. The whole sample is then, submerged into an etchant, normally an acid (e.g. nitric acid), to etch away the metal. After the catalyst is gone, both the graphene sheet and the polymer are floating on the liquid surface because of its hydrophobic nature [32]. After the sample is dried, the transferred graphene is ready. Besides PMMA, PDMS and thermal release tape are commonly used as support materials too. The main characteristic of transfer with PDMS and thermal tape is that these materials are not dissolved at the last step; instead they are peeled off by hand. It is crucial that the interface bonding

between graphene and substrate is stronger than that between PDMS and graphene to ensure graphene is left on substrate while being peeled off.

Direct transfer: The advantage of the direct transfer is that it is a simpler process which reduces the possibility of introducing potential environment impacts. However, the efficiency of the direct scooping method is limited by the requirement of high stability of the transferring setup to avoid the fragile graphene sheet from breaking during the process. Therefore, it is a method of reduced/limited efficiency. In addition, the etchant goes in between transferred graphene and its target substrate, which behaves as chemical dopants and enhances carrier scattering to degrade the electrical properties of graphene. [33]

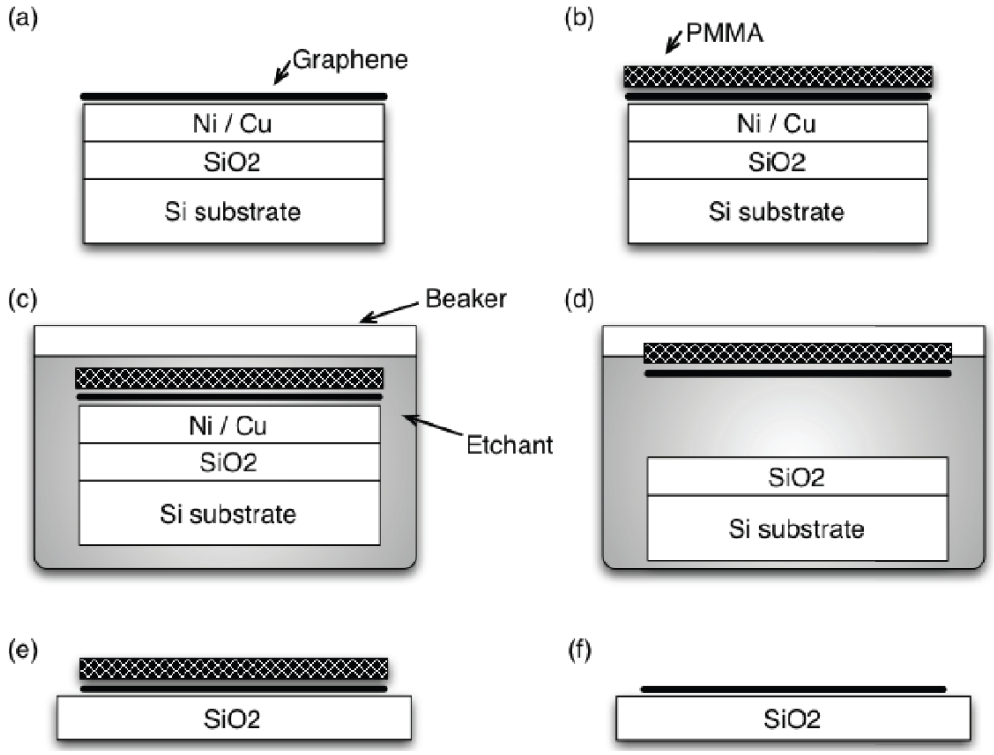

Figure 3.10: Schematic diagram of graphene transfer with PMMA as a support. (a) The CVD-grown graphene on Ni or Cu catalyst. (b) A PMMA layer is spin-coated on top of graphene. (c) The graphene sample is submerged into the metal (Ni or Cu) etchant. (d) The Ni or Cu is etched and the graphene is floating with PMMA on the etchant surface, while the remaining SiO_2 and Si substrate sinks to the bottom of the beaker. (e) The floating graphene/PMMA is transferred onto a SiO_2 substrate. (f) The PMMA top layer is removed (if needed) by acetone or other PMMA solvent and graphene remains on SiO_2. [33]

More modern versions of the method are being carried out, approaching the technique to an industrial scalability of the graphene production, like the roll-to-roll transfer [34]. There are essentially the same steps as in a normal transfer process, but in the polymer step, the graphene grown on a copper foil, is attached to a thin polymer film coated with an adhesive layer by passing between two rollers (figure 3.11). In the subsequent step, the copper layers are removed by electrochemical reaction with aqueous $(NH_4)_2S_2O_8$. Finally, the graphene films are transferred from the polymer support onto a target substrate by removing the adhesive force holding the graphene films. When using thermal release tapes the graphene films are detached from the tapes and released to counter-substrates by thermal treatment. The third step is not necessary when the target substrate is directly attached to the copper foil in the first step by permanent adhesion.

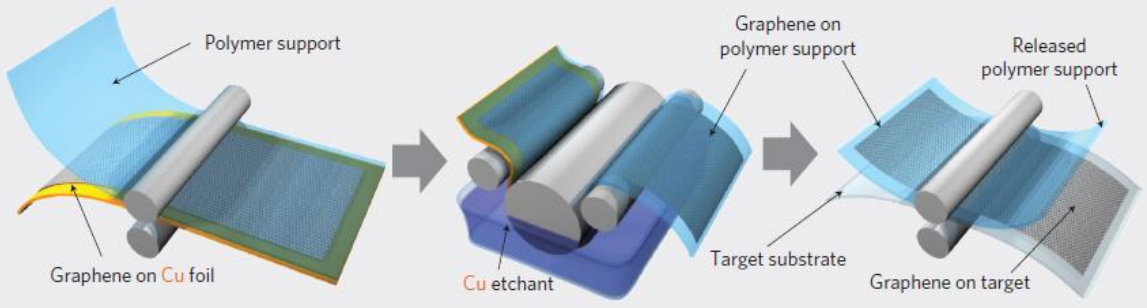

Figure 3.11: Schematic of the roll-based production of graphene films grown on a copper foil. The process includes adhesion of polymer supports, copper etching (rinsing) and dry transfer-printing on a target substrate. [34]

Nonetheless, by removing the transferring step, scalable graphene on non-conductive substrates rises as key technology for implementing graphene on electronics and optoelectronics. Very recently it has been shown that the decreasing of the CVD process temperature and increasing the copper film thickness allow the carbon atoms to penetrate 300 nm thick copper films and to form nearly continuous graphene beneath the copper films (on the other side of the substrate). On the other hand, thinner copper films and high temperatures could evaporate the copper once the catalytic effect has finished, in order to deposit the synthesized graphene on the substrate (Si/SiO_2). This opens promising opportunities in the direct deposition of the graphene on dielectrics. [35]

3.5. References

[1] Y. Zhang, J.P. Small, W.V. Pontius, P. Kim, *Fabrication and electric-field-dependent transport measurements of mesoscopic graphite devices*, Appl. Phys. Lett. 86, 073104 (2005).

[2] K.S. Novoselov, A.K. Geim, S.V. Morozovk, D. Jiang, Y. Zhang, S.V. Dubonos, I.V. Grigorieva, A.A. Firsov, *Electrical Field Effect in Atomically Thin Carbon Films*, Science 306, 666- 669 (2004).

[3] K.S. Novoselov, A.H. Castro-Neto, *Two-dimensional crystals-based heterostructures: materials with tailored properties*, Phys. Scr. T146, 014006 (2012).

[4] H.O. Pierson, *Handbook of Chemical Vapor Deposition (CVD): Principles, Technology, and Applications*, William Andrew Inc. (1999).

[5] P. Lucas, A. Marchand, *Pyrolytic Carbon Deposition from Methane, Carbon* 28 (1), 207–219 (1990).

[6] H.O. Pierson, M.L. Lieberman, *The Chemical Vapor Deposition of Carbon on Carbon Fibers*, Carbon 13, 159–166 (1975).

[7] C. Mattevi, H Kim, M. Chowalla, *A review of chemical vapour deposition on copper*, J. Mater. Chem. 21, 3324-3334 (2011).

[8] X. Li, W. Cai, L. Colombo, R.S. Ruoff, *Evolution of Graphene Growth on Ni and Cu by Carbon Isotope Labelling*, *Nano Lett.* 9 (12), 4265-4272 (2009).

[9] X. Li, C.W. Magnuson, A. Venugopal, J. An, J.W. Suk, B. Han, M. Borysiak, W. Cai, A. Velamakanni, Y. Zhu, L. Fu, E. M. Vogel, E. Voelkl, L. Colombo, R.S. Ruoff, *Graphene Films with Large Domain Size by a Two-Step Chemical Vapour Deposition process*, *Nano Lett.* 10, 4328-4334 (2010).

[10] I. Vlassiouk, S. Smirnov, I. Ivanov, P.F. Fulvio, S. Dai, H. Meyer, M. Chi, D. Hensley, P. Datskos, N.V. Lavrik, *Electrical and thermal conductivity of low temperature CVD graphene: the effect of disorder*, *Nanotechnology* 22, 275716 (2011).

[11] Y.H. Lee, J.H. Lee, *Scalable growth of free-standing graphene wafers with copper catalyst on SiO_2/Si substrate: Thermal conductivity of the wafers*, Appl. Phys. Lett. 96, 083101 (2010).

[12] J. Robertson, *Diamond-like amorphous Carbon*, Mater. Sci. Eng. R37, 129 (2002).

[13] T. Wu, G. Ding, H. Shen, H. Wang, L. Sun, Y. Zhu, D. Jianga, X, Xie, *Continuous graphene films synthesized at low temperatures by introducing coronene as nucleation seeds*, Nanoscale 5, 5456–5461 (2013).

[14] J.H. Choi, Z. Li, P. Cui, X. Fan, H. Zhang, C. Zeng, Z. Zhang, *Drastic reduction in the growth temperature of graphene on copper via enhanced London dispersion force*, Sci. Rep. 3, 1925 (2013).

[15] M.P. Levendorf, C.S. Ruiz-Vargas, S. Garg, J. Park, *Transfer-Free Batch Fabrication of Single Layer Graphene Transistors*, Nano Lett. 9 (12), 4479-4483 (2009).

[16] L. Zhao, K.T. Rimb, H. Zhou, R. He, T.F. Heinz, A. Pinczuk, G.W. Flynn, A.N. Pasupathy, *Influence of copper crystal surface on CVD growth of large area monolayer graphene*, Solid State Communications 151, 509-513 (2011).

[17] Z. Han, A. Kimouche, A. Allain, H. Arjmandi-Tash, A. Reserbat-Plantey, S. Pairis, V. Reita, N. Bendiab, J. Courax, V. Bouchiat, *Suppression of Multilayer Graphene Patches during Graphene Growth*, arXiv:1205.1337.

[18] X. Li, W. Cai, J. An, S. Kim, J. Nah, D. Yang, R. Piner, A. Velamakanni, I. Jung, E. Tutuc, S. K. Banerjee, L. Colombo, R. S. Ruoff, *Large-Area Synthesis of High-Quality and Uniform Graphene Films on Copper Foils*, Science 324, 1312 (2009).

[19] V-M. Freire, J. Badia-Canal, C. Corbella, E. Pascual, E. Bertran, J-L. Andujar, *Hot-Wire Chemical Vapor Deposition of Few-Layer Graphene on Copper Substrates*, Jpn. J. Appl. Phys. 52, 01AK02 (2013).

[20] W. Umrath, H. Adam, A. Bolz, H. Boy, H. Dohmen, K. Gogol, W. Jorisch, W. Mönning, H.J. Mundinger, H.D. Otten, W. Scheer, H. Seiger, W.

Schwarz, K. Stepputat, D. Urban, H.J. Wirtzfeld, H.J. Zenker, *Fundamentals of Vacuum Technology,* Oerlikon Leybold Vacuum, Cologne (2007).

[21] L.I. Maissel, R. Glang, *Handbook of Thin Film Technology*, McGraw-Hill, New York (1970).

[22] E. Bertran, V.-M. Freire, A. Ramírez, E. Pascual, J.-L. Andújar, *Process for the controlled production of graphene at very low pressure and device to carry out the process (Procedimiento para la producción controlada de grafeno a muy baja presión y dispositivo para llevar a cabo el procedimiento)*. ES201330585 (OEPM), PCT/ES2014/070295 (PCT) and AVCRI189 (FBG). (accepted and to be published in BOPI) www.fbg.ub.edu/images/AVCRI189_Flyer_Physical-materials-nanotechnology.pdf, (2013).

[23] M. Ohring*, Materials Science of Thin Films: Deposition and Structure*, Elsevier Inc. (2002).

[24] www.stoner.leeds.ac.uk/Research/TutSputtering

[25] R. Carmina, *Auger neutralization and ionization processes for charge exchange between slow noble gas atoms and solid surfaces*, arXiv:1402.2080, (2014).

[26] W.D. Westwood, *Sputter Deposition*, AVS Education Committee Book Series Vol. 2, New York (2003).

[27] K. Sarakinos, J. Alami, S. Konstantinidis, *High power pulsed magnetron sputtering: A review on scientific and engineering state of the art*, Surface & Coatings Technology 204, 1661–1684 (2010).

[28] C. Corbella, *Thin film structures of diamond-like carbon prepared by pulsed plasma techniques*, PhD Thesis, Universitat de Barcelona (2005).

[29] G. Bräuer, B. Szyszka, M. Vergöhl, R. Bandorf, *Magnetron sputtering – Milestones of 30 years*, Vacuum 84, 1354–1359 (2010).

[30] Stanford Research Systems, *Operating Manual and Programming Reference: Models RGA100, RGA200, and RGA300 Residual Gas Analyzer*, SRS (2009).

[31] J. Garcia-Céspedes, *Nanotubos de carbono: síntesis, caracterización y aplicaciones*, PhD Thesis, Universitat de Barcelona (2009).

[32] O. Leenaerts, B. Partoens, F.M. Peeters, *Adsorption of small molecules on graphene*, Microelectronics Journal 40 (4-5), 860 862 (2009).

[33] C. Miao, C. Zheng, O. Liang, Y.H. Xie (edited by S. Mikhailov), *Physics and Applications of Graphene - Experiments*, InTech, University of California, Los Angeles (2011).

[34] S. Bae, H. Kim, Y. Lee, X. Xu, J.S. Park, Y. Zheng, J. Balakrishnan, T. Lei, H.R. Kim, Y.I. Song, Y.J. Kim, K.S. Kim, B. Özyilmaz, J.H. Ahn, B.H. Hong, S. Iijima, *Roll-to-roll production of 30-inch graphene films for transparent electrodes*, Nature Nanotechnology 5, 574-578 (2010).

[35] T. Kaplas, D. Sharma, Y. Svirko, *Few-layer graphene synthesis on a dielectric substrate*, Carbon 50 (4), 1503–1509 (2012).

Chapter 4

CHARACTERIZATION TECHNIQUES

4. Characterization techniques

4.1. Structural and chemical characterizations

4.1.1. Raman spectroscopy

Raman spectroscopy is the most used non-invasive technique for carbon materials identification and characterization: be it three-dimensional form like diamond, graphite, diamond like carbon and amorphous carbon; two-dimensional graphene; one-dimensional carbon nanotubes; and zero-dimensional carbon fullerenes.

The basic concept of Raman dispersion states that when a light ray interacts with a material, light can be transmitted, reflected, and absorbed. The dispersed light corresponds to a portion of the transmitted light. More than 99% of the dispersed radiation has the same frequency as the incident beam (Mi and Rayleigh dispersion). A small portion of the dispersed radiation has different frequencies from the incident beam (Raman and Brillouin dispersions), the inelastic dispersion. The frequency differences between the incident v_0 and the dispersed inelastic v_v are determined by the properties of the molecules that constitute the material under study. The dispersed frequency (with an energy of $\sigma = h(v_0-v_v)$) defines the frequency detected in a Raman spectrum (emitted) respect to the incident frequency; being h the Planck's constant (figure 4.1). If the incident photon has lost energy to a phonon is called Stokes scattering (smaller frequency than the incident), and if the photon has gained energy from the phonon is called Anti-Stokes scattering (higher frequency than the incident).

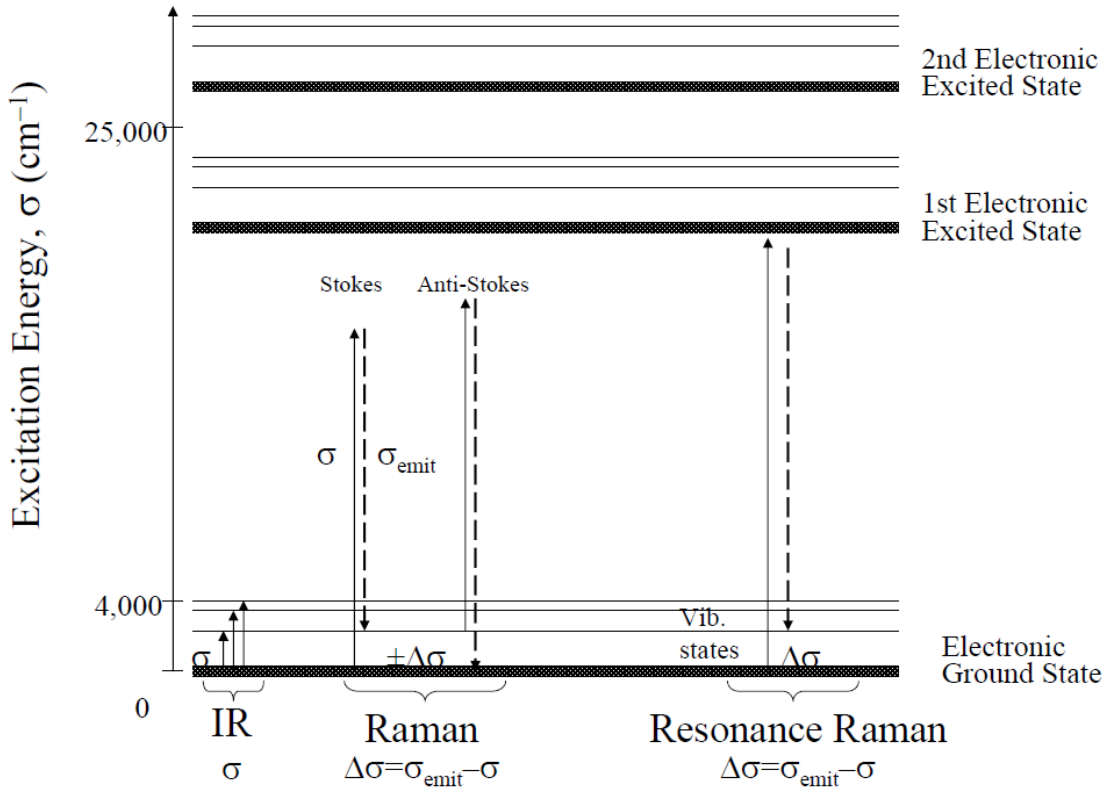

Figure 4.1: Vibrational states diagram involved in Raman spectroscopy; where σ is the energy related to harmonic oscillator. [1]

Unfortunately, these processes are not very efficient. The respective intensity ratios for Rayleigh and Raman scattering are 10^{-3} and 10^{-6}. Also, with the same Raman system, it is possible to measure the photoluminiscence of a material. If that phenomenon exists, it normally has a much bigger Raman intensity and it can be easily detected. Due to the fact that the atomic vibrations are very sensitive (to the order of the interatomic forces), Raman spectroscopy can provide information about the crystallographic order and the presence of stress in the material; not only of its chemical composition. Raman spectra of crystalline solids are composed by broad peaks centered in the characteristic frequency of the vibration of the material bonds, and the vibrational modes can also be plotted by a sinusoidal flat wave. [2]

Raman microscopy is then, based on the inelastic scattering (Raman scattering) of a monochromatic light generated by a laser in the ultra-violet, visible or IR. In the conventional Raman spectroscopy, visible laser beams are used (e.g. Ar, Kr, Nd: YAG, He-Ne, diode). For more sensitive

samples, generally a near IR laser is used, reducing the risk of damaging the sample through high power application. However, the light has a certain penetration depth inside the sample, which is directly related with the wavelength. The green laser (514 nm) has a penetration depth of 700 nm in the case of Si, and a few tens of nm for the Cu.

A typical Raman microscope consists basically on a standard optical microscope with the mentioned excitation laser, a monochromator and a sensitive detector (CCD or photomultiplier). The same incident optical path is used to collect the light (with a lens) that has interacted with vibrational, rotational or other low-frequency modes in a system. A monochromator filters the elastically scattered light (Rayleigh scattering) and the energy shifted up or down (normally expressed in terms of the wave number in cm^{-1}) of the rest of the light spectrum is analyzed. The final spectrum gives information on the different excitation processes, like phonon modes, that are specific of each material and crystallographic structure.

Particularly useful for graphene, therefore, are Raman techniques [3], because the absence of a bandgap makes all wavelengths of incident radiation resonant, thus the Raman spectrum contains information about both atomic structure and electronic properties. Resonance could also be reached by ultraviolet excitation. [4,5]

The relative simplicity of Raman measurements is balanced by the complicated data interpretation. The spectra of all carbon-based materials show only a few prominent features, regardless of their structure. However, the shapes, intensities and positions of these peaks give a considerable amount of information, often comparable to that obtained by competing techniques that are more complicated and destructive. [6]

The phonon dispersions of single-layer graphene (SLG) comprise three acoustic (A) and three optical (O) branches. The modes with out-of-plane (Z) motion are considerably softer than the in-plane longitudinal (L) and transverse (T) ones. Graphene has two atoms per unit cell, thus six normal modes (two being doubly degenerate) at the Brillouin zone centre Γ: $A_{2u} + B_{2g} + E_{1u} + E_{2g}$ [7]. There is one degenerate in-plane optical mode, E_{2g}, and one out-of-plane optical mode B_{2g}. The E_{2g} phonon generates an infrared-active E_{1u} phonon and a Raman-active E_{2g} phonon, the B_{2g} phonon

goes into an infrared-active A_{2u} phonon and an inactive B_{2g} phonon. The E_{2g} phonons are Raman active, whereas the B_{2g} phonon is neither Raman nor infrared active (optically inactive) [8]. The symmetric combinations of the acoustic modes remain A_{2u} and E_{1u}. Figure 4.2 shows the optical phonon dispersions of SLG, relevant for the interpretation of the Raman spectra. [9-11]

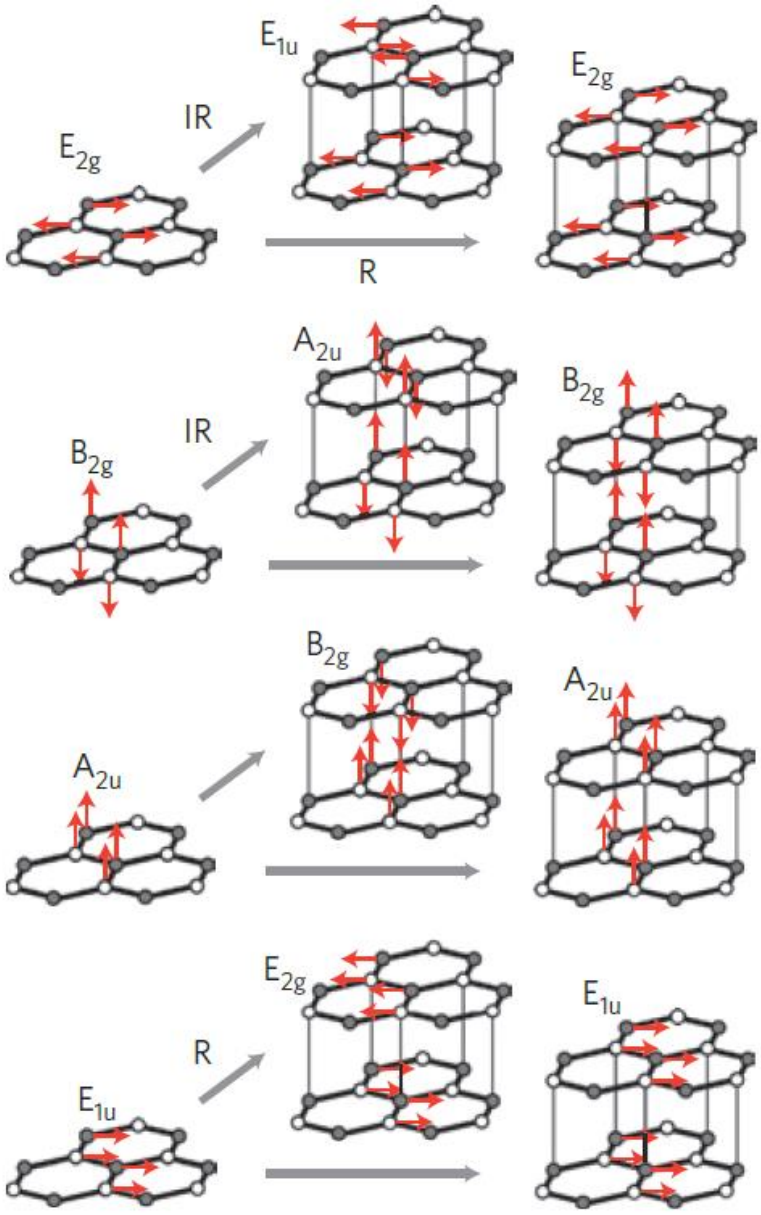

Figure 4.2: Γ-point phonon-displacement pattern for graphene and graphite. Empty and filled circles represent inequivalent carbon atoms. Red arrows show atom displacements. Grey arrows show how each phonon mode in graphene gives rise to two phonon modes of graphite. Their labelling shows Raman-active (R), infrared-active (IR) and inactive (unlabelled) modes. [3]

The Raman spectrum of SLG consists of distinct bands [12] (figure 4.3). Three main peaks can be observed: called G, D and 2D band; and will be explained in detail.

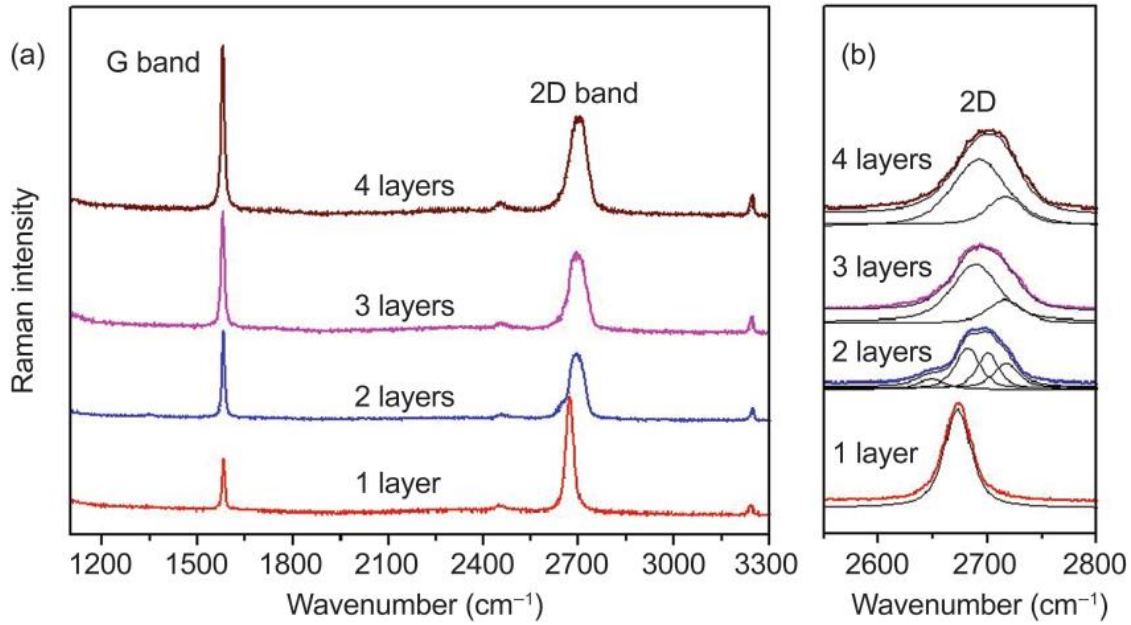

Figure 4.3: (a) Raman spectra of graphene with 1, 2, 3, and 4 layers. (b) The enlarged 2D band regions with curve fitting. [13]

- The **G band** appears at ~1580 cm^{-1}. This peak corresponds to the high-frequency E_{2g} phonon at the center of Brillouin zone Γ, which corresponds to in-plane vibrations of sp^2 carbon atoms. Although the intensity increases with the number of graphene layers, the intensity of one monolayer graphene is surprisingly comparable to the bulk graphite signal.

- The **D band** is located at ~1350 cm^{-1}. The phonon mode responsible of this peak is related to the breathing modes of the sp^2 six-atom rings and their excitation is forbidden for the Raman fundamental selection rules. D band can only appear in the presence of defects or in the edges of a graphene flake. That is why it is called the defective band and is usually used as a measure of the quality of the graphene flakes. It comes from TO phonons around the Brillouin zone corner **K** [14], it is active by double resonance [15,16], and is strongly dispersive with excitation energy [17], due to a Kohn anomaly at **K**. [18]

- Finally, the **2D band**, at ~2700 cm^{-1}, is the second order effect of the D band and it does not need the presence of defects or edges for its activation. To this 2D band relies most of the graphene characterization because its shape and intensity strongly depend on the number of graphene layers. [12]

The origin of the differences in the 2D band while increasing the number of layers, is the appearance of multiple vibration modes when, in spite of having one monolayer of graphene, the measured sample has several layers. In multilayer graphene the D band is the result of the addition of two peaks and the 2D band results from the addition of four different peaks. The shape of the 2D band changes because of the relative intensity of these peaks varies depending on the number of the layers. Hence, **graphene monolayer has a very narrow 2D band with intensity roughly four times greater than those of the G band whereas increasing the number of graphene layers makes the 2D/G intensity ratio decrease and the 2D band becomes broader and upshifted**. [12]

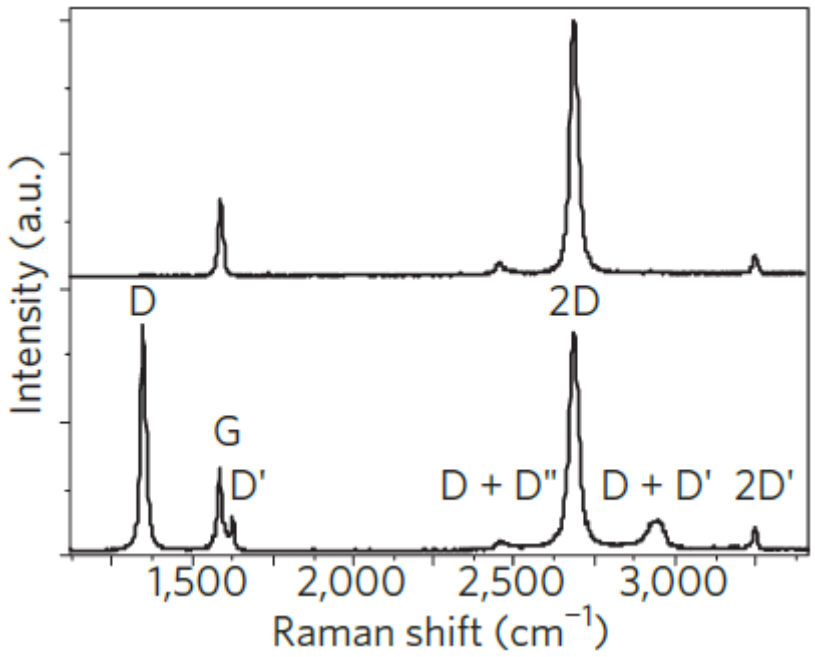

Figure 4.4: Raman spectra of pristine (top) and defected (bottom) graphene. The main peaks are labelled.

Although these are the main peaks and they are reliable enough to characterize graphene, double resonance can also happen as an

intravalley process, giving the so-called D' peak. The 2D peak is the D peak overtone, and the 2D' peak (~3248 cm^{-1}) is the D' overtone (~1620 cm^{-1}). Because the 2D and 2D' peaks originate from a process where momentum conservation is satisfied by two phonons with opposite wave vectors, no defects are required for their activation, and are thus always present. [12,19]

The band at ~2450 cm^{-1} in figure 4.4 was first reported in graphite by Nemanich and Solin. Its interpretation was subject to debate but it is assigned a combination of a D phonon and a phonon belonging to the LA branch, seen at ~1100 cm^{-1} in defected samples when measured with visible light, and called D'' peak [20], it is indicated as D + D'' in figure 4.4.

All the peaks explained above are due to in-plane vibrations [12], but there are others, such as the shear (C) modes [21] and the layer-breathing modes (LBMs) [22], due to relative motions of the planes themselves, either perpendicular or parallel to their normal. The low-frequency E_{2g} mode in graphite was first measured by Nemanich et al. in 1975 [23] at ~42 cm^{-1}. They called this mode C, because it is sensitive to the interlayer coupling. The absence of the C peak is consistent with the observation of SLG. On the other hand, this mode scales with the number of layers, going to ~31 cm^{-1} for bilayer graphene (BLG). [21]

However, special considerations must be made regarding the exact position of the peaks. The possible defects of the substrates, like copper, nickel or silicon, and the interference of their signals with those characteristic of the film make difficult to determine the theoretical shape of the spectrum. Another explanation for the shift and the widening of the Raman peaks is the heating of the samples during the laser irradiation, what creates perturbations of the interatomic potential. If the substrate is not a good thermal conductor, the energy dissipation is not effective and the temperature of the material increases, which can lead to its degradation too. To overcome this and other problems, Raman signal can be enhanced using certain substrates, such as the common Si/SiO_2, due to interference in the SiO_2 layer, resulting into enhanced field amplitudes within graphene [24]. This optical cavity will be commented in section 4.2.1.

Apart from the determination in the number of graphene layers, Raman spectroscopy can be also used to determine the doping concentration, the crystallographic orientation, the surface functionalization and other physical properties in graphene. The variation of the intensity or the position of the peaks in the spectrum, together with the appearance of new peaks, indicates modification of the mentioned physical properties. [25]

For the exfoliated samples of graphene on Si/SiO_2, an inVia Raman microscope from Renishaw was used; which enables high resolution confocal measurements, it supports multiple lasers with automatic software switching of excitation wavelength (532 and 633 nm), and it comprises a reasonable range of Rayleigh filter options with motorized switching. Both diffraction grating of 1800-2400 lines/mm were used. This equipment is located in the Fakultät für Physik of the Duisburg-Essen Universität, Duisburg (Germany).

The main spectrometer used in this work for the graphene samples grown by CVD was the Jobin Yvon LabRam HR 800, with a 532 nm laser under micro-Raman conditions (100X objective). Generally the incident power used was 3.3 mW at most, and the size of the spot is 2 μm; the diffraction grating used was 600-1800 lines/mm. The equipment is property of the CCiT-UB (Barcelona).

Regarding the Raman mappings, we worked with the equipment WITec Confocal Raman Microscope Alpha 300R on loan to the CCiT-UB during few months in 2012 by the company WITec Gmbh. The spectrometer consisted on an ultrasensitive-fast Raman Imaging, which allows to measure simultaneously with an attached Atomic Force Microscopy (AFM).

4.1.2. Energy Dispersive X-ray Spectrometry (EDS)

There are many characterization techniques that permit to analyze the composition of samples surface. Among all of them, Energy Dispersive X-ray Spectrometry (EDS) allows to characterize the composition of the

sample surface very easily. In this case, the scanning electron microscope (SEM) is used for element point analysis (local), line scan and even element mapping (regional), if an X-ray spectrometer is added.

EDS makes use of the X-ray spectrum emitted by a solid sample bombarded with a focused beam of high-energy electrons to obtain a localized chemical analysis. The EDS characterization capabilities are due in large part to the fundamental principle that each element has a unique atomic structure allowing unique set of peaks on its X-ray spectrum. These "characteristic" X-rays result from electron transitions between inner atomic orbitals, which are normally full. An electron must first be removed in order to create a vacancy, which is eventually occupied by an electron decaying from a more energetic level, thus stimulating the emission of X-rays with an energy that matches the energy difference of the involved levels. (Figure 4.5)

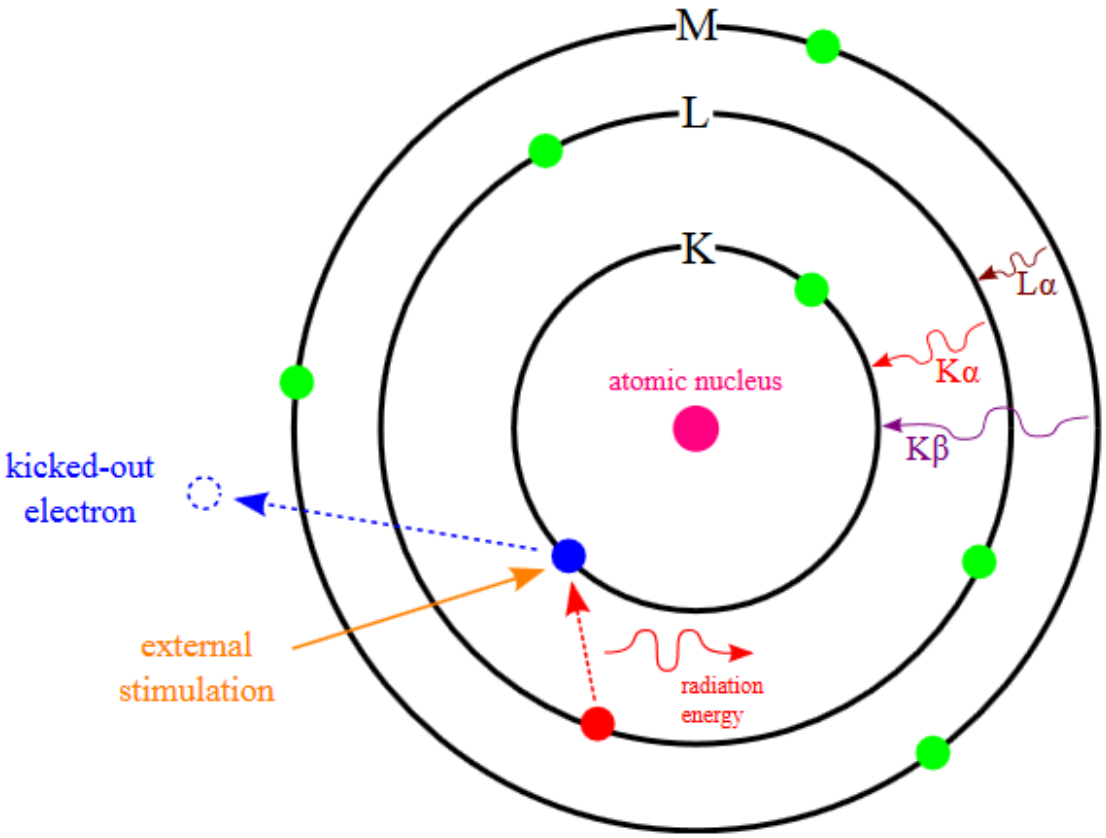

Figure 4.5: Inner atomic shell: where K, L and M lines and their transitions are shown. [26]

Normally, X-ray lines are identified by a capital Roman letter indicating the shell containing the inner vacancy (K, L or M), a Greek letter specifying the group to which the line belongs (α, β, etc., α: departure from shell above, β: departure from second shell above in the Siegbahn notation; not recommended by the IUPAC), and a number denoting the intensity of the line within the group in descending order (1, 2, etc.). Thus the most intense K line is $K_{\alpha 1}$, the less intense $K_{\alpha 2}$ line is usually not resolved, and the combined line is designated $K_{\alpha 1,2}$ or just K_{α}. Although we treated X-rays as photons possessing a specific energy (E), sometimes it is more appropriate to describe X-rays by their wavelength (λ), which is related to energy by the expression: [27]

$$\lambda[\text{Å}] = 12396/E[eV] \tag{4.1}$$

EDS employs pulse height analysis: a detector is used in conjunction with a pulse height analyzer (a multichannel type). A solid state detector is used because of its better energy resolution, Si(Li) or Si drift detectors (SDD) are commonly in use. Incident X-ray photons cause ionization in the detector, producing an electrical charge, which is amplified by a sensitive preamplifier located close to the detector. Both detector and preamplifier are cooled with liquid nitrogen to minimize electronic noise. To sum up, the four primary components of the EDS setup are:

1. The excitation source (electron beam or x-ray beam)
2. An X-ray detector
3. The pulse processor
4. The analyzer

All elements from atomic number 4 (Be) to 92 (U) can be detected in principle, though not all instruments are equipped for “light” elements detection (Z<10). By scanning the electron beam with electrostatic deflection lenses and displaying the intensity of a selected X-ray line, element distribution images or “maps” can be produced. Also, images produced by electrons collected from the sample (the different electrons detected: reflected, secondary…, will be classified in section 4.2.2.) reveal surface topography (topographical contrast) or mean atomic number differences (chemical contrast). Qualitative analysis involves the

identification of the lines in the spectrum and is fairly straightforward owing to the simplicity of X-ray spectra. On the other hand, quantitative analysis (determination of the concentrations of the elements present) entails measuring line intensities for each element in the sample and for the same elements in calibration standards of known composition [27]. This analysis will be determined by the volume interaction created by the incident electrons inside the sample (see section 4.2.2.). The penetration depth depends strongly on the acceleration voltage and the *Z* number of the sample, but for 20 kV (usual value in our measurements) and with Cu as sample: 1 nm for Auger electrons, the secondary electrons reach down to 5-50 nm, 300 nm for the backscattered electrons, and 1.5 μm for X-rays.

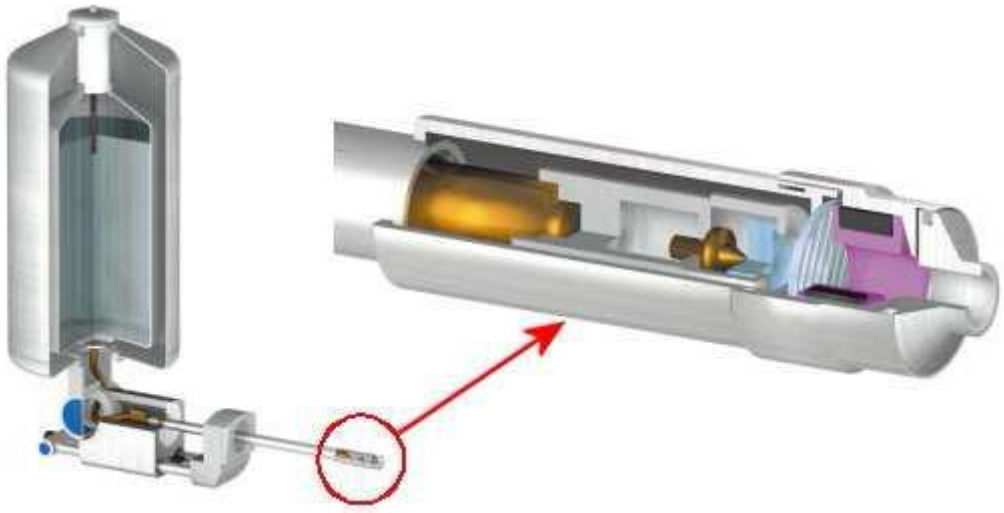

Figure 4.6: Internal scheme of a standard EDS attachable to a SEM. [28]

Qualitative analysis is used to find what elements are present in an "unknown" specimen by identifying the lines in the X-ray spectrum using tables of energies or wavelengths, or facilities for superimposing the positions of the lines of a given element for comparison with the recorded spectrum.

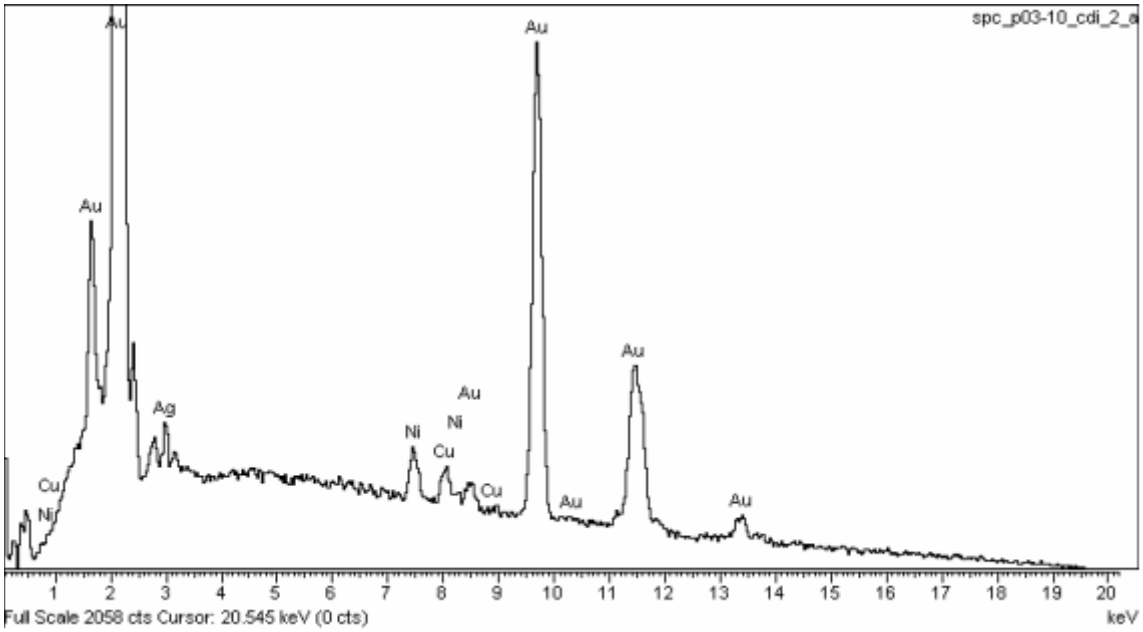

Figure 4.7: Typical EDS spectrum with the peaks denoting the chemical composition of a multilayer sample: CuSn bulk, Au 1 μm - 2 μm of Ni, and a top layer of 0.5 μm of AuCo; a noticeable background continuum can be seen.

Quantitative analysis can be done with EDS because the relative intensity of an X-ray line is approximately proportional to the mass concentration of the element concerned, as shown by Castaing in 1951. An ”apparent concentration” (C') can be derived using the following relationship:

$$C' = \left(\frac{I_{sp}}{I_{st}} \right) C_{st} \tag{4.2}$$

Where I_{sp} and I_{st} are the intensities measured for specimen and standard respectively, and C_{st} is the concentration of the element concerned in the standard. To obtain the true concentration, certain corrections are required. [27]

Electron bombardment also results in a continuous X-ray spectrum or continuum, covering all energies from zero to E_0 (the incident electron energy). This continuum arises from interactions between incident electrons and atomic nuclei, and it contributes the “backgrounds” upon which characteristic elemental lines are superimposed. The intensity of the continuum decreases monotonically with increasing X-ray energy, and is approximately proportional to *Z* (averaged over the detected elements).

In summary, EDS is an attractive tool for qualitative (and even quantitative) X-ray microanalysis because a complete spectrum can be obtained very quickly. The fact that the total spectrum of interest, from 0.1 keV to the beam energy (e.g. 20 keV) can be acquired in a short time (10 -100 s) allows for a rapid evaluation of the specimen.

In order to approach the chemical composition of the substrates grown by sputtering, we analyzed the spectra with the Oxford Link ISIS EDS system from Oxford Instruments, attached to the Scanning Electron Microscope Jeol JSM-840, located in the CCiTUB (Barcelona).

4.2. Morphological characterization

4.2.1. Optical microscopy

The optical absorbance of graphene is about 2.3% for the visible light, which is a significant value for a single-atom thick material. Anyway, it is still a small value in global terms, which is why graphene can be considered almost transparent for the human eyes. One could imagine then, that the optical microscopy may not be a suitable characterization technique.

To overcome this problem, multi-reflection/interference effects can improve the contrast of the sample. Si substrates with a thick enough top layer of SiO_2 create a multilayer interference of incident light based on Fresnel's equation. Consider the incident light from air onto a graphene sheet/SiO_2/Si trilayer system, as shown in figure 4.8. When a surface wavefront of light reaches an interface, as for example the air/graphene or graphene/SiO_2 interface, a portion of the beam is reflected and the rest is transmitted, and thus, an infinite number of optical paths is possible. [29]

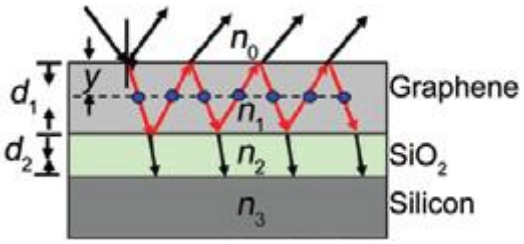

Figure 4.8: Schematic laser reflection and transmission at a certain depth y in graphene sheets deposited on a SiO_2/Si substrate (Fabry-Perot configuration). Where n_0=1 is the refractive index of air, n_1=2.6-1.3i, n_2=1.46, n_3=4.15-0.044i, are the refractive indices of graphite, SiO_2, and Si at 532 nm, respectively, d_1 is the thickness of graphene which is estimated as $d_1 = N\Delta d$, where Δd= 0.335 nm is the thickness of single layer graphene and N is the number of layers, and d_2 is the thickness of SiO_2 (conveniently 90 or 300 nm), and the Si substrate is considered as semi-infinite.

The graphene deposited on this kind of substrates adds a small optical path to the Fabry-Perot cavity created by the silicon dioxide layer. The required substrates that provide interference conditions for maximum light intensity at about 550 nm (the wavelength of maximal sensitivity of the human eye sensitivity) are silica layers of 90 and 300 nm over silicon. This short optical path added by graphene can make the contrast reach values up to 6-8%. Graphene flake color is blueshift and the lighter contrast indicates thinner samples. On the other hand, the thicker samples remain white. In addition, the contrast can be improved by adjusting the irradiation wavelength, and of course, by changing the type of substrate. [30]

The surface morphology of graphene flakes transferred onto Si/SiO_2 was studied with the optical microscope Zeiss AXIO Scope A1. It is a standard microscope equipped with 5X, 10X, 20X, 50X, and 100X objectives and a digital AxioCam ICc1 (Zeiss). The images were processed with ZEN software. This microscope is available at the Fakultät für Physik in the Duisburg-Essen Universität, Duisburg (Germany).

Although less relevant, other images were taken as well with the standard optical or confocal microscopes that are equipped with the different Raman microscopes.

4.2.2. Scanning Electron Microscopy (SEM)

The scanning electron microscope (SEM) uses a very thin and focused beam of high-energy electrons to generate an image and a variety of signals at the surface of solid specimens. The signals that derive from electron-sample interactions reveal information about the surface morphology, chemical composition, and crystalline structure and orientation of materials constituting the sample. In most applications, data are collected over a selected area of the surface of the sample, and a 2D image is generated that displays spatial variations in these properties. Areas ranging from approximately 1 cm to 1 μm in width can be imaged in a scanning mode using conventional SEM techniques (magnification ranging from 20X to approximately 30.000X, spatial resolution of 50 to 100 nm). The SEM is also capable of measuring chemical compositions (using EDS, see section 4.1.2.), crystalline structure, and crystal orientations (using EBSD).

As basic principle of operation, a SEM uses electron beams to form an image instead of light. The reason is that the optical microscope resolution is in part limited by the light wavelength (550 nm), as suggested by Rayleigh. The Rayleigh criterion is the generally accepted criterion for the minimum resolvable detail: the imaging process is said to be diffraction-limited when the first diffraction minimum of the image of one source point coincides with the maximum of another. As shown in the equation, it depends normally on the wavelength of light and the diameter of the lens.

$$\sin\theta \cong \theta = \frac{1.22\lambda}{D} \tag{4.3}$$

Where θ is the angular resolution (radians), λ is the wavelength of light, and D is the diameter of the circular lens' aperture. Taking into account that de Broglie's equation associates a wavelength to any particle in movement: $\lambda = h/p$, electrons (with a smaller wavelength than light) can be used to decrease the diffraction limit, i.e. to increase the resolution of the image.

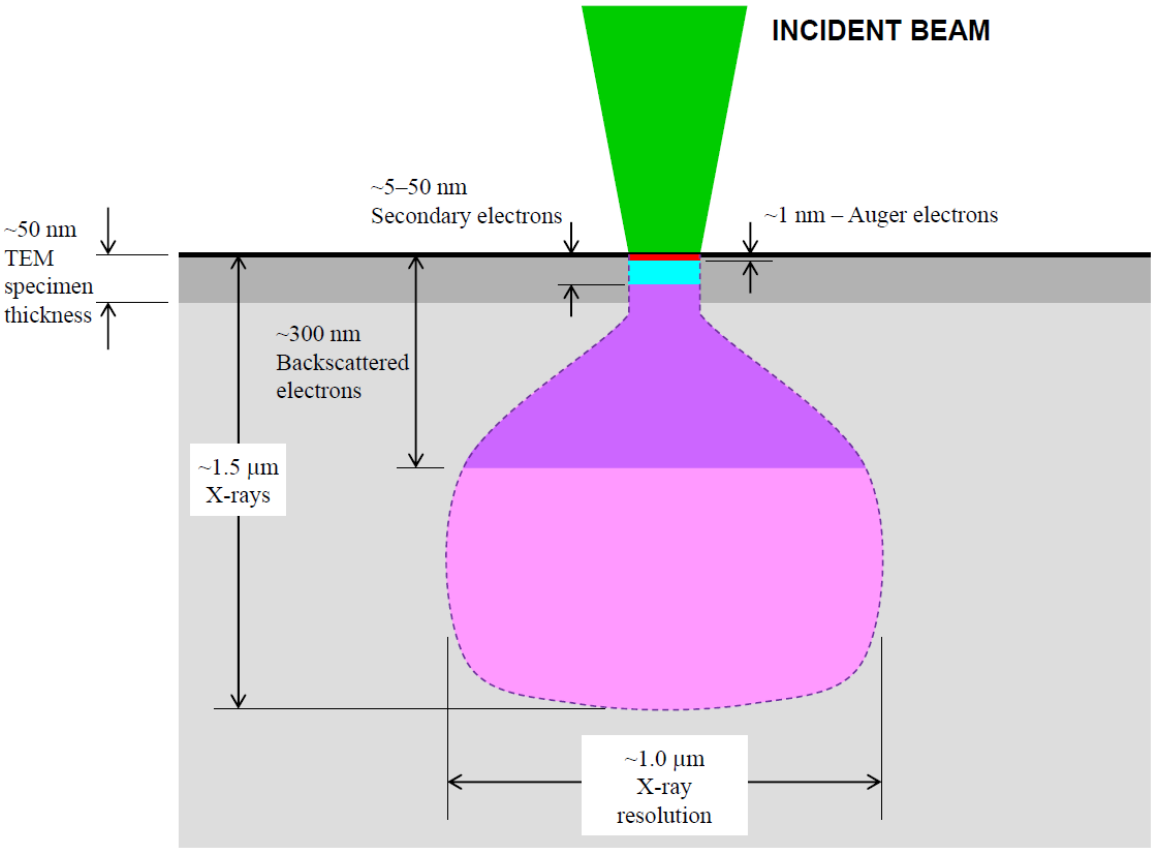

Figure 4.9: Interaction volume scheme in a sample, Z=29 (copper), irradiated by an electron beam with an accelerating voltage of 20 kV. [31]

Accelerated electrons in an SEM carry significant amounts of kinetic energy, which is dissipated as a variety of signals produced by electron-sample interactions when the incident electrons are decelerated in the solid sample, thus generating the interaction volume (figure 4.9). The penetration depth of the electrons depends directly on the acceleration voltage and inversely with the *Z* number of the sample. These signals include secondary electrons (that produce SEM images), backscattered electrons (BSE), diffracted backscattered electrons (EBSD that are used to determine crystal structures and orientations of minerals), photons (characteristic X-rays that are used for elemental analysis and continuum X-rays), visible light (cathodoluminescence-CL), and heat. Secondary electrons and backscattered electrons are commonly used for imaging samples: secondary electrons are most valuable for showing morphology and topography on samples and backscattered electrons are most valuable for illustrating contrasts in composition in multiphase samples.

X-ray generation is produced by inelastic collisions of the incident electrons with electrons in discrete orbitals (shells) of atoms in the sample (see EDS section in 4.1.2.). The penetration depth of the electrons are, for 20 kV (usual value in our measurements) and with Cu as sample, 1 nm for Auger electrons, 5-50 nm for secondary electrons, 300 nm for the backscattered electrons, and 1.5 μm for X-rays (figure 4.9). The standard components of all SEMs include the following:

- Electron Source ("Thermionic or Field Emission Gun")
- Electromagnetic Lenses
- Mechanical apertures
- Sample holder
- Detectors (Scintillators, photomultipliers, CCD cameras…)
- Display/Data output devices
- Infrastructure requirements (Vacuum and cooling systems, vibration-free floor, magnetic/electric-free room…)

The electron beam works normally at voltages from 5-30 kV. SEM scans the surface and the contrast arises from the different number of electrons out of the sample arriving at the detector.

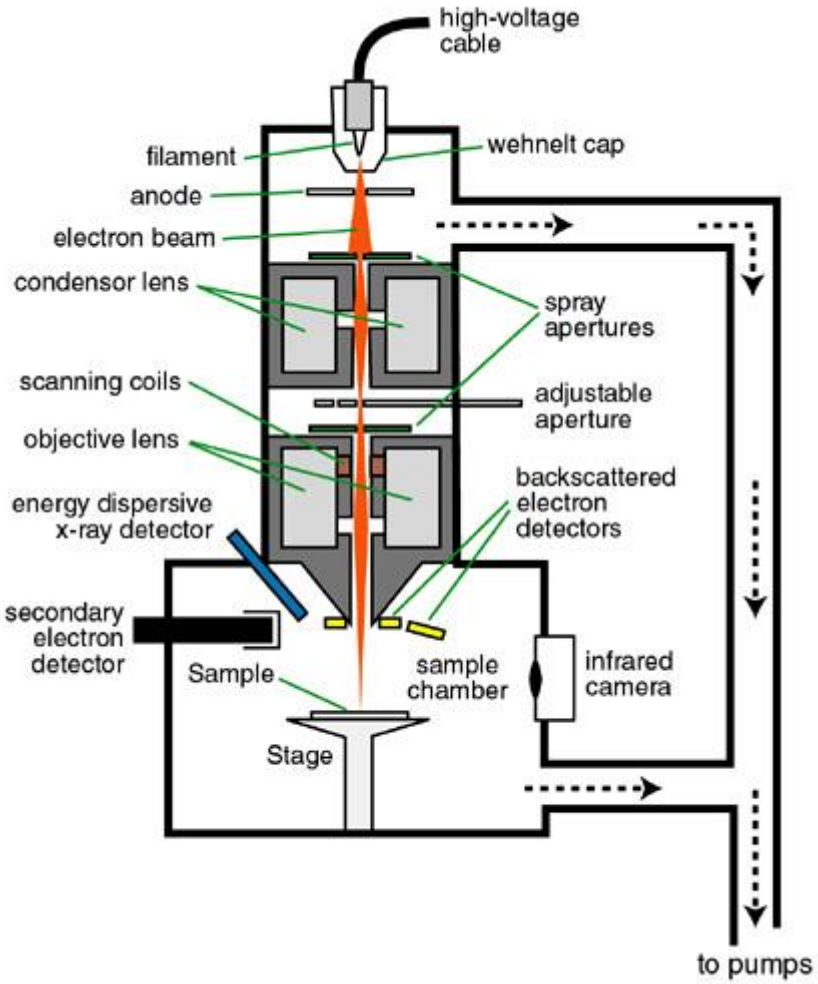

Figure 4.10: Diagram of a SEM. Image courtesy of the Northern Arizona University [32]

In this thesis, SEM was used to characterize the prepared substrate surfaces (copper, nickel and silicon), and the resulting surface after annealing of the sputtered samples. In addition, with this microscopy, it was possible to observe the different growth patterns of graphene. Both Field Emission Hitachi S2300 and S4100 were preferentially used for high resolution images, being usually operated at voltages between 15 and 20 kV. On the other hand, for a first evaluation of the substrates and their chemical composition, we used a Jeol JSM-840 with thermionic gun equipped with an EDS detector. All of them are located in the CCiTUB (Barcelona).

4.2.3. Atomic Force Microscopy (AFM)

This Scanning Probe Microscopy (SPM) technique permits to study the surface topography of a sample with atomic vertical resolution. It is based on the repulsive and attractive atomic forces (10^{-8}-10^{-11} N) experienced by a cantilever, when its sharpened tip is brought within atomic distances above the sample surface by moving either the sample with piezoelectric transducers or the scanning head of the AFM. The atomic forces can be of short and long range. Short range interactions are repulsive and manifested at a distance of about 0.1 nm, due to the proximity of the electron orbitals in the sample with those at the cantilever surface. Long range interactions dominate when the AFM tip and the sample surface are separated around 1 nm, and can be attractive and repulsive (electric, magnetic), or just attractive (van der Waals). Among other relevant interactions, it is worth mentioning mechanical contact forces, capillary forces, chemical bonding, Casimir forces and solvation forces. [33]

This microscope basically consists of a cantilever with a sharp tip (probe) at its end that is used to scan the specimen surface. The cantilever is typically made of silicon or silicon nitride with a nanometer-size tip radius. When the tip is approached to a sample surface, forces between the tip and the sample lead to a deflection of the cantilever according to Hooke's law. Along with force, additional quantities may simultaneously be measured through the use of specialized types of probes (local temperature, distribution temperature, and thermal conductivity in scanning thermal microscopy, scanning joule expansion microscopy, and photothermal microspectroscopy).

Typically, the deflection of the tip is measured using a laser spot reflected from the top surface of the cantilever into an array of photodiodes. Other methods that are used include optical interferometry, capacitive sensing or piezoresistive AFM cantilevers. These cantilevers are fabricated with piezoresistive elements that act as a strain gauge. In order to avoid the tip crushing into the sample, a feedback mechanism is employed to maintain a constant force between the tip and the sample, thus setting the tip-to-sample distance to a constant value.

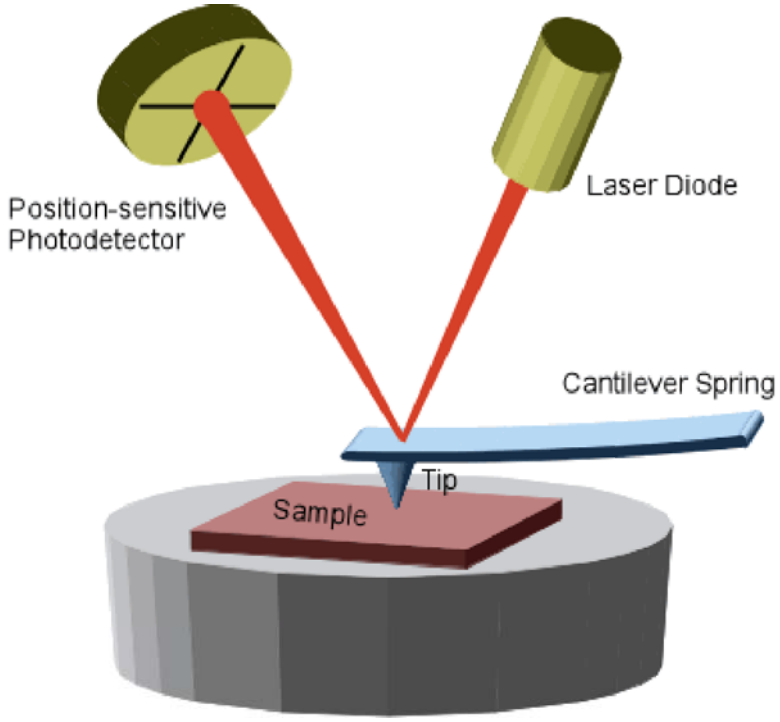

Figure 4.11: Schematic of the operation principle of an AFM. Laser deflection owes to the deformation of the cantilever, which transmits surface features. [34]

There are three main operation modes for an AFM: contact, non-contact and tapping. Contact mode is normally destructive because it implies the scratch of the tip against the sample surface. Here, the bending of the cantilever transmitted by the surface features deflects a laser beam additionally to the topographical bending. The laser spot points to a photodetector screen that registers the signal evolution. In non-contact mode, the tip scans the surface between 1 and 2 nm away from it. The main interactions are attractive, so the measurements require the use of a fast feedback system in order to avoid the crush of the tip into the sample surface. The most used mode is tapping. In this case, the cantilever oscillates at a characteristic resonant frequency, with amplitude of hundreds of nanometers. Thus, tapping mode gives information about topography and eliminates the surface wear due to damage by the cantilever tip, because now the contact is not constant, but intermittent.

Non-contact mode (substrates)

In this mode, the tip of the cantilever does not contact the sample surface. The cantilever is instead oscillating at either its resonant frequency (frequency modulation) or just above (amplitude modulation) where the

amplitude of oscillation is typically a few nanometers (< 10 nm) down to a few picometers. The van der Waals forces, which are dominant from 1 nm to 10 nm above the surface, or any other long-range force that extends above the surface, tend to reduce the resonance frequency of the cantilever. This decrease in resonant frequency combined with the feedback loop system maintains a constant oscillation amplitude or frequency by adjusting the average tip-to-sample distance. Measuring the tip-to-sample distance at each (x,y) data point allows the scanning software to construct a topographic image of the sample surface.

Tapping mode (exfoliated graphene)

In tapping mode, the cantilever is driven to oscillate up and down at near its resonance frequency by a small piezoelectric element mounted in the AFM tip holder similar to non-contact mode. However, the amplitude of this oscillation is greater than 10 nm, typically 100 to 200 nm. The interaction of forces acting on the cantilever when the tip comes close to the surface, van der Waals forces, dipole-dipole interactions, electrostatic forces, etc. cause the amplitude of this oscillation to decrease as the tip gets closer to the sample. An electronic servo uses the piezoelectric actuator to control the height of the cantilever above the sample. The servo adjusts the height to maintain a set cantilever oscillation amplitude as the cantilever is scanned over the sample. The image is therefore produced by imaging the force of the intermittent contacts of the tip with the sample surface. This mode reduces the damage done to the surface and the tip compared to the amount done in contact mode. [35]

AFM is one of the most valuable choices to characterize the morphology of graphene. The 0.34 nm step height for each successive layer lies within the detection limits for modern AFMs. However, in this thesis, resolving the substrate-graphene height profile was challenging due to the strong differences in tip attraction/repulsion forces between the insulating substrate and semimetallic graphene. This issue was exacerbated under ambient conditions by the preferential adsorption of a thin layer of water on graphene. With such complications, height profiles by AFM have typically ranged from 0.6 to 1.0 nm for single layers. Nevertheless, the

folded edges of graphene have provided a more reliable and accurate measurement of thickness because there is no change in material associated with the location of the step. It was a fold that allowed the Manchester group (A. Geim and K. Novoselov) to confirm the single layer step height of 0.4 nm in their original report. In spite of the simplicity of the method, it is only reasonably reliable with graphene flakes obtained by mechanical exfoliation. Due to the mean roughness of the metallic substrates in CVD samples and the smaller chance of localizing flakes deposited on copper or nickel, AFM was mainly used to explore the surface of the catalysts rather than that of graphene itself. [36]

For the exfoliated graphene on silicon, the graphene flakes were analyzed with a Veeco Dimension 3100 from Digital Instruments in tapping mode. This microscope is located in the Fakultät für Physik in the Duisburg-Essen Universität, Duisburg (Germany).

AFM measurements of the substrates were performed with a Park XE-70 from Park Systems operated in non-contact mode. This AFM is property of the Física Aplicada i Òptica department of the Universitat de Barcelona (Barcelona).

4.3. Electrical properties

4.3.1. Van der Pauw method

One of the most important features of graphene is the electric behavior, especially its high electric conductivity (low resistivity) and its Hall coefficient value. Thus, electric characterization is an important way to evaluate the graphene samples.

Resistivity

Normally, the easiest way to measure the resistivity (conductivity) of a certain material is to measure the voltage drop between two electrodes where electric current is being injected. The use of four terminals (four point probe method) ensures that the measured voltage does not include the voltage drop due to the current contacts. However, a precise

knowledge of the placement of the contacts and of the sample geometry is needed. This supposes an important drawback when the material under study is difficult to cut with great precision. Moreover, it is necessary that the current density is equal on each point of the sample cross-section and that equipotential surfaces are planes parallel to the current electrodes.

The advantage of the van der Pauw technique lies in that allows measuring electric properties of samples of an arbitrary shape as long as they are considered 2-dimensional (thin and flat enough). Leo J. van der Pauw proved in 1958 [37] that one can determine the resistivity of a certain material without knowledge of the electric current pattern if:

1. The contacts are on the edge of the sample. Actually, if the thickness of the sample is not negligible, the contacts should have the shape of very thin vertical lines across the whole thickness. This requirement is due to the fact that the thickness *d* is a merely multiplicative factor and the equipotential surfaces in the sample are taken to be cylindrical (if the contacts are point-like and the thickness is not negligible, they rather assume a spherical shape).

2. The contacts are sufficiently small. In principle, they should be point-like (in a very thin sample) or have a negligible section (in thicker samples).

3. The sample is homogeneous in thickness. Again, this is necessary to ensure that the 3D geometry can be reduced to a flat geometry by simply dividing by the thickness *d* that is, equipotential surfaces are cylindrical.

4. The surface of the sample is simply connected, i.e., the sample does not have isolated holes.

Although these requirements are difficult to fulfill experimentally, some geometries were suggested to minimize the errors. Figure 4.12 shows some van der Pauw disks and the peripherical contacts of the sample.

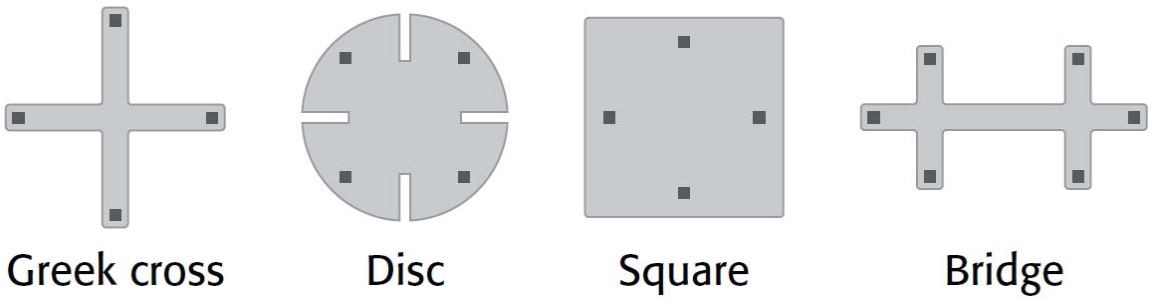

Figure 4.12: Van der Pauw disks or preferable geometries. [38]

In a general case, a single resistance measure is not sufficient to evaluate the resistivity, and an explicit expression for the resistivity ρ cannot be obtained. Nevertheless, it is possible to write it in the form:

$$\rho = \frac{\pi d}{\ln 2} \frac{R_{AB,CD} + R_{BC,DA}}{2} f\left(\frac{R_{AB,CD}}{R_{BC,DA}}\right) \tag{4.4}$$

Where current is injected through contact A and drained from contact B, the voltage drop is measured between contact C and D (figure 4.13); and f is the "correction function" and the values are tabulated for any value of the resistance ratio $\frac{R_{AB,CD}}{R_{BC,DA}}$.

If there is no certainty about the homogeneity of the material under study, a slight modification of the method is advisable, which allows testing the internal consistency of resistance data. In this version of the technique, eight DC resistance measurements are required, corresponding to as many permutations of the four contacts. The remaining permutations are obtained by these ones by swapping the positive and negative poles of the current leads. The absolute values of voltages such as V_{AB} and V_{BA}, measured with opposite directions of current flow, are not expected to be identical because of the possible presence of thermoelectric effects, which can be eliminated by averaging the two values. Another possibility consists in using AC current instead of DC current, so that this average is automatically performed. In the AC version of the van der Pauw technique, only four measurements are necessary. The corresponding (positive) resistances will be designated by $R_{AB,CD}$, $R_{CD,AB}$, $R_{AD,BC}$, and $R_{BC,AD}$.

In addition to resistivity, more properties can be calculated from this method: the doping type (i.e. whether it is a P-type or N-type material), the sheet carrier density of the majority carrier (the number of majority carriers per unit area). From this, the charge density and doping level can be found, the mobility of the majority carrier.

Hall Effect

The Hall Effect is the generation of a voltage difference (the Hall voltage) across an electrical conductor due to a separation of charge carriers forming a current perpendicular to the created electric field and to the applied magnetic field. The Hall coefficient, R_H, is defined as the ratio of the induced electric field to the product of the current density and the applied magnetic field.

$$V_H = -\frac{IB}{nte} \tag{4.5}$$

$$R_H = \frac{V_H t}{IB} = -\frac{1}{ne} \tag{4.6}$$

Where *I* is the current across the plate length, *B* is the magnetic field, *t* is the thickness of the plate, *e* is the elementary charge, and *n* is the charge carrier density. The units of R_H are usually expressed as m^3/C, or Ω·cm/G. The sign of the Hall voltage indicates the type of material the sample is made of; if it is positive, the material is P-type, and if it is negative, the material is N-type.

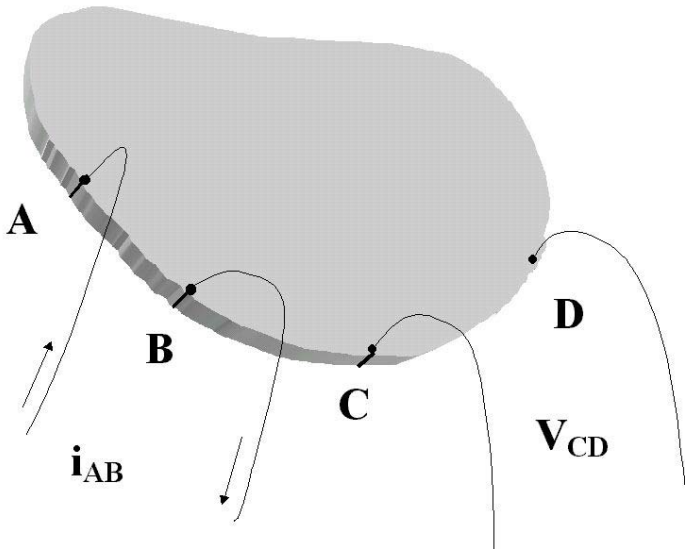

Figure 4.13: Example of contact disposition on the edge of an arbitrarily-shaped sample, as in the van der Pauw technique. The current flows from A to B and the voltage is measured across C and D: the resistance $R_{AB,CD}$ is given by $(V_D - V_C)/i_{AB}$. [39]

The objective of the Hall measurement by means of the van der Pauw technique is to determine the sheet carrier density n_s by measuring the Hall voltage V_H. The Hall voltage measurement consists of a series of voltage measurements with a constant current I and a constant magnetic field B applied perpendicular to the plane of the sample. To measure the Hall voltage V_H, a current I is generated through the opposing pair of contacts (A and C) and the Hall voltage V_H (= V_{BD}) is measured across the remaining pair of contacts (B and D) (figure 4.13). Once the Hall voltage V_H is acquired, the sheet carrier density n_s can be calculated via $n_s = IB/et|V_H|$ from the known values of I, B, and e. This can then be rearranged to give the majority carrier mobility in terms of the previously calculated sheet resistance R_s and charge density.

$$\mu = \frac{|V_H|}{R_S IB} = \frac{1}{qn_S R_S} \tag{4.7}$$

For the electrical characterization, Ti/Au was deposited by photolithography onto an appropiate flake of graphene to perform a four-probe measurement, and the test of a Field Effect Transistor (see Chapter 9).

4.4. References

[1] D.T. Schwartz, *Raman Spectroscopy: Introductory tutorial*, University of Washington, depts.washington.edu/ntuf/facility/docs/NTUF-Raman-Tutorial.pdf

[2] M.J. Inestrosa, *Producción de Nanopartículas de Si Monodispersas obtenidas mediante Plasma Modulado*, PhD Thesis, Universitat de Barcelona (2012).

[3] A.C. Ferrari, D.M. Basko, *Raman spectroscopy as a versatile tool for studying the properties of graphene*, Nature Nanotechnology 8, 235 (2013).

[4] A.C. Ferrari, J. Robertson, *Interpretation of Raman spectra of disordered and amorphous carbon*, Phys. Rev. B 61, 14095–14107 (2000).

[5] A.C. Ferrari, J. Robertson, *Resonant Raman spectroscopy of disordered, amorphous, and diamondlike carbon*, Phys. Rev. B 64, 075414 (2001).

[6] A.C. Ferrari, J. Robertson, *Raman spectroscopy in carbons: from nanotubes to diamond, Theme Issue*, Phil. Trans. R. Soc. A 362, 2267–2565 (2004).

[7] S. Reich, C. Thomsen, *Raman spectroscopy of graphite*, Phil. Trans. R. Soc. A 362, 2271–2288 (2004).

[8] R.J. Nemanich, G. Lucovsky, S.A. Solin, *Infrared active optical vibrations of graphite*, Solid State Comm. 23, 117–120 (1977).

[9] A. Grüneis, J. Serrano, A. Bosak, M. Lazzeri, S. L. Molodtsov, L. Wirtz, C. Attaccalite, M. Krisch, A. Rubio, F. Mauri, T. Pichler, *Phonon surface mapping of graphite: Disentangling quasi-degenerate phonon dispersions*, Phys. Rev. B 80, 085423 (2009).

[10] S. Piscanec, M. Lazzeri, F. Mauri, A.C. Ferrari, J. Robertson, *Kohn anomalies and electron-phonon interactions in graphite*, Phys. Rev. Lett. 93, 185503 (2004).

[11] J. Maultzsch, S. Reich, C. Thomsen, H. Requardt, P. Ordejón, *Phonon dispersion in graphite*, Phys. Rev. Lett. 92, 075501 (2004).

[12] A.C. Ferrari, J. C. Meyer, V. Scardaci, C. Casiraghi, M. Lazzeri, F. Mauri, S. Piscanec, D. Jiang, K.S. Novoselov, S. Roth, A.K. Geim*, Raman spectrum of graphene and graphene layers,* Phys. Rev. Lett. 97, 187401 (2006).

[13] Y.Y. Wang, Z.H. Ni, T. Yu, H.M. Wang, Y.H. Wu, W. Chen, A.T.S. Wee, Z.X. Shen, *Raman studies of monolayer graphene: the substrate effect,* J. Phys. Chem. C *112*, 10637-10640 (2008).

[14] F. Tuinstra, J.L. Koenig, *Raman spectrum of graphite*, J. Chem. Phys. 53, 1126–1130 (1970).

[15] C. Thomsen, S. Reich, *Double resonant Raman scattering in graphite*, Phys. Rev. Lett. 85, 5214–5217 (2000).

[16] A.V. Baranov, A.N. Bekhterev, Y.S. Bobovich, V.I. Petrov*, Interpretation of certain characteristics in Raman spectra of graphite and glassy carbon*, Opt. Spectroscopy 62, 612–616 (1987).

[17] I. Pocsik, M. Hundhausen, M. Koos, L. Ley, *Origin of the D peak in the Raman spectrum of microcrystalline graphite*, J. Non-Cryst. Solids 227–230, 1083–1086 (1998).

[18] S. Piscanec, M. Lazzeri, F. Mauri, A.C. Ferrari, J. Robertson, *Kohn anomalies and electron-phonon interactions in graphite*, Phys. Rev. Lett. 93, 185503 (2004).

[19] D.M. Basko, S. Piscanec, A.C. Ferrari, *Electron-electron interactions and doping dependence of the two-phonon Raman intensity in graphene*, Phys. Rev. B 80, 165413 (2009).

[20] P. May, M. Lazzeri, P. Venezuela, F. Herziger, G. Callsen, J.S. Reparaz, A. Hoffmann, F. Mauri, J. Maultzsch, *Signature of the two-dimensional phonon dispersion in graphene probed by double-resonant Raman scattering*, Phys. Rev. B 87, 075402 (2013).

[21] P.H. Tan, W. P. Han, W. J. Zhao, Z. H. Wu, K. Chang, H. Wang, Y. F. Wang, N. Bonini, N. Marzari, N. Pugno, G. Savini, A. Lombardo, A. C. Ferrari*, The shear mode of multilayer graphene*, Nature Mater. 11, 294–300 (2012).

[22] C.H. Lui, L.M. Malard, S. Kim, G. Lantz, F.E. Laverge, R. Saito, T.F. Heinz*, Observation of layer-breathing mode vibrations in few-layer graphene through combination Raman scattering*, Nano Lett. 12, 5539–5544 (2012).

[23] R.J. Nemanich, G. Lucovsky, S.A. Solin, *Proc. Int. Conf. on Lattice Dynamics,* ed. Balkanski, M. 619–621, Flammarion (1975).

[24] F. Schedin, E. Lidorikis, A. Lombardo, V.G. Kravets, A.K. Geim, A.N. Grigorenko, K.S. Novoselov, A.C. Ferrari, *Surface-Enhanced Raman Spectroscopy of Graphene*, *ACS Nano* 4 (10), 5617–5626 (2010).

[25] A. Das, B. Chakraborty, A.K. Sood, *Raman spectroscopy of graphene on different substrates and influence of defects*, Bull. Mater. Sci. 31 (3), 579–584 (2008).

[26] Wikipedia.org

[27] University of California Riverside: Central Facility for Advanced Microscopy and Microanalysis, micron.ucr.edu/public/manuals/EDS-intro.pdf

[28] S. Estrade, Microscopy Techniques, Nanotechnology and Nanoscience Master lessons, Universitat de Barcelona (2010).

[29] Z. Ni, Y. Wang, T. Yu, Z. Shen, *Raman spectroscopy and Imaging of graphene*, Nano Res 1, 273-291 (2008).

[30] C. Soldano, A. Mahmood, E. Dujardin, *Production, properties and potential of graphene*, Carbon 48, 2127-2150 (2010).

[31] Capston Engineering, *Analytical methods for Materials: Scanning Electron microscopy and X-Ray Spectroscopy*, Capston Engineering university lesson 21 pp 824.

[32] Northern Arizona University, www4.nau.edu/homepage

[33] C. Corbella, *Thin film structures of diamond-like carbon prepared by pulsed plasma techniques*, PhD Thesis, Universitat de Barcelona (2005).

[34] Angewandte Physik, www3.physik.uni-greifswald.de/method/afm/eafm.htm

[35] Wikipedia.org

[36] M.J. Allen, V.C. Tung, R.B. Kaner, *Honeycomb Carbon: A Review of Graphene*, Chem. Rev. 110, 132–145 (2010).

[37] L.J. van der Pauw, *A method of measuring the resistivity and Hall coefficient on lamellae of arbitrary shape*, Philips Tech. Rev 20, 220 (1958).

[38] Keithley Instruments Inc., *Performing van der Pauw Sheet Resistance Measurements Using the Keithley S530 Parametric Tester*, Application Note Series, No 3180 (2012).

[39] D. Daghero, *Experimental study of non-conventional gap features in novel superconductors*, PhD Thesis, La.T.E.S.T. Lab (2002).

Part III

Results

Chapter 5

MECHANICAL EXFOLIATION

5. Mechanical exfoliation

This method is described in Chapter 3 and was an important part of my PhD stay in the Duisburg-Essen Universität, Germany. The main purpose of the production of graphene samples by this technique was the afterwards irradiation of Swift Heavy Ions (SHI) on the graphene surface at glancing angles, see Chapter 8. Other samples were used for electrical measurements and Field Effect Transistors (FETs), see Chapter 9.

5.1. Technique

The base graphite used was a Highly Ordered Pyrolytic Graphite (HOPG), grade ZYA (mosaic spread angle of 0.4° +/- 0.1°) of around 1 cm^2, provided by *HQgraphene.com*.

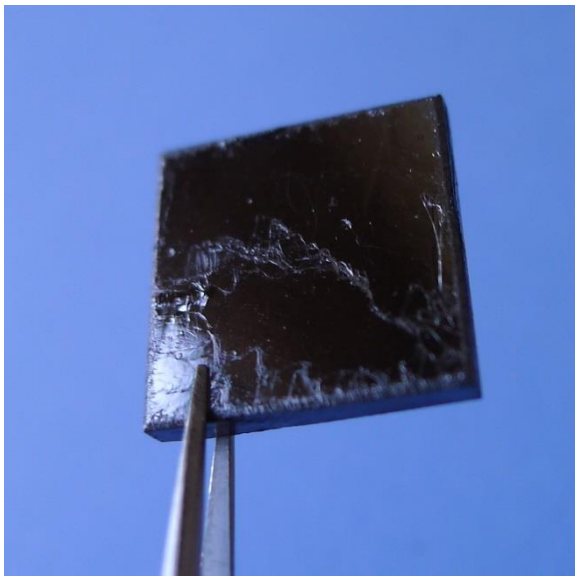

Figure 5.1: HOPG crystal picture from HQgraphene.com.

The substrate where the graphene was transferred was P-doped crystalline silicon <100> provided by *Graphene supermarket*, with a 90 nm layer of SiO_2 on top to enhance the optical contrast. The diameter of the wafers was 100 ± 0.5 mm, with a resistivity of 0.001-0.005 ohm·cm, and a thickness of 500 ± 25 μm.

In order to facilitate the transfer and the search of flakes, the wafers were cut in substrates of 1 cm^2 (the same size as the HOPG) with a diamond tip, and the surface was cleaned properly with isopropanol. The HOPG must be prepared while the samples dried.

Using a standard scotch tape, the base crystal was exfoliated once. From this tape we exfoliated with another tape around 3 or 4 times before transfer it gently with moderate force onto the silicon substrate. Although the technique is quite simple and reproducible, there is room to improvement due to the highly empirical performance. For instance, it is well known that any commercial scotch tape will do the work; however, the transparent tape will deposit less glue on the substrate than the white one. It is important to obtain a small ratio of contaminated flakes. Statistically one can obtain an average of 3-4 monolayer flakes of graphene in every sample with an average size of around 20 μm. The shape of the flakes is normally squared or triangular.

5.2. Samples

5.2.1. Optical microscopy

Once the graphene have been transferred onto silicon, the next step was finding and localizing flakes optically on the substrate. Although the flakes are quite small (~μm) compared to the size of the silicon substrate (~cm), the monolayers are normally located around the main graphite crystallites, whose deep violet color is very noticeable, making the searching much easier. The microscope used was the Zeiss AXIO Scope 1, already commented in Chapter 4. After the assumption that one has found one flake of monolayer graphene, a picture of the sample with the surroundings had to be made. This was an especially important step in order to localize the flakes for the further characterization through Raman spectroscopy, AFM, and electrical measurements.

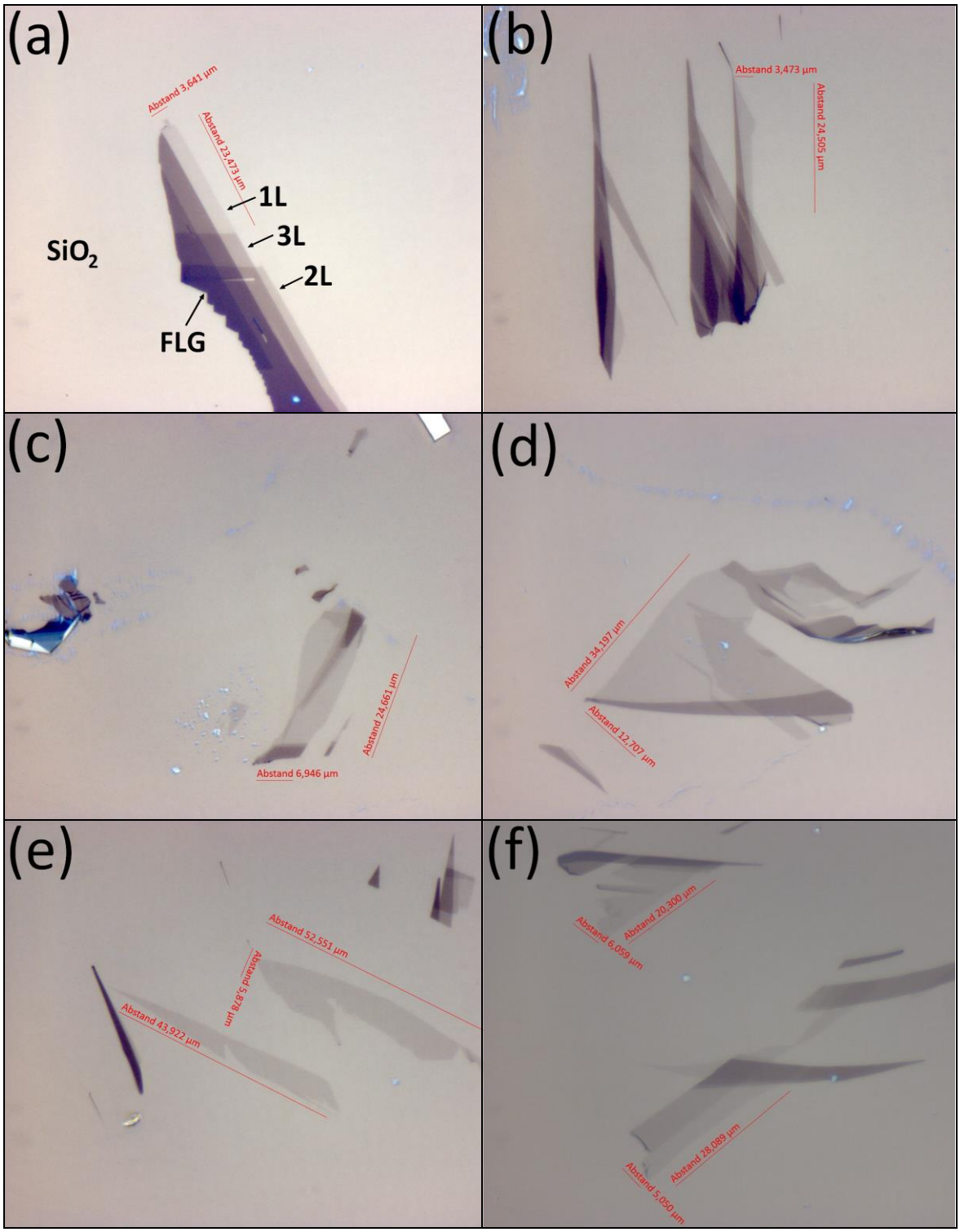

Figure 5.2: Optical images from samples: (a) A2, (b) B3, (c) C1, (d) E1, (e) E5, and (f) F2. Where the size of the flakes ("Abstand" in German means distance) is in µm. The less contrast films correspond to monolayer graphene.

As seen in figure 5.2, the pictures show the less optical contrast possible for graphene flakes of around 6-8% on 90 nm of SiO_2, against the 2.3% which can be expected for the optical transmittance of graphene.

This image is a selection of the most representative types of samples; a complete list of all the samples is in Appendix C. Normally bulk pieces of graphite crystal are white, followed by thinner layers colored blue. It comes to violet when the bulk becomes FLG, then turns into pink (2-4 layers) and pale pink to monolayer graphene (more greyish in the images than in the binocular mode).

As a useful sample on how the graphene flakes are normally overlapped, we have figure 5.2a. The different optical contrast for every *n*-layer flake is clearly seen from one to few-layer graphene. All the flakes in figure 5.2 are standard and common shapes for graphene, and the sizes have the biggest of the dimensions around 20 μm and the other a minimum of 5 μm. The blue/white dots are normally glue droplets from the scotch tape after the exfoliation process. If there is glue on one of our flakes, we will consider that the sample is contaminated.

It is also important to notice that the monolayer samples are usually surrounded by one or more layers of graphene. It is especially complicated to find isolated samples, like figure 5.2e, which are appropriate for avoiding an external interference of any kind for the subsequent characterization or purpose.

5.2.2. Raman spectroscopy

The optical identification of the samples is completely necessary, although it does not confirm the presence of graphene. Probably the fastest and easiest way to differentiate among one, two, three and few-layer graphene is Raman spectroscopy.

Relocating again the same samples found in the optical microscope, we focused the laser spot exactly in the desired flake through the optical microscope of the Renishaw inVia Raman. After a proper calibration of the Sr green laser (532 nm) with a Si reference, the power of the measurements was set to 0.4 μW for graphene to prevent heating effects. Normal spectra were acquired during 20-30 s of time centered in a 2100 cm^{-1} shift. A reduced collection of typical Raman measurements of our samples is shown in figure 5.3.

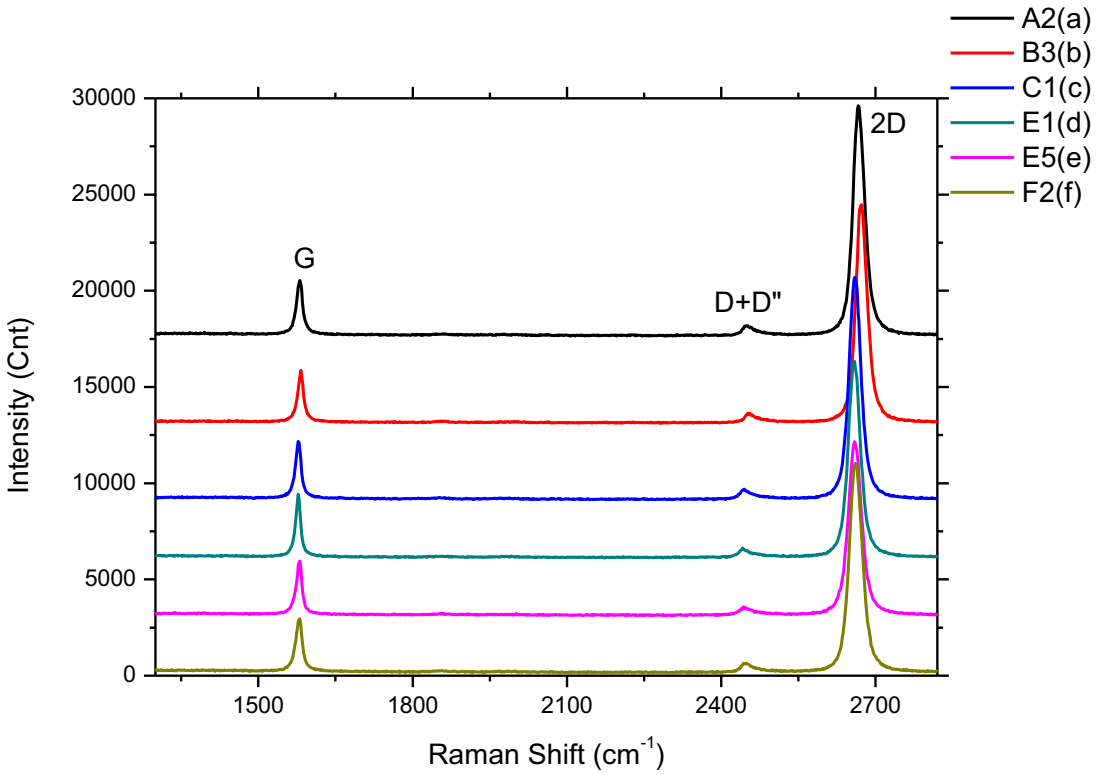

Figure 5.3: Raman spectra of the samples: A2, B3, C1, E1, E5, and F2, shown in figure 5.2. The intensity of the 2D peak is approximately four times the intensity of G, which confirms the presence of graphene monolayers. The absence of D peak reflects the high quality characteristics of the samples.

The drawn spectra of the samples of figure 5.3 correspond unequivocally to monolayer graphene, and are very similar to those found in literature [1-3]. We can see G, 2D, and even the overtone D+D" peak. The intensity ratio between the 2D and the G peak is approximately four times. D peaks remain unobservable due to the high-quality and non-defective graphene layers made by mechanical exfoliation.

We also see that the six spectra match almost exactly, the little shifts among them are probably due to the temperature effects and small displacements of the Si calibration.

For completeness, we found interesting to measure a typical spectrum of a graphene bilayer (BLG), see figure 5.4. Although the flake seems noticeable darker in the optical image, it is mandatory to check if the 2D peak is different: a bit wider, non-symmetrical, and the intensity is comparable to the G peak: the number of layers is 2. In figure 5.5, there is a sample of FLG (strictly dark) taken with the same equipment. The 2D

peak is much smaller than G, and shows its feature shape. We also detected more vibrational modes, like the D' peak, while in this case, we slightly sense the D peak.

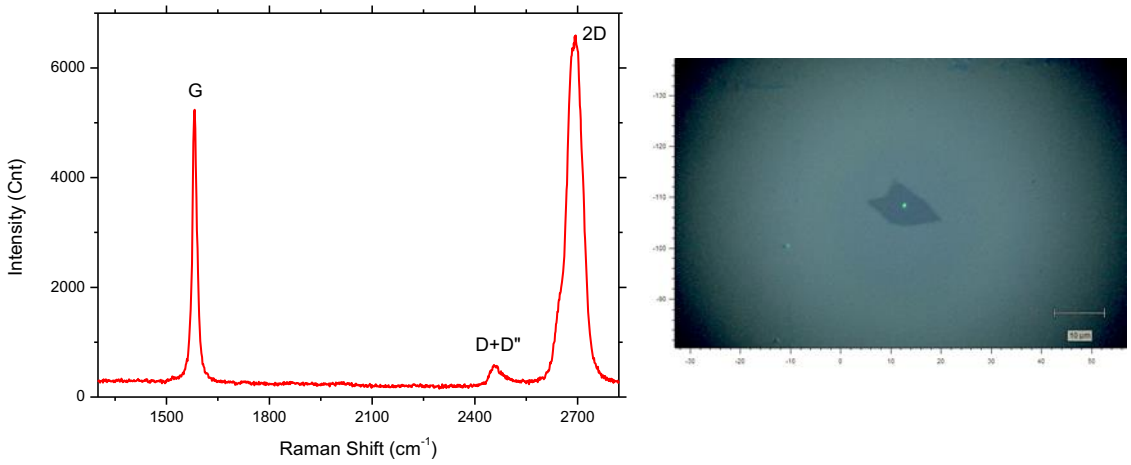

Figure 5.4: Raman spectrum of the sample B5. This spectrum corresponds to an isolated flake of bilayer graphene. The peak 2D is slightly wider and its intensity is similar to G, although the D peak is still inexistent.

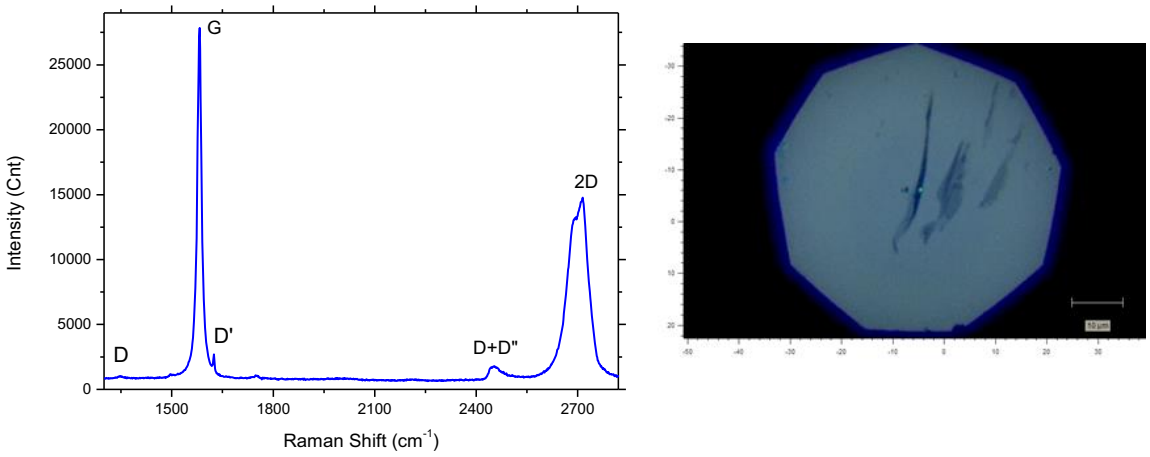

Figure 5.5: Raman spectrum of a FLG sample (darkest part of the flake in the optical image). The differences in the spectrum between FLG and a graphite crystal are almost negligible; they only rely on the shape of the 2D peak.

One of the goals of these experiments was obtaining suitable samples in order to perform a SHI irradiation. The idea was evaluating the graphene modification upon ion bombardment. To this end, defects as a function of

the ion fluences (5-10 ions/μm^2, 100 MeV with Xe^{23+}, and U^{28+}) with glancing angles of 1-3° were induced. See Chapter 8. To improve the quality of the spectra acquired regarding the defects (D peak), the red laser (633 nm) was used in these samples due to its better sensitivity in this region of the spectrum. The power was set a bit higher than that with the green laser, to 2 μW, but the typical acquisition time was the same as before, 20-30 s. Figure 5.6 plots two Raman spectra of the same sample (D3): one is the normal spectrum (before irradiation), and the other is after the SHI irradiation. Although the intensities of the peaks are different, the ratios do not vary. However, the appearance of the D and the D' peaks reflects the defects induced by the SHI irradiation.

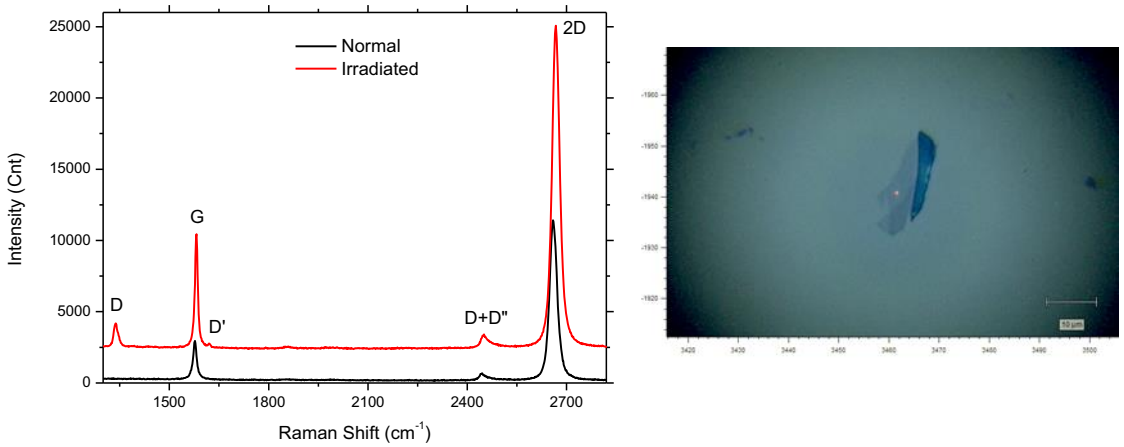

Figure 5.6: Raman comparison of the sample D3. The spectra were acquired with the red laser (633 nm) before and after the irradiation of SHI. It is clearly seen how the D peak grows as a proof of the defects induced by the irradiation while the intensity ratio 2D/G remains constant.

The irradiation caused clearly a raise in the quantity of defects in a graphene layer, thus the growth of the intensity ratio D/G. The higher ion fluences triggered more destruction in the surface of graphene. (figure 5.7)

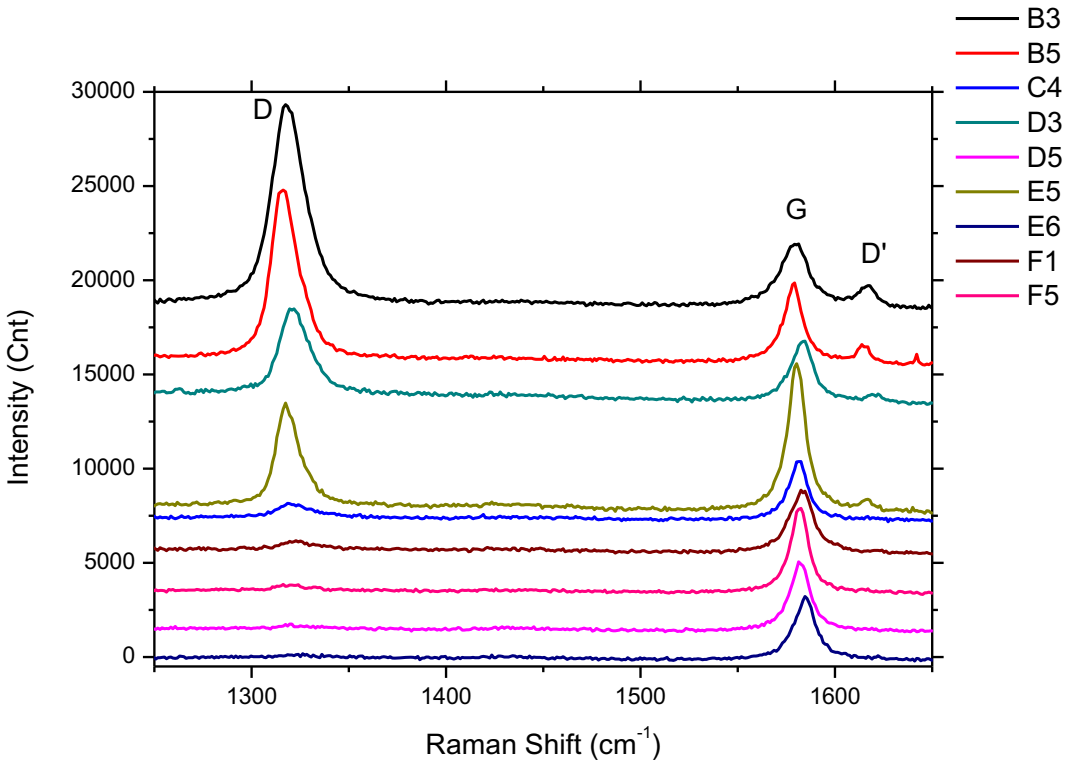

Figure 5.7: Amplified Raman spectra of irradiated samples (B3, B5, C4, D3, D5, E5, E6, F1, and F5) focused on the D, D', and G peaks. The higher ion fluences correspond to the higher intensity D/G ratios.

The SHI experiments were performed to quantify the damage of graphene due to the irradiation effects, but could also be used to understand the roles of D and D' peaks and the effects of different kind of defects: edges, grain boundaries, vacancies, implanted atoms, and defects associated to a change of carbon-hybridization (e.g. from sp^2 into sp^3). The intensity ratio of the D and D' peak is maximum (~13) for sp^3-defects, it decreases for vacancy-like defects (~7), and it reaches a minimum for boundaries in graphite (~3.5). [4]

5.2.3. AFM

Finally, AFM measurements were performed in order to test the homogeneity of the surface of the studied sample and the presence of contamination by glue or dust. The measurements were made with a Veeco Dimension 3100 from Digital Instruments in tapping mode.

Naturally, nanometer-scale details in graphene cannot be observed with an optical microscope. The appearance of foldings or cracks in the flakes can induce defects in a global scale and cannot be considered as convenient samples. But what is more important is the glue contamination (from the scotch tape), which reduces the effective area of the layer and can affect the properties of graphene, thus the consequent characterization and aim. The figure 5.8d is a good example of glue contamination, almost invisible in the optical microscopy since the defect sizes are usually smaller than 1 μm, but quite noticeable in the AFM with many sizes and shapes. Nevertheless, all the samples of figure 5.8 (corresponding to the samples of figure 5.2) are clean enough (without the presence of glue, cracks or foldings), and pristine layers of graphene, ready for further work.

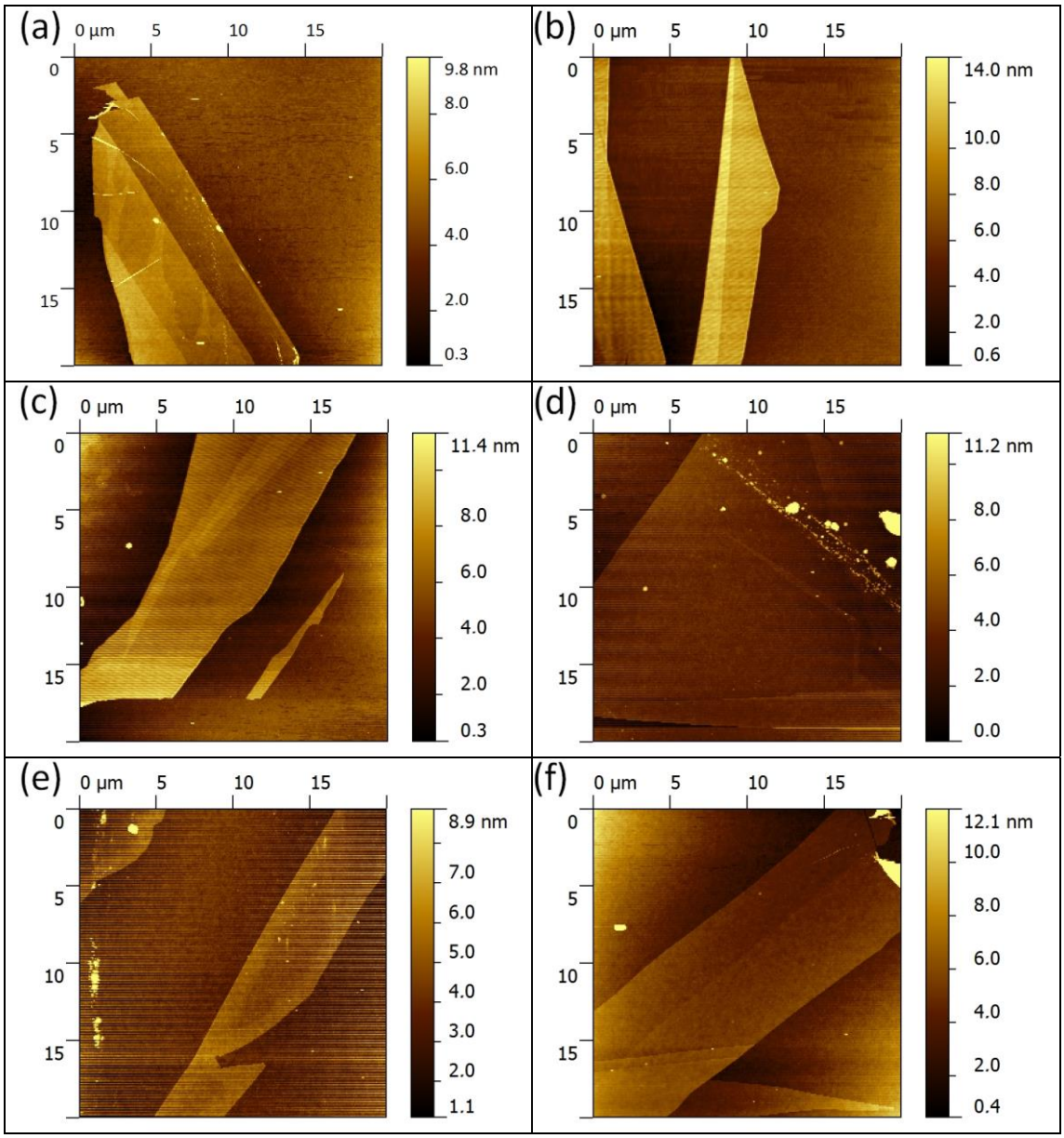

Figure 5.8: AFM images of samples (a) A2, (b) B3, (c) C1, (d) E1, (e) E5, and (f) F2; already shown optically in figure 5.2 and their Raman spectra in figure 5.3. Both the SiO_2 surface and the graphene are normally clean and homogeneus, however, still glue residue from the scotch tape are commonly found.

In addition to the AFM topography images, we checked the profiles of some samples through the phase imaging, which monitors (in tapping mode) the phase lag between the signal that drives the cantilever to oscillate and the cantilever oscillation output signal, and shows better surface contrast The figure 5.9 plots the images corresponding to the samples A2 and B3, both in phase image and the cross-sectional profile. The figure 5.9a analyzes a terrace with 1, 2, and 3 layers of graphene along

the blue line (9.5 μm), while the figure 5.9b is only a terrace with a mono and bilayer graphene across a distance of 6 μm. The small profile insets in the corners reflect the step height in nm.

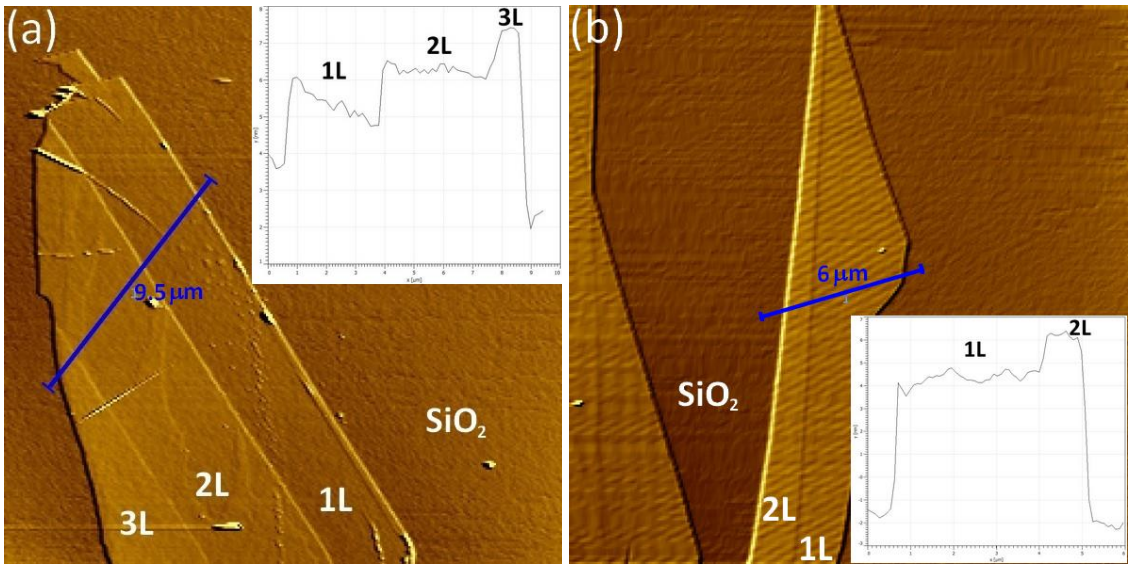

Figure 5.9: Phase image acquired with the AFM of the samples (a) A2, and (b) B3. The inset corresponds to a cross-sectional profile (blue line) of the sample across the layers of graphene. The height is expressed in nm.

Theoretically, one expects a 0.34 nm (3.4 Å) step height for each successive layer, but resolving the substrate-graphene height profile proved difficult, due to the differences in tip attraction/repulsion between the insulating substrate (SiO_2) and semi-metallic graphene. This issue was exacerbated under ambient conditions by the preferential adsorption of a thin layer of water on graphene. With such complications, height profiles by AFM have typically ranged from 1.0 to 2.0 nm for single layers.

The first graphene layer (from the substrate) has typically the highest step (around 2 nm), whereas the rest of the overlapped layers have a smaller step of around 1 nm. The sample B3 (figure 5.9b) shows an example of a high first step due to trapped water between the first layer of graphene and the silica substrate. Water concentration was proportional to the storing time between fabrication and AFM measurements. In a way, the water content is a signature of sample aging (see figure 5.10b). Notice also that the water remained always between the first layer and the substrate, and not among the rest of the upper layers.

The folded edges of graphene, then, have provided a more reliable and accurate measurement of thickness by removing the change in the material associated with the location of the step, and decreasing the probability of trapped water between surfaces.

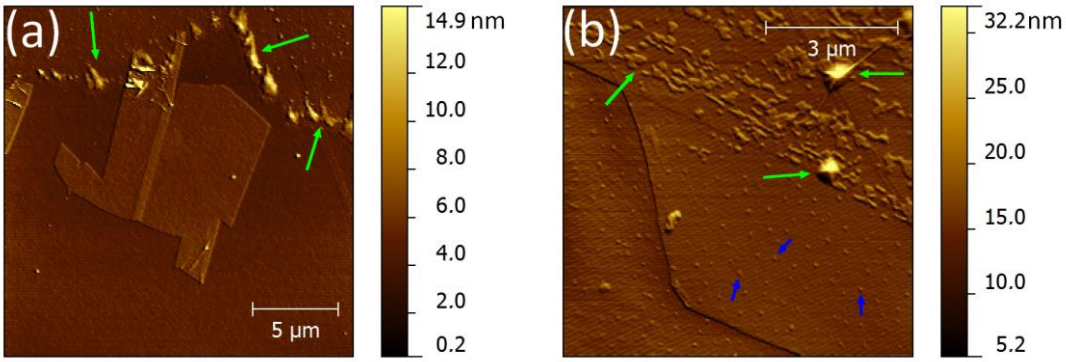

Figure 5.10: AFM phase image of two samples of graphene, where it is shown in detail the contamination by glue (a) sample C5 (green and big arrows), and also droplets of water (blue and small arrows) in sample C2 (b).

5.3. Summary and conclusions

Mechanical exfoliation is a simple and reliable process to obtain monolayer graphene with a reasonable ratio of success (output of ~20 useful samples/day). The Raman spectra acquired demonstrated the presence of high-quality monolayer graphene. A small G peak and a 2D peak around four times the G (in intensity) are present, and a complete absence of D peak. However, the size of the flakes (of around 20 µm) is not suitable for industrial applications, concretely for large area applications. The main conclusions are:

- The thin oxide layer of 90 nm of SiO_2 (or 300 nm) proved critical to enhance the contrast of any process related with the optical detection and tracing of graphene.
- The D peak is easily tuneable by inducing defects on the surface of graphene, e.g. with SHI irradiation.
- AFM in tapping mode was especially sensitive in order to detect the presence of contamination on the sample, like glue or trapped water among layers. However, it was not that efficient

to measure the step height of a monolayer of carbon due mainly to the interface graphene-substrate and the thin layer of water formed between them.

- The flakes of graphene obtained by this method can be easily prepared for electrical characterization or for the construction of a FET, as we will see in Chapter 9.

5.4. References

[1] Z. Ni, Y. Wang, T. Yu, Z. Shen, *Raman spectroscopy and Imaging of graphene*, Nano Res 1, 273-291 (2008).

[2] A.C. Ferrari, J. C. Meyer, V. Scardaci, C. Casiraghi, M. Lazzeri, F. Mauri, S. Piscanec, D. Jiang, K.S. Novoselov, S. Roth, A.K. Geim*, Raman spectrum of graphene and graphene layers,* Phys. Rev. Lett. 97, 187401 (2006).

[3] Y.Y. Wang, Z.H. Ni, T. Yu, H.M. Wang, Y.H. Wu, W. Chen, A.T.S. Wee, Z.X. Shen, *Raman studies of monolayer graphene: the substrate effect,* J. Phys. Chem. C *112*, 10637-10640 (2008).

[4] A. Eckmann, A. Felten, A. Mishchenko, L. Britnell, R. Krupke, K.S. Novoselov, C. Casiraghi, *Probing the Nature of Defects in Graphene by Raman Spectroscopy*, Nano Lett. 12, 3925−3930 (2012).

Chapter 6

CVD PRELIMINARY STUDIES

6. CVD preliminary studies

Mechanical exfoliation turned out to be one of the most efficient techniques to obtain high quality graphene, but its major drawback is the maximum size of the samples, limited to a few tens of μm. On the other hand, CVD is a promising technology to overcome this problem. The aim of this part of the work was to study the growth of graphene/FLG by a thermally activated hot-wire system technique CVD in order to test the different issues regarding the CVD conditions, with special attention to different kinds of Cu substrates (the catalyst), which constitute also an important factor in the final quality of graphene. [1]

6.1. Substrates and treatment

In this study, we used different types of Cu samples: 250 μm thick Cu foils (A series), Cu plates of 2 mm of thickness (B series), Cu-sputtered films on Si wafers (C series) and bulk Cu substrates with a diamond-lapped surface (D series). The main issue of Cu foils (A series) and plates (B series) were their low purity. These substrates (A and B series) were just used to test the experimental procedure.

Cu films on Si wafers (C series) were deposited by magnetron sputtering, which allows obtaining pristine and very smooth Cu films with desired thicknesses. The system was pre-calibrated by profilometry (*DEKTAK*). The deposition rate of the sputtered Cu films on glass substrates was 0.67 nm/s. Cu films were deposited on crystalline silicon (c-Si) wafers <100> of 2” of diameter and 300 μm of thickness. Moreover, the native SiO_2 layer of the c-Si wafer can play an important role in limiting the diffusion of the Cu in Si when the sample is annealed [2]. The Cu substrates with the diamond-lapped surface (D series), which consist of a piece of bulk Cu with a very flat surface, showed a higher quality and the best results.

The exposition of the Cu samples to the atmosphere under room temperature conditions resulted in the formation of a thin oxide layer on their surface. In principle, this oxide should be removed when the samples were exposed to H_2 in the CVD process. However, in order to remove it totally an extra treatment was applied, which consisted in immersing the

samples in a glacial acetic acid solution at 40 °C during 20 min [3]. Furthermore, the crystallographic orientation of Cu is of fundamental importance in the quality and domain size of graphene. Mismatches at the edges of the graphene preclude obtaining large area graphene domains. [4]

6.2. Growth process

The most relevant parameters in the experimental process are: pressure, flow of the reactant gases, substrate temperature, and sample surface. The experimental conditions used are based on previous works [5-7] and are shown in Table I. Unless specified otherwise, these will be the values used for the graphene growth on the different substrates of this chapter.

Table I. Parameters of the three steps involved in the whole CVD with the hot-wire heating process: gases, gas flow rate, pressure, and time. Step 1: heating ramp; Step 2: annealing and CVD; and Step 3: cooling stage.

	Atmosphere	**Gas flow rate (sccm)**	**Pressure (Pa)**	**Time (min)**
Step 1	H_2	5	10	10
Step 2	C_2H_2	30	50	10
Step 3	Residual gas	0	$\sim 10^{-4}$	60

The substrates were placed on the CVD stage of the reactor, which was pumped down until a base pressure of $2 \cdot 10^{-4}$ Pa was achieved. The details of the reactor used in this section are explained in Chapter 3. In these tests, graphene/FLG was grown by CVD from C_2H_2 (acetylene) as the precursor gas. The first step in the CVD process consisted of a temperature ramp of the hot-wire for 10 min up to the process temperature in the range of 800-900 °C. During this ramp a constant H_2 flux of 5 sccm at 10 Pa was applied. Figure 6.1 shows a T(t) diagram of the entire process.

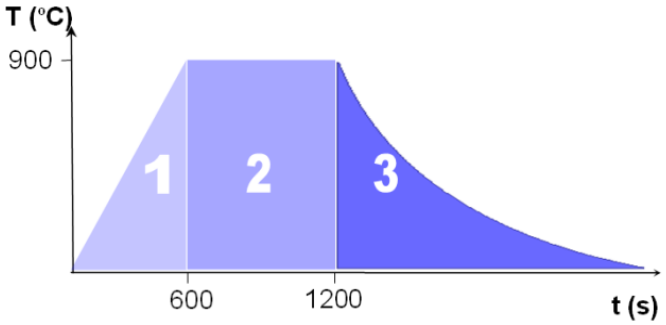

Figure 6.1: T(t) diagram of the CVD process. The atmospheric conditions at every step of the process are indicated in Table I. Step 1: heating ramp; Step 2: annealing and CVD; and Step 3: cooling stage.

The CVD process started once the substrate reached the process temperature, the acetylene was then introduced in the chamber under controlled conditions of pressure and flux, 50 Pa and 30 sccm, respectively. In these conditions, surface temperature of the substrate induces the decomposition of the acetylene molecules in different radical species (including carbon), which become adsorbed, whereas the continuous gas flow removes the rest of by-products. During the process, H_2 was also introduced to catalyze the reaction (reactive gases) and to remove the by-products (carrier gases). Finally, the CVD process ended after stopping the gas fluxes and by cooling down the hot-wire until room temperature.

Most of the publications report the use of methane gas (CH_4) as a precursor for the growth of graphene by CVD and at temperatures around 1000 °C or higher but always below 1084 °C, which is the melting point of Cu. Here acetylene was used, a less common and poorly explored precursor of graphene growth [5,7]. Acetylene is explosive and less pure than methane, but its pyrolysis starts at lower temperature, 800-900 °C, than methane pyrolysis. Thus, at a given temperature, a higher deposition rate is expected using acetylene instead of methane [8]. However, the lower deposition rate of methane leads to longer process times, which promotes the nucleation of carbon atoms on the substrate surface, which in turn increases the quality of graphene. Therefore, acetylene allows growth of graphene at lower temperatures, although graphene final quality continues to be dependent on temperature. [5]

6.3. Samples

6.3.1. SEM and EDS

Low quality Cu substrates (A and B series)

After the CVD process, Cu foils (A series) and plate samples (B series) got substantially blackened to the naked eye (see figure 6.2). This is the first indication that amorphous carbon was deposited rather than graphene or FLG. Figure 6.3 shows SEM images of both types of substrate. The samples appeared fully covered with wrinkles, cracks, and dispersed fragments of carbon. The EDS analysis showed a carbon concentration that is much higher than those in the other types of substrate, among other elements such as Zn (probably from the alloy with Cu, generally used to make brass).

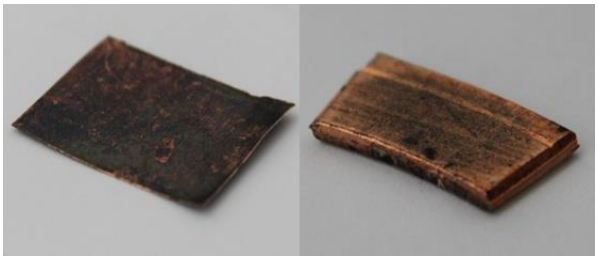

Figure 6.2: Pictures of an A series substrate (left) and a B series substrate (right) after the same CVD process. The dimensions of these substrates are around 2 cm.

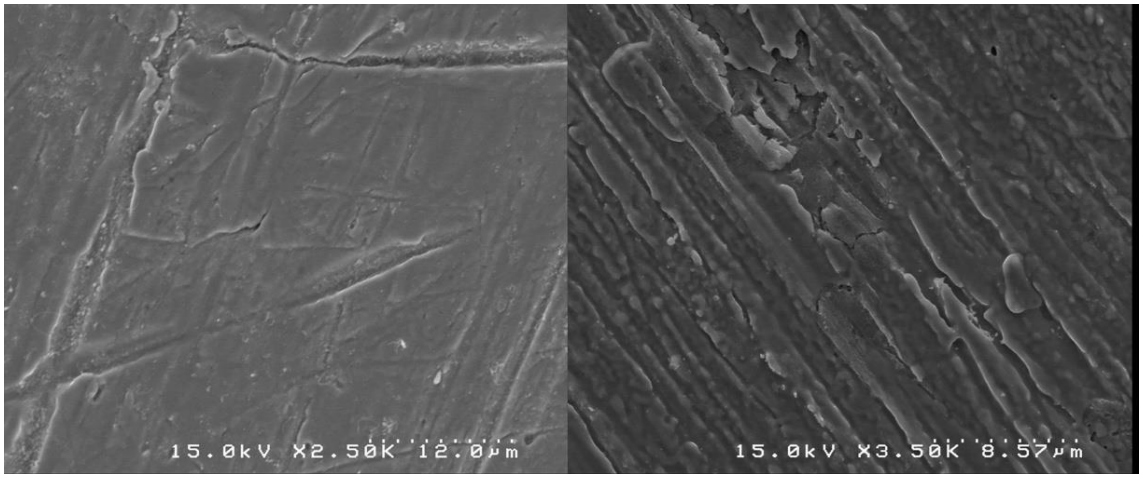

Figure 6.3: SEM images of an A series substrate (left) and a B series substrate (right) after the same CVD process.

Cu films deposited by sputtering on Si wafers (C series)

A Cu film of 400 nm of thickness was deposited on a silicon wafer with native oxide. Because of the thickness of the film, it was expected that diffusion induced by a thermal treatment could strongly modify the surface of the Cu film. The analysis by SEM demonstrates that a dewetting process of Cu occurred during the annealing step (figure 6.4a). The thermal treatment induced the diffusion of Cu atoms, which agglomerated into small droplets/islands of about 5 μm. Then, part of the silicon substrate remained exposed to the environment, the color of the sample turned grey, like the copper silicide, and the specular reflection disappeared because the surface became rough. Figure 6.4b also shows the presence of some crystallites with two preferential orientations.

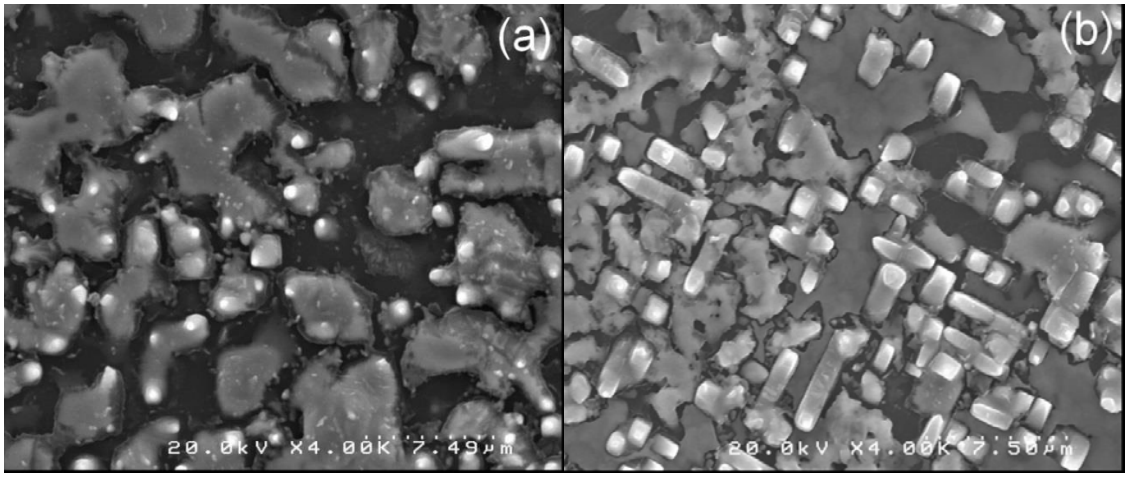

Figure 6.4: SEM image of a 400 nm sputtered Cu film on a c-Si wafer after the annealing process (figure 6.1). The temperature induced diffusion of Cu and it agglomerated in small droplets/islands of about 5 μm. The EDS results (figure 6.5) indicated the formation of a particular copper silicide compound ($Cu_{3.17}Si$) with crystallites that grew in the [011] and [0-11] crystallographic directions.

EDS: Cu films deposited by sputtering on Si wafers (C series)

In this kind of substrates the thermal treatment induced the diffusion of Cu atoms, which agglomerated into small droplets/islands. Figure 6.4b also shows the presence of some crystallites with two preferential orientations. Although not relevant for the main goal of this work, the

crystals were analyzed with the EDS in order to determine how the copper and the silicon wafer interacted with each other.

The results of the EDS indicated the formation of a particular copper silicide compound $Cu_{3.17}Si$ (figure 6.5). Apparently, Cu diffused inside the silicon substrate resulting in the formation of "nanobeams", which grew in the [011] and [0-11] crystallographic directions in the underlying silicon substrate. [9,10]

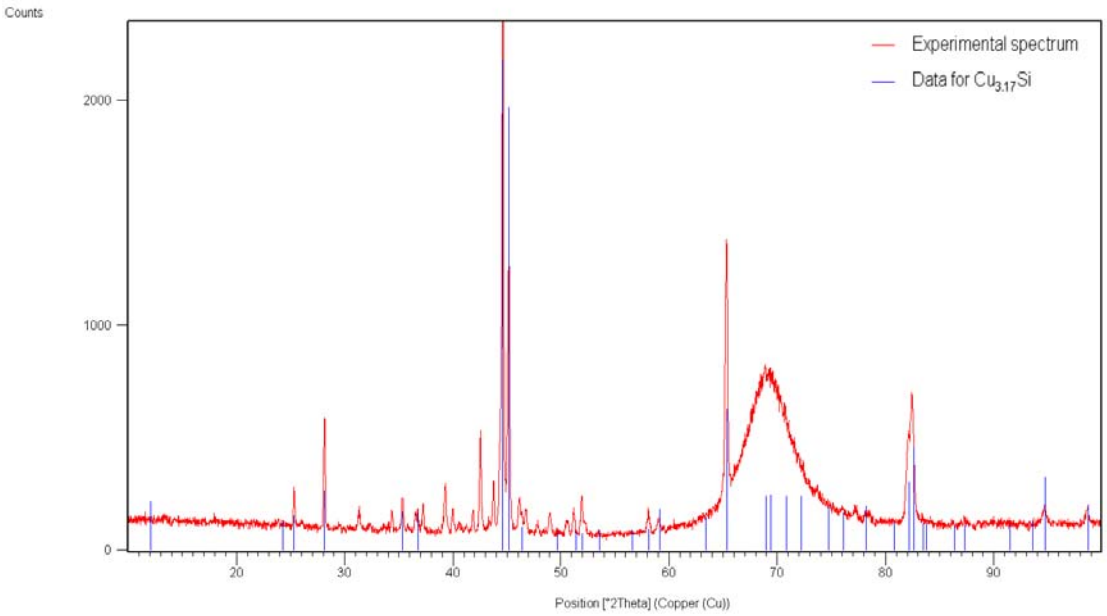

Figure 6.5: EDS spectrum of the sample shown in figure 6.4. The red line corresponds to the experimental spectrum and the blue lines correspond to the preset peak positions for the $Cu_{3.17}Si$ compound.

Once the effects of annealing were determined, the whole CVD process was performed. The SEM images of the final sample are shown in figure 6.6. Two different regions appear in the image: the darkest one with silicon, and the brightest one with copper silicide, both covered with carbon. Figure 6.9 shows the Raman spectrum of this sample, which confirms the presence of carbon in the two different regions. Nonetheless, most of the carbon films were amorphous and FLG grew locally only in dispersed locations. This kind of substrate also induced the combined growth of carbon nanotubes (CNT) and FLG, as shown in the SEM images (figure 6.6). This is not extraordinary because Cu is also a catalyst used for CNT growth.

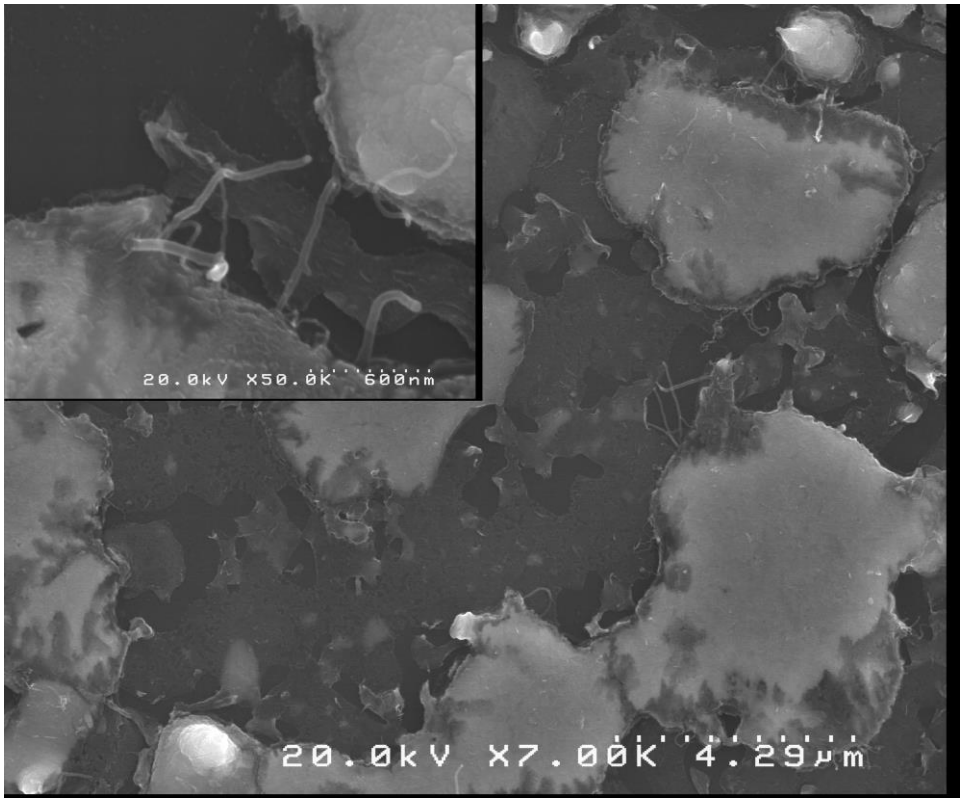

Figure 6.6: SEM images of a 400 nm sputtered Cu film (C series) after the CVD process. The inset in the top left corner shows the details of a combination of CNTs, amorphous carbon and, locally few-layer graphene in the same sample. See related Raman spectra in figure 6.9.

The CVD temperatures in graphene growth are very close to the melting temperature of Cu. This implies that significant evaporation of Cu occurs during the process, but the dewetting process can be avoided by increasing the thickness of the Cu films. However, as a recent work reports, if very thin Cu layers were used, dewetting and evaporation of the Cu could be controlled during or immediately after the CVD process by the direct deposition of carbon on the silicon substrate [9]. This can explain why in figure 6.6 there are films of carbon on the top of silicon. This could be interesting for the growth of graphene directly on silicon without the need to transfer it from Cu.

Also a 600-nm-thick Cu-coated silicon wafer with native oxide was tested. In principle, native oxide of sufficient thickness should hinder the Cu-Si diffusion. Moreover, a thicker Cu film could prevent the dewetting process. The successful growth of continuous films of graphene with the same Cu thickness and type of substrate has been reported [3]. However,

in this work, the results were similar to those of 400 nm Cu-coated Si wafer. Unlike in the previous work process [3], in this case, a 600 nm Cu film was insufficient for avoiding the dewetting process. Raman spectroscopy showed the presence of amorphous carbon from the shape of the spectrum. However, inspection of the sample by SEM also showed FLG flakes in some regions. Figure 6.7 shows a FLG or graphene layers suspended on the Si wafer.

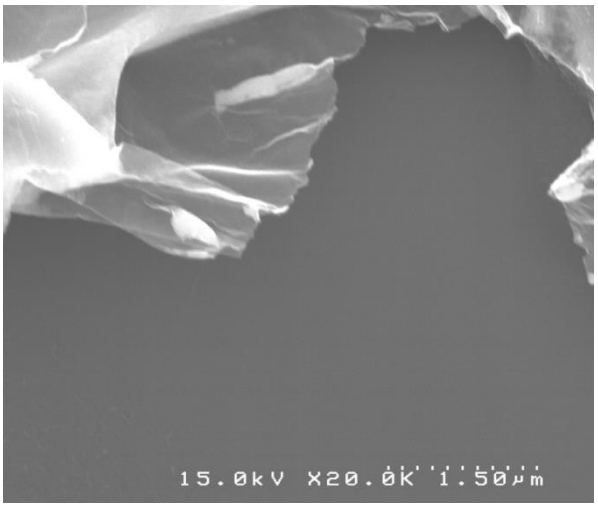

Figure 6.7: SEM image of the 600-nm-thick Cu-coated silicon wafer with native oxide (C series). The image was taken after the CVD process (11E1703), showing detachment of the layer from the silicon substrate.

Cu samples with diamond lapped surface (D series)

The results are for samples treated, again, under the same conditions as those shown in Table I. The SEM images of the samples without acid treatment (first row in figure 6.8) show a flat and smooth carbon layer, with a thickness of about 4-10 layers. The carbon film appears continuous and covers the entire surface with domains of few tens of μm in size. At some edges of these domains the carbon layers apparently overlap one on the other. This is consistent with the idea that carbon layers start to nucleate in some specific sites and then expand during the CVD process until they fully cover the Cu surface. [6]

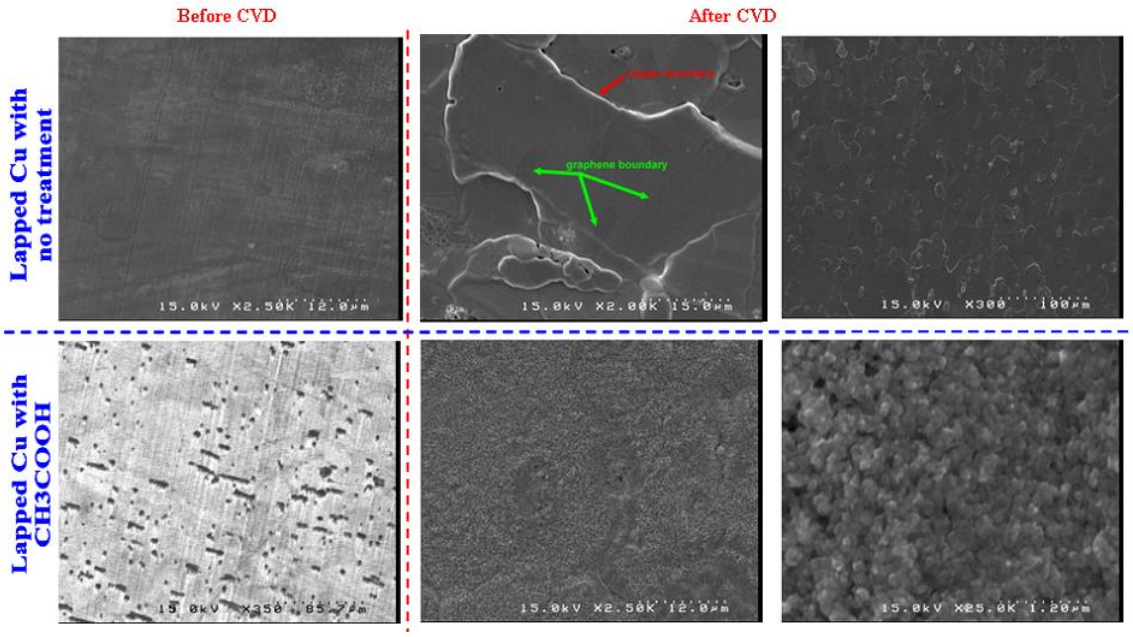

Figure 6.8: SEM images of D series substrates without (first row, 11D0501) and with (second row, 11D0502) acetic acid treatment, before (first column) and after (second and third columns) CVD process.

In order to verify the effect of the oxide layer on the process, the same conditions were used to grow graphene using the same type of substrate but pre-treated with acetic acid. After pre-treatment with acid, the specular surface disappeared. SEM images in figure 6.8 show the differences before and after the acid treatment. The acid dissolves the surface unevenly, and in regions where the oxide layer was initially thicker, holes appear. SEM images of samples treated with the acid after the CVD process are significantly different from those of the same samples with no treatment (figure 6.8). The surface is not smooth and small grains of the order of 100 nm are formed.

6.3.2. Raman spectroscopy

Cu films deposited by sputtering on Si wafers (C series)

Figure 6.9 shows the typical Raman spectrum of this type of samples, which confirms the presence of carbon (G peak around 1600 cm^{-1}) in the two different regions. Carbon peaks appear more intense in the regions where silicon is exposed to the environment than in the brighter zones of

copper silicide. However, the intensity and shape of the peaks point to a low crystallinity: The D peak (around 1350 cm^{-1}) has the same intensity as G, and both peaks are almost overlapped.

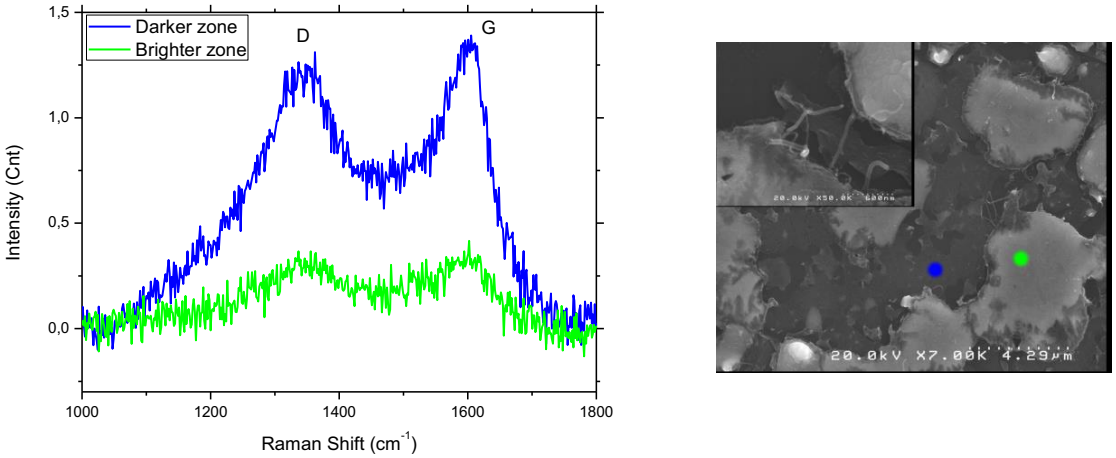

Figure 6.9: Raman spectrum of the figure 6.6 sample. The measurements were performed with 0.35 mW of incident power and 90 s of acquisition time. Blue line corresponds to the zones in figure 6.6 where the silicon substrate is exposed whereas green line corresponds to the brighter zones with copper silicide, whose chemical composition was previously analyzed with EDS.

Cu samples with diamond lapped surface (D series)

Figure 6.10 shows the Raman spectrum taken from the diamond lapped sample without acid treatment. D band indicates the presence of defects and the small I_{2D}/I_G ratio shows the existence of FLG. These results were obtained by the CVD process at 800-900 °C. The effects of lowering the processing temperature could explain why the obtained graphene is partially defective. [5]

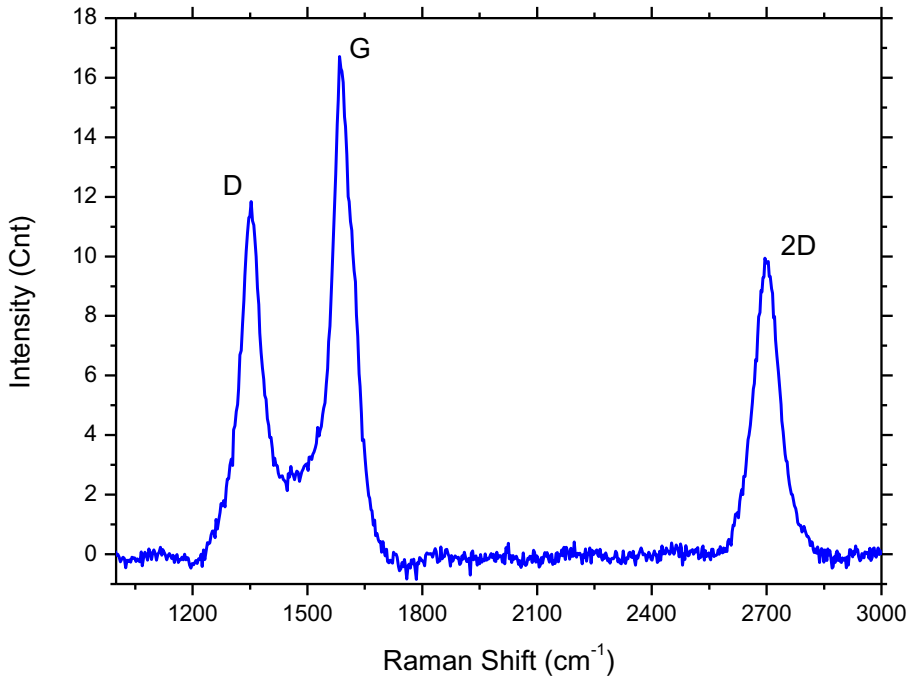

Figure 6.10: Raman spectrum of a D series sample (11E1704) without acid treatment. The measurement was performed at an incident power of 0.35 mW and for an acquisition time of 30 s.

After pre-treatment with acid, the samples changed substantially compared to the ones with no treatment (figure 6.8). The surface is not smooth and small grains of the order of 100 nm are formed. Raman analysis showed that the carbon of samples is amorphous, as expected from the SEM images.

6.4. Summary and conclusions

Although this work demonstrated the feasibility of few-layer graphene (FLG) growth by hot-wire CVD, there are differences between the graphene prepared in this work and that reported in the literature [6,11]. The nature of the copper substrates is probably the main reason in these differences. If the starting copper surface is too rough or it has crystalline defects, the carbon species would find too many nucleation sites, producing defects in the graphene layer. These defects can facilitate the formation of disordered islands of a-C, graphene multilayers, and other defective carbon structures on the surface of the copper. Therefore, a

method of optimizing the process could be decreasing the deposition time, which will be one of the important highlights of the method described in the next chapter. This should prevent the generation of excess of carbon and the formation of most disordered islands of a-C on the copper surface, facilitating the formation of monolayer graphene or high-quality FLG. Moreover, the copper substrates should be improved with purer, more crystalline, and flatter surfaces. The main conclusions obtained out of this preliminary work are shown below:

- The presence of pure, crystalline, and flat enough surface is needed for high-quality graphene layers.
- Thin sputtered Cu films (C series), which are amorphous but thick enough to avoid the complete diffusion and evaporation, proved to be useful for the successful deposition of carbon directly onto Si wafers. Although most of the carbon layers were amorphous, FLG grew locally in the form of flakes.
- Raman measurements showed the presence of FLG on bulk Cu substrates with a diamond lapped surface (D series). The D band suggests a low crystallinity of FLG sheets of about 4-10 layers. Taking into account the crystal domains of Cu, it was estimated an average domain of 10 μm for graphene. However, the properties of the obtained graphene can still be interesting for some applications like conductive and transparent electrodes, or protective coatings.
- The results also demonstrated the feasibility of the hot-wire heating to grow graphene on copper substrates and the use of acetylene for the growth process at lower temperatures.
- The understanding of the CVD extracted from this work was very relevant for the improvement of the method developed in the next Chapter 7, the Low-pressure Pulsed-CVD.

6.5. References

[1] V-M. Freire, J. Badia-Canal, C. Corbella, E. Pascual, E. Bertran, J-L. Andujar, *Hot-Wire Chemical Vapor Deposition of Few-Layer Graphene on Copper Substrates*, Jpn. J. Appl. Phys. 52, 01AK02 (2013).

[2] N. Benouattas, A. Mosser, A. Bouabellou, *Surface morphology and reaction at Cu/Si interface—Effect of native silicon suboxide*, Appl. Surf. Sci. 252, 7572 (2006).

[3] M.P. Levendorf, C.S. Ruiz-Vargas, S. Garg, J. Park, *Transfer-Free Batch Fabrication of Single Layer Graphene Transistors*, Nano Lett. 9 (12), 4479 (2009).

[4] L. Zhao, K.T. Rimb, H. Zhoua, R. Hea, T.F. Heinz, A. Pinczuk, G.W. Flynn, A.N. Pasupathy, *Influence of copper crystal surface on the CVD growth of large area monolayer graphene*, Solid State Commun. 151, 509 (2011).

[5] I. Vlassiouk, S. Smirnov, I. Ivanov, P.F. Fulvio, S. Dai, H. Meyer, M. Chi, D. Hensley, P. Datskos, N.V. Lavrik, *Electrical and thermal conductivity of low temperature CVD graphene: the effect of disorder*, Nanotechnology 22, 275716 (2011).

[6] X. Li, C.W. Magnuson, A. Venugopal, J. An, J.W. Suk, B. Han, M. Borysiak, W. Cai, A. Velamakanni, Y. Zhu, L. Fu, E.M. Vogel, E. Voelkl, L. Colombo, R.S. Ruoff, *Graphene Films with Large Domain Size by a Two-Step Chemical Vapor Deposition Process*, Nano Lett. 10, 4328 (2010).

[7] Y.H. Lee, J.H. Lee, *Scalable growth of free-standing graphene wafers with copper (Cu) catalyst on SiO_2/Si substrate: Thermal conductivity of the wafers*, Appl. Phys. Lett. 96, 083101 (2010).

[8] C. Miao, C. Zheng, O. Liang, Y.H. Xie (edited by S. Mikhailov), *Physics and Applications of Graphene - Experiments*, InTech, University of California, Los Angeles (2011).

[9] R. Clearfield, J.G. Railsback, R.C. Pearce, D.K. Hensley, J.D. Fowlkes, M. Fuentes, M.L. Simpson, P.D. Rack, A.V. Melechko, *Reactive solid-state dewetting of Cu–Ni films on silicon*, Appl. Phys. Lett. 97, 253101 (2010).

[10] A. Ismach, C. Druzgalski, S. Penwell, A. Schwartzberg, M. Zheng, A. Javey, J. Bokor, Y. Zhang, *Direct Chemical Vapor Deposition of Graphene on Dielectric Surfaces*, Nano Lett. 10, 1542 (2010).

[11] X. Li, W. Cai, L. Colombo, R.S. Ruoff, *Evolution of graphene growth on Ni and Cu by carbon isotope labeling*, Nano Lett. 9 (12), 4268 (2009).

Chapter 7

LOW-PRESSURE PULSED-CVD

7. Low-pressure Pulsed-CVD

Finally, and as the core of this thesis, the growth of monolayer graphene with a very Low-pressure Pulsed-CVD technique has been studied by means of a theoretical approach, the monolayer formation time, which has never been used before for this purpose. [1]

CVD of graphene using copper as a catalyst is one of the most promising technologies for producing high quality graphene for large areas. Nevertheless, still high pressures and big quantities of precursor gas are currently required. The objective, then, is to deposit graphene using the monolayer-formation-time concept (τ) from the kinetic theory of gases (explained in Chapter 3), which leads to an economization of the precursor gas, a minimization of the process pressure and the time needed to grow a graphene monolayer. All the process has been designed taking into account the dependence of τ on the pressure, the mass particle of the gas, the sticking coefficient, and the growth temperature.

7.1. Preparation of substrates

The principal metal catalyst used to grow graphene was copper, basically as thin layers made by sputtering, and in the form of foil. Both are presented in detail in this section.

Sputtered-Cu substrates

Copper is commonly used as a catalyst for the graphene growth in the copper foil shape. However, sputtered copper was also chosen because sputtering allows obtaining pristine and very smooth copper films with accurate control of thicknesses, and it is still poorly explored. Not much literature of sputtered copper has been published [2]. Copper films on c-Si wafers were deposited by magnetron sputtering.

As well as the CVD, the sputtering process for depositing Cu was performed in the *GRAPHMAN* reactor (figure 3.3). Cu films of 600 nm were deposited on 2" diameter and 300 μm thick <111> c-Si wafers. One could expect that the native SiO_2 layer of the c-Si wafer played an important role in limiting the diffusion of the Cu in Si when the sample is annealed [3]. However, a Ni diffusion barrier turned out to be much more

effective, because after annealing tests, samples with a Ni barrier of 100 nm successfully avoided a complete diffusion of Cu into Si. The sputtering process for the Ni thin layer was performed in *PEDRO* reactor (figure 3.9), because its sputter head allows changing the target much easily than *GRAPHMANs*, which is fixed. Figure 7.1 shows a sketch of the final cross-sectional appearance of the sputtered substrates.

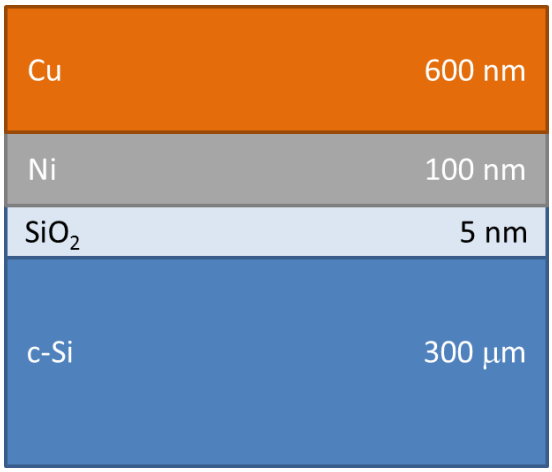

Figure 7.1: Cross-sectional schematic view (not in scale) of the substrate-catalyst of the sputtered samples: Sputtered Cu (nucleation layer) on top, an anti-diffusion layer of sputtered Ni, the native SiO_2 layer, and finally the monocrystalline Si wafer <111>.

A previous calibration of the Cu and Ni deposition rate was performed by profilometry (*DEKTAK*). The diameter of the metallic target of Cu was 3'', and we used a RF power of 100 W (the power supply available) and at 0.25 Pa of pure Ar (99.999%) to drive the plasma. A base pressure before the sputtering of ~10^{-3} Pa was always required. The pressure during the process was kept constant using an automatic conductance valve, and it was monitored by an absolute capacitance pressure meter. The substrate-target distance was 8 cm, which was selected to produce a homogenous film of Cu with a deposition rate of 72 nm/min.

Regarding the Ni deposition, the target was the same size as the Cu one, but the plasma was driven with an asymmetrical pulsed-DC power of 100 W at pulse frequency of 100 kHz, and a positive pulse of 2016 ns (80% negative duty cycle), at 1 Pa of Ar. The process pressure was also kept constant using conductance valve, and it was monitored by a capacitance

absolute pressure meter too. In this case, the substrate-target distance was 4 cm, which produced a homogenous layer of Ni with a deposition rate of 18 nm/min.

Substrate interactions (eutectica)

One of the main problems we found in our previous work with CVD, especially with the sputtered layer of Cu on c-Si, was the diffusion and dewetting between both surfaces during a high-temperature annealing (approx. 1000 °C). In principle, one could overcome the diffusion problem by increasing the thickness of the Cu layer, and the dewetting by reducing the process temperature; or even by adding an anti-diffusion layer of Ni between the Cu and c-Si, as seen in this chapter. One of the experiments consisted of the annealing of copper foil in contact with a portion of silicon. The temperature process was in that case 850 °C, which is clearly under the melting point of Cu (1083 °C) and also under the melting point of Si (1414 °C). The result of the experiment was the copper foil and the portion of silicon melted together, because of the formation of an eutectic alloy Cu/Si.

This phenomenon consists in the decrease of the melting point of a system formed by more than one solid component, below the melting point of the former components, as can be seen in the figure 7.2. The formation of the liquid phase in contact melting is initiated by mutual diffusion of the solid components, which causes the formation of supersaturated solid solutions or metastable intermetallic compounds at the contacts between interacting crystals. These intermetallics pass into the liquid phase rather easily (compared to the separated metals), which corresponds to a more profitable energy state of the system. [4]

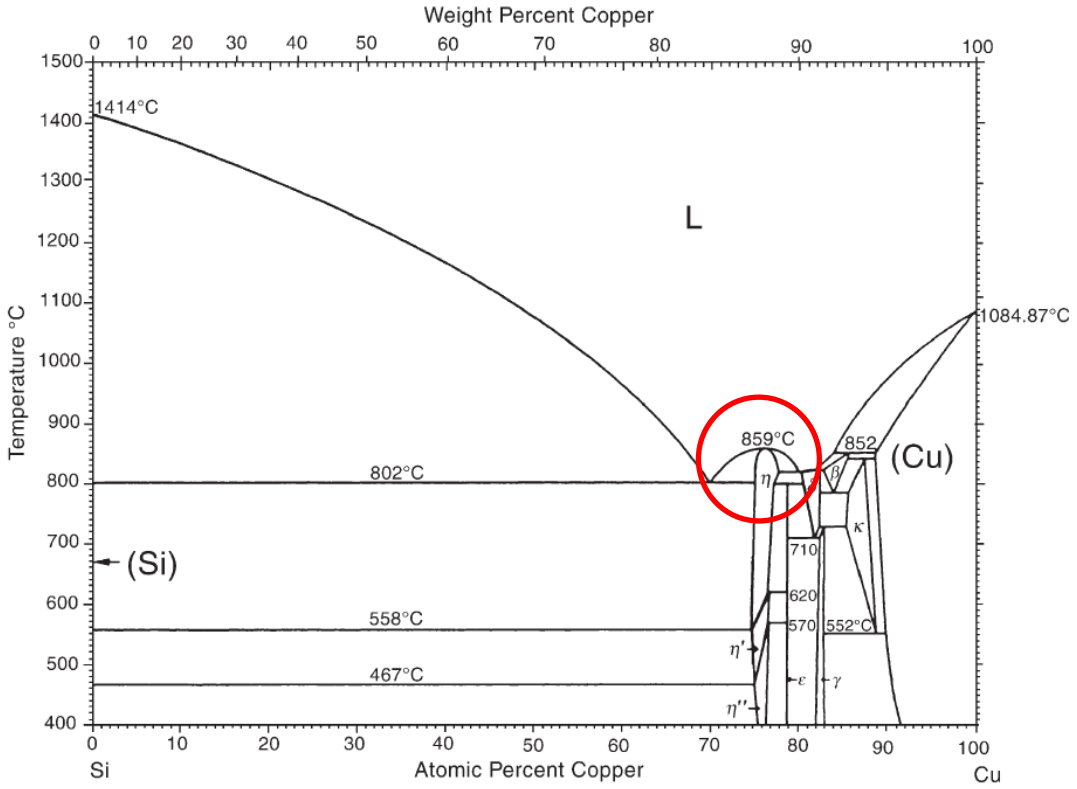

Figure 7.2: Cu–Si phase diagram regarding their atomic and weight percentage and their melting point. [5] The silicide formed in our samples is the $Cu_{3.17}Si$, and its ~76 at.% of Cu locates the melting point at 802-859 °C (red circle).

Another viewpoint binds the formation of the liquid phase at eutectic melting due to the adsorptive interaction between atoms at the interface, or force fields in the contact region of crystals. According to this model, eutectic melting is preceded by the formation of a metastable strained epitaxial layer at the interface between the solid particles in contact, which is the reason for the decrease in melting points [4]. In addition, there is the problem concerning the direction of the diffusion flux at the moment when the liquid phase has already formed at the interface with the solids. It is assumed that the dissolution of solid metal in the liquid occurs by means of atoms passing from the surface of the solid phase into the liquid phase and their diffusion carry-off into the melt, away from the interface. But on the contrary, other models imply the decisive role of the diffusion of atoms from the liquid phase into the solid phase. [6]

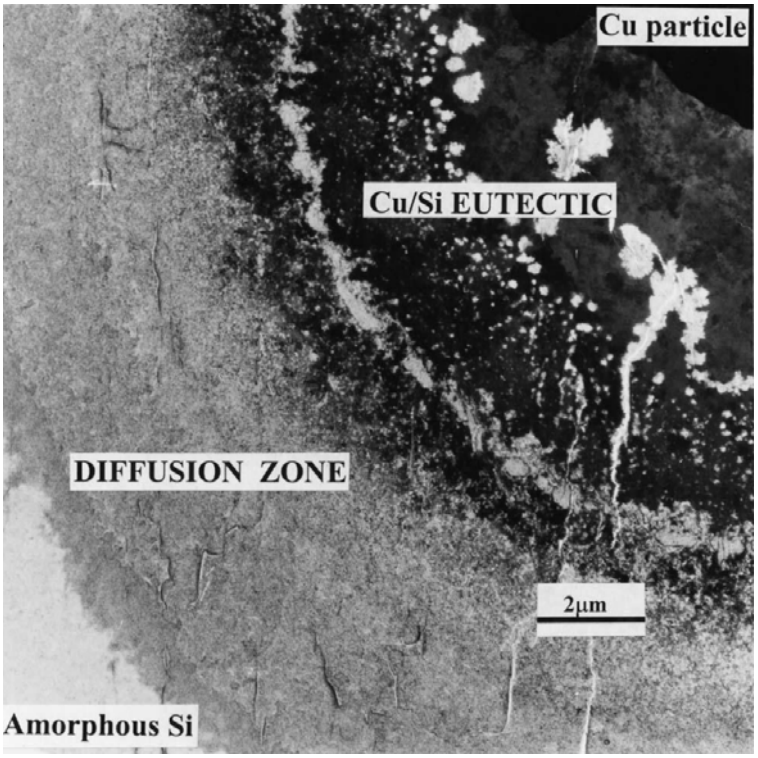

Figure 7.3: Electron micrograph of the diffusion zone and eutectic alloy formed during the interaction of copper particles (microcrystals) with an amorphous silicon film under isothermal conditions (T = 810 °C). [4]

This phenomenon does not appear for all the materials, but in our case it does, making the melting point of the system decrease to 802-859 °C [7] due to the $Cu_{3.17}Si$ silicide formation (see Chapter 6); this temperature is clearly below the melting point of the Cu and the Si (figure 7.2). The formation of an eutectic Ni/Si is also possible, having a melting point of 964 °C [8], which is definitely below the Ni melting point (1455 °C), but it is much less noticeable than the Cu case due to its higher eutectic formation temperature. This experiment forced us to design the experiments depositing Cu layers thicker than 500 nm and with a Ni thin layer of 100 nm under the copper. The main reason is that after the formation of the alloy, the melted Cu/Si can get inside the thicker Si wafer avoiding the carbon atoms to deposit in the graphene form.

However, the formation of an eutectic Cu/Si opens the possibility of having high surface mobility of atoms at relatively low temperatures of 800-900 °C, which can facilitate the correct placement of carbon atoms and the formation of graphene (as we will see in the next sections) by the presence of Cu exposed to methane at temperatures above its

decomposition (cracking of methane without catalyst can start at temperatures above 700 °C, under non oxidative environment).

Copper foils

Apart from the sputtered copper substrates, which were the most frequently used, the CVD processes were performed with copper foils as well. These foils are easy to handle, there is no specific preparation needed, and they are also economically cost-effective. Moreover, they do not undergo the eutectic phenomenon, as well as any diffusion or dewetting effect.

The thicknesses of the copper foils used were 3 and 5 mil (*mil* is a thousandth of an inch), or 76.2 and 127 μm respectively, and they have a purity of 99.90% (copper alloy 110, 0.04% of oxygen). The foils were supplied by *BasicCopper.com*. Although they were already smoothed and annealed, a simple thermal treatment was applied to the copper foils. This kind of substrates allows annealing the copper before the CVD process during much more time, 15-20 min at 950-1000 °C, rather than our sputtered copper on silicon with a maximum of 10 min due to diffusion.

Furthermore, in the final experiments of this work, we used other precursor gases than methane (CH_4) or acetylene (C_2H_2), which constitute the standard precursors for CVD-graphene. Hydrocarbons like Benzene (C_6H_6) or Toluene ($C_6H_5CH_3$) have a reasonable resemblance with the hexagonal shape of graphene and lower pyrolysis temperatures, permitting also lower the temperature process [9,10]. These tests were performed only with copper foil as a substrate/catalyst.

7.2. Growth process

Normally, the most relevant parameters in a standard CVD process are: pressure, flow rate of the reactant gases, substrate temperature and substrate surface (roughness, composition, crystallinity…). Several recipes to grow CVD-graphene have been reported in previous publications [11-14]. However, in this work we used a very Low-pressure Pulsed-CVD method based on the monolayer formation time concept. (see Chapter 3)

On the assumption that every molecule will stick to the surface (S = 1), working temperatures of 1273 K (1000 °C), and using methane (CH_4) as a precursor gas, one-atom thick layer of carbon spread onto a surface can be formed in a time defined by:

$$\tau = \frac{2.1\times10^{-3}}{\mathrm{P}} \tag{3.5}$$

This equation means that a monolayer formation time only depends on the pressure of the precursor gas. Thus, for a ~2x10^{-3} Pa of methane, the monolayer formation time would be ~1 s. From now on and in the case of methane, the pulses will have a pressure of ~10^{-4} Pa and, thus, a monolayer formation time of around ~10 s.

Once the pressure and the process time were estimated, we placed the substrates in the CVD quartz tube of the reactor, which was pumped down until a base pressure of ~10^{-5} Pa was achieved. The first step in the CVD process consisted of a linear temperature ramp of the cylindrical oven with a heating rate of 25 °C/min up to the process temperature reaches 970-1000 °C, the annealing temperature. Methane decomposes at temperatures above 527 °C [15], so the methane CVD processes must be performed at this minimum temperature.

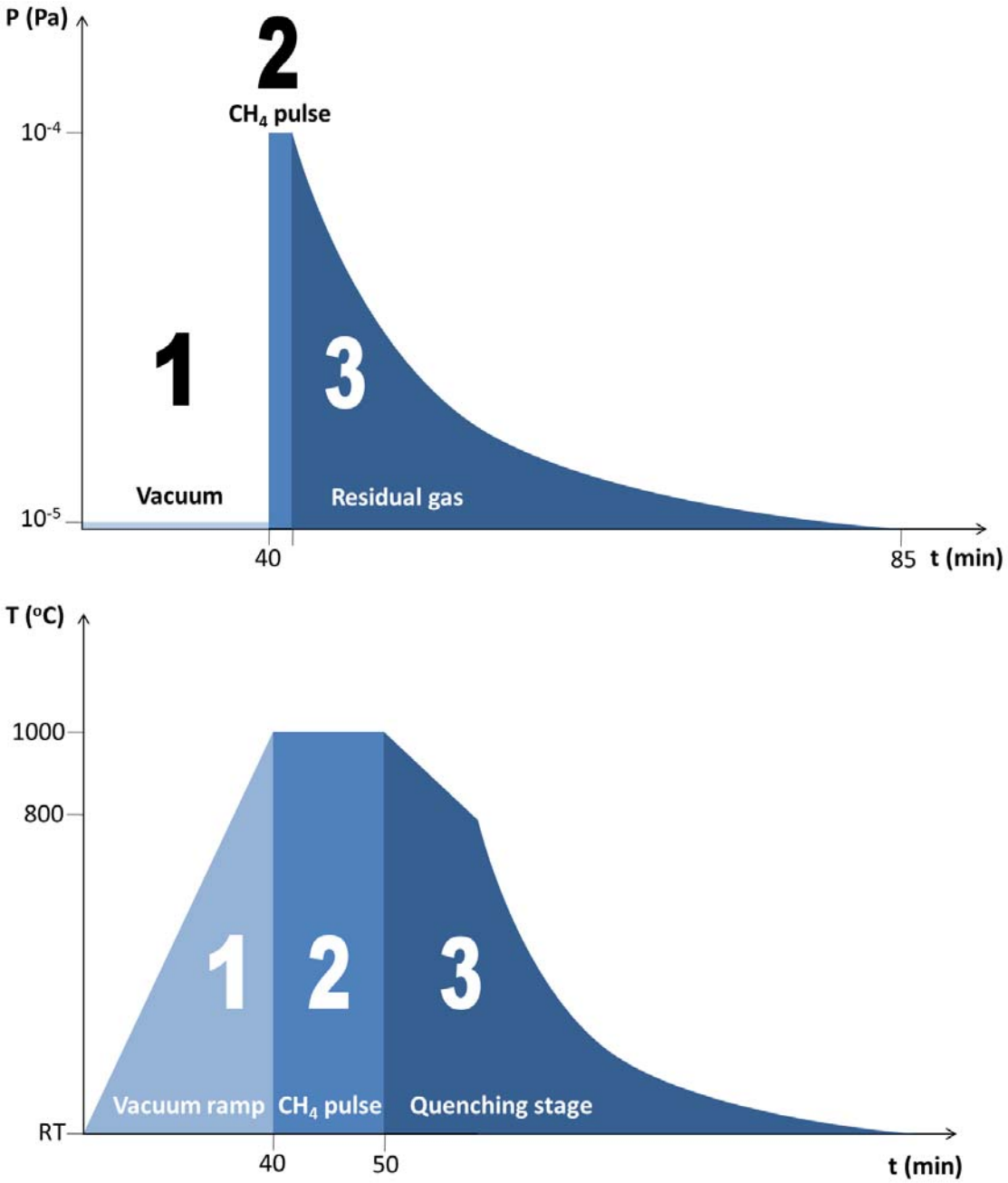

Figure 7.4: (Up) P(t) diagram of the whole Pulsed-CVD process (not in scale). In the Step (1) the reactor is under HV conditions while a linear ramp temperature up to 1000 °C is applied during 40 min, the Step (2) corresponds to the instantaneous release of a CH_4 pulse of 10^{-4} Pa during 10 s, and the final Step (3) only with the residual gas and the quenching stage to room temperature (RT) during 45 min. (Down) T(t) diagram of the whole Pulsed-CVD process (not in scale). The Step (1) corresponds to the linear ramp under HV. The second Step (2) represents the annealing stage (e.g. 10 min) just before the pulse of the precursor gas. And the final Step (3), where the quenching stage has two parts: a slowest first part until 800 °C, and a second moderately fast until RT.

The CVD process started once the substrate reached the process temperature and after a short annealing stage of 5-10 min, the methane was then introduced in the chamber under a controlled pulse of ~10^{-4} Pa of pressure. Figure 7.4 shows a P(t) diagram of the entire process. Under these conditions, surface temperature of the substrate induces the decomposition of the methane molecules in different radical species, which become adsorbed, whereas the rest of by-products are pumped down. During the process, H_2 can be introduced to catalyze the reaction (reducing the copper oxide present on copper, which is not suitable as a catalyst) and to drag the by-products (radicals). However, the reductive action of hydrogen exposure at high temperature is known to efficiently etch graphene and to limit its growth. A hydrogen atmosphere is also expected to suppress carbon enrichment at high temperature at the defect sites in copper, thus allowing to efficiently inhibit carbon segregation [16]. The etching effect of a constant hydrogen flux over the silicon oxide (reduction) during the annealing also triggered a lift-off process of the sputtered films of Cu, destroying the substrate with its catalytic effect and limiting dramatically the graphene growth for the low-pressures used in this work. Finally, the CVD process ended with a cooling down to room temperature by switching off the oven.

We have observed that quality of graphene depends on the quenching curve too. Fast-cooling processes (sudden and forced) have been used to suppress the excess of precipitated carbon. However, this process still yields films with a wide range of graphene layer thicknesses, from one to a few tens of layers and with defects associated with fast cooling [17]. Slow cooling (free cooling to RT, negative exponential) induces the total diffusion of the carbon atoms deep into the bulk catalyst, leaving nothing on the surface; and medium cooling (combination of both) led to graphene. Therefore, we opened the oven cover when the CVD chamber achieved a temperature of 800 °C (see figure 7.4 (down)). From that point, the quenching time reduced to half an hour. Several samples were produced by means of the above described process. See the details in Table II and Table III.

7.2.1. CVD Pulses

The complete CVD process and the methane pulse was monitored by a Residual Gas Analyzer (SRS RGA300), a quadrupolar mass spectrometer (QMS) attached to the reactor. It allows measuring simultaneously the partial pressures of up to 10 gases inside the chamber by means of the relation *m/q* (see Chapter 3)*;* and actually, it was the only way to confirm the shape and pressure of the pulse, as well as its composition.

The surface temperature of the substrate during the CVD induces the decomposition of the precursor gas. In the case of methane (CH_4), it decomposes not only in carbon and hydrogen, also a series of different radical species (CH_3, CH_2, CH, and C) appeared, which become adsorbed and desorbed in the catalyst surface, whereas the gas pumping removes the rest of by-products. Actually, the most probable and abundant radical is the CH_3.

The screen capture of the QMS controller in figure 7.5 (up), shows some of the radical species involved in the process; it can be seen the whole family of methane (including carbon) and the pulsed-shape of the release of the gas (figure 7.5 (down)), confirming that the carbon presence in the reactor indeed came from the precursor gas with the previously calculated pressure of ~10^{-4} Pa (~10^{-3} mTorr). These radicals are present among other typical but less significant compounds inside the reactor like N_2, H_2O, O_2, and H_2. It is important to comment that although the pulse is just one order of magnitude above the base pressure, which means that 1 of every 10 molecules present is unwanted, species like N_2, H_2O and O_2 do not affect the main reactions that take place and the final quality of graphene. In addition, they are extremely difficult to remove completely by the pumping system.

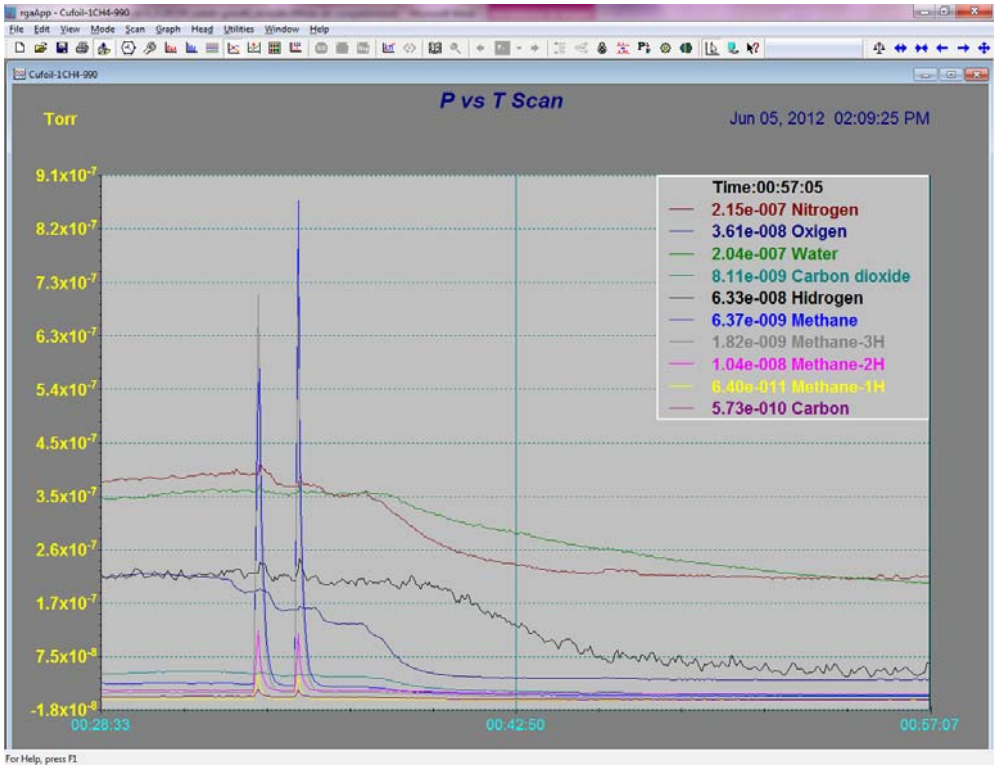

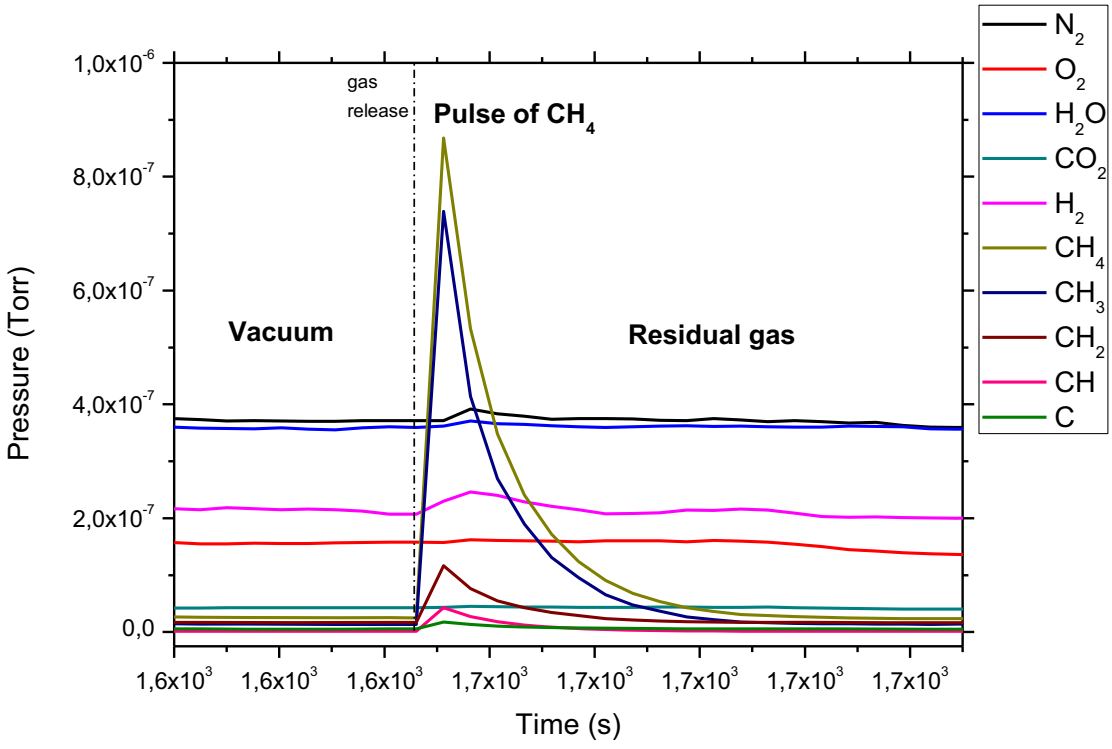

Figure 7.5: (Up) Screen capture of the QMS controller, rgaApp, with two consecutive pulses of methane. (Down) Plot representing one methane pulse in detail with its decomposition in the different radicals due to the temperature: CH_3, CH_2, CH, and C; also the presence of other common gases as H_2, N_2, H_2O, O_2, are represented. The pressure of the methane pulse is ~10^{-3} mTorr (~10^{-4} Pa).

During the annealing and the CVD, the hydrogen can play an important role catalyzing the reaction; it reduces most of the copper oxide present on copper (much less catalytic effect), and it drags the by-products (radicals) of the CVD reaction. Figure 7.6 plots a simultaneous pulse of both gases, methane and hydrogen, at the same time.

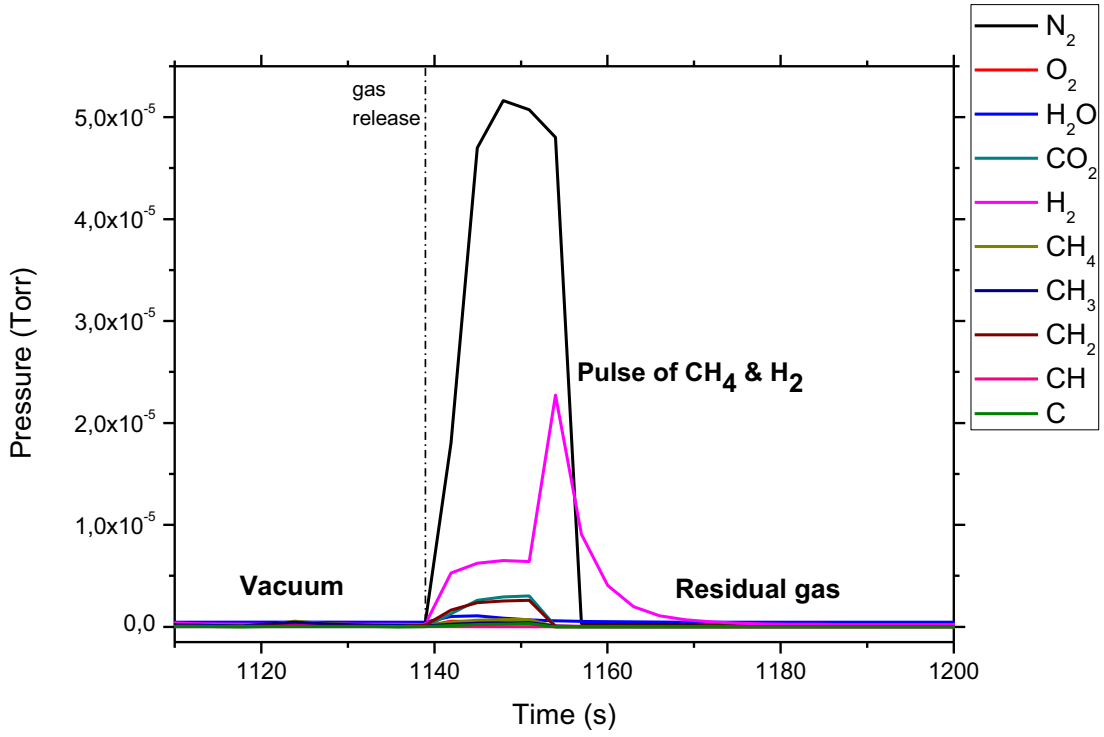

Figure 7.6: Graph of the simultaneous release a of CH_4 and H_2 pulse (from the QMS controller).

7.2.2. Scaling parameters

Once the deposition method and the equipment were determined, a series of experiments were performed to set up the most important graphene-dependent variables: the thickness of the Cu/Ni film (in the case of the sputtered substrates), the temperature of the process, the annealing time, the precursor gas, the pressure of the pulse(s), and the presence of hydrogen during the different steps of the process.

7.3. Samples

Sputtered Samples

Graphene was produced by Low-pressure Pulsed-CVD on Cu and Si (uncovered parts due to the Cu dewetting) as described before. The study of the Cu/Ni catalyst and graphene layers deposition consisted on a morphological surface characterization by optical microscopy and SEM; and a chemical/structural surface analysis by EDS and Raman spectroscopy. The Table II is a summary of some representative samples of this work:

TABLE II. Sputtered samples details

Sample	Temperature (°C)	Substrate	# Layers	# Pulses of CH_4 (10^{-4} Pa)
1 (12E1002)	980	Cu	1	1
2 (12E1002)	980	Si	1	1
3 (12E1501)	990	Cu	2	1
4 (12E1504)	980	Si	1	4 (with H_2)
5 (12E1502)	1000	Cu	1	1

Copper foils

Graphene and FLG were also produced by the same method as the sputtered samples described before. However, two major differences were tested: the precursor gases and process temperature, which are coupled parameters. Benzene (C_6H_6) and Toluene ($C_6H_5CH_3$) have a reasonable resemblance (chemical and structural) with the hexagonal shape of graphene acting as preferred nucleation seeds, and permit lower the temperature process due to their lower pyrolysis temperatures (500-600 °C) too.

Different mass (precursor gas) and temperature will lead to a different monolayer formation time equation. Again we will assume that every molecule will stick to the surface (S = 1, common value in most of metals [18]), and the new working temperatures of 823 K (550 °C). The mass of the next precursor gas used was benzene, then, $m_{C6H6}=6m_C+6m_H$. Thus, from equation 3.4, a SLG formation time can be redefined by:

$$\tau_B = 3.4\times10^{8}\frac{\sqrt{mT}}{SP} = \frac{3.5\times10^{-3}}{\mathrm{P}} \tag{7.1}$$

And in the case of Toluene ($C_6H_5CH_3$ or C_7H_8), with a mass of $m_{C7H8}=7m_C+8m_H$, and the same temperature as Benzene, 550 °C:

$$\tau_T = \frac{3.8\times10^{-3}}{\mathrm{P}} \tag{7.2}$$

Therefore, a Low-pressure Pulsed-CVD process under a ~3x10^{-3} Pa of benzene or toluene would have a monolayer formation time of graphene of only ~1 s. Nevertheless, benzene and toluene are liquid precursors, what means that only the vapor phase is profitable. As their vapor pressure is at least one order of magnitude higher than ~3x10^{-3} Pa, the monolayer formation time will be one order of magnitude smaller; probably too small taking into account the exhausting time of the pump. To overcome this problem, a minimum of 3 pulses will be delivered; although the precursor bottle can also be cooled down.

The Cu foil and the graphene layers deposited were studied by means of a morphological surface characterization with optical microscopy and SEM; and a chemical/structural surface analysis by Raman spectroscopy. The EDS analysis was discarded since the manufacturer ensured a purity of 99.9% of Cu in the foils. The Table III summarizes some of these samples:

TABLE III. Cu foil samples details

Sample	**Temperature (°C)**	**Precursor gas**	**# Layers**	**# Pulses of gas (Pa)**
6 (13L0401)	1000	CH_4	1	4 (~10^{-4} Pa)
7 (14B0603)	550	C_6H_6	2	3 (0.06 Pa)
8 (14C1402)	550	C_7H_8	FLG	4 (0.02 Pa)

7.3.1. Optical microscopy

Sputtered samples

The graphene/Cu/Ni/c-Si multi-layer evolution at different annealing times is shown in the optical microscope pictures of figure 7.7. The annealing was done under HV conditions during the CVD stage, when the process temperature is achieved but just before the gas pulse. This kind of study had already been done in Cu thin films [19]; the novelty in our case is the presence of Ni.

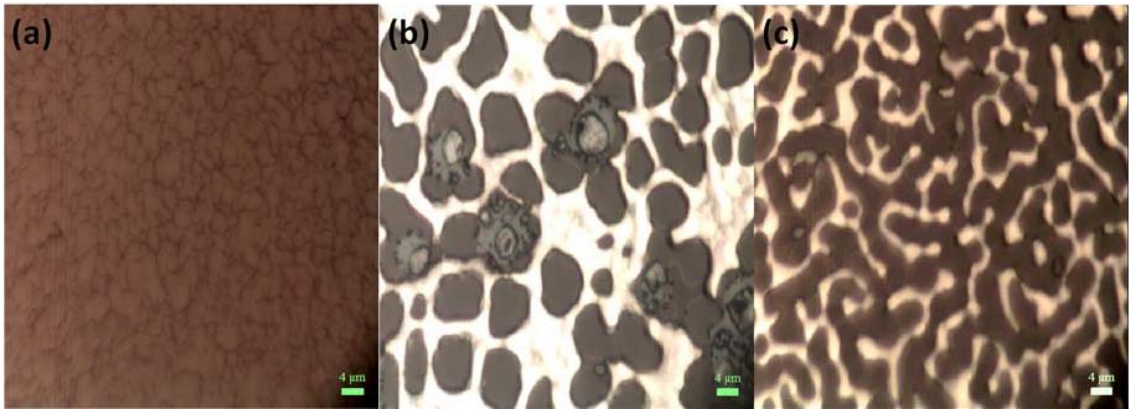

Figure 7.7: The optical images show the effect of the different annealing times at 980 °C on the bilayer Cu/Ni deposited on c-Si wafers. The image (a) corresponds to an annealing time of 2 min, (b) annealing time of 7 min, and (c) annealing time of 10 min (samples 12E3001, 12E1001, and 12E1002 respectively). Graphene was present in all these three substrates (see next sections).

The figure 7.7 shows the effect of the different annealing times: 2, 7, and 10 min carried out at 980 °C. A continuous and uniform surface of copper crystals appears for 2 min of annealing or less. For longer times copper crystals begin significantly to evaporate and both metallic phases separate dewetting in copper islands and droplets of nickel (both shown as brighter parts), while the silicon substrate smoothly uncovers and becomes visible (darker parts). From the EDS analysis that it will be detailed later, we can identify the composition of the structures shown in these images.

Copper foils

Substantially different is the annealing in the case of the copper foils. Being a much thicker substrate (76.2 or 127 μm) and not having influence

of a back-substrate made of silicon, allows a standard thermal treatment without side effects like dewetting or diffusion. We can see the results of the annealing/CVD in figure 7.8.

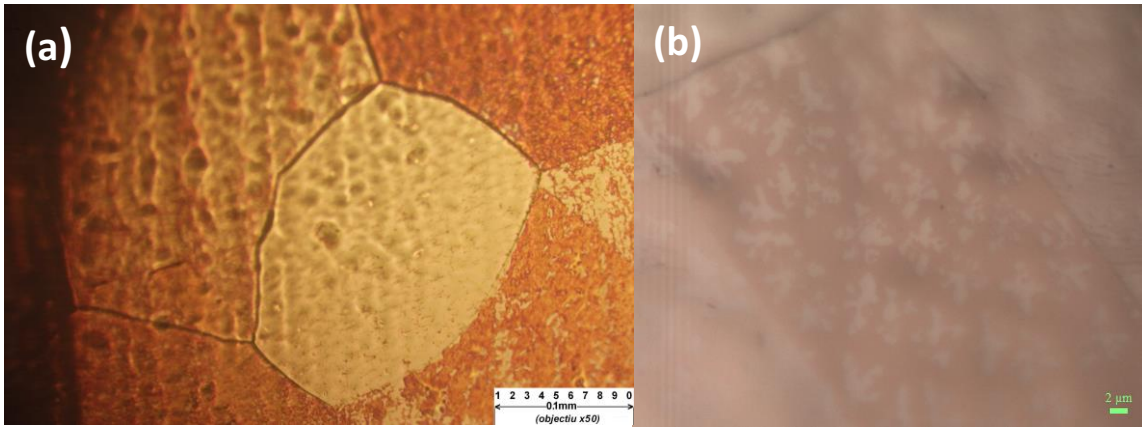

Figure 7.8: Optical images of the surface of the copper foils after the annealing and CVD process. (a) The copper crystals grow randomly oriented during the annealing separated by cracks. The right image (b) shows in detail the graphene dendrites in specific domains.

The crystal domains can be clearly seen in both images of figure 7.8. Figure 7.8a corresponds to copper crystal domains randomly oriented; different crystallographic orientations affect the oxidation rate of copper (different range of colors) and the subsequent growth of graphene. Although graphene is present in all the copper foil (confirmed by SEM and Raman in the next sections), the dendritic growth is only noticeable in some domains (figure 7.8b). The graphene dendrites obtained have already been reported, and are very similar to the ones found in literature. [20,21]

7.3.2. AFM

AFM was probably the key technique to demonstrate that the first obtained graphene (by mechanical exfoliation) was, in fact, a single layer of atoms of carbon. Due to the interaction substrate-graphene of the samples obtained by mechanical exfoliation on silicon, it was reasonably easy to measure the step height between the Si/SiO_2 and a SLG, or a SLG folding. However, when it comes to CVD graphene, the presence of a metallic catalyst under the sample complicates most of the

characterization, as well as the absence of the optical cavity (SiO_2) that enhances the optical contrast. CVD graphene is normally continuous or presents a dendritic shape, which makes it really difficult to localize and detect optically a SLG, moreover taking into account the low optical contrast between copper and graphene.

That is why AFM was used only to explore the surface of the Cu sputtered substrates after the CVD process. The shape and size of the Cu crystals shown before (optically) are confirmed in figure 7.9. This 3D AFM image plots the Cu nucleation islands due to the sputtering process and the thermal treatment at 950-1000 °C.

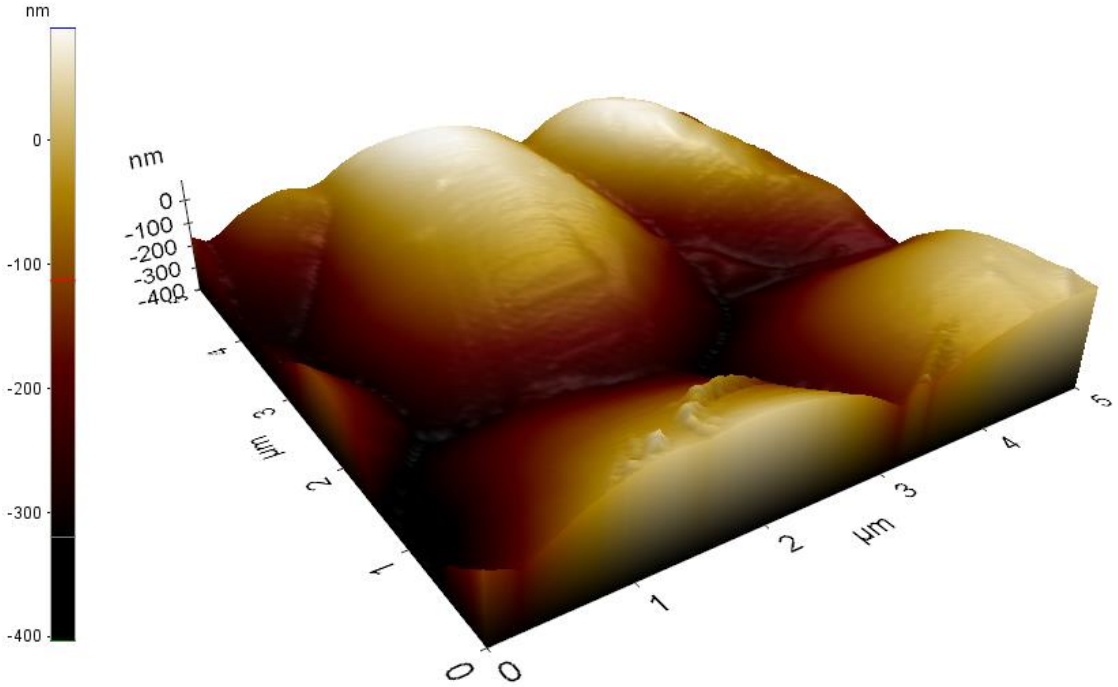

Figure 7.9: 3D AFM image with the sputtered Cu/Ni/Si surface in detail, while graphene is on top. The image was acquired with the Park XE-70 AFM in non-contact mode.

As it will be demonstrated in the next sections (EDS, SEM and Raman spectroscopy), graphene is more likely to grow in the valleys (dark parts of the figure 7.9), where the silicon begins to get uncovered due to the dewetting process during the annealing. That is probably because, once the catalytic effect of the copper has ended, the copper retracts forming islands, and the grown graphene rests on the visible silicon.

7.3.3. EDS

We performed EDS in the SEM setup in order to identify the chemical composition of the different structures obtained by sputtering the copper and nickel on silicon, during 30 s for the metals and 60 s for the silicon. The dewetting phenomenon was shown before in the preliminary observation by optical microscope in figure 7.7, it was evidenced later by SEM, and it was finally analyzed by EDS (figure 7.10). From these spectra we concluded that the zones are mainly composed of Cu, Ni, and Si. By correlating every SEM image with the corresponding spectrum, the continuous phase (bright color) corresponds to Cu, the dark zones correspond to Si substrate, and Ni appears forming clusters (bright color too) separated inside the Si zones and completely separated from the Cu phase. Although Ni is also a common catalyst to grow graphene, the Ni clusters separated from the Cu phase present a less quantity of carbon deposited, what probably makes this Ni-structure not optimal for the growth of graphene.

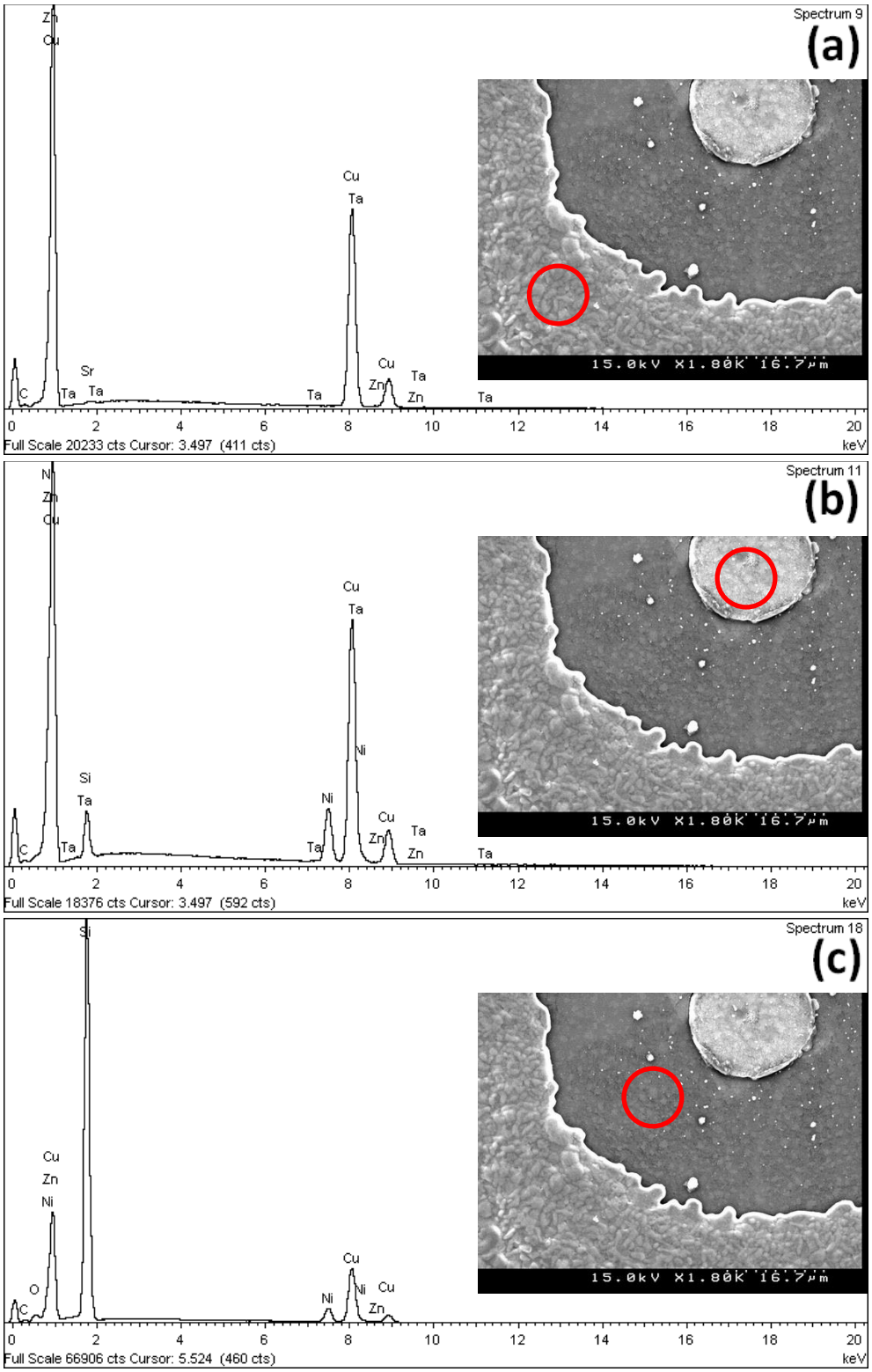

Figure 7.10: EDS analysis performed on the uniform regions of the sputtered Cu/Ni/Si samples of figure 7.7, with the areas of interest (red circle) shown in detail in the SEM insets. The plot (a) shows the EDS performed on the bright areas (Cu), the graph (b) corresponds to the clusters (Ni), and graph (c) shows the EDS performed on the dark areas (Si). Spectra acquired with the Jeol JSM 840.

The graphs of figure 7.10 show the elemental composition present in each zone of the sputtered samples after the process. A small amount of carbon appears in all the tests, which is consistent with the idea of a completely-covered sample by graphene. Although part of this carbon could be "adventitious carbon", Raman confirmed the presence of graphene. The atomic and mass percentage of carbon was quantified by the *INCA* software of the Oxford Link ISIS EDS at an electron accelerating voltage of 20 kV, and is, respectively (a) 22.02% and 0.98% on copper, (b) 16.02% and 1.01% on nickel, and (c) 16.24% and 2.04% on silicon.

Spectra (b) and (c) indicate the presence of impurities, probably because the annealing has not completely separated the phases of the different elements present on the surface. Another explanation is that the minimum area that can be measured by the EDS is 10 μm^2, what means that the analysis could also be wider than the "real" selected zone, including surrounding elements. Other impurities present in all the spectra, such as Zn and Ta, may come from the target (Zn is usually used with Cu as an alloy), or even from the sputtering head.

7.3.4. SEM

Sputtered copper

The SEM inspection is complementary to the optical pictures if we want to explore the result of the substrate and the detection of graphene nucleation sites. The SEM image of figure 7.11 shows the effect of the 10 min annealing time carried out at 980 °C. The continuous phase (bright color) corresponds to Cu crystals, the dark zones correspond to Si substrate, and Ni (bright color too) appears forming clusters (from 1-5 μm) completely separated from the Cu phase and inside the Si areas. This image shows the dewetting isolating a Ni island and the graphene growth on Si; it also shows how the graphene wrinkles formed on graphene terraces overlap. This process usually takes place during annealing/CVD of the Cu/Ni bilayer previously sputtered on c-Si. These images give an estimate of the quality of graphene: continuity, uniformity and the number of layers; and how the layers and the wrinkles take the form of the boundaries of Cu crystals.

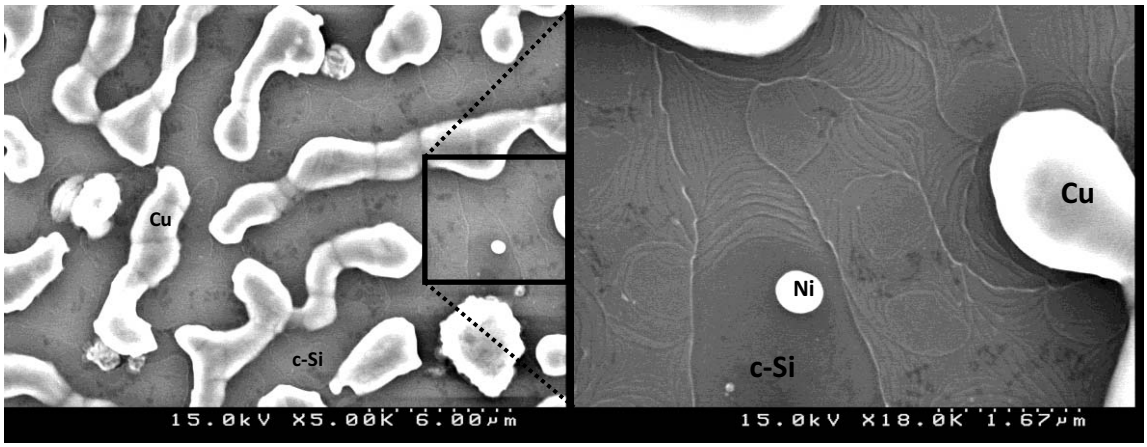

Figure 7.11: SEM image of a graphene sample. This image shows again the dewetting of the Cu/Ni bilayer: Cu crystals (bright), a Ni island (also bright), and the graphene terraces grown on Si (dark). The chemical composition of the three main zones was confirmed by the EDS (figure 7.10), and the presence of graphene by Raman spectroscopy. The annealing was performed during the CVD stage at 980 °C during 10 min.

Graphene appeared continuous and covered almost the entire surface with domains of few tens of μm in size. In some edges of these domains the graphene layers apparently overlap one on the other (figure 7.11). This is consistent with the idea that carbon layers start to nucleate in some specific sites and then expand during the CVD process until fully covering the Cu surface [12]. In the zones where the Cu is still forming crystals, dendritic growth is also frequent, as shown in figure 7.12.

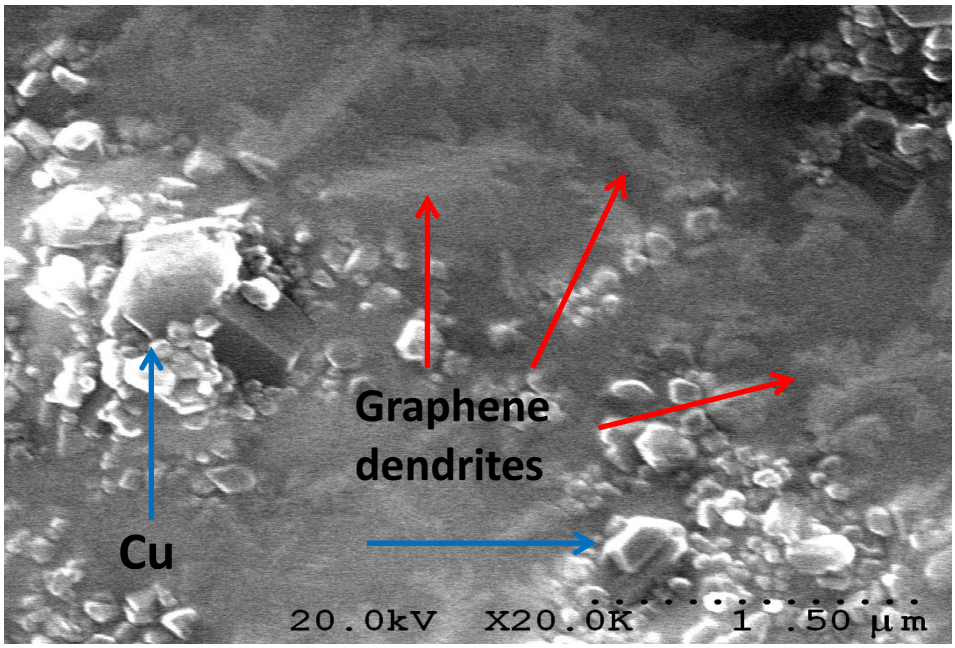

Figure 7.12: SEM detail of the dendritic growth of graphene on Si and also between the Cu crystals. Image from Hitachi S2300 field emission SEM.

The graphene on Cu has normally more layers than the graphene present on Si. This is because, first graphene grows on Cu and later, upon evaporation during annealing/CVD of Cu, graphene is transferred onto bare Si areas. In this process, the carbon could be rearranged, increasing 2D peak, which appeared as a reduction in the number of layers; and reducing D peak, a reduction in the defects, as we will see in the Raman section.

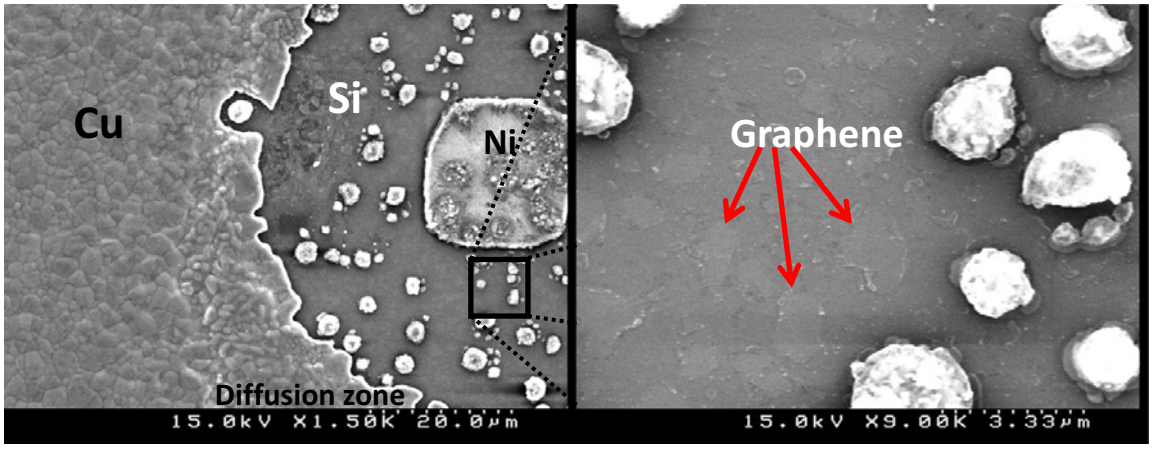

Figure 7.13: These SEM images show the dewetting surrounding a Ni island and the graphene growth on Si; the right image is a magnification of the left image. In this sample, the annealing was performed during 4 min at 980 °C before the CVD. Graphene grains can be observed in both images. Here, it can be clearly seen the eutectic alloy Cu/Si with its diffusion zone.

Several research papers [11,19,22-25] have reported that wrinkles like those shown in our SEM images are folds of graphene and the slightly darker areas are additional graphene layers. However, SEM is not a reliable method to estimate the real number of graphene layers. The presence of foldings and wrinkles means, then, that the graphene grown by this method still has some defects, as indicated by the Raman spectrum and a D peak fairly significant (figure 7.17).

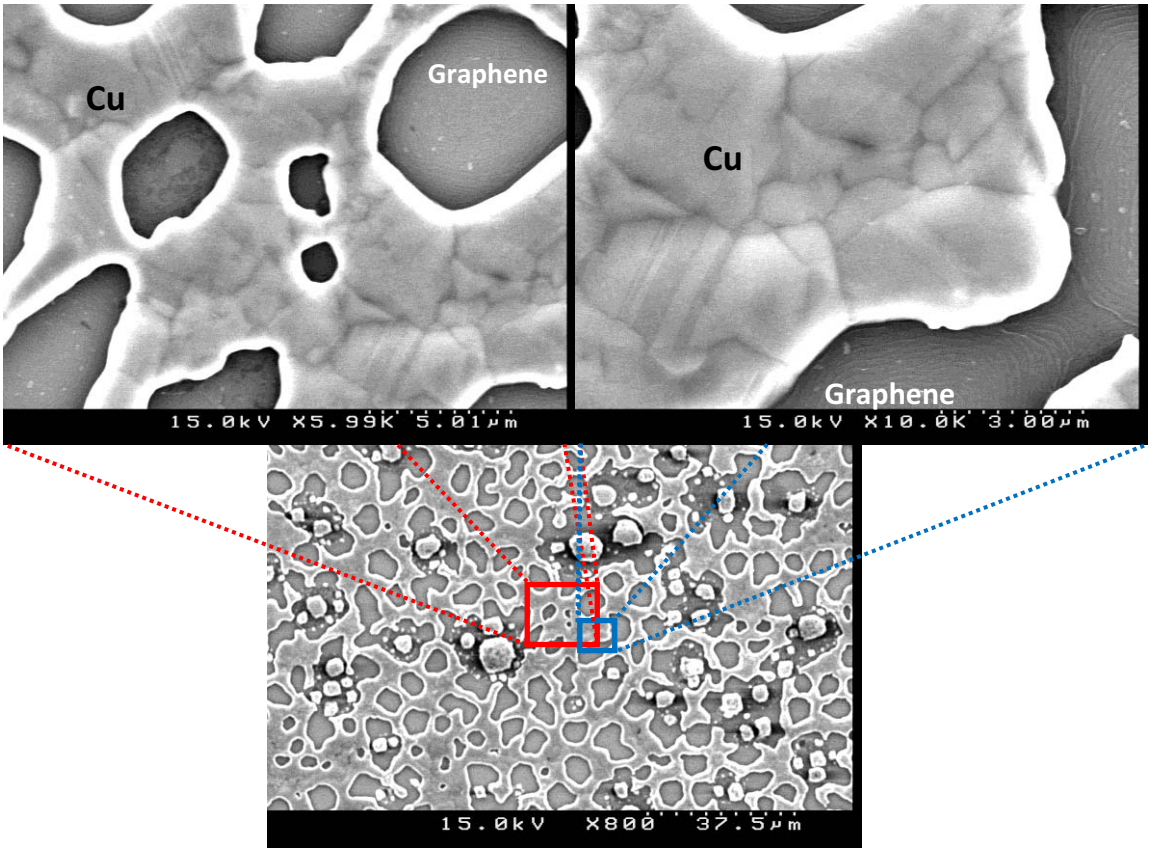

Figure 7.14: SEM images of graphene grown by CVD on the sputtered Cu/Ni on c-Si. The CVD process was carried out at 980 °C after a 7 min annealing. These images correspond to sample (b) of figure 7.7. In the magnified images, the formation of graphene terraces can be clearly observed. Also, how the graphene wrinkles formed on graphene terraces overlap.

Copper foils

In the case of Cu foils, the figure 7.15a presents a Cu surface with a smoother look, while the crystal domains are much bigger than those of the sputtered samples. The crystallography of the domains is also randomly oriented but still allows growing SLG. The figure 7.15b (right)

confirms that the graphene growth on Cu foil is mainly dendritic-shaped (nucleation points) regardless of the domain.

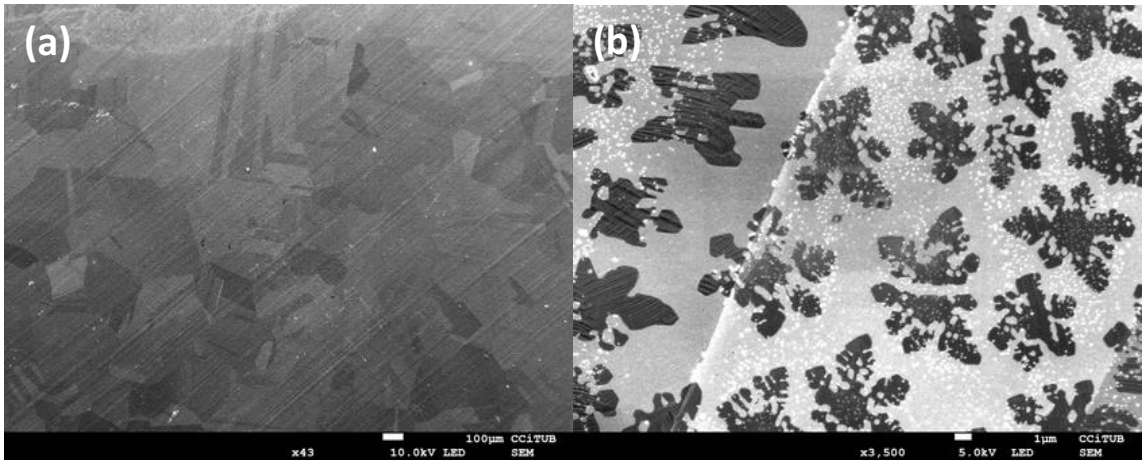

Figure 7.15: SEM images of the surface of the copper foils after the annealing and the CVD process. (a) The copper crystals grow randomly oriented during the annealing, notice the big sizes of the domains. The right image (b) shows in detail the graphene dendrites even growing in different domains.

7.3.5. RAMAN spectroscopy

Sputtered copper

The Raman spectra were obtained with the Jobin Yvon LabRam HR 800 and a green laser of 532 nm. These spectra were taken at arbitrary points of the samples after graphene CVD process with an acquisition time of 30 s. The ratio between D peak versus G peak intensities (I_D/I_G) evaluates the amount of defects, and the ratio between 2D peak versus G peak intensity (I_{2D}/I_G) gives an estimate of the number of graphene layers [26,27]. The exact position of peaks should also be taken into account because the peak position varies depending on the substrate (whether the graphene is on Cu or Si) and growth temperature, which makes more difficult the theoretical fit.

A typical SLG Raman spectrum is plotted in figure 7.16. The 2D peak is big enough (in intensity) than G (actually is around 4 times). As we can see, D peak is remarkable because the graphene deposited on Si has wrinkles and is polycrystalline. The influence of the inhomogeneous substrate/catalyst or the randomly oriented crystals of Cu is also a possible explanation.

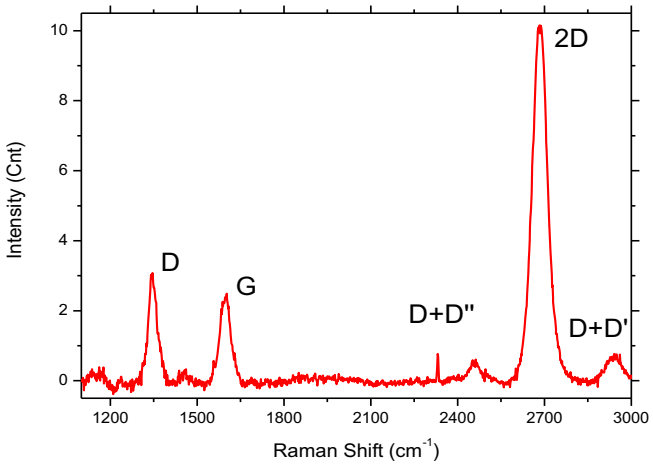

Figure 7.16: Raman spectrum of a graphene monolayer of sample 2 (Si). It was acquired with a 532 nm laser, 3.3 mW of power and an acquisition time of 30 s. The 2D peak is approximately four times the G peak, which corresponds to monolayer graphene [28]. Still a small amount of defects can be observed probably due to the non-flat surface of the sputtered substrates.

The more representative samples are summarized in Table II, and the related spectra are plotted in figure 7.17. All of them have a 2D peak comparable or bigger than G, which demonstrates the effectiveness of the method to synthesize SLG and BLG (bilayer graphene) on this kind of substrates, both on the parts covered by Cu, and on the Si zones. However, the presence of defects, still comparable to G is somehow constant probably because of the grain formation in the annealed sputtered surfaces. This suggests that an improvement of the process and the substrates treatment is still possible/factible.

There is, however, a major difference in the graphene spectra acquired directly on Si (mechanical exfoliation) and the spectra from a CVD grown graphene on Cu. The fluorescence created by Cu because of the Raman signal, adds a substantial baseline to the graphene spectrum adding also new peaks, overlapping the measured region. This problem can be alleviated by decreasing the laser intensity. This, and the subsequent treatment to remove this baseline and reveal the real spectrum of graphene, decreases the signal-to-noise ratio.

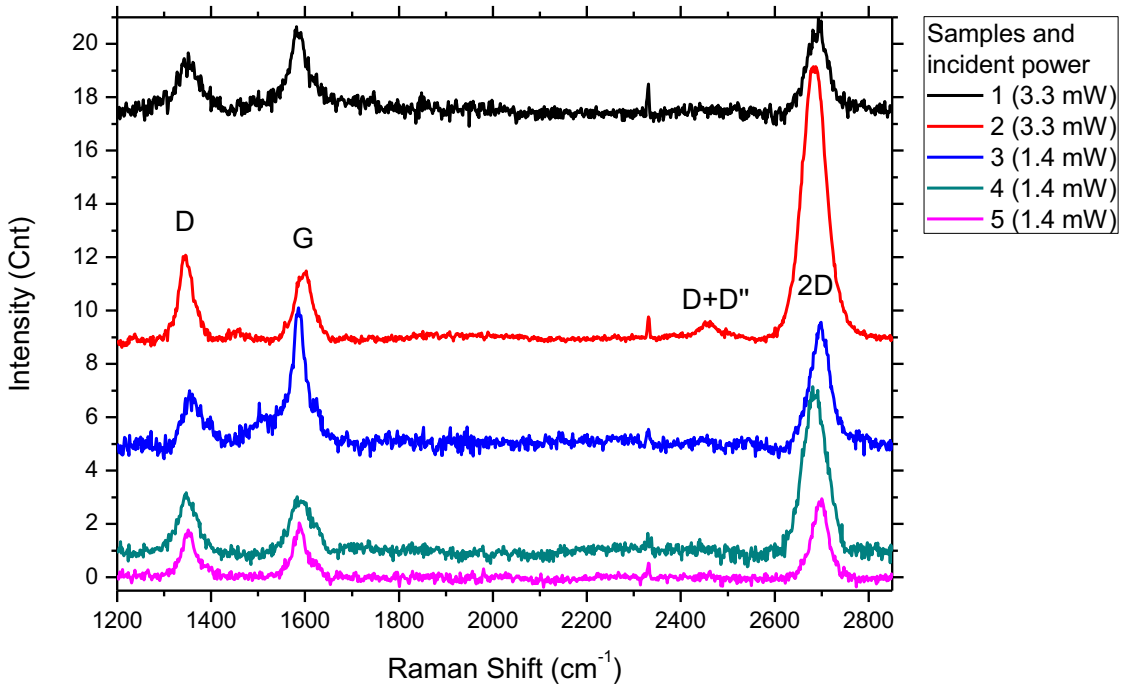

Figure 7.17: Collection of Raman spectra of the Table II samples including the incident power. The acquisition time for all the spectra is always 30 s, and the 2D/G ratio is always ≥1, which confirms the presence of mono and bi-layer graphene.

In figures 7.18 and 7.19 graphene on Cu was studied by means of confocal microscopy and Raman mapping. Figure 7.18 plots mappings of the peak intensities. It shows that the 2D peak of graphene is non-zero almost everywhere on Cu crystals. The images showing the intensity of graphene peaks, G and 2D, as well as their ratio, I_{2D}/I_G are the most significant ones, because they reflect the number of graphene layers depending on the position.

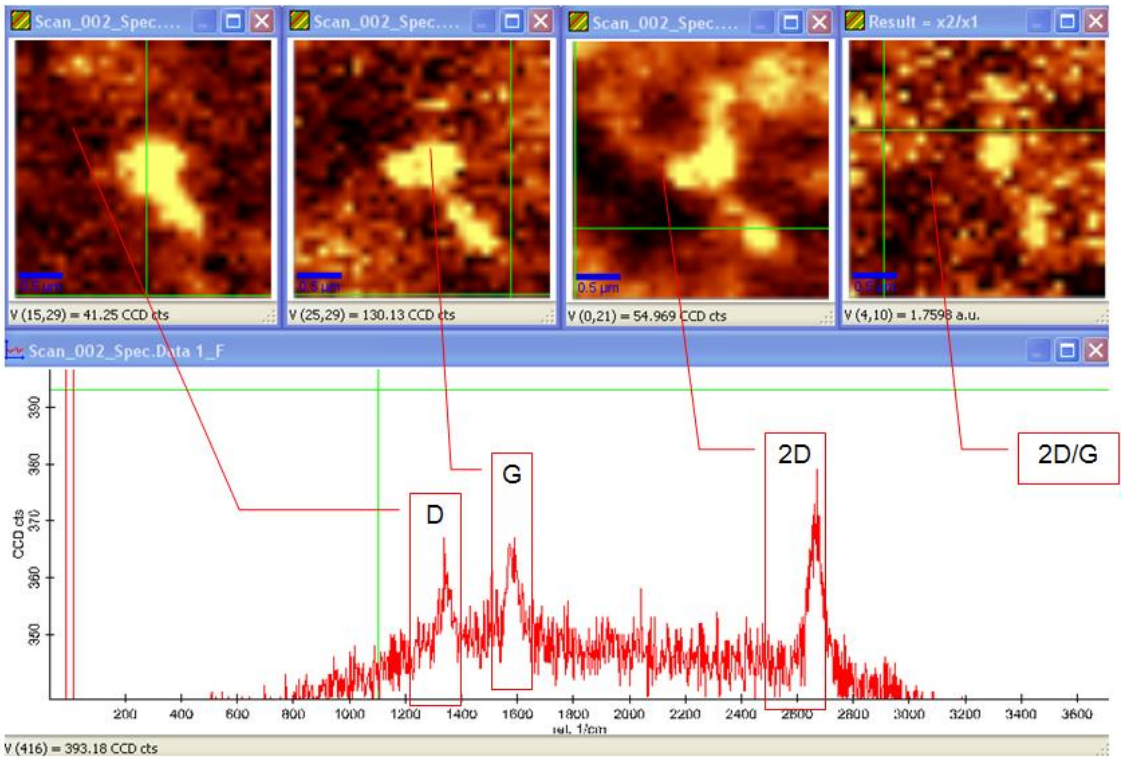

Figure 7.18: Raman mapping of the intensities of every independent peak of the sample 12E1501: D, G, and 2D. And finally a mapping of the intensity ratio between 2D/G: the most important parameter to confirm the number of graphene layers. The smooth baseline is due to the fluorescence of Cu.

In figure 7.19, graphene on Cu/Ni/Si is studied by means of Raman mapping with its ratio I_{2D}/I_G. This image shows the number of graphene layers depending on the position. The domains of graphene on polycrystalline Si (valleys/cracks) reach a dimension of 50 μm^2, while the domain areas of graphene on polycrystalline Cu (islands) are greater than 1 mm^2. If one compares this picture with the corresponding image obtained with the confocal microscope, less graphene layers are observed on the borders of the Cu crystals.

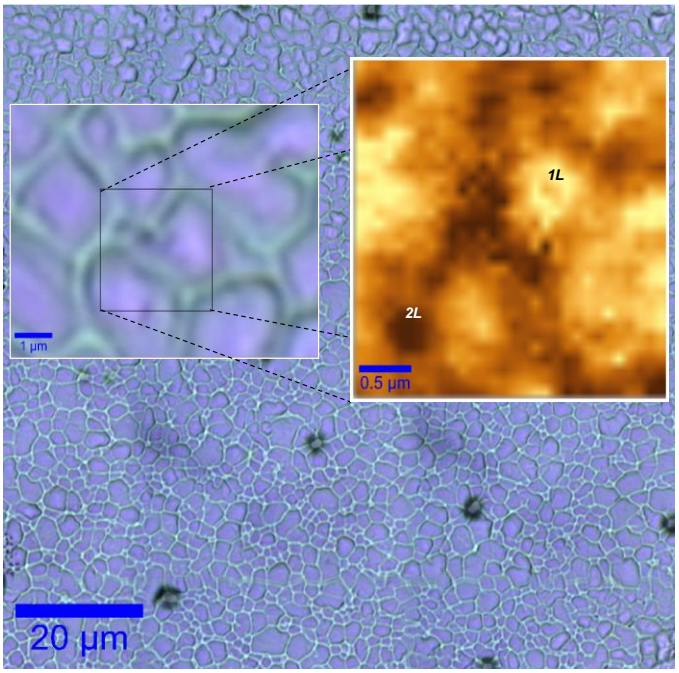

Figure 7.19: Image composition of the confocal view of the sample 12E1501 with the corresponding Raman mapping acquired with the Witec Raman microscope. The intensity ratio between 2D and G peaks is depicted with >1 (monolayer graphene - yellow), and ~1 (bilayer graphene - dark brown). Most of the surface (~80%) is covered by monolayer graphene (1L, yellow) and the rest by bilayer graphene (2L, dark brown).

Copper foils

When it comes to the Cu foil, the fluorescence issue increased substantially, as well as the decrease of the signal-to-noise ratio. This is because the Cu foils are way thicker than the films deposited by sputtering (76.2-127 μm of the Cu foil against 600 nm of the sputtered layers). However, the system still allows detecting enough Raman signal without too much interference.

The spectrum of figure 7.20 corresponds to a SLG grown on Cu foil using CH_4 as a precursor gas, and the CVD process was carried out at 1000 °C. The almost inexistent D peak confirms the idea that: having a flat and homogeneous catalyst surface, and a process temperature high enough, suppress the defects on graphene, as stated previously in Chapter 6.

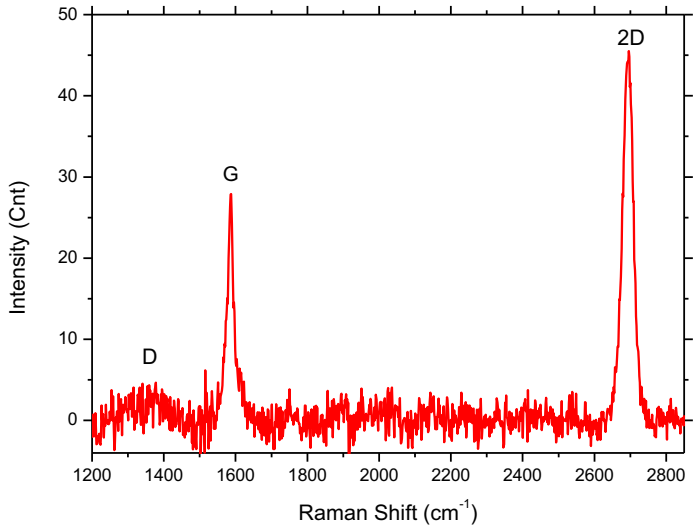

Figure 7.20: Raman spectrum of a CVD SLG deposited on Cu foil using methane (CH_4) as a precursor gas. The D peak, fairly insignificant, denotes the low defects of the graphene grown, and it is consistent with the idea of a flatter and more homogeneous surfaces of the Cu foil instead of the Cu-sputtered ones.

Regarding the graphene grown using Benzene and Toluene as precursor gases over Cu foil, the Raman results are plotted in figure 7.21. The Low-pressure Pulsed-CVD showed fairly effective to deposit graphene/FLG with Benzene. Nevertheless, the too high deposition rate (due to the six atoms of carbon per molecule, related to a very fast monolayer formation time) and the low process temperature (550 °C) led to an excess of carbon deposited on Cu, and to an excess of defects in the synthesized layer.

Not that effective was the deposition of graphene using Toluene. The even higher deposition rate of this precursor gas, caused the deposition of FLG or graphite with more defects too. Nonetheless, the experiments carried out with these precursors opened an interesting window by using liquid precursors that can lower the process temperature dramatically. Thus, further work is encouraged in this direction.

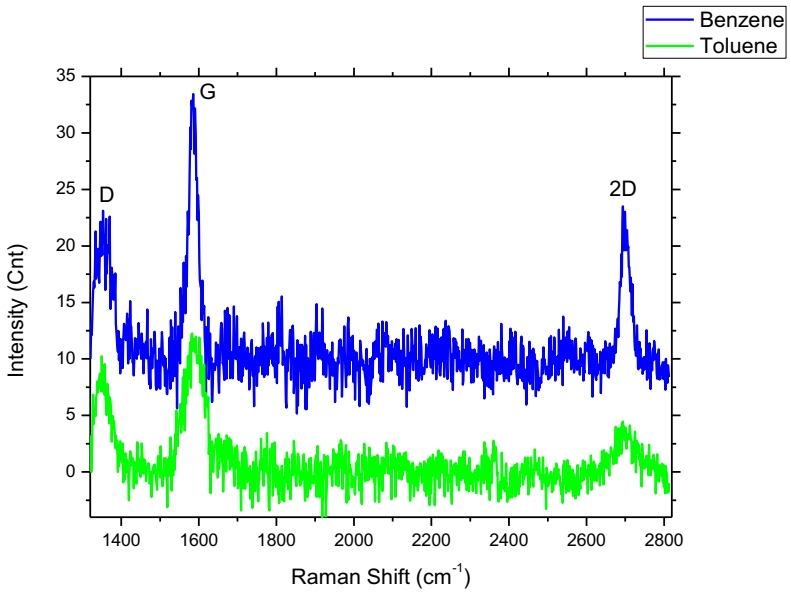

Figure 7.21: Raman spectra of graphene/FLG CVD deposited on Cu foil using benzene (C_6H_6) and toluene ($C_6H_5CH_3$) as precursors. In the case of benzene and due to the shape of the 2D we can confirm the presence of bilayer or FLG; but for toluene, the spectrum obtained reflects the presence of FLG or even graphite.

7.4. Transfer to silicon

It is well known that graphene on copper permits only a basic characterization of the samples: like SEM, Raman, EDS, or in the best of cases TEM (transmission electron microscopy). Moreover, it drastically reduces the amount of possible applications. For that reason, the transfer of graphene from the metallic catalyst (still necessary for any CVD process) to any insulating substrate becomes a crucial step in the total process chain.

In our case, the intermediate insulating substrate chosen was the polymer Polymethyl methacrylate (PMMA), mr-I 75K300, from *Micro Resist Technology*. The experimental steps are described as follows:

1) The surface of the graphene on a sputtered Cu/Si or on a Cu foil must be coated with the resist. For that purpose a spin coater (*POLOS*) was used in order to cover the surface homogeneously. Regarding the manufacturer, a speed of ω = 3000 rpm would led to a 30 nm thick layer of PMMA. That means that the polymer would be extremely thin, it will easily break or decompose as well as it will be difficult to take. In order to obtain a 1-5 μm of

thickness, we applied a speed of $\omega =$ 500-1000 rpm with a ramp of 500 rpm/s during t = 40 s.

As reported elsewhere, other works used the variety 996K of the PMMA, which allows having a more accurate control of the thickness of the layer since we could obtain a 10/15 μm with 500 rpm, or 3 μm with 1000 rpm.

2) Once the spin coater finished, the samples were taken and dried a minimum of 1 h. An optional pre-bake of 0.5-1 h at 95-100 °C can be done to make it faster or more efficient.

3) The etching step, which consists on removing the Cu under graphene, was done normally from a solution of HNO_3 (nitric acid) in water: purity of 69% (weight) and a concentration of C = 15 M (1 l = 1.42 kg). It is also frequent to use salts as $Fe(NO_3)_3$ or $Zn(NO_3)_2$ solved in water in order to attack the metallic catalyst. To avoid a too fast reaction and its thermal effects, the concentration of the acid should be lower down to C = 1 M (0.05 g/ml) taking 1.61 ml of HNO_3 and mixing it with 23.39 ml of H_2O for a total solution of V_{total} = 25 ml. $Fe(NO_3)_3$ was also used, and in that case, a small quantity of 5.6 g (or 6.6 g if Cu is too oxidized) diluted in 15 ml of water, will have similar results.

It took approximately one whole day (or even less) until the PMMA peeled off gradually from the copper with the mentioned acid concentration. When the process is completed, the PMMA remains floating on the surface of the liquid with the graphene attached to it. The sample should be cleaned with distilled water and in principle, is ready to use or ready for another step. (Also PDMS (Polydimethylsiloxane) is frequently used because it presents an easier removal; this polymer can be easily peeled off by hand once is dried, but it has not the film quality of PMMA.)

4) An optional and final step is the transfer from the PMMA to another insulating substrate, as SiO_2. Although the graphene transferred onto PMMA is already useful, it can be of interest to place it onto Si (e.g. for electronic applications). We placed and

pressed the PMMA gently onto a Si wafer with a layer of SiO_2 120 nm thick on top. After that, we evaporated the PMMA on a hot plate at a temperature of 400 °C.

The transferred sample corresponds to graphene/FLG grown on copper foil (76 μm) using benzene as precursor gas, and the result is shown in figure 7.22.

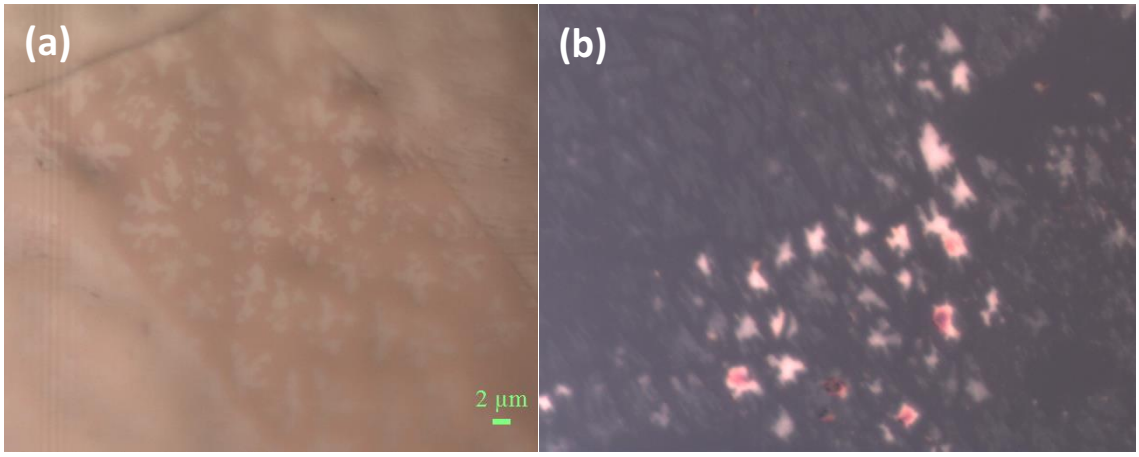

Figure 7.22: Optical image of graphene dendrites on Cu foil from the Raman optical microscope (a) before the transfer, and (b) optical image of the transferred graphene onto SiO_2, where the brighter zones are remains of the PMMA not fully evaporated. The same scale bar applies in both images.

After the transfer onto silicon, an optical observation revealed the effective transfer of the graphene/FLG dendrites present on the copper foil. It is possible also to see the contamination produced by the residual PMMA that has not been removed (figure 7.22b). The only step left is the afterwards confirmation of the real presence of graphene via Raman spectroscopy.

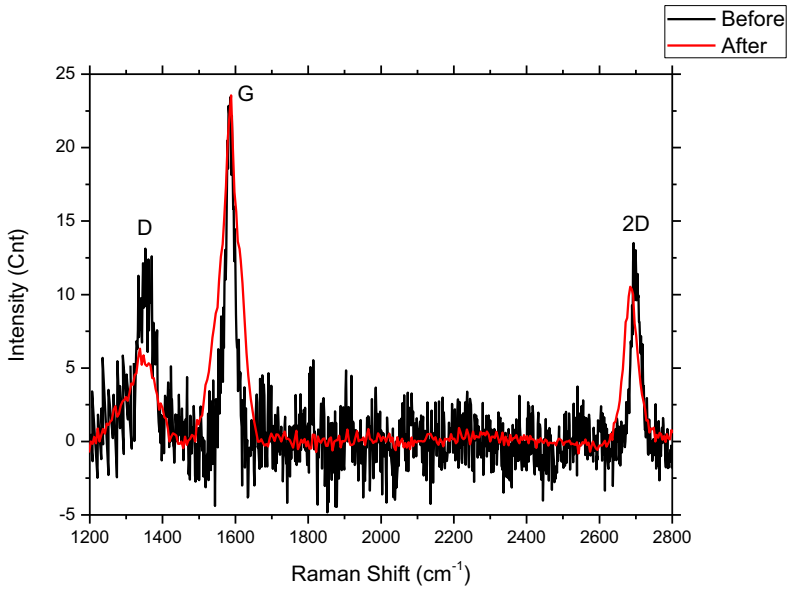

Figure 7.23: Raman spectrum of graphene on Cu foil (before the transfer), and finally transferred onto 120 nm thick SiO_2.

As we can see in figure 7.23, the spectra before and after the transfer is fairly coincident. Although the 2D peak is slightly smaller after the transfer, the amount of defects has surprisingly decreased. One of the reasons could be the 400 °C annealing done to the sample in order to evaporate the PMMA; it is well known that graphene reorders itself with temperature. Another possibility is the change of substrate: SiO_2 is way more suitable because in the measured region there are no peaks, and the surface roughness is considerably low. On the other hand, the spectrum on Cu is normally more complicated due to fluorescence and the presence of other peaks; the surface is also rougher.

7.5. Summary and conclusions

Although related works have been published [16,29], we consider that the monolayer graphene is obtained from *instant* and *very-low pressure pulses* of gas. Han et al. succeeded in growing graphene dividing the growth process into a sequence of short time slots during which methane was introduced at a constant flux (as well as a mixture of Ar/H_2), but they needed around 100-300 of these cycles to obtain graphene. In the case of Puretzky et al. they used acetylene as a carbon source and Ni films as a catalyst, but in spite of using pulses in a CVD system, the pressure they

used, around 18 Pa, cannot be considered as very low pressure. Therefore, the present work demonstrates the agreement between the monolayer-formation-time (τ) equation to grow graphene through an alternative very-low-pressure Pulsed-CVD system developed for this purpose. The main conclusions are:

- 600 nm films of Cu with 100 nm Ni barrier previously deposited on polished c-Si wafers slightly dewetted intro droplets and islands during the annealing process. These structures were observed by optical and electronic microscopes, and the EDS confirms the chemical composition of these structures: Cu, Ni, Si, and C are present in the surface after the whole process.

- The real phenomenon occurring in the sputtered substrate during the annealing is affected by the eutectic alloy between Cu and Si. This lowers the melting point of both elements creating a more complex surface where the graphene affinity is surprisingly high.

- AFM was not a very profitable characterization tool when it comes to graphene. The dendrites and layers of carbon are not optically detectable, thus, impossible to localize. The interference between the copper substrate and graphene did not improve the observation. However, AFM was really useful to characterize and determine the characteristics of the surface of our substrates/catalyst.

- Graphene was successfully grown on thin films of sputtered Cu/Ni and on c-Si; reducing the deposition time to the order of 10 s using pulses of methane of a partial pressure up to 10^{-4} Pa. The Raman analysis, SEM and EDS assessed the only presence of graphene of one-two layers by showing the characteristic 2D band and a ratio $I_{2D}/I_G \geq 1$.

- Most of the best results of the synthesized graphene were with no hydrogen added. Although it works as a catalyst as well, the

etching effect of hydrogen over graphene limits its growth dramatically for the low-pressures used in this work.

- Raman analysis presented the side effects of the fluorescence of the underlying copper, and the addition of new peaks from copper. This hampered the extraction of high signal to noise ratio spectra compared to the Raman signals from exfoliated graphene directly on silicon oxide. However, it still was a valuable, fast and easy tool to check the presence of carbon in any form.

- Raman spectra reflect the presence of graphene defects, probably due to the existence of multiple crystalline terraces and edges, evidenced by SEM. And also probably because of the irregular surface of the substrate/catalyst. Nonetheless, Raman mapping assessed the presence of large-area graphene up to 10^4 μm^2.

- Graphene also grew on Cu foils efficiently, having large crystalline domains and much less defective layers, as we expected from the reported works found in literature. The importance of flat and smooth surfaces of the metallic catalyst, and high process temperatures are translated into smaller D peaks from the Raman analysis.

- The use of new precursor like benzene or toluene can enlarge the list of parameters to obtain a high-performance graphene-based product. Having a lower pyrolysis temperature (500 °C), allows reducing the process temperature up to the half of the standard processes facilitating the industrial scalability. Even so, the change in the precursor gas suggests other changes in the system and the method in order to obtain high-quality graphene.

- The transfer process is still a drawback in the production of graphene by CVD. The removal of the underlying metal adds a few chemical steps that complicate the final quality of graphene.

In this work a standard transfer process from copper to silicon (through PMMA) was made with good results. The graphene transferred had similar characteristics to the one present on copper, but the addition of this step reduces the industrial scalability.

- Further work is necessary to optimize the theoretical approach of the monolayer-formation time equation: the sticking coefficient needs to be strictly evaluated; as well as the very Low-pressure Pulsed-CVD method: the importance of the copper layer thickness, the optimal annealing conditions, and the removing of the Cu/Ni during annealing after the CVD process to grow graphene only on silicon or silicon dioxide. This is especially important in the application of lithographic processes and the possibility to produce graphene-based electronic devices.

- Finally, the results assessed the use of our Low-pressure Pulsed-CVD technology, based on very low pressure pulses. It allows the growth of large area single and bi-layer graphene with a formation/deposition time of 10 s.

7.6. References

[1] V.-M. Freire, A. Ramírez, E. Pascual, E. Bertran, J.-L. Andújar, *Investigation of monolayer-formation time for the synthesis of graphene on copper/nickel/silicon using very-low pressure pulses of methane*, arXiv:1406.2640 (2014).

[2] C.A. Howsare, X. Weng, V. Bojan, D. Snyder, J.A. Robinson, *Substrate considerations for graphene synthesis on thin copper films*, Nanotechnology 23, 135601 (2012).

[3] N. Benouattas, A. Mosser, A. Bouabellou, *Surface morphology and reaction at Cu/Si interface—Effect of native silicon suboxide*, Appl. Surf. Sci. 252, 7572 (2006).

[4] B. Bokhonov, M. Korchagin, *In-situ investigation of the formation of eutectic alloys in the systemssilicon–silver and silicon–copper*, Journal of Alloys and Compounds 335, 149–156 (2002).

[5] T.B. Massalski, *Binary Alloy Phase Diagram*, ASM International (1990).

[6] W.A. Kaysser, G. Petzow, *Present state of liquid phase sintering*, Powder Met. 28 (3), 145 (1985).

[7] Y. Yao, S. Fan, *Si nanowires synthesized with Cu catalyst*, Science Direct. Materials Letters. 61, 177-181 (2007).

[8] V. Osterman, H. Antes, *Critical Melting Points and Reference Data for Vacuum Heat Treating*, Vacuum Furnace Reference Series (Solar atmospheres Inc.) 1 , 22 (2010).

[9] T. Wu, G. Ding, H. Shen, H. Wang, L. Sun, Y. Zhu, D. Jianga, X, Xie, *Continuous graphene films synthesized at low temperatures by introducing coronene as nucleation seeds*, Nanoscale 5, 5456–5461 (2013).

[10] J.H. Choi, Z. Li, P. Cui, X. Fan, H. Zhang, C. Zeng, Z. Zhang, *Drastic reduction in the growth temperature of graphene on copper via enhanced London dispersion force*, Sci. Rep. 3, 1925 (2013).

[11] I. Vlassiouk, S. Smirnov, I. Ivanov, P.F. Fulvio, S. Dai, H. Meyer, M. Chi, D. Hensley, P. Datskos, N.V. Lavrik, *Electrical and thermal conductivity of low temperature CVD graphene: the effect of disorder*, Nanotechnology 22, 275716 (2011).

[12] X. Li, C.W. Magnuson, A. Venugopal, J. An, J.W. Suk, B. Han, M. Borysiak, W. Cai, A. Velamakanni, Y. Zhu, L. Fu, E. M. Vogel, E. Voelkl, L. Colombo, R.S. Ruoff, *Graphene Films with Large Domain Size by a Two-Step Chemical Vapor Deposition Process*, Nano Lett. 10, 4328 (2010).

[13] V-M. Freire, J. Badia-Canal, C. Corbella, E. Pascual, E. Bertran, J-L. Andujar, *Hot-Wire Chemical Vapor Deposition of Few-Layer Graphene on Copper Substrates*, Jpn. J. Appl. Phys. 52, 01AK02 (2013).

[14] Y.H. Lee, J.H. Lee, *Scalable growth of free-standing graphene wafers with copper (Cu) catalyst on SiO_2/Si substrate: Thermal conductivity of the wafers*, Appl. Phys. Lett. 96, 083101 (2010).

[15] C. Hwang, K. Yoo, S.J. Kim, E.K. Seo, H. Yu, L.P. Biró, *Initial Stage of Graphene Growth on a Cu Substrate*, J. Phys. Chem. C. 115 (45), 22369–22374 (2011).

[16] Z. Han, A. Kimouche, A. Allain, H. Arjmandi-Tash, A. Reserbat-Plantey, S. Pairis, V. Reita, N. Bendiab, J. Courax, V. Bouchiat, *Suppression of Multilayer Graphene Patches during CVD Graphene growth on Copper*, arXiv:1205.1337, (2012).

[17] X. Li, W. Cai, J. An, S. Kim, J. Nah, D. Yang, R. Piner, A. Velamakanni, I. Jung, E. Tutuc, S.K. Banerjee, L. Colombo, R.S. Ruoff, *Large-Area Synthesis of High-Quality and Uniform Graphene Films on Copper Foils*, Science 324 (5932), 1312 (2009).

[18] W.D. Westwood, *Sputter Deposition*, AVS Education Committee Book Series Vol. 2, New York (2003).

[19] A. Ismach, C. Druzgalski, S. Penwell, A. Schwartzberg, M. Zheng, A. Javey, J. Bokor, Y. Zhang, *Direct Chemical Vapor Deposition of Graphene on Dielectric Surfaces*, Nano Letters 10, 1542–1548 (2010).

[20] W. Fei, J. Yin, X. Liu, W. Guo, *Dendritic graphene domains: Growth, morphology and oxidation promotion*, Materials Letters 110, 225–228 (2013).

[21] Y. Zhang, L. Zhang, C. Zhou, *Review of Chemical Vapor Deposition of Graphene and Related Applications*, Accounts of Chemical Research 46 (10), 2329–2339 (2013).

[22] C. Mattevi, H. Kim, M. Chhowalla, *A review of chemical vapour deposition of graphene on copper*, J. Mater. Chem. 21, 3324 (2011).

[23] H. Ji, Y. Hao, Y. Ren, M. Charlton, W.H. Lee, Q. Wu, H. Li, Y. Zhu, Y. Wu, R. Piner, R.S. Ruoff, *Graphene Growth Using a Solid Carbon Feedstock and Hydrogen*, ACS Nano 5 (9), 7656–7661 (2011).

[24] J. Sun, N. Lindvall, M.T. Cole, K.T.T. Angel, T. Wang, K.B.K. Teo, D.H.C. Chua, J. Liu, A. Yurgens, *Low Partial Pressure Chemical Vapor Deposition of Graphene on Copper*, IEEE T. Nano. 11 (2), 255-260 (2012).

[25] Q. Yu, L.A. Jauregui, W. Wu, R. Colby, J. Tian, Z. Su, H. Cao, Z. Liu, D. Pandev, D. Wei, T.F. Chung, P. Peng, N.P. Guisinger, E.A. Stach, J. Bao, S-S. Pei, Y.P. Chen, *Control and characterization of individual grains and grain boundaries in graphene grown by chemical vapour deposition*, Nature Materials 10, 443-449 (2011).

[26] A.C. Ferrari, *Raman spectroscopy of graphene and graphite: Disorder, electron–phonon coupling, doping and nonadiabatic effects*, Solid State Commun. 143, 47–57 (2007).

[27] Y.Y. Wang, Z.H. Ni, T. Yu, Z.X. Shen, H.M. Wang, Y.H. Wu, W. Chen, A.T.S. Wee, *Raman Studies of Monolayer Graphene: The Substrate Effect*, J. Phys. Chem. C. 112, 10637–10640 (2008).

[28] A.C. Ferrari, J.C. Meyer, V. Scardaci, C. Casiraghi, M. Lazzeri, F. Mauri, S. Piscanec, D. Jiang, K.S. Novoselov, S. Roth, A.K. Geim, *Raman Spectrum of Graphene and Graphene Layers*, Phys. Rev. Lett. 97, 187401 (2006).

[29] A.A. Puretzky, D.B. Geohegan, S. Pannala, C.M. Rouleau, M. Regmi, N. Thonnard, G. Eres, *Real-time optical diagnostics of graphene growth induced by pulsed chemical vapor deposition*, Nanoscale 5, 6507 (2013).

Chapter 8

STUDY OF THE EFFECT OF SWIFT HEAVY ION IRRADIATION ON 2D CRYSTALS

8. Study of the effect of Swift Heavy Ion irradiation on 2D crystals

Ion irradiation of graphene has been successfully applied to induce various modifications in the graphene crystal, like the formation of origami-like foldings, which are created by swift heavy ion (SHI) irradiation under glancing incidence angles. These foldings can be applied to locally alter the physical properties of graphene like mechanical strength or chemical reactivity. In this section we show that the formation of foldings in two dimensional crystals is not restricted to graphene but can be applied for other materials like MoS_2 and h-BN as well. The production and characterization of graphene and MoS_2 samples, as well as the subsequent treatment after the irradiation, was part of my work in the research stay done in Duisburg University (Germany). *

8.1. Introduction

The interaction of swift heavy ions (SHI, ions with energies that are typically around the maximum of the energy loss curve) with matter is based almost exclusively on electronic excitation and ionization processes [1]. Besides basic research, this unique interaction is applied in material research to e.g. create ion-tracks and nanostructures in materials [2], surface tracks on insulators [3] or study the radiation hardness of materials [4]. For two dimensional materials, however, the experimental and theoretical studies of the interaction with SHI are still sparse. It has been shown that for graphene, swift heavy ion irradiation under glancing incidence angle can cause foldings in this material [5,6]. Furthermore, it has been shown that SHI irradiation can be used to manipulate the doping level of graphene [7] and the radiation hardness of graphene and MoS_2 devices has been tested. [4]

The ability to fold atomically thin materials opens up the opportunity to alter the physical properties of these materials on the nanoscale. In the case of graphene, the folding introduces two changes in the atomically thin sheet. On the one hand, the folded area consists of a bilayer which locally strengthens the material [8]. On the other hand, at the point where the material is bended, a close bilayer edge is formed,

** This study was done with the collaboration of Oliver Ochedowski, who was the main contributor to this work, and it was extracted from the paper: "Folding Two Dimensional Crystals by Swift Heavy Ion Irradiation, O. Ochedowski, H. Bukowska, V.-M. Freire, L. Brökers, B. Ban-d'Etat, H. Lebius, M. Schleberger, Nucl. Instrum. Methods (2014)", with the permission of Prof. Dr. Marika Schleberger.*

where the covalent bonds are bended changing the chemical reactivity and transport properties [9]. Because of this, a strong magnetophotoelectric effect is expected in graphene folding [10] as well as bandgap openings. [11,12]

In this work, the formation of foldings induced by SHI irradiation was investigated to confirm whether it is limited to the semi-metal graphene or not. For this other two dimensional materials in form of MoS_2 (direct bandgap semi conductor), hexagonal BN (insulator) and carbon nanomembranes (CNM, a polymeric membrane) have been irradiated and studied using atomic force microscopy (AFM).

8.2. Experimental

For the ion irradiations experiments single layers of graphene, MoS_2 and hexagonal BN have been prepared by mechanical exfoliation of their respective bulk crystals (*HQ Graphene* - Groningen, Netherlands) [13]. Prior to the irradiation the thickness of the crystals has been checked by Raman spectroscopy [14-16]. These exfoliated samples were compared to large area two dimensional materials which are commercially available, CVD graphene (*Graphenea* - Spain, San Sebastian), CVD MoS_2 (*HQ Graphene* - Groningen, Netherlands) and carbon nanomembranes (*CNM Technologies* - Germany, Bielefeld).

The SHI irradiation was performed at the GANIL (Grand accelerateur d`ions lourds - France, Caen) for the Xe^{23+} irradiation and at the M-branch of the GSI (Gesellschaft für Schwerionenforschung - Germany, Darmstadt) for the U^{28+} irradiation. The samples have been irradiated under glancing incidence angle of below 3° with respect to the surface, which is necessary for folding formation [5]. The ion fluence was kept below 10 ions/μm^2 to avoid overlapping foldings. After the irradiation, the samples were analyzed using an atomic force microscope (AFM) in tapping mode with standard Si cantilevers (*Nanosensors NCHR* – Switzerland, Neuchatel).

8.3. Results

The results of the SHI irradiation of the exfoliated two dimensional crystals are shown in figure 8.1. All three crystals were irradiated under the same

conditions (91 MeV Xe^{23+}, incidence angle below 3°) which results in the formation of foldings in each single layer sheet. In graphene (figure 8.1a) about 50% of the foldings consists of two folded areas which are positioned along the incident SHI impact. For about 35% an additional third folded area can be observed which is located at the end. Foldings with more than three folded areas are very rare and mostly caused by multiple SHI impacts. The zoom-in shows a typical folding with three folded areas and the corresponding line profile. The line profile reveals a typical height of about 0.7 nm to 1.0 nm which is significantly more than the expected height of bilayer graphene.

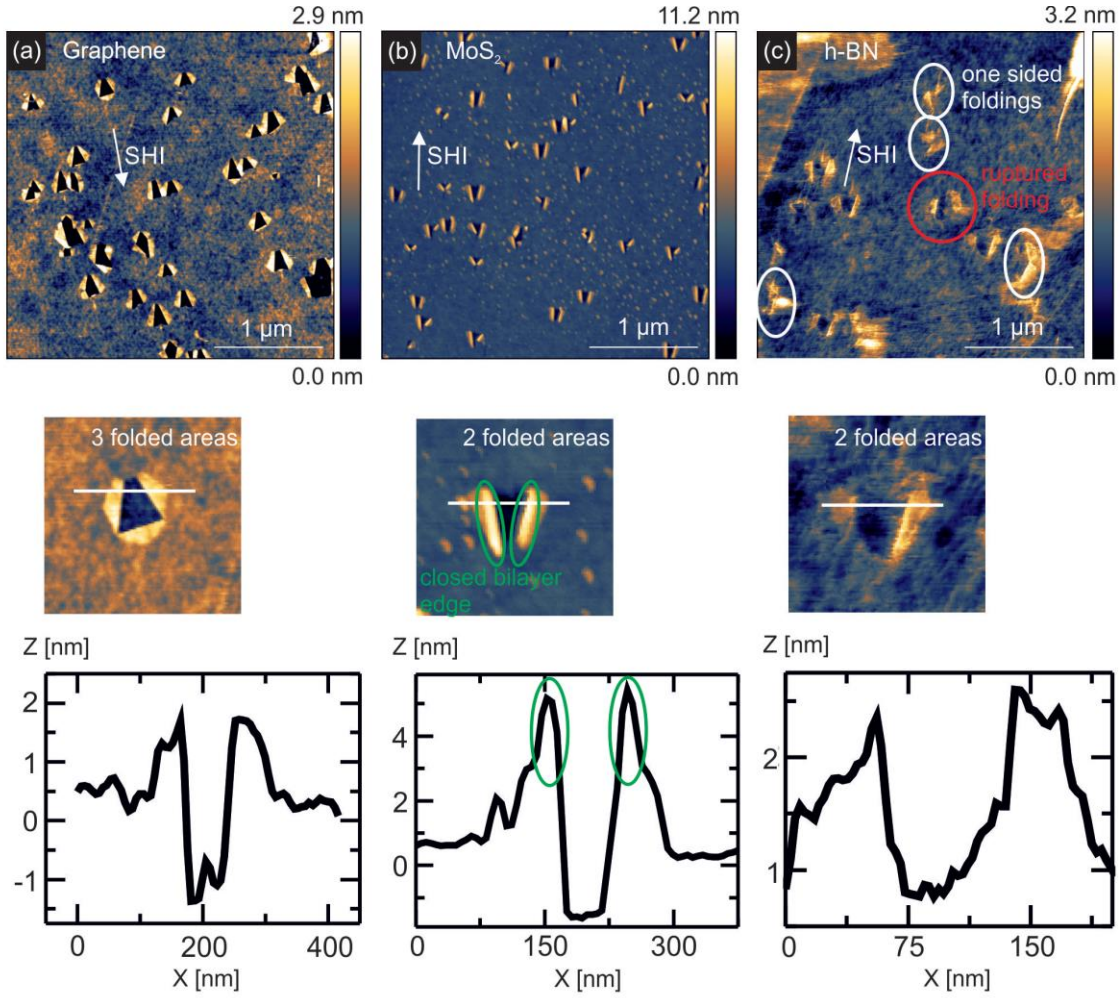

Figure 8.1: AFM topography of (a) single layer graphene, (b) single layer MoS_2 and (c) single layer hexagonal BN irradiated with Xe^{23+} ions (E_{kin} = 91 MeV, grazing incidence θ = 1-3°). All three two dimensional materials show foldings upon SHI irradiation.

Foldings in single layer MoS_2 show some different characteristics when compared to graphene. No folded areas at the end can be observed and a very large percentage of 80% shows only two foldings. Moreover, for about 13% of the foldings, only one folded area is created. The line profile of the zoom-in (figure 8.1b) shows that the height of the bilayer MoS_2 is about 2 nm and the height of the edge is significantly increased to 4 nm. Note, that the edge consists of a closed bilayer edge or half nanotube like structure.

Compared to graphene and MoS_2, foldings in single layers h-BN show a large fraction of incomplete foldings with about 40% of one sided folding as marked in figure 8.1c. Furthermore, not more than two folded areas are observed per SHI impact and even ruptured foldings can be observed. The foldings on h-BN show the smallest average height ranging from 0.5 nm to 1.0 nm.

Next, we shown that the folding formation is not limited to exfoliated crystals, which have the highest crystalline quality, but can be applied for CVD grown materials as well. In figure 8.2a an optical image of CVD grown graphene flake can be seen which has been transferred from copper foil, where it has been grown on, onto a SiO_2 substrate. The graphene sheet is covering the whole sample, the small dots in the image with a higher contrast are most likely remnants of the transfer process. The Raman spectrum of this graphene sheet shown as an inset in 2a shows a typical spectrum for single layer graphene. The disorder induced D-Peak is almost not present in the Raman spectrum, displaying the high crystalline quality of the CVD graphene sheet. An AFM topography image of the irradiated sample is shown in figure 8.2b. The CVD graphene sheet folds upon SHI irradiation comparable to exfoliated graphene. The foldings do not look as uniform as the ones on the exfoliated sample in figure 8.2a. This is most likely caused by the higher surface roughness of the CVD graphene sheet with a rms of 1.5 nm compared to the 0.5 nm of the exfoliated graphene flake and the occurence of wrinkles which locally cause heavy stress in the CVD graphene sheet.

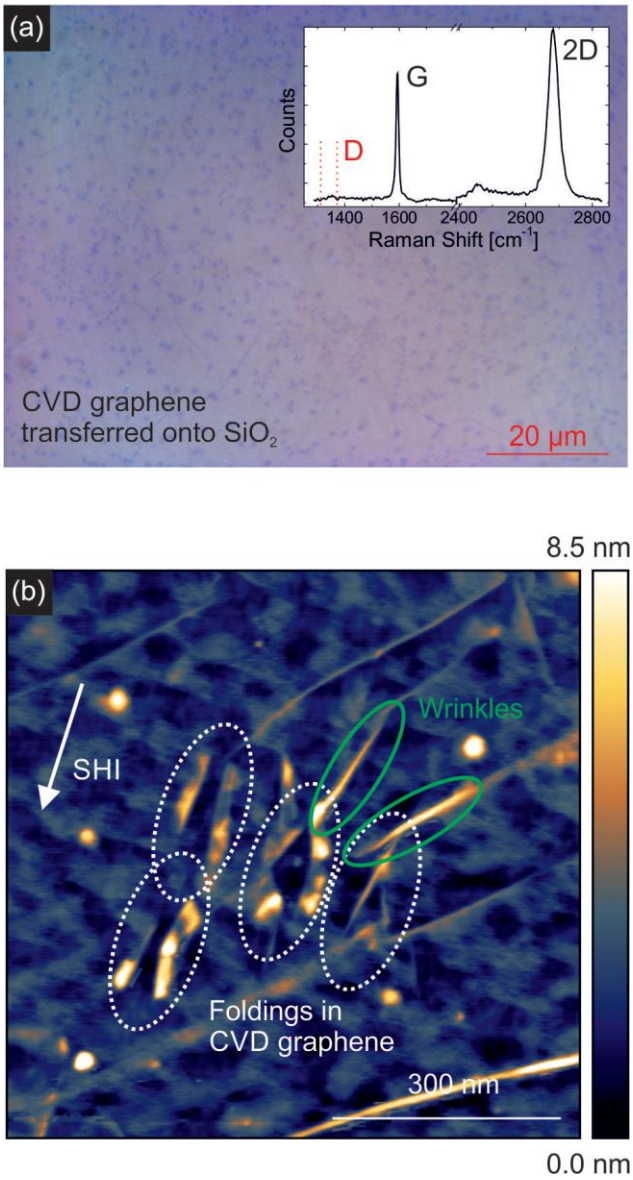

Figure 8.2: (a) Optical image of CVD graphene on SiO_2 with the corresponding Raman spectrum as an inset. Absence of the D Peak reveals a high structural quality. (b) AFM topography of CVD graphene after Xe^{23+} irradiation (E_{kin} = 91 MeV, grazing incidence θ = 0.5°) showing foldings in CVD graphene.

In contrast to graphene, MoS_2 can be easily grown by CVD directly on the SiO_2 and no transfer step is necessary. In figure 8.3a an optical image of such a CVD grown MoS_2 sample is shown. The CVD MoS_2 sheet is not covering the whole subtrates surface as it grows in form of single islands with a typical size of several hundred μm^2 in case of our sample. In the AFM topography in figure 8.3b it can be observed that contrary to exfoliated MoS_2, CVD MoS_2 is not folding upon SHI irradiation. Instead,

rifts with a length of about 400 nm are formed which are decorated on both sides with atoms and/or adsorbates. Since CVD MoS_2 is directly grown on the substrate and no transfer process is necessary, the sample shows a low surface roughness and no wrinkles as in CVD graphene are observed.

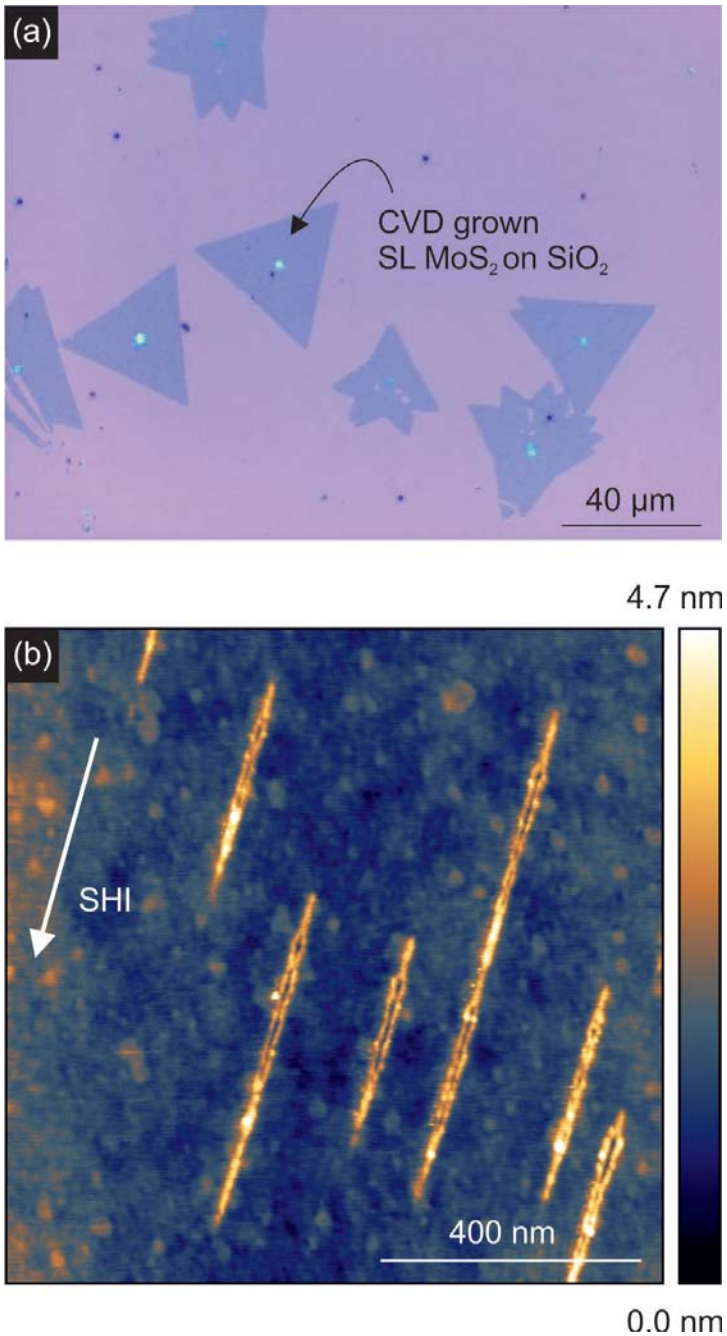

Figure 8.3: (a) Optical microscope image of CVD grown MoS_2. (b) AFM topography after Xe^{23+} irradiation (E_{kin} = 91 MeV, grazing incidence θ = 0.5°). In CVD MoS_2 no folding but rifts along the ion trajectory are created.

To investigate to what extent the crystalline quality of the sample plays a role in the folding formation, a 1 nm thick carbon nanomembrane (CNM) has been irradiated. The CNM used in this experiment are obtained by electron radiation induced cross-linking of self-assembled monolayers (aromatic molecules) on a gold substrate. In figure 8.4a an optical image of a CNM transferred in solution to a SiO_2 substrate is shown. The Raman spectrum in the inset reveals that the CNM is amorphous. Irradiation of this CNM leads to the formation of foldings as well as rifts, as can be observed in the AFM topography in figure 8.4b. Typically, the SHI induced modification consists of a rift located at the beginning followed by folding. However, the SHI modifications in the CNM are very diverse, i.e. the folding is sometimes discontinued by a rift and sometimes no folding at all is created.

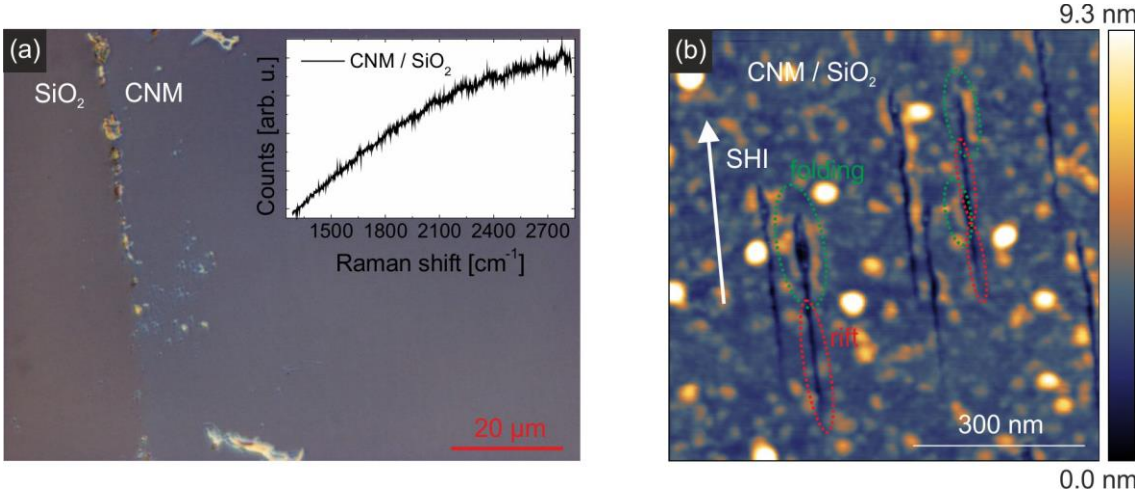

Figure 8.4: (a) Optical image of CNM transferred to a SiO_2 substrate. The inset shows a typical Raman spectrum of this amorphous material. (b) AFM topography of CNM after U^{28+} irradiation (E_{kin} = 857 MeV, grazing incidence θ = 2°) showing incomplete foldings in CNM.

8.4. Summary and conclusions

The formation of foldings in two dimensional crystals due to grazing SHI irradiation is not limited to the semi-metallic graphene, but can be applied to single layers of semiconducting MoS_2 and insulating h-BN as well. However, the foldings in these three materials do show different characteristics. First, the number of folded areas varies depending on the irradiated material. In this study, more than two foldings per SHI impact

are only observed in the irradiated graphene sheet, where up to four folded areas are created.

Second, the height of the folded areas varies on a large scale for these materials. As expected, MoS_2 shows the highest folded areas because the interlayer spacing of the three-atomic single layer is with 0.75 nm about twice as high as the interlayer spacing of graphene and h-BN. However, the folded areas are in general far higher than what is to be expected for a bilayer MoS_2, graphene or h-BN sheet. This might be caused by adsorbates trapped during the folding process and/or not perfect stacking of the bilayer which has to be investigated in future studies.

For CVD grown materials the picture is different, as CVD graphene and CNMs show foldings while MoS_2 does not fold. From the comparison of CVD graphene and CNMs it can be seen that the crystalline quality is obviously an important parameter in the folding process. CVD graphene folds almost equally in comparison to exfoliated graphene while CNM with its amorphous structure is just partially folded and even rifts are created.

Even more important than the crystalline quality, is the interfacial layer between the two dimensional material and its substrate. For exfoliated crystals, water is always trapped during the exfoliation process, causing an interfacial water layer. The same is expected for CVD graphene and CNM, which are transferred in a solution to the SiO_2 substrate. The only material that does not fold upon SHI irradiation is CVD MoS_2. Although it is highly crystalline, the direct growth on SiO_2 prevents the formation of an interfacial water/adsorbate layer and without this water layer, SHI irradiation leads to the creation of rifts instead of foldings.

- SHI irradiation under glancing incidence can be used to introduce foldings in a variety of two dimensional materials like graphene, MoS_2 and h-BN.
- Foldings can be introduced in two dimensional materials like CVD graphene and CNM, which are grown on a large scale, as well.
- It has been shown that an interfacial layer of water or adsorbates is necessary for the folding mechanism to take place

and that crystalline quality of the material determines the quality of the resulting folding.

8.5. References

[1] F. Aumayr, S. Facsko, A.S. El-Said, C. Trautmann, M. Schleberger, *Single ion induced surface nanostructures: a comparison between slow highly charged and swift heavy ions*, J. Phys.: Condens. Matter 23, 393001 (2011).

[2] M. Toulemonde, C. Trautmann, E. Balanzat, K. Hjort, A. Weidinger, *Track formation and fabrication of nanostructures with mev-ion beams*, Nuclear Instruments and Methods in Physic Research B 216, 1 (2004).

[3] E. Akcoeltekin, T. Peters, R. Meyer, A. Duvenbeck, M. Klusman, I. Monnet, H. Lebius, M. Schleberger, *Creation of multiple nanodots by single ions*, Nature Nanotechnology 2, 290 (2007).

[4] K. Ochedowski, O. Marinov, G. Wilbs, G. Keller, N. Scheuschner, D. Severin, M. Bender, J. Maultzsch, F.J. Tegude, M. Schleberger, *Radiation hardness of graphene and MoS_2 field effect devices against swift heavy ion irradiation*, Journal of Applied Physics 113, 214306 (2013).

[5] S. Akcoeltekin, H. Bukowska, T. Peters, O. Osmani, I. Monnet, I. Alzaher, B. Ban dEtat, H. Lebius, M. Schleberger, *Unzipping and folding of graphene by swift heavy ions*, Applied Physics Letters 98, 103103 (2011).

[6] O. Ochedowski, S. Akcltekin, B. Ban-dEtat, H. Lebius, M. Schleberger, *Detecting swift heavy ion irradiation effects with graphene*, Nuclear Instruments and Methods in Physic Research B 314, 18 (2013).

[7] O. Ochedowski, B. Kleine Bussmann, B. Ban dEtat, H. Lebius, M. Schleberger, *Manipulation of the graphene surface potential by ion irradiation*, Applied Physics Letters 102, 153103 (2013).

[8] Y. Zheng, N. Wei, Z. Fan, L. Xu, Z. Huang, *Mechanical properties of grafold: a demonstration of strengthened graphene*, Nanotechnology 22, 405701 (2011).

[9] L. Ortolani, E. Cadelano, G.P. Veronese, C.D.E. Boschi, E. Snoeck, L. Colombo, V. Morandi, *Folded graphene membranes: Mapping curvature at the nanoscale*, Nano Letters 12, 5207 (2012).

[10] F. Queisser, R. Schuetzhold, *Strong magnetophotoelectric effect in folded graphene*, Physical Review Letters 111, 046601 (2013).

[11] D. Zhan, L. Liu, Y.N. Xu, Z.H. Ni, J.X. Yan, C. Zhao, Z.X. Shen, *Low temperature edge dynamics of ab-stacked bilayer graphene: Naturally favored closed zigzag edges*, Scientific Reports 1, 12 (2011).

[12] L. Feng, L. Qi, J.Y. Huang, J. Li, *Geometric and electronic structure of graphene bilayer edges*, Physical Review B 80, 165407 (2009).

[13] K.S. Novoselov, G. Jiang, F. Schedin, B.T.J., Proc. Natl Acad. Sci. 102, 10451 (2004).

[14] A.C. Ferrari, J.C. Meyer, V. Scardaci, C. Casiraghi, M. Lazzeri, F. Mauri, S. Piscanec, D. Jiang, K.S. Novoselov, S. Roth, A.K. Geim, *Raman spectrum of graphene and graphene layers*, Physical Review Letters 97, 187401 (2006).

[15] C. Lee, H. Yan, L.E. Brus, T.F. Heinz, J. Hone, S. Ryu, *Anomalous lattice vibrations of single- and few-layer MoS_2*, ACS Nano 4, 2695 (2010).

[16] R.V. Gorbachev, I. Riaz, R.R. Nair, R. Jalil, L. Britnell, B.D. Belle, E.W. Hill, K.S. Novoselov, K. Watanabe, T. Taniguchi, A.K. Geim, P. Blake, *Hunting for monolayer boron nitride: Optical and raman signatures*, Small 7, 465 (2011).

Chapter 9

FABRICATION AND CHARACTERIZATION OF A GRAPHENE TRANSISTOR

9. Fabrication and characterization of a graphene transistor

9.1. Graphene-based FET

The ability to control electronic properties of a material by externally applied voltage is the core of modern electronics. Normally, it is the electric field effect that allows one to vary the carrier concentration in a semiconductor device and, therefore, change an electric current through it [1]. Just after its discovery, graphene was shown to be an excellent material for the fabrication of field effect devices. Due to its ballistic transport properties, very large field-effect mobilities as high as 15000 $cm^2/V{\cdot}s$ and a Fermi velocity of ~10^8 cm/s have been demonstrated at room temperature (RT) [2]. In addition, graphene is a gapless semiconductor, it shows an ambipolar behaviour, i.e., both charge carrier types contribute to its conductivity [3]. This lack of a bandgap, however, limits the usage of two dimensional graphene for digital switching, where high on/off ratios are necessary. Despite this fact, several potential advantages may be listed: the perfect 2D confinement of carriers, electron/hole symmetry originating from a conical bandstructure, and the possibility of opening bandgaps lithographically by fabricating graphene nanoribbons (GNRs). Furthermore, the large area graphene opens the possibility to make 2D graphene devices for RF/analog amplification [4]. Superior frequency performance of such devices makes it a promising application: a graphene Field-Effect Transistor (FET) operating at GHz frequencies was reported by IBM researchers in 2008. [5]

In this work, a simple FET device was prepared from single layer graphene (SLG). The first step was the mechanical exfoliation from single crystals (HOPG) onto 90 nm SiO_2 on a Si wafer (in this case <100> p-doped boron, ρ = 0.001-0.005 $\Omega{\cdot}$cm, and 525 μm thick) to obtain monolayer flakes of graphene. Afterwards, we located and selected appropriate flakes; graphene films more than 10 μm in size were needed to make electrical measurements; and in order to deposit easily the contacts we needed a flake with a size around 20x20 μm^2, see figure 9.1. Further characterization was made to confirm their layer number with micro-Raman spectroscopy. The details of this standard step are well explained in Chapter 5.

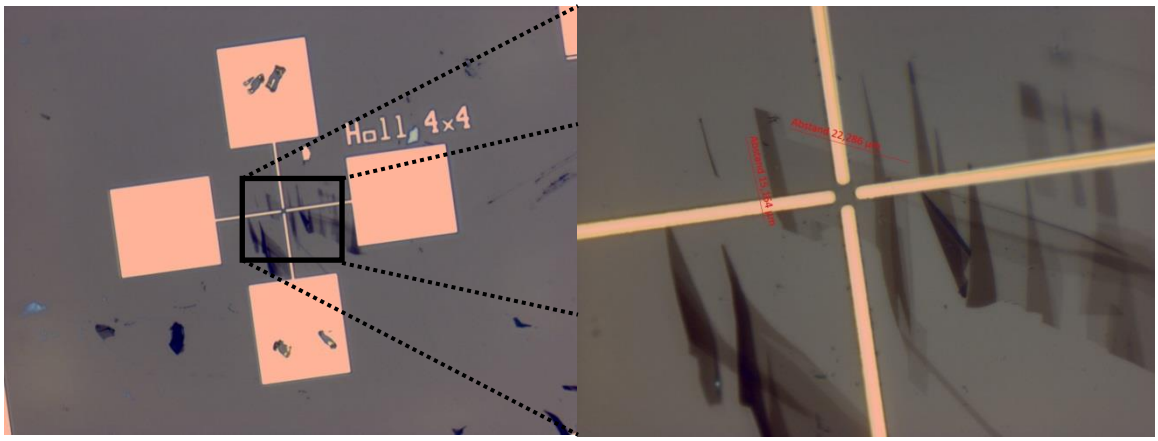

Figure 9.1: Optical image of the metallic contacts deposited on the sample. The right inset shows in detail the graphene flake of 22x15 μm with the four electrodes (only the two vertical ones in use).

Once a SLG flake was selected, then it is contacted using photolithography and vacuum evaporation. A titanium adhesion layer of 10 nm is deposited first, followed by a deposition of two gold contacts of 100 nm of thickness serve as source and drain. On the other hand the silicon substrate was used as a global back-gate, see scheme in figure 9.2. The channel length and width of our device is L = 4 μm and W = 2 μm.

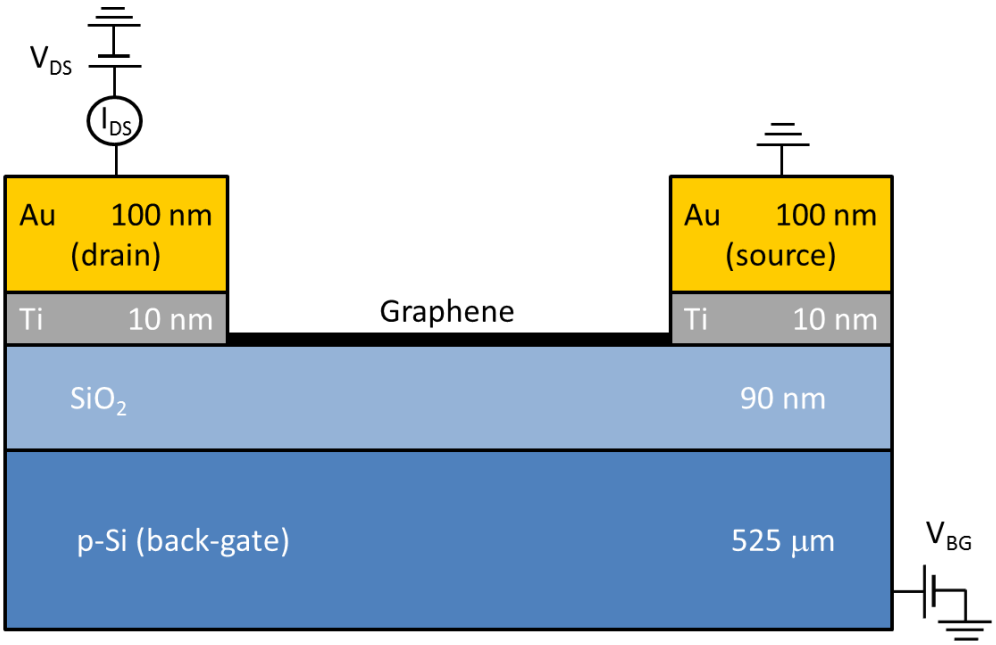

Figure 9.2: Cross-sectional scheme of the electrical setup of the FET based on graphene. Au leads are used for the source and drain electrodes with a Ti bonding agent. The Si substrate was used as a back-gate with a 90 nm SiO_2 layer used as a dielectric.

The next step then, was the electrical characterization of the FET with respect to its output ($I_{DS}(V_{DS})$) and transfer ($I_{DS}(V_{GS})$) characteristics. I_{DS} is the drain-source current, V_{GS} is the voltage between gate and source, and V_{DS} is the voltage between drain and source. The results of the device are shown in figure 9.3, where the transfer characteristics, i.e. the drain current as a function of the gate voltage is plotted.

The SLG FET shows basically the same characteristics as reported in the literature [6,7]. However, device performance is below the reported record values, see below. In our device, amplification sets in at a gate voltage of about V_{GS}=-6V (pinch-off) with an output compliance (drain-gate) of 1 mA, and at RT. The minimum conductance (resistivity maximal) is obtained when the Fermi level is at the Dirac point (change neutrality point). Thus, the Dirac voltage was observed around 38.3 V. [8]

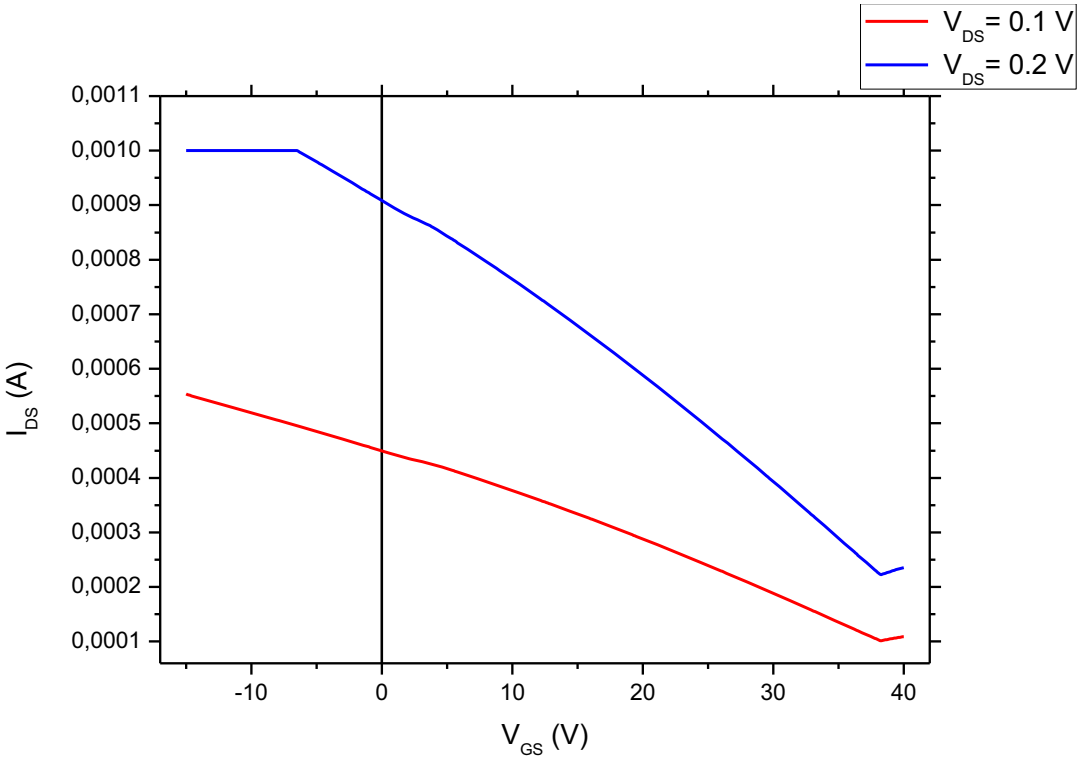

Figure 9.3: Transfer characteristics of the graphene-based FET device with a drain-source voltage of 0.1 V and 0.2 V. The point where the graphene conductivity is minimum, the Dirac point, is around 38.2 V.

Important physical properties as conductivity σ and mobility μ are directly derived from the experiment as follows [3,9]:

$$\mu = \frac{dI_{DS}}{\mathrm{dV_{GS}}} \times \frac{L}{WC_i V_{DS}} \qquad \sigma = \frac{dI_{DS}}{\mathrm{dV_{DS}}} \tag{9.1}$$

Here, I_{DS} is the drain-source current, V_{GS} is the voltage between gate and source, and V_{DS} is the voltage between drain and source, see figure 9.2. $C_i = \varepsilon\varepsilon_r/d = 3.837 \cdot 10^{-4}$ F/m^2 is the capacitance between the channel and the back-gate per unit area, ε and ε_r are the dielectric constants of air and of the dielectric (SiO_2: $\varepsilon_r = 3.9$), respectively, and *d* is the thickness of the oxide layer (90 nm).

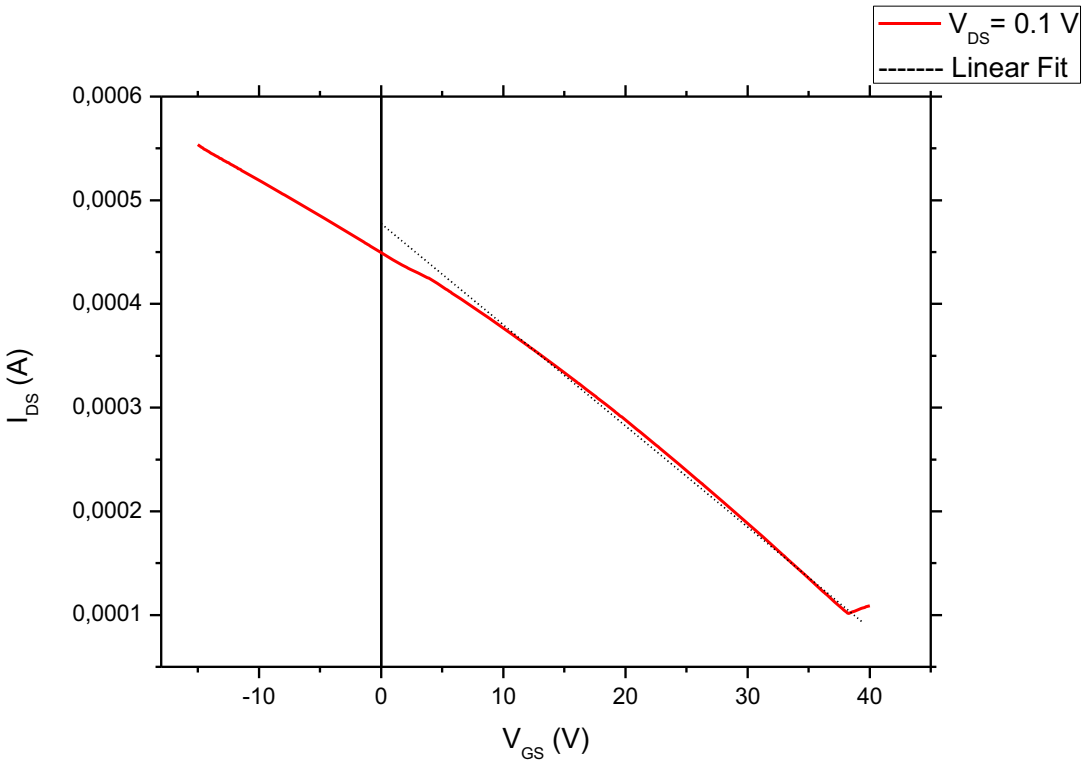

Figure 9.4: Linear fit corresponding to the V_{DS}=0.1 V linear regime of the graphene-FET transfer characteristic: $y = 0.000470219 - 9.82386 \cdot 10^{-6}x$ (the slope corresponds to the electrical conductance).

Using the transfer characteristic curve of the SLG FET, we fit the linear regime into a linear polynomial (*y = a+bx*) as:

$$y = 0.000470219 - 9.82386 \cdot 10^{-6} x \tag{9.2}$$

Where the slope of this fit is $\frac{dI_{DS}}{dV_{GS}}$, or *g,* the low bias conductance from equation 9.1. Already known the rest of the values $C_i = 3.837 \cdot 10^{-8}$ F/cm^2, L = 4 μm, W = 2 μm, V_{DS} = 0.1 V; we obtained a carrier mobility of:

μ = -5120.59 cm^2/V·s (electrons)

Finally, the charge carrier density can be directly derived from this data by $n_{e,h} = \frac{\sigma}{e\mu_n}$ with *e* the elementary charge. Note, that the conductivity σ can be calculated while V_{GS} = 0 V ($\sigma = 4.59 \cdot 10^{-3}\ \Omega^{-1}$), and n($V_{GS}$ = 0 V):

n = 5.59·10^{12} n$_e$/cm^2

Which is a typical value of carrier concentration found in literature.

9.2. Summary and conclusions

- Mechanical exfoliation provides a good example of high-quality monolayer graphene: easy to obtain and characterize, homogeneously non defective, and big enough domains for the current technologies to fabricate FET devices.
- The transfer characteristics of the FET device obtained are similar to the ones reported previously, which can ensure the reproducibility of the process from small to big scale.
- The results in the carrier mobility of our graphene-based transistor on silica are comparable to the ones obtained in literature. Low-field mobility values for graphene on SiO_2 are reported as 4000 cm^2/V·s at RT and the highest reported value at >10^{13} cm^{-2} carrier concentration is around 9000 cm^2/V·s [1]. It is widely believed that ionized charged impurities at the graphene-oxide interface limits the carrier mobility in graphene [10]. It seems that use of very high ε substrate instead of SiO_2 can improve the carrier mobility of graphene at low fields. But use of high ε dielectrics for graphene transistors comes with an extra scattering mechanism—the remote interface phonon or

surface optical phonon (SO) scattering. Due to the fact that graphene is an atomically thin (0.3-0.4 nm) membrane, the decaying polarization field (also known as surface-phonon field) can scatter the carriers in the graphene channel and limit the low-field mobility. [4]

- Although our single layer graphene FET can be improved with respect to conductivity, it might prove very interesting for applications in transistors and in transparent-conductive layers.

9.3. References

[1] K.S. Novoselov, A.K. Geim, S.V. Morozov, D. Jiang, Y. Zhang, S.V. Dubonos, I.V. Grigorieva, A.A. Firsov, *Electric Field Effect in Atomically Thin Carbon Films*, Science 306, 666 (2004).

[2] A.K. Geim, K.S. Novoselov, *The rise of graphene*, Nature Materials 8, 183 (2007).

[3] O. Ochedowski, K. Marinov, G. Wilbs, G. Keller, N. Scheuschner, D. Severin, M. Bender, J. Maultzsch, F. J. Tegude, and M. Schleberger, *Radiation hardness of graphene and MoS_2 field effect devices against swift heavy ion irradiation*, Journal of Applied Physics 113, 214306 (2013).

[4] S. Mikhailov, *Physics and Applications of Graphene - Theory*, InTech, Rijeka (2011).

[5] Y.-M. Lin, K.A. Jenkins, A. Valdes-Garcia, J.P. Small, D.B. Farmer, P. Avouris, *Operation of graphene transistors at gigahertz frequencies*, Nano Letters 9 (1), 422–426 (2009).

[6] A. Venugopal, J. Chan, X. Li, C. W. Magnuson, W.P. Kirk, L. Colombo, R.S. Ruoff, E.M. Vogel, *Effective mobility of single-layer graphene transistors as a function of channel dimensions*, J. Appl. Phys. 109 (10), 104511 (2011).

[7] D.J. Late, B. Liu, H.S.S.R. Matte, V.P. Dravid, C.N.R. Rao, *Hysteresis in Single-Layer MoS_2 Field Effect Transistors*, ACS Nano 6 (6), 5635–5641 (2012).

[8] A.V. Klekachev, A. Nourbakhsh, I. Asselberghs, A.L. Stesmans, M.M. Heyns, S. De Gendt, *Graphene Transistors and Photodetectors, The Electrochemical Society*, *Interface* (2013).

[9] P.K. Ang, S. Wang, Q. Bao, J.T.L. Thong, K.P. Loh, *High-Throughput Synthesis of Graphene by Intercalation-Exfoliation of Graphite Oxide and Study of Ionic Screening in Graphene Transistor*, ACS Nano 3 (11), 3587-94 (2009).

[10] E.H. Hwang, S. Adam, S. Das Sarma, *Carrier Transport in Two-Dimensional Graphene Layers*, Physical Review Letters 98, 186806 (2007).

Part IV
Conclusions

Conclusions

The main conclusions extracted from all the experiments done and the results obtained are:

- Mechanical exfoliation is a simple and reliable process to obtain monolayer graphene with a reasonable ratio of success. The Raman spectra acquired demonstrated the presence of high-quality monolayer graphene: a small G peak and a 2D peak around four times the G (in intensity) are present, and a complete absence of D peak. However, the size of the flakes (of around 20 μm) is not suitable for industrial applications, concretely for large area applications.

- The thin oxide layer of 90 nm of SiO_2 (or 300 nm) proved critical to enhance the contrast of any process related with the optical detection and tracing of graphene.

- AFM in tapping mode was especially sensitive in order to detect the presence of contamination on the graphene samples obtained by mechanical exfoliation, like glue or trapped water among layers. However, it was not that efficient to measure the step height of a monolayer of carbon due mainly to the interface graphene-substrate and the thin layer of water formed between them. On the other hand, in CVD graphene, AFM was not a very profitable characterization tool. The dendrites and layers of carbon are not optically detectable, thus, impossible to localize. The interference between the copper substrate and graphene did not improve the observation. However, AFM was really useful to characterize and determine the characteristics of the surface of our substrates/catalyst.

- Mechanical exfoliation provides a good example of high-quality monolayer graphene: easy to obtain and characterize, homogeneously non-defective, and big enough domains for the current technologies to fabricate FET devices. The transfer characteristics of the FET device obtained are similar to the ones

reported previously, which can ensure the reproducibility of the process from small to big scale. The results in the carrier mobility of our graphene-based transistor on silica are comparable to the ones obtained in literature. Although our SLG FET can be improved with respect to conductivity, it might prove very interesting for applications in transistors and in transparent-conductive layers.

- SHI irradiation under glancing incidence can be used to introduce foldings in a variety of two dimensional materials like graphene, MoS_2 and hexagonal BN. Foldings can be introduced in two dimensional materials like CVD graphene and CNM, which are grown on a large scale, as well. It has been shown that an interfacial layer of water or adsorbates is necessary for the folding mechanism to take place and that crystalline quality of the material determines the quality of the resulting folding.

- Regarding the CVD technique, the presence of pure, crystalline, and flat enough surface of the catalysts is needed for high-quality graphene layers. If the starting copper surface is too rough or it has crystalline defects, the carbon species would find too many nucleation sites, producing defects in the graphene layer. These defects can facilitate the formation of disordered islands of a-C, graphene multilayers, and other defective carbon structures on the surface of the copper.

- Thin sputtered Cu/Si films, which are amorphous but thick enough to avoid the complete diffusion and evaporation, proved to be useful substrates for the successful deposition of carbon directly onto Si wafers. Although in the preliminary work most of the carbon layers were amorphous, FLG grew locally in the form of flakes.

- Raman measurements showed the presence of FLG on bulk Cu substrates with a diamond lapped surface. The D band suggests a low crystallinity of FLG sheets of about 4-10 layers. Taking into account the crystal domains of Cu, it was estimated an average domain of 10 μm for graphene. These results also demonstrated the feasibility of the hot-wire heating to grow graphene on copper

substrates and the use of acetylene for the growth process at lower temperatures.

- In the sputtered substrates, 600 nm films of Cu with 100 nm Ni barrier previously deposited on polished c-Si wafers slightly dewetted intro droplets and islands during the annealing process. These structures were observed by optical and electronic microscopes, and the EDS confirms the chemical composition of these structures: Cu, Ni, Si, and C are present in the surface after the whole process. The real phenomenon occurring in this type of substrate during the annealing is affected by the eutectic alloy between Cu and Si. This lowers the melting point of both elements creating a more complex surface where the graphene affinity is surprisingly high.

- Graphene was successfully grown on thin films of sputtered Cu/Ni and on c-Si by the Low-Pressure Pulsed-CVD; reducing the deposition time to the order of 10 s using pulses of methane of a partial pressure up to 10^{-4} Pa. The Raman analysis, SEM and EDS assessed the only presence of graphene of one-two layers by showing the characteristic 2D band and a ratio $I_{2D}/I_G \geq 1$. Raman spectra also reflect the presence of graphene defects, probably due to the existence of multiple crystalline terraces and edges, evidenced by SEM. And also probably because of the irregular surface of the substrate/catalyst. Nonetheless, Raman mapping assessed the presence of large-area graphene up to 10^4 μm^2.

- Most of the best results of the synthesized graphene were with no hydrogen added. Although it works as a catalyst as well, the etching effect of hydrogen over graphene limits its growth dramatically for the low-pressures used in this work.

- Raman analysis presented the side effects of the fluorescence of the underlying copper, and the addition of new peaks from copper. This hampered the extraction of high signal to noise ratio spectra compared to the Raman signals from exfoliated graphene directly

on silicon oxide. However, it still was a valuable, fast and easy tool to check the presence of carbon in any form.

- Graphene also grew on Cu foils efficiently, having large crystalline domains and much less defective layers, as we expected from the reported works found in literature. The importance of flat and smooth surfaces of the metallic catalyst, and high process temperatures are translated into smaller D peaks from the Raman analysis.

- The use of new precursors like benzene or toluene can enlarge the list of parameters to obtain a high-performance graphene-based product. Having a lower pyrolysis temperature (500 °C), allows reducing the process temperature up to the half of the standard processes facilitating the industrial scalability. Even so, the change in the precursor gas suggests other changes in the system and the method in order to obtain high-quality graphene.

- The transfer process is still a drawback in the production of graphene by CVD. The removal of the underlying metal adds a few chemical steps that complicate the final quality of graphene. In this work a standard transfer process from copper to silicon (through PMMA) was made with good results. The graphene transferred had similar characteristics to the one present on copper, but the addition of this step reduces the industrial scalability.

- Finally, the results assessed the use of our Low-pressure Pulsed-CVD technology, based on very low pressure pulses of precursor gas by means of the monolayer formation time equation. It allows the growth of large area single and bi-layer graphene with a formation/deposition time of only 10 s with just a 10^{-4} Pa pulse of methane. However, further work is necessary to optimize the theoretical approach of the monolayer-formation time equation: the sticking coefficient needs to be strictly evaluated; as well as the the importance of the copper layer thickness, the optimal annealing conditions, and the removing of the Cu/Ni during annealing after the CVD process to grow graphene only on silicon or silicon dioxide.

This is especially important in the application of lithographic processes and the possibility to produce graphene-based electronic devices.

Publications and communications

Articles

- "Investigation of monolayer-formation time for the synthesis of graphene on copper/nickel/silicon using very-low pressure pulses of methane", V.-M. Freire, A. Ramírez, E. Pascual, E. Bertran, J.-L. Andújar, arXiv:1406.2640 (2014) (submitted)

- "Folding two dimensional crystals by Swift Heavy Ion irradiation", O. Ochedowski, H. Bukowska, V.-M. Freire, L. Brökers, H. Lebius, M. Schleberger, Nuclear Instruments and Methods in Physics Research (2014) (accepted)

- "Hot Wire Chemical Vapor Deposition of Few-layer Graphene on Copper", V.-M. Freire, J. Badia-Canal, C. Corbella, E. Pascual, E. Bertran, J.-L. Andújar, Japanese Journal of Applied Physics 52 (2013) 01AK02 (http://jjap.jsap.jp/link?JJAP/52/01AK02/)

- "Anisotropic surface properties of micro/nanostructured a-C:H:F thin films with self-assembly applications", V.-M. Freire, C. Corbella, E. Bertran, S. Portal-Marco, M. Rubio-Roy, J.-L. Andújar, Journal of Applied Physics 111 (2012) 124323 (http://scitation.aip.org/content/aip/journal/jap/111/12/10.1063/1.4730783)

- "Nanostructured DLC coatings for self-assembly applications", E. Bertran, V.-M. Freire, E. J. Cabrera, C. Corbella, S. Portal, E. Pascual, J.-L. Andújar, Proceedings of the ICCE-19 Shanghai in World Journal of Engineering, p. 109 (2011) (http://wjoe.hebeu.edu.cn/mulu.sup.1.2011.htm)

- "Nanostructured DLC coatings for self-assembly applications", V.-M. Freire, Dipòsit digital de la UB (2010) (http://diposit.ub.edu/dspace/handle/2445/14103)

Patents

- "Process for the controlled production of graphene at very low pressure and device to carry out the process" ("Procedimiento para la producción

controlada de grafeno a muy baja presión y dispositivo para llevar a cabo el procedimiento"). E. Bertran, V.-M. Freire, A. Ramírez, E. Pascual, J.-L. Andújar. ES 201330585 (OEPM), PCT/ES2014/070295 (PCT) and AVCRI189 (FBG). (2013) (accepted and to be published in BOPI) http://www.fbg.ub.edu/images/AVCRI189_Flyer_Physical-materials-nanotechnology.pdf

Congresses

2014

- Campus Physis 2014. Barcelona (Spain)
  Oral contribution, plenary session: Grafè: El material del segle XXI
  V.-M. Freire

- VI Jornada IN^{2}UB. Universitat de Barcelona, Barcelona (Spain)
  Poster: Investigation of monolayer-formation time for the synthesis of graphene on copper/nickel/silicon using very-low pressure pulses of methane
  V.-M. Freire, A. Ramírez, S. Chaitoglou, E. Bertran, E. Pascual, J.-L. Andújar

2013

- Trends in NanoTechnology (TNT 2013). Sevilla (Spain)
  Poster: Modified Chemical Vapor Deposition Technology to Produce Graphene with Very-Low Pressure Pulses of Methane
  V.-M. Freire, S. Chaitoglou, A. Ramírez, E. Pascual, J.-L. Andújar, E. Bertran

- Campus Physis 2013. Barcelona (Spain)
  Oral contribution, plenary session: Grafè: És el material del segle XXI?
  V.-M. Freire

- ImagineNano, Graphene 2013. Bilbao (Spain)
  Oral contribution: Exploring new ways of chemical vapor deposition technology to produce graphene
  V.-M. Freire, S. Chaitoglou, A. Ramírez, M. Reza Sanaee, E. Pascual, J.-L. Andújar, E. Bertran
  Poster: Design and synthesis of carbon encapsulated iron nanoparticle for drug delivery (NanoBio 2013)
  M. Reeza Sanaee, S. Chaitoglou, V.-M. Freire, N. Aguiló-Aguayo, E. Bertran

Poster: Study of carbon encapsulated iron nanoparticles produced by a modified arc discharge by applying nitrogen, argon and helium (NanoSpain 2013)
M. Reeza Sanaee, S. Chaitoglou, V.-M. Freire, N. Aguiló-Aguayo, E. Bertran

- Jornada d'Investigadors Predoctorals Interdisciplinària (JIPI). Barcelona (Spain)
  Oral presentation: Synthesizing graphene by Chemical Vapor Deposition
  V.-M. Freire

2012

- V Jornada IN^2UB. Barcelona (Spain)
  Poster: Single and bilayer graphene growth at very low methane pressure
  V.-M. Freire, A. Ramírez, E. Bertran, E. Pascual, J.-L. Andújar

- Graphene Nanoscience: from Dirac Physics to Applications (GRANADA'12). Granada (Spain)
  Poster: Structural characterization of CVD few layers graphene by Raman
  V.-M. Freire, A. Ramírez, I. Rodríguez-García, E. Pascual, J.-L. Andújar, C. Corbella, N. Ferrer-Anglada, E. Bertran

- 23rd International Conference on Diamond and Carbon Materials (Diamond 2012)
  Poster: Single and bilayer graphene growth at very low methane pressure
  V.-M. Freire, A. Ramírez, E. Bertran, E. Pascual, J.-L. Andújar

- 4th International Symposium on Advanced Plasma Science and its Applications for Nitrides and Nanomaterials (ISPlasma 2012). Nagoya (Japan)
  Poster: Micro/Nanostructured patterns with a-C:H:F thin films of anisotropic properties grown by plasma CVD
  V.-M. Freire, E. Bertran, C. Corbella, S. Portal, J. Ingla, J.-L. Andújar
  Poster: Graphene deposited on copper substrate by hot wire CVD
  V.-M. Freire, J. Badia-Canal, C. Corbella, E. Pascual, E. Bertran, J.-L. Andújar

- 1st Flash Talks Meeting. Barcelona (Spain)
  Oral contribution: Synthesis of graphene by CVD
  V.-M. Freire

2011

- IV Jornada IN^{2}UB. Barcelona (Spain)
  Poster: Graphene deposited on copper by Hot Wire CVD
  V.-M. Freire, E. Bertran, J. Badia-Canal, C. Corbella, E. Pascual, J.-L. Andújar

- Specialist Meeting on Carbon, SMC 2011. Puerto Vallarta (Mexico)
  Oral contribution: Micro/nanostructured surfaces of amorphous carbon films with anisotropic properties
  C. Corbella, S. Portal-Marco, M. Rubio-Roy, G. Oncins, V.-M. Freire, M.A. Vallvé, J. Ignés-Mullol, E. Bertran, J.-L. Andújar

- IV International Conference on Surfaces, Materials and Vacuum. Puerto Vallarta (Mexico)
  Oral contribution: Micro/nanostructured surfaces of DLC-based films grown by plasma CVD
  C. Corbella, V.-M. Freire, S. Portal-Marco, M. Rubio-Roy, G. Oncins, M.A. Vallvé, J. Ignés-Mullol, E. Bertran, J.-L. Andújar

- European Conference on Diamond, Diamond-Like Materials, Carbon Nanotubes, and Nitrides. Garmisch-Partenkirchen (Germany)
  Poster: Graphene layers deposition on copper substrates by hot wire CVD
  V.-M. Freire, E. Bertran, J. Badia-Canal, C. Corbella, E. Pascual, J.-L. Andújar

- The Nineteenth Annual International Conference on Composites/Nano Engineering, ICCE-19. Shanghai (China)
  Invited oral contribution: Nanostructured DLC coatings for self-assembly applications
  E. Bertran, V.-M. Freire, E.J. Cabrera, C. Corbella, S. Portal, E. Pascual, J. Ingla, J.-L. Andújar

- 38th International Congres of Metallic Coatings and Thin Films (ICMTCF 2011). San Diego (USA)
  Oral contribution: Micro/Nanostructured Surfaces of a-C:H:F Films with Anisotropic Properties
  V.-M. Freire, C. Corbella C., S. Portal, G. Oncins, E. Bertran, J.-L. Andújar
  Poster: Graphene Layers Deposited by Hot Wire CVD
  C. Corbella, J. Badia-Canal, V.-M. Freire, E. Bertran, J.-L. Andújar
  Poster: Fabrication of Nanoimprint Molds by Sub-Micron Sphere

Lithography
S. Portal, C. Corbella, E. Cabrera, V.-M. Freire, E. Pascual, J.-L. Andújar, E. Bertran

- ImagineNano, Graphene2011. Bilbao (Spain)
  Poster: Graphene layers deposited on copper substrate by hot wire CVD
  J. Badia-Canal, V.-M. Freire, C. Corbella, M. Rubio-Roy, E. Pascual, E. Bertran, J.-L. Andújar

2010

- 11th European Vacuum Conference, EVC-11. Salamanca (Spain)
  Invited oral contribution: Tribological and Surface Behaviour of DLC Coatings
  E. Bertran, M. Rubio-Roy, C. Corbella, V.-M. Freire, J.-L. Andújar

Research stay

Research stay of 3 months (September-December 2013) in Duisburg-Essen Universität, Duisburg (Germany). The responsible of the group was Prof. Dr. Marika Schleberger of the Fakultät für Physik (Experimentalphysik). My work, with Oliver Ochedowski, consisted on mastering the technique of mechanical exfoliation of graphene and MoS_2; characterization of the samples by means of Raman spectroscopy and AFM; field effect devices and transport characteristics; and implementing experiments at the swift heavy ion accelerator (GANIL) in Caen, France. Successful results were included in a publication.

FEMAN seminars (oral contributions)

- PhD stay in the Duisburg-Essen University: Swift Heavy Ion irradiation effects on graphene (2013)
  V.-M. Freire, O. Ochedowski, M. Schleberger

- Diamond 2012: Single and bilayer graphene growth at very low methane pressure (2012)
  V.-M. Freire, A. Ramírez, E. Bertran, E. Pascual, J.-L. Andújar

- ICTMCF 2011: Micro/Nanostructured Surfaces of a-C:H:F Films with Anisotropic Properties (2011)
  V.-M. Freire, C. Corbella, S. Portal, G. Oncins, E. Bertran, J.-L. Andújar

- Master Thesis: Nanostructured DLC coatings for self-assembly applications (2010)
  V.-M. Freire, C. Corbella, E. Bertran

Attended Seminars

2014

- Festival Ciència, Tecnologia i Innovació: "Grafè, recerca i empresa. Una aposta excepcional per a la innovació i la competitivitat a Europa", A. Ferrari. Ajuntament de Barcelona, Barcelona (Spain)
  V.-M. Freire, E. Bertran, E. Pascual
- CCiTUB seminars on "RamanDay: Workshop on Advanced Applied Raman Spectroscopy". CCiTUB, Barcelona (Spain)
  V.-M. Freire, S. Chaitoglou
- 2ª Jornada d'Investigadors Predoctorals Interdisciplinària (JIPI 2014). Universitat de Barcelona, Barcelona (Spain)
  V.-M. Freire, S. Chaitoglou

2013

- CCiTUB seminars on "Determinació de l'estructura cristal·lina a partir de dades de difracció de raigs X de pols. Resultats amb dades procedents de difractòmetres dels CCiTUB". CCiTUB, Barcelona (Spain)
  V.-M. Freire
- Closing Meeting on *Graphene*. ICMM, Madrid (Spain)
  V.-M. Freire, E. Bertran, E. Pascual
- Thermo Fisher Scientific Webinar on "Characterizing New Graphene Devices with Raman and X-ray Photoelectron Spectroscopy"
  V.-M. Freire

2012

- Train2 Nanoscience International Conference. World Trade Center, Barcelona (Spain)
  V.-M. Freire

2011

- Sectorial Meeting on *Graphene* for ITC's. ICFO, Barcelona (Spain)
  V.-M. Freire, E. J. Cabrera, E. Bertran, E. Pascual

- BCNano'11. Barcelona (Spain)
  Live AFM-RAMAN combination: new perspectives with RENISHAW / NANONICS (SCIENTEC)
  V.-M. Freire

- European Conference on Diamond, Diamond-Like Materials, Carbon Nanotubes, and Nitrides. Garmisch-Partenkirchen (Germany)
  V.-M. Freire
  Workshop: Combined approaches to graphene and carbon analysis using Raman spectroscopy and XPS

- Thermo Fisher Scientific Webinar on Raman Spectroscopy "Rethinking Raman"
  V.-M. Freire

- Raith GmbH 17th Seminar on Electron and Ion Beam Lithography for Applications in Nanotechnology. Dortmund (Germany)
  V.-M. Freire, S. Portal-Marco

Appendixes

A. REVIEW ON CHEMICAL VAPOR DEPOSITION

History

CVD is not a new process. As stated in the pioneer work of Powell, Oxley, and Blocher, its first practical use was developed in the 1880s in the production of incandescent lamps to improve the strength of filaments by coating them with carbon or metal. In the same decade, the carbonyl process was developed by Ludwig Mond and others for the production of pure nickel. A number of patents were issued during that period covering the basis of CVD.

CVD developed slowly in the next fifty years and was limited mostly to extraction and pyrometallurgy for the production of high-purity refractory metals such as tantalum, titanium, and zirconium. Several classical CVD reactions were developed at that time including the carbonyl cycle (the Mond process), the iodide decomposition (the de Boer-Van Arkel process) and the magnesium-reduction reaction (the Kroll process). At the end of World War II, CVD expanded rapidly and its importance has been growing ever since:

1960: Introduction of the terms *CVD* and *PVD* to distinguish "Chemical Vapor Deposition" from "Physical Vapor Deposition." Introduction of CVD in semiconductor fabrication. First TiC coating on cemented carbide tools introduced and development of CVD tungsten.

1963: Introduction of Plasma CVD in electronics.

1968: Start of industrial use of CVD coated cemented carbides.

1980s: Introduction of CVD diamond coatings.

1990s: Rapid expansion of metallo-organic CVD (MOCVD) for ceramic and metal deposition.

1990s: Development of cluster tools combining CVD, PVD and other processing steps in a single tool for semiconductor fabrication. Major development of CVD in optics and optoelectronics.

It took over a century of steady and continuous scientific and engineering efforts to reach the present state of the art. Yet, many formidable

challenges remain, such as the accurate prediction of a given CVD composition and its structure and properties. In fact, even though the understanding of the theory and mechanism of CVD has made great advances, the process is still often considered as much an art as a science and progress continues to rely for a large part on experimental developments.

Basics

Chemical vapor deposition is a synthesis process in which the chemical constituents react in the vapor phase near or on a heated substrate to form a solid deposit. The CVD technology combines several scientific and engineering disciplines including thermodynamics, plasma physics, kinetics, fluid dynamics, and of course chemistry. The number of chemical reactions used in CVD is considerable and include thermal decomposition (pyrolysis), reduction, hydrolysis, disproportionation, oxidation, carburization, and nitridation. They can be used either singly or in combination. The most important methods to activate these reactions are as follows:

- Thermal activation which typically takes place at high temperatures, i.e., >900 °C, although the temperature can also be lowered considerably if metallo-organic precursors are used (MOCVD).
- Plasma activation which typically takes place at much lower temperatures, i.e., from Room Temperature to 500 °C.
- Photon activation, usually with shortwave ultraviolet radiation, which can occur by the direct activation of a reactant or by the activation of an intermediate.

Until recently, most CVD operations were relatively simple and could be readily optimized experimentally by changing the reaction chemistry, the activation method, or the deposition variables until a satisfactory deposit was achieved. However, many of the CVD processes are becoming increasingly complicated with much more exacting requirements, which would make the empirical approach too inconvenient. A theoretical

analysis is, in most cases, an essential step which should predict any of the following:

- Chemistry of the reaction (intermediate steps, by-products).
- Reaction mechanism.
- Composition of the deposit (i.e., stoichiometry).
- Structure of the deposit (i.e., the geometric arrangement of its atoms).

This analysis may then provide a guideline for an experimental program and considerably reduce its scope and save a great deal of time and effort.

A CVD reaction is governed by *thermodynamics,* that is the driving force which indicates the direction the reaction is going to proceed; and by *kinetics*, which defines the transport process and determines the rate-control mechanism, in other words, how fast it is going.

Thermodynamics

Chemical thermodynamics is concerned with the interrelation of various forms of energy and the transfer of energy from one chemical system to another in accordance with the first and second laws of thermodynamics. In the case of CVD, this transfer occurs when the gaseous compounds, introduced in the deposition chamber, react to form the solid deposit and by-products gases.

The first step of a theoretical analysis is to ensure that the desired CVD reaction will take place; if the transfer of energy—the free energy change of the reaction known as ΔGr—is negative. The relationship is expressed by the following equation:

$$\Delta G_r^\circ = \sum \Delta G_f^\circ \text{ products} - \sum \Delta G_f^\circ \text{ reactants} \quad \text{(A.1)}$$

The free energy of formation is not a fixed value but varies as a function of several parameters which include the type of reactants, the molar ratio of these reactants, the process temperature, and the process pressure. This relationship is represented by the following equation:

$$\Delta G_r = \Delta G_f^\circ + RT\, lnQ \quad \text{(A.2)}$$

where: $\Delta G_r^o = \sum z_i^i \Delta G_{f,i}^o$, z_i = stoichiometric coefficient of species "i" in the CVD reaction (negative for reactants, positive for products), $\Delta G^o{}_{f,i}$ = standard free energy of formation of species "i" at temperature T and 1 atm, R = gas constant, T = absolute temperature, $Q = \prod_i a_i^{zi}$, a_i = activity of species "i" which is = 1 for pure solids and = $p_i = x_i P_T$ for gases, p_i = partial pressure of species "i", x_i = mole fraction of species "i", and P_T = total pressure.

It should be first realized that any CVD process is subject to complicated fluid dynamics. The fluid, in this case a combination of gases, is forced through pipes, valves, and various chambers and, at the same time, is the object of large variations in temperature and to a lesser degree of pressure before it comes in contact with the substrate where the deposition reaction takes place. The reaction is heterogeneous, which means that it involves a change of state, in this case from gaseous to solid. The sequence of events taking place during a CVD reaction can be summarized as follows:

a) Transport of the reactants from the gas inlets by forced flow to the reaction zone.
b) Reactions in vapor-phase that form the gas precursors of the film and by-products.
c) Transport of the reactants and their products from the gas phase to the substrate through the boundary layer.
d) Adsorption of these species on the substrate surface.
e) Surface diffusion, chemical reactions and incorporation of these species on different growth sites.
f) Desorption of the volatile by-products of surface reactions, through the boundary layer.
g) Transport of the by-products away from the reaction zone.

These steps occur in the sequence shown and the slowest step determines the deposition rate. The rules of the boundary layer apply in most CVD depositions in the viscous flow range where pressure is relatively high. In cases where very low pressure is used (i.e., in the mTorr range), the rules could no longer be applicable.

Kinetics and mass transport

The behavior of the gas as it flows down the tube is controlled by fluid mechanics. The Reynolds number, R_e, which is a dimensionless parameter that characterizes the flow of a fluid, is such that the gas flow is generally laminar, although in some instances the laminar flow may be disturbed by convective gas motion and may become turbulent. In the case of laminar flow, the velocity of the gas at the deposition surface (the inner wall of the tube) is zero. The boundary is that region in which the flow velocity changes from zero at the wall to essentially that of the bulk gas away from the wall. This boundary layer starts at the inlet of the tube and increases in thickness until the flow becomes stabilized. The reactant gases flowing above the boundary layer have to diffuse through this layer to reach the deposition surface. The thickness of the boundary layer, Δ, is inversely proportional to the square root of the Reynolds number as follows:

$$\Delta = \sqrt{\frac{x}{\mathrm{R_e}}} \qquad \text{(A.3)}$$

Where: $\mathrm{R_e} = \frac{\rho u_x}{\mu}$, ρ = mass density, u = flow density, x = distance from inlet in flow direction, and μ = viscosity. This means that the thickness of the boundary layer increases with lower gas-flow velocity and with increased distance from the tube inlet.

As mentioned above, a steep velocity gradient is noticeable going from maximum velocity at the center of the tube to zero velocity at the surface of the wall. The gradient is also shallow at the entrance of the tube and increases gradually toward downstream.

The temperature boundary layer is similar to the velocity layer. The flowing gases heat rapidly as they come in contact with the hot surface of the tube, resulting in a steep temperature gradient. The average temperature increases toward downstream.

The boundary layers for these three variables (gas velocity, temperature, and concentration) may sometimes coincide, although in slow reactions, the profiles of velocity and temperature may be fully developed at an early stage while the deposition reaction is spread far downstream the tube.

The rate-limiting step is generally determined by either the surface reaction kinetics or by mass transport. In the case of control by surface reaction kinetics, the rate is dependent on the amount of reactant gases available. But, when the process is limited by mass-transport phenomena, the controlling factors are the diffusion rate of the reactant through the boundary layer and the diffusion out through this layer of the gaseous by-products. This usually happens when pressure and temperature are high; the decomposition reaction occurs more rapidly since the temperature is higher and any molecule that reaches the surface reacts instantly.
To sum up, the surface kinetics (or near surface kinetics) is the limiting step at lower temperature and diffusion is the rate limiting step at higher temperature. Pressure is similar to temperature as a rate limiting factor since the diffusibility of a gas is inversely related to its pressure. At low pressure, surface reaction is the rate determining step and the mass-transfer variables are far less critical than at atmospheric pressure.

It can be now seen that, by proper manipulation of the process parameters and reactor geometry, it is possible to control the reaction and the deposition to a great degree. The gas velocity is essentially constant and the boundary layer gradually increases in thickness toward downstream. This means that the thickness of the deposit will decrease as the distance from the tube inlet increases. This thickness decrease can be offset and a more constant thickness obtained simply by tilting the susceptor (substrate), as shown in figure 3.3. This increases the gas velocity due the flow constriction; the Reynolds number goes up; the boundary layer decreases and the deposition rate is more uniform.

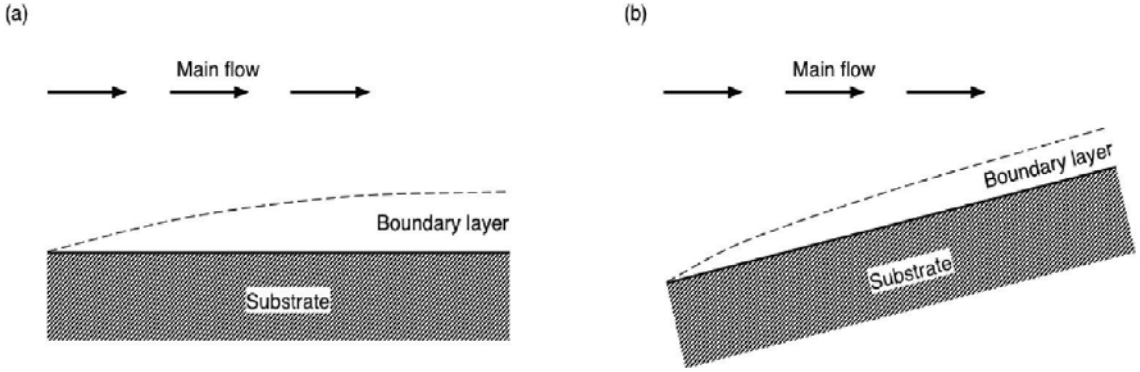

Figure A.1: An example of a boundary layer above the substrate surface. (a) The substrate surface is parallel to the main flow. (b) The substrate is tilted to enhance the thickness uniformity of the boundary layer based on fluid dynamics.

CVD mechanisms

The manner in which a film is formed on a surface by CVD is still a matter of controversy and several theories have been advanced to describe the phenomena. A thermodynamic theory proposes that a solid nucleus is formed from supersaturated vapor as a result of the difference between the surface free energy and the bulk free energy of the nucleus. Another and newer theory is based on atomistic nucleation and combines chemical bonding of solid surfaces and statistical mechanics. There are, however, three important factors that control the nature and properties of the deposit to some degree which must be reviewed at this time: epitaxy, gas-phase precipitation, and thermal expansion.

The nature of the deposit and the rate of nucleation at the very beginning of the deposition are affected, among other factors, by the nature of the substrate. A specific case is that of epitaxy where the structure of the substrate essentially controls the structure of the deposit. Epitaxy can be defined as the growth of a crystalline film on a crystalline substrate, with the substrate acting as a seed crystal.

A CVD reaction may occur in the gas phase instead of at the substrate surface if the supersaturation of the reactive gases and the temperature are sufficiently high. The CVD reactions can be classified in several major categories:

- **Thermal-Decomposition (or Pyrolysis) Reactions:** In thermal-decomposition reactions, a molecule is split into its elements and/or a more elementary molecule. Such reactions are the simplest since only one precursor gas is required. ***Hydrocarbon Decomposition:*** This reaction is used extensively in the general production of carbon, graphite, diamond, nanotubes and graphene, and it is the one mainly used in this work. There are also the ***Halide***, ***Carbonyl*** and ***Hydride Decomposition*****.**

- **Hydrogen Reduction:** Reduction is a chemical reaction in which an element gains an electron; the oxidation state is lowered. Reduction reactions are widely used, particularly the hydrogen reduction of the halides. It is also performed in some of the experiments in this thesis.

- **Coreduction:** The deposition of a binary compound can be achieved by a coreduction reaction. In this manner, ceramic materials such as oxides, carbides, nitrides, borides, and silicides can be produced readily and usually more readily than the parent metal.

- **Metal Reduction of the Halides:** Although hydrogen is the most common reductant, there are other elements which are more powerful, such as zinc, cadmium, magnesium, sodium, and potassium.

- **Oxidation and Hydrolysis Reactions:** Oxidation and hydrolysis are used in the formation of oxides. Common sources of oxygen are the element itself and CO_2.

- **Carbidization and Nitridation:** The deposition of carbides (carbidization) is usually obtained by reacting a halide with a hydrocarbon, such as methane.

Moreover, the choice of the proper reactants (the precursors) is very important, and is governed by certain general characteristics: Stability at room temperature, ability to react cleanly in the reaction zone, sufficient volatility at low temperature so that it can be easily transported to the reaction zone without condensing in the lines, capability of being produced in a very high degree of purity, and ability to react without producing side reactions or parasitic reactions.

Carbon

In the case of carbon produced by CVD processes, graphite is probably the most similar case to graphene. Here is exposed a series of hints that could be of interest as an introduction to our case.

Graphite is commonly produced by CVD and is often referred to as pyrolytic graphite. The CVD of graphite is theoretically simple and is based on the thermal decomposition (pyrolysis) of a hydrocarbon gas. The most common precursor is methane (CH_4), which is generally pyrolyzed at 1000 °C, over a wide range of pressure from about 100 Pa (0.001 atm) to 10^5 Pa (1 atm). The reaction in a simplified form is as follows:

$$CH_4(g) = C(s) + 2H_2(g) \quad (A.4)$$

Other common precursors are acetylene (C_2H_2) and ethylene (C_2H_6). Acetylene can also be decomposed at lower temperatures (300–750 °C) and at pressures up to 1 atm, in the presence of a nickel catalyst. Another common precursor is propylene (C_3H_6), which decomposes in the 1000–1400 °C temperature range at lower pressure (≈1.3 x 10^4 Pa or 100 Torr).

The effect of Pressure. CVD graphite with greater uniformity, better coverage, and improved quality is generally obtained at low deposition pressure. Pressure controls the thickness of the surface boundary layer and consequently the degree of diffusion. At low pressure, the diffusion process is minimized and surface kinetics becomes the rate-controlling factor. Deposits obtained at low pressure tend to be isotropic. At higher pressure (i.e., atmospheric), the reactant gas must be diluted with a non-reactive gas, such as hydrogen or argon, to prevent vapor-phase precipitation, while generally no dilution is necessary at low pressure.

The effect of C/H Ratio. The carbon-to-hydrogen (C/H) ratio of the gas mixture (CH_4 and H_2) entering the reaction chamber is an important factor in the control of the nature of the deposition. Higher C/H ratios (such as 1/4) favor laminar deposition and lower ratios (such as 1/14) favor isotropic deposition.

The effect of Temperature. Generally, isotropic deposits are obtained at higher temperatures (> 1400 °C) and laminar and columnar deposits at lower temperatures.

In summary, isotropic deposits are obtained at high temperature, low pressures, and low C/H ratio. The opposite conditions favor the deposition of laminar and columnar deposits.

Equipment

A CVD reaction can occur in one of two basic systems: a closed or an open reactor. The closed-reactor system, was the first type to be used for the purification of metals. It is a hybrid process which combines vapor-phase

transfer with solid-state diffusion. As the name implies, the chemicals are loaded in a container which is then tightly closed. A temperature differential is then applied which provides the driving force for the reaction.

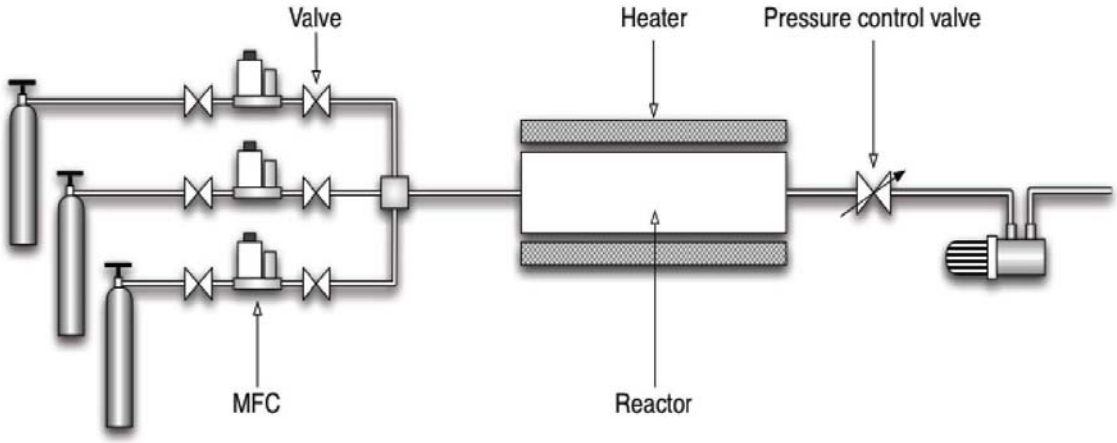

Figure A.2: The schematic diagram of a typical tube-furnace CVD system. Gas flows are regulated by MFCs, and fed into the reactor through a gas-distribution unit. Chemical deposition takes place in the reactor that is heated by the outside heaters. The exhaust gases are removed by vacuum pumps.

As opposed to closed-reactor CVD, is the other CVD system is known as open-reactor or flowing-gas CVD, where the reactants are introduced continuously and flow through the reactor. Closed-reactor CVD was by far the most common system, but now flowing-gas reactors are becoming more popular. It comprises three interrelated components:

• **The reactant supply:** The reactants must be transported and metered in a controlled manner into the reactor. In the case of **gaseous reactants**, this does not present any particular problem and is accomplished by means of pressure controllers, gauges, flow meters, and mass-flow controllers.

Other CVD reactants are **liquid** at room temperature. They must be heated to their evaporation temperature and transported into the reaction chamber by a carrier gas, which may be an inert gas such as argon, or another reactant such as hydrogen.

And reactants which are **solid** at room temperature present more of a problem since they must be heated to their vaporization temperature, which in some cases may be relatively high.

Presently, there is the need for an ever increasing degree of purity of the precursor materials since impurities are the major source of defects in the deposit. The purity of a gas is expressed in terms of nines, for instance, five nines, meaning a gas that is 99.999% pure, which is now a common requirement. It is also expressed in ppm (parts per million) or ppb (parts per billion) of impurity content.

• **The deposition system or reactor:** As stated in the introduction to this chapter, CVD can be classified by the method used to apply the energy necessary to activate the CVD reaction (temperature, photon, or plasma). Thus, different heating methods will affect the reactor design.

Thermal CVD requires high temperature, generally from 800 to 2000 ^{o}C, which can be generated by resistance heating, high-frequency induction, radiant heating, hot plate heating, or any combination of these. Thermal CVD can be divided into two basic systems known as hot-wall reactor and cold-wall reactor.

Hot-Wall Reactors. A hot-wall reactor is essentially an isothermal furnace, which is often heated by resistance elements. The parts to be coated are loaded in the reactor, the temperature is raised to the desired level, and the reaction gases are introduced.

Cold-Wall Reactors. In a cold-wall reactor, the substrate to be coated is heated directly either by induction or by radiant heating while the rest of the reactor remains cool, or at least cooler. Most CVD reactions are endothermic (they absorb heat) and deposition takes place preferentially on the surfaces where the temperature is the highest, in this case the substrate. The walls of the reactor, which are cooler, remain uncoated.

Atmospheric and Low-Pressure Reactors. As shown before, the effect of pressure on the nature of the deposit is considerable. In practical terms, this means that low pressure generally provides deposits with greater uniformity, better step coverage, and improved quality.

Ultra-High Vacuum (UHV) Reactors. CVD reactions at extremely low pressures ($< 10^{-7}$ Torr) are being developed for the deposition of

semiconductor materials, such as silicon-germanium and some optoelectronic materials. Advantages appear to be better control of the deposit structure and reduction of impurities.

• **The exhaust system (and by-product disposal):** CVD can usually work under higher pressures than the ones necessary with sputtering, MBE, and other PVD processes. Consequently the vacuum system can be simpler and less costly. Mechanical pumps are adequate for many operations, although turbomolecular pumps translate into purer processes and can reach the UHV range. A major disadvantage of CVD (as opposed to PVD) is that many precursors are toxic and in some cases lethal even at low concentration (for instance nickel carbonyl, diborane, arsine, and phosphine).

Thermal CVD is the most used variation of any Chemical Vapor Deposition process and the one being developed in this work, but there are other popular choices:

- Laser and Photo CVD
- Chemical Vapor Infiltration (CVI): the gaseous reactants penetrate (or infiltrate) a porous structure which acts as a substrate and which can be an inorganic open foam or a fibrous mat or weave. It is used for the fabrication of carbon-carbon composites for aircraft brakes and silicon carbide composites for aerospace applications.
- Fluidized-bed CVD: is used primarily in coating particles, such as nuclear fuel. A flowing gas imparts quasi-fluid properties to the particles.
- Plasma-CVD: also known as plasma-enhanced CVD (PECVD) or plasma-assisted CVD (PACVD), the reaction is activated by plasma and the deposition temperature is substantially lower. Plasma CVD combines a chemical and a physical process and may be said to bridge the gap between CVD and PVD.

Applications

Coatings are by far the largest area of application of CVD at the present but by no means the only one. Other areas of CVD, such as production of powders, fibers, monoliths, and composites, are growing rapidly. With CVD, it is possible to produce almost any metal and non-metallic element, including carbon or silicon, as well as compounds such as carbides, nitrides, oxides, inter-metallics and many others. This technology is now an essential factor in the manufacture of semiconductors and other electronic components, in the coating of tools bearing and other wear resistant parts and in many optical, opto-electronic and corrosion applications. The reasons for the success of CVD are simple:

- CVD is a relatively uncomplicated and flexible technology which can accommodate many variations.
- With CVD, it is possible to coat almost any shape of almost any size: It is not restricted to a line-of-sight deposition which is a general characteristic of sputtering, evaporation and other PVD processes. As such, CVD has high throwing power.
- Unlike other thin film techniques such as sputtering CVD can also be used to produce fibers, monoliths, foams and powders.
- CVD is economically competitive: The deposition rate is high and thick coatings can be readily obtained (in some cases centimeters thick)

A wide range of CVD products has been released so far and here some examples are shown:

- Diffusion barrier layers for advanced semiconductor integrated circuits of titanium nitride deposited by metallo-organic CVD (MOCVD).
- Diamond-like carbon (DLC) coatings produced by Plasma-CVD for bushings and textile components with much improved wear resistance.

- Titanium carbide and titanium nitride coatings for carbide tools that greatly outperform uncoated tools and are taking an increasing share of the market.
- Iridium, deposited by MOCVD, which has shown remarkable resistance to corrosion in small rocket nozzles at temperatures up to 2000 °C.
- Metallization of semiconductors with copper deposited by MOCVD, replacing aluminum, minimizing electromigration. CVD is now the major process in the production of advanced semiconductor components.
- Energy saving optical coatings for architectural glass by atmospheric-pressure CVD, produced in situ during the processing of float glass.
- Pyrolytic boron-nitride crucibles produced by CVD with outstanding chemical inertness, which are used extensively in the electronic industry.
- CVD boron fibers which are extremely stiff and strong and are used as reinforcement in structural components in aerospace designs.
- High thermal conductivity CVD-diamond films deposited on heat spreaders or heat slugs to dissipate the heat of high-density integrated circuits.
- Synthesis of carbon nanotubes (single and multi-wall) and graphene.

Besides CVD, there are various physical-vapor deposition processes (PVD) such as evaporation, sputtering, molecular-beam epitaxy, and ion plating. CVD has several important advantages which make it the preferred process in many cases. However, it has some disadvantages, a major one being that it is most versatile at temperatures of 600 °C and above; many substrates are not thermally stable at these temperatures. Nevertheless, the development of Plasma-CVD and metallo-organic CVD partially offsets

this problem. Another disadvantage is the requirement of having chemical precursors (the starter materials) with high vapor pressure which are often hazardous and at times extremely toxic. The by-products of the CVD reactions are also toxic and corrosive and must be neutralized, which may be a costly operation.

Extracted and summarized from "Handbook of Chemical Vapor Deposition: Principles, Technology and Applications", Hugh O. Pierson, Noyes Publications, New Jersey (1992), and "Physics and Applications of Graphene – Experiments", Sergey Mikhailov, InTech, Rijeka (2011).

B. PATENT: ES201330585 (OEPM), PCT/ES2014/070295 (PCT), & AVCRI189 (FBG). E. Bertran, V.-M. Freire, A. Ramírez, E. Pascual, J.-L. Andújar. Universitat de Barcelona (Spain).

"Process for the controlled production of graphene at very low pressure and device to carry out the process" (English version)

ABSTRACT

Process for the controlled production of graphene at very low pressure and device to carry out the process

Process and device for preparing a graphene structure from 1 to 5 layers, having control of the number of layers, by chemical vapor deposition process over a specific substrate, at a vacuum pressure up to between 10^{-4}-10^{-5} Pa, and at a temperature of from 500-1050 ºC; based on using a carbon precursor gas with a synchronized sequence of pulses, each pulse has a specific time of exhaustion of the carbon precursor gas due to the pumping, the pulse of pressure consisting of an instantaneous increase of pressure due to the instantaneous opening of a valve, followed by an exponential decrease of the pressure, the number of pulses being in function of the amount of layers to be obtained, and the time between pulses being in function of the specific time of exhaustion of the carbon precursor gas.

C. SAMPLE LIST

TABLE C1: Graphene samples on SiO_2/Si from exfoliated HOPG for SHI experiments

Sample	# graphene flakes	Condition	Size (μm)	Raman results	AFM	SHI
A1_1	1	Clean	11.8	Monolayer	Yes	-
A1_2	2	Clean	21.8 32.4	Monolayer	-	-
A1_3	1	Contaminated	3.7	-	-	-
A2_1	1	Clean	23.6	-	-	-
A2_2	1	Clean	23.5	Monolayer	Yes	-
A2_3	1	Clean	22.2	-	-	-
A3_1	2	Clean	23.1	-	-	-
A3_2	1	Clean	24.4	Monolayer	-	-
A3_3	1	Contaminated	7.4	Monolayer	-	-
A3_4	1	Clean	8.2	Monolayer	Yes	Yes
A4	1	Contaminated	2.1	Bilayer	Yes	-
A5_1	1	Contaminated	6.4	Monolayer	Yes	-
A5_2	1	Contaminated	9.5	Monolayer	-	-
A6_1	2	Clean	14.8 22.5	Monolayer	Yes	Yes
A6_2	1	Clean	24.9	Monolayer	-	-
A6_3	1	Clean	18.3	Monolayer	-	-
A6_4	1	Clean	21.5	Monolayer	-	-
B1_1	2	Clean	19.8 16.9	Monolayer	-	-
B1_2	1	Clean	12.3	Monolayer	-	-
B1_3	2	Clean	19.7 10.9	Monolayer	-	-
B1_4	1	Clean	26.6	Monolayer	Yes	Yes
B2_1	1	Contaminated	13.3	Monolayer	-	-
B2_2	3	Contaminated	7.5 8.1 7.2	Bilayer	Yes	-
B2_3	1	Contaminated	8.8	Bilayer	-	-
B3_1	2	Clean	6.7 6.3	Bilayer	-	-
B3_2	1	Clean	24.5	Monolayer	Yes	Yes
B4_1	1	Clean	8.1	Monolayer	-	-
B4_2	2	Contaminated	14.3 12.5	Monolayer	Yes	-

Sample	# graphene flakes	Condition	Size (μm)	Raman results	AFM	SHI
B5_1	1	Clean	4.4	Bilayer	-	-
B5_2	1	Clean	14.3	Bilayer	Yes	-
B5_3	1	Clean	9.4	Monolayer	Yes	Yes
B5_4	1	Clean	14.2	Bilayer	-	-
B6_1	1	Clean	7.8	Monolayer	Yes	-
B6_2	1	Clean	6.9	Monolayer	-	-
C1_1	1	Clean	6.9	Monolayer	-	-
C1_2	1	Clean	5.3	Monolayer	-	-
C1_3	1	Clean	9.2	Monolayer	-	-
C1_4	1	Clean	24.6	Monolayer	Yes	Yes
C2_1	1	Clean	2.1	Monolayer	-	-
C2_2	1	Clean	4.7	Monolayer	-	-
C2_3	1	Clean	7.4	Monolayer	Yes	Yes
C3_1	1	Clean	4.8	Monolayer	-	-
C3_2	1	Clean	7.1	Monolayer	-	-
C3_3	1	Clean	13.0	Monolayer	-	-
C3_4	2	Clean	18.6 7.5	Monolayer	-	-
C3_5	1	Clean	8.1	Monolayer	Yes	Yes
C4_1	1	Clean	7.1	Monolayer	-	-
C4_2	1	Clean	6.6	Monolayer	Yes	Yes
C5_1	1	Clean	11.6	Monolayer	-	-
C5_2	1	Clean	8.3	Monolayer	Yes	Yes
C5_3	1	Clean	9.9	Monolayer	-	-
C5_4	1	Clean	14.5	Monolayer	-	-
C6_1	1	Cracked	11.6	Monolayer	Yes	-
C6_2	1	Clean	14.6	Monolayer	-	-
C6_3	1	Clean	10.6	Monolayer	-	-
D1_1	2	Clean	7.1 9.0	Monolayer	-	-
D1_2	2	Clean	5.6 7.3	Monolayer	-	-
D1_3	1	Contaminated	5.1	Monolayer	-	-
D1_4	1	Clean	7.1	Monolayer	-	-
D1_5	1	Clean	14.9	Monolayer	Yes	Yes
D1_6	1	Clean	5.9	Monolayer	-	-
D2_1	1	Contaminated	8.4	Monolayer	-	-
D2_2	1	Clean	11.2	Monolayer	-	-
D2_3	1	Clean	8.0	Monolayer	Yes	Yes
D2_4	1	Clean	11.9	Monolayer	-	-
D3_1	1	Clean	13.1	Monolayer	Yes	Yes

Sample	# graphene flakes	Condition	Size (μm)	Raman results	AFM	SHI
D3_2	1	Clean	12.7	Monolayer	-	-
D3_3	1	Clean	10.5	Monolayer	-	-
D4_1	1	Clean	7.7	Monolayer	-	-
D4_2	1	Clean	45.1	Monolayer	Yes	Yes
D4_3	1	Clean	14.3	Monolayer	-	-
D5_1	1	Clean	16.5	Monolayer	-	-
D5_2	1	Clean	9.6	Monolayer	-	-
D5_3	1	Clean	19.1	Monolayer	Yes	Yes
D5_4	1	Clean	14.7	Monolayer	-	-
D6_1	4	Clean	14.7 13.8 12.3 23.1	Monolayer	-	-
D6_2	1	Clean	50.2	Monolayer	Yes	Yes
D6_3	1	Clean	16.9	Monolayer	-	-
E1_1	1	Clean	34.2	Monolayer	Yes	Yes
E1_2	1	Clean	23.3	Monolayer	-	-
E1_3	1	Clean	36.6	Monolayer	-	-
E2_1	1	Clean	9.4	Monolayer	-	-
E2_2	1	Contaminated	8.6	Monolayer	Yes	-
E2_3	1	Clean	8.2	Monolayer	Yes	Yes
E3_1	1	Clean	14.6	Monolayer	-	-
E3_2	1	Clean	14.2	Monolayer	-	-
E3_3	1	Clean	14.3	Monolayer	-	-
E3_4	1	Clean	7.9	Monolayer	Yes	Yes
E4_1	1	Clean	11.0	Monolayer	-	-
E4_2	2	Clean	32.5 9.0	Monolayer	Yes	Yes
E4_3	2	Clean	14.1 18.3	Monolayer	-	-
E5_1	1	Clean	52.5 43.9	Monolayer	Yes	Yes
E5_2	1	Clean	6.8	Monolayer	-	-
E5_3	1	Clean	17.4	Monolayer	-	-
E5_4	1	Clean	39.6	Monolayer	-	-
E6_1	1	Clean	37.6	Monolayer	Yes	Yes
E6_2	2	Clean	11.9 17.7	Monolayer	-	-
F1_1	1	Clean	34.2	Monolayer	-	-
F1_2	1	Clean	33.4	Monolayer	Yes	Yes
F2_1	2	Clean	10.7 5.6	Monolayer	-	-

Sample	# graphene flakes	Condition	Size (μm)	Raman results	AFM	SHI
F2_2	2	Clean	28.1 20.3	Monolayer	Yes	Yes
F3_1	1	Clean	22.6	Monolayer	Yes	Yes
F3_2	1	Clean	9.1	Monolayer	-	-
F3_3	1	Clean	13.4	Monolayer	-	-
F4_1	1	Contaminated	14.9	Monolayer	Yes	-
F4_2	1	Clean	24.7	Monolayer	Yes	-
F5	1	Clean	4.4	Monolayer	Yes	-
F6_1	1	Clean	31.5	Monolayer	-	-
F6_2	1	Clean	23.2	Monolayer	-	-
F6_3	1	Clean	26.4	Monolayer	Yes	Yes

The size represents the biggest of the two dimensions of every flake, with a minimum of 2 μm for the smallest dimension. Anyway, the flakes are normally square and triangle-shaped.

TABLE C2: Graphene samples on SiO_2/Si from exfoliated HOPG for electrical measurements and FET

Sample	# graphene flakes	Condition	Size (μm)	Raman results	FET
1-1	2	Clean	7.9 13,6	-	-
1-2	2	Contaminated	13.4 9.7	-	-
1-3	2	Clean	16.7 13.8	Monolayer	Yes
1-4	1	Contaminated	16.8	-	-
2-1	1	Clean	7.2	-	-
2-2	1	Clean	12.8	-	-
2-3	3	Clean	13.7 11.5 11.3	-	-

The size represents the biggest of the two dimensions of every flake, with a minimum of 2 μm for the smallest dimension. The flakes are normally square and triangle-shaped.

TABLE C3: Graphene samples from the preliminary CVD work

Name	Type	Acid pre-treatment	P_{H2} (mbar)	$P_{process}$ (mbar)	Gas flow rate C_2H_2 (sccm)	Gas flow rate H_2 (sccm)	T_{CVD} (°C)	Raman results
10G15A	Sputtering	No	0,1	0,1	0	87	800	-
10L2101	Sputtering	No	0,1	-	-	35	750	-
10D22A	Sputtering	No	0,1	2,5	60	87	800	a-C
10C25A	Sputtering	No	0,1	2,5	60	35	800	a-C
10C26B	Sputtering	No	0,1	2,5	60	87	800	a-C
11C0101	Sputtering	No	0,5	-	0	0	800	FLG
11C1501	Sputtering	No	0,1	0,5	30	0	800	FLG
11C2201	Cu foil	No	0,1	0,5	30	0	800	a-C
11C3101	Cu foil	No	0,1	0,5	30	0	900	a-C
11C3102	Bulk Cu	No	0,1	0,5	30	0	900	a-C
11D0401	Lapped	No	0,1	0,1	30	0	900	FLG
11D0402	Bulk Cu	No	0,1	0,1	30	0	900	FLG
11D0501	Lapped	No	0,1	0,5	30	0	900	FLG
11D0502	Lapped	Si	0,1	1,0	30	0	900	a-C
11D0503	Bulk Cu	Si	0,1	1,0	30	0	900	a-C
11D0701	Lapped	No	0,1	0,5	35	0	900	FLG
11D0702	Lapped	Si	0,1	0,5	30	0	900	a-C
11D0703	Bulk Cu	Si	0,1	0,5	30	0	900	a-C
11E0702	Bulk Cu	No	0,1	0,5	30	0	900	FLG
11E0703	Sputtering	No	0,1	0,5	30	0	900	FLG
11E0704	Bulk Cu	No	0,1	0,5	30	0	900	FLG
11E2301	Bulk Cu	No	0,1	0,5	35	0	770	FLG

The H_2 pressure corresponds to the gas pressure during the temperature ramp and the CVD.

TABLE C4: Graphene samples from the Pulsed-CVD method

Sample	Type	Thickness (nm)	P_0 (10^{-4} Pa)	Gas	# Pulses	P_{pulses} (Pa)	T_{CVD} (°C)	Raman
12E1001	Sputtering Cu/Ni	100 Ni 600 Cu	1	H_2	1	3	980	Bilayer
12E1002	Sputtering Cu/Ni	100 Ni 600 Cu	3	CH_4	1	$1.3X10^{-4}$	980	Mono & Bilayer
12E1101	Sputtering Cu/Ni	100 Ni 600 Cu	1.7	CH_4 H_2	2 2	$1.3X10^{-5}$ 5	980	Bilayer
12E1501	Sputtering Cu/Ni	100 Ni 600 Cu	1.5	CH_4	1	$1.4X10^{-4}$	990	Mono & Bilayer
12E1502	Sputtering Cu/Ni	100 Ni 600 Cu	1.5	CH_4	1	$1.4X10^{-4}$	1000	Mono & Bilayer
12E1503	Sputtering Cu/Ni	100 Ni 600 Cu	2.4	CH_4 H_2	6 3	$5.3X10^{-5}$ 5	990	Bilayer
12E1504	Sputtering Cu/Ni	100 Ni 600 Cu	2	CH_4 H_2	4 2	$6.6X10^{-4}$ 5	980	Mono & Bilayer
12E2601	Sputtering Cu/Ni	100 Ni 600 Cu	1.8	CH_4	2	$5.3X10^{-5}$	980	Bi & Monolayer
12E3001	Sputtering Cu/Ni	100 Ni 600 Cu	1	-	-	-	965	Bilayer
---	---	---	---	---	---	---	---	---
12K12a	Sputtering Cu	30	1.1	CH_4	1	$1.1X10^{-4}$	900	a-C
12K13a	Sputtering Cu	100	4	-	-	-	700	a-C
12K16a	Sputtering Cu	10	3.6	CH_4	1	$1.2X10^{-4}$	700	Bi & Trilayer
12K19a	Sputtering Cu	55	4.2	CH_4 H_2	3 cnt	$2.1X10^{-4}$ 2.5	850	No C
12K26a	Sputtering Cu	55	5	CH_4	3 cnt	$1.8X10^{-4}$ 2.5	1000	No C
12K27a	Sputtering Cu	100	4.6	H_2	1	5	700	FLG
13B1401	Sputtering Cu	10	0.8	CH_4	2	$7.4X10^{-5}$	1000	a-C
13B1402	Sputtering Cu	10	1.3	-	-	-	1000	a-C
13B1901	Sputtering Cu	10	3.2	CH_4	2	$4.5X10^{-5}$	700	a-C
13B2001	Sputtering Cu	10	2.8	-	-	-	700	No C

Sample	Type	Thickness (nm)	P_0 (10^{-4} Pa)	Gas	# Pulses	P_{pulses} (Pa)	T_{CVD} (°C)	Raman
13B2002	Sputtering Cu	10	6	CH_4 H_2	2 cnt	- 0.5	1000	No C
13B2101	Sputtering Cu	10	5	CH_4 H_2	2 cnt	$4.8X10^{-5}$ 0.5	850	No C
13B2501	Sputtering Cu	50	5	CH_4	1	$2.8X10^{-5}$	700	No C
13B2601	Sputtering Cu	50	2.8	H_2	cnt	2.5	700	N/A
13B2801	Sputtering Cu	50	6	-	-	-	700	a-C
13C0101	Sputtering Cu	10	0.3	CH_4 H_2	2 cnt	$8X10^{-5}$ 2.5	700	No C
13C0401	Sputtering Cu	50	0.7	H_2	cnt	2.5	1000	FLG
13C0402	Sputtering Cu	50	1.5	CH_4	2	$8X10^{-5}$	1000	FLG
13C0501	Sputtering Cu	50	4	H_2	cnt	2.5	700	No C
13C1101	Sputtering Cu	50	5	H_2	cnt	2.5	1000	N/A
13D0901	Sputtering Cu	100	3.8	CH_4	2	$4.8X10^{-4}$	700	N/A
13D1002	Sputtering Cu	100	4.4	CH_4	2	$4.6X10^{-4}$	700	a-C
13D1101	Sputtering Cu	300	3.5	CH_4	2	$3.7X10^{-4}$	1000	No C
13D1102	Sputtering Cu	100	0.2	-	-	-	1000	No C
13D1501	Sputtering Cu	300	1.8	CH_4	2	$2.9X10^{-4}$	1000	No C
13D1601	Sputtering Cu	300	5	CH_4	2	$7.2X10^{-4}$	700	No C
13D1602	Sputtering Cu	300	4.6	-	-	-	700	No C
13D1701	Sputtering Cu	100	4.3	-	-	-	700	FLG
13D2201	Sputtering Cu	100	4.2	H_2	cnt	0.5	850	N/A
13E0701	Sputtering Cu	100	7.8	CH_4 H_2	2 cnt	$5.7X10^{-4}$ 0.5	1000	No C
13E0801	Sputtering Cu	300	6.7	H_2	cnt	0.5	1000	No C

Sample	Type	Thickness (nm)	P_0 (10^{-4} Pa)	Gas	# Pulses	P_{pulses} (Pa)	T_{CVD} (°C)	Raman
13E0901	Sputtering Cu	300	7.2	H_2	cnt	0.5	700	a-C
13E1301	Sputtering Cu	300	8.5	CH_4 H_2	2 cnt	$4.6X10^{-4}$ 0.5	700	No C
13E1302	Sputtering Cu	100	1.7	CH_4 H_2	2 cnt	$3.4X10^{-4}$ 0.5	850	No C
13E1501	Sputtering Cu	100	2.8	CH_4 H_2	2 cnt	$4.1X10^{-4}$ 0.5	700	a-C
13E1601	Sputtering Cu	100	1.5	CH_4 H_2	2 cnt	$4.6X10^{-4}$ 0.5	1000	No C
13F1001	Sputtering Cu	300	1.1	-	-	-	1000	No C
13F1201	Sputtering Cu	300	0.9	CH_4	2	N/A	1000	No C
13F1301	Sputtering Cu	300	2.5	CH_4	2	N/A	1000	No C
13F1701	Sputtering Cu/Ni	100 Ni 300 Cu	0.6	CH_4	2	N/A	1000	No C
13F1702	Sputtering Cu/Ni	100 Ni 500 Cu	0.8	CH_4	2	N/A	1000	a-C
13F1703	Sputtering Cu	500	0.9	CH_4	2	N/A	1000	a-C
13F1801	Sputtering Cu/Ni	100 Ni 500 Cu	0.8	-	-	-	1000	No C
13F2001	Sputtering Cu	600	0.8	-	-	-	1000	No C
13F2002	Cu foil	76200	0.6	CH_4 H_2	8 cnt	N/A 0.5	950	a-C
13F2101	Sputtering Cu	300	0.9	CH_4 H_2	2 2	N/A 5	800-1000	No C
13F2102	Sputtering Cu	300	0.8	CH_4 H_2	3 3	N/A 5	800-900	FLG
13F2501	Sputtering Cu	300	0.9	CH_4 H_2	3 3	N/A 5	800	a-C
13F2502	Sputtering Cu	100	1.2	CH_4	3	N/A	800	a-C
13F2601	Sputtering Cu	300	0.5	-	-	-	980	FLG
13F2602	Sputtering Cu	100	3	CH_4	1	N/A	800	FLG
13F2603	Sputtering Cu	100	2	-	-	-	800	N/A

Sample	**Type**	**Thickness (nm)**	**P_0 (10^{-4} Pa)**	**Gas**	**# Pulses**	**P_{pulses} (Pa)**	**T_{CVD} (°C)**	**Raman**
13F2801	Sputtering Cu	300	0.7	CH_4	1	N/A	892	FLG
13F2901	Sputtering Ni	300	3.1	CH_4	5	N/A	1000	FLG
13F2902	Sputtering Cu/Ni	100 Ni 600 Cu	2.5	CH_4	2	N/A	1000	No C
13F2903	Sputtering Ni	100	5.5	CH_4	1	N/A	1000	No C
13G0101	Cu foil	127000	4	CH_4 H_2	5 cnt	$1.9X10^{-4}$ 0.5	950	FLG
13G0102	Cu foil	76200	3.6	CH_4 H_2	5 cnt	$2.3X10^{-4}$ 0.5	950	FLG
13G0201	Sputtering Cu/Ni (o)	100 Ni 500 Cu	2	CH_4	1	$5.2X10^{-4}$	950	FLG (transfer)
13G0202	Sputtering Cu/Ni (h)	100 Ni 500 Cu	1.5	CH_4	1	$4.1X10^{-4}$	950	a-C
13G0203	Sputtering Cu/Ni (f)	100 Ni 500 Cu	1.8	CH_4	1	$4.8X10^{-4}$	950	FLG
13G0301	Sputtering Cu	500	1.5	CH_4	1	$2.6X10^{-4}$	950	a-C
13G2501	Sputtering Cu/Ni (h)	100 Ni 500 Cu	7.2	CH_4	1	$3.3X10^{-4}$	980	a-C
13G2502	Sputtering Cu/Ni (h)	100 Ni 500 Cu	6.3	CH_4	20	$9.6X10^{-4}$	980	a-C
13L0401	Cu foil	127000	8.5	CH_4	4	$9.1X10^{-4}$	1000	Monolayer
13L0601	Cu foil	127000	7.8	CH_4 H_2	4 cnt	$9.3X10^{-4}$ 0.09	1000	a-C
---	---	---	---	---	---	---	---	---
14A2801	Sputtering Cu	300	-	C_6H_6	3	0.04	550	No C
14A2901	Sputtering Cu	300	-	C_6H_6	3	0.06	550	FLG
14A3101	Sputtering Cu	300	-	C_6H_6	3	0.06	550	FLG
14B0301	Cu foil	127000	-	C_6H_6	5	-	510	FLG
14B0601	Sputtering Cu	50	-	C_6H_6	cnt	5	500	No C
14B0603	Cu foil	127000	-	C_6H_6 H_2	cnt cnt	3 0.05	500	Bilayer
14B1301	Cu foil	127000	-	C_7H_8	cnt	4	500	No C

				H_2	cnt	0.05		
Sample	**Type**	**Thickness (nm)**	**P_0 (10^{-4} Pa)**	**Gas**	**# Pulses**	**P_{pulses} (Pa)**	**T_{CVD} (°C)**	**Raman**
14B1701	Cu foil	127000	-	C_6H_6	30	0.03	500	FLG
				H_2	cnt	46.7		
14B1901	Cu foil	76200	-	C_6H_6	Cnt	20	550	Monolayer
14B2602	Cu foil	76200	-	C_6H_6	40	0.15	700	No C
				H_2	cnt	0.22		
14C0601	Cu foil	76200	-	C_7H_8	30	0.15	600	a-C
				H_2	cnt	0.05		
14C1301	Cu foil	76200	-	C_6H_6	8	0.06	550	a-C
14C1401	Cu foil	76200	-	C_7H_8	8	0.03	550	FLG
14C1402	Cu foil	76200	-	C_7H_8	4	0.02	550	a-C
14C2101	Cu foil	76200	-	C_6H_6	6	0.4	550	Monolayer (transfer)
14C2103	Si (100)	-	-	C_6H_6	16	0.08	600	No C
14C2501	Si (100)	-	-	C_6H_6	10	-	350	a-C
14C2502	Cu foil	76200	-	C_6H_6	3	0.07	500	a-C
14D1701	Cu foil	76200	-	C_6H_6	3	0.04	500	FLG
14D2801	Cu foil	76200	-	C_6H_6	1	0.05	550	Bilayer
14D2802	Cu foil	76200	-	C_6H_6	2	0.07	550	FLG

The H_2 flow is at a constant flux of 10 sccm when constant. Cu foil has a thickness of 3 mil (76.2 μm) and 5 mil (127 μm). The tilted samples are: oposed (o), horizontal (h), or faced (f).